VRIJE UNIVERSITEIT BRUSSEL

ÉCOLE POLYTECHNIQUE DE BRUXELLES
UNIVERSITÉ LIBRE DE BRUXELLES

AUTOMATED UNIT-CELL MODEL GENERATION FOR MICRO-MECHANICAL SIMULATIONS OF 3D REINFORCED COMPOSITES

Thesis submitted in fulfilment of the requirements for the award of the degree of Doctor in Engineering Sciences by

GERRIT PIERREUX

03 Dec 2018

Promotor VUB: Prof. dr. ir. Danny Van Hemelrijck
Promotor ULB: Prof. dr. ir. Thierry J. Massart

Printed by
Crazy Copy Center Productions
VUB Pleinlaan 2, 1050 Brussel
Tel / fax : +32 2 629 33 44
crazycopy@vub.ac.be
www.crazycopy.be

ISBN : 9789493079090
NUR CODE : 971

Abstract

3D reinforced composites are favored for aerospace, automotive and wind turbine application because of their high specific stiffness and strength in the in-plane and out-of-plane directions. In these composites, pins, stitching yarns and binder yarns are inserted through-the-thickness of the in-plane fiber-reinforced regions. Binder parameters as diameter, content, pattern and tensioning can further be varied to regulate the out-of-plane properties. However, the insertion of these binders distorts the reinforcement which further can affect the global and local mechanical behaviour. Unit-cell models offered a valuable approach to assess the effect of the distortions on these mechanical features.

An approach is presented to include the main geometrical features of pinned, stitched and 3D woven composites into mesoscopic unit-cell models. Discretised lines, which represent the main geometrical features, are hereby gradually shaped by geometrical operations while a geometrical contact treatment account for line interactions. The local fiber volume fraction and fiber direction distributions are afterwards modelled on cross-sections in a post-processing step. Tools are further proposed to automatically transform the geometrical models into finite element models. The effect of distortions, local fiber volume fraction and fiber direction, and typical geometrical features for each 3D reinforced composite, on the stiffness and damage initiation stress levels is investigated by means of elastic finite element (FE)-computations.

The shape of geometrical features corresponding to the different binder parameters could automatically be generated and the dimensions of features could be controlled by the parameters of the geometrical operations. The stiffness of a 3D reinforced composite have been observed to be either decreased or increased (dependent on the stacking sequence, the binder type and the loading direction). Early damage initiation in the FE-models was observed to take place near the binder locations, which was mainly caused by transverse and shear cracking in the fiber-reinforced regions. Local fiber volume fraction and fiber direction have shown to affect damage initation mechanisms and stress levels, and should therefore be properly included in the models. In future work, the possibility of the framework to generate unit-cells including voids and micro-vascular networks can be investigated and the finite element models can be extended with damage and crack propagation mechanisms for damage and failure computations.

Acknowledgements

Firstly, I would like to thank Thierry Massart and Danny Van Hemelrijck, as the promoters for my research work. Thierry, thank you for the numerous possibilities you gave me to discuss my research. Your insights and drive for research excellence contributed largely to the quality of this work. I also highly appreciate the way you interacted with me by asking questions and giving advice, rather than directly giving the answer. Danny, thank you for having given me the opportunity to start pursuing a PhD at the VUB, and the freedom in both setting my own research directions as in finding the working environment best suiting my research needs. I also highly appreciate the positive atmosphere you bring to the MeMC-department, contributing directly to the close connections being held between all the MeMC-members. In scope of the research, I would also like to thank Lincy Pyl and Ling Wu, for their research insights and support during this PhD trajectory, as well as the Flemish government for their financial support.

Secondly, a research at both departments would not be as successful as they did not have amazing colleagues. To my VUB-colleagues, thank you for the MeMC-parties we had after PhD defenses, on the BBQ and on the civil engineering dinners, and for your unconditional support even if I was not always there. Special thanks to my office mates Sander, Alexandros, Eleni and Brendan, and simulation buddies Xing and Bin. To my ULB-colleagues, thank you for the kicker-games and the cosy christmas dinner celebrations, and for the discussion moments we had together on research. Special thanks to the older generation PhD buddies Alexis, Hector, Roland, Battoma, Karim, and Bernard. Also thanks to Peter Berke for his endeavors in strengthening the social and research connections between the PhD students, and Guy Paulus in helping me out on Linux and others.

To my colleagues and friends from the VUB governance committees and NSE PhD Network, thank you for the insightful discussions and for the organisation of events together. Also thanks to the MeMC-football team, for winning three cups in a row, but especially for being one team all together. Last but not least, the BAV buddies, thank you for your support and for giving me the space and opportunity to relieve my thoughts after tough working days.

Finally, to my friends and family, for their unconditional support. Milena, Bernard, Jonathan, Florent, Stefaan, Anli, Marta, Frank, thank you for the moments we shared. Special thanks to Jens for all the activities we did together during our PhD, as well as for sharing your interests and advice. To my sisters, brothers, mother and father, and tante Tonia, thank you for providing me a support to which I always could rely on.

Members of the Jury

President	Prof. dr. ir. Patrick Guillaume	VUB
Promoter	Prof. dr. ir. Danny Van Hemelrijck	VUB
Promoter	Prof. dr. ir. Thierry J. Massart	ULB
	Prof. dr. ir. Ludovic Noels	ULiege
	Prof. dr. ir. Wim Van Paepegem	UGent
	Prof. dr. ir. Ling Wu	VUB, ULiege
	Prof. dr. ir. Pierre Gérard	ULB
Secretary	Prof. dr. ir. Peter Berke	ULB
	Prof. dr. ir. Rik Pintelon	VUB

Contents

Nomenclature

Symbols:

R_{line}	radius of a line
$V_{f,lam}^{(,x,y)}$	global fiber volume fraction of the in-plane fiber-reinforced regions (total, in x-direction, in y-direction)
$V_{f,lam}^{x}, V_{f,lam}^{y}$	global fiber volume fraction in x and y direction
$V_{f,stitch}$	the fiber volume fraction in a cross-section of the stitching yarn
V_f	local fiber volume fraction
V_f^{max}	maximum fiber volume fraction in a fiber-reinforced region
$V_{f,c}(u)$	the constant but increased fiber volume fraction near the resin-rich region in a cross-section at position u
$\vec{f}_{lam}$	main fiber direction in a lamina
$\vec{f}_{loc}$	local fiber direction in a lamina
θ_{mis}	local fiber misalignment
$\theta_{mis}^{xy}, \theta_{mis}^{z}$	in-plane and out-of-plane local fiber misalignment
α_i, α_f	initial and final inclination angle of a pin
α_{xy}	angle defining the pin inclination direction
k	distorted zone parameter
s, s_1, s_2, s_3	number of straightening operations
q, q_{sl}, q_{bl}	contact parameter
c	number of lines in the inner-line configuration of a fiber-bundle
E_{norm}, E_{norm^*}	normalised stiffness (normalisation by an equivalent configuration)(normalisation by a corresponding configuration with binder content 0.50%)
f_{22}, f_{12}	transverse and shear damage initiation indicator
f_{int}, f_m	interface and matrix damage initiation indicator
$f_{\cdot}^{97\%}$	97-percentile of the damage initiation indicator
E_{11}, E_{22}, E_{33}	longitudinal and transverse modulus
G_{12}, G_{13}, G_{23}	in-plane and transverse shear modulus
$\mu_{12}, \mu_{13}, \mu_{23}$	Poisson ratio
$X_{11,t/c}, X_{12}$	longitudinal tensile/compressive and shear strength in tension (t) or compression (c)

Abbreviations:

CT	Computed Tomography
NCF	non-crimp fabric
FE	finite element

Glossary:

binder	a through-thickness reinforcement, binding different lamina together (pin, stitching yarn or binder yarn)
binder content	the relative fraction of binder in the unit-cell which is defined by the cross-section area of the binder divided by the in-plane dimensions of the unit-cell
boundary-line configuration	a representation of a lamina or fiber-bundle with lines positioned at the boundaries of the region
crimp	the misalignment of fiber-bundles in textile composites that is inherent to the weave pattern (see Fig. 2.1b)
fiber	the smallest building unit of fiber-reinforced regions
fiber-bundle (or yarn)	a collection of fibers
fiber-reinforced distorted zone	the part of the fiber-reinforced region in Z-pinned and stitched composites which is distorted by the Z-pin or stitching yarn insertion
fiber-volume fraction	the amount of fibers in a given unit-cell
inner-line configuration	a representation of a lamina or fiber-bundle with lines positioned at the interior of the region
in-plane, out-of-plane	the direction in or transverse on the plane of the unit-cell
lamina	a layer of fiber-reinforcement (see Fig. 2.1a)
laminate	a stack of laminae (see Fig. 2.1b)
line	the geometrical tool which is used to generate different shapes of geometrical features
nesting	the configuration where adjacent fibrous layers are penetrating the openings of neighbouring layers (see Fig. 2.1b-c)
out-of-plane undulations	the out-of-plane fiber-waviness in the surface lamina of the stitched laminates underneath the top segment of the stitching yarn
pin content	the relative fraction of the pin in the unit-cell which is defined by the cross-section area of the pin divided by the in-plane dimensions of the unit-cell
pin inclination direction	the direction in which the Z-pin is inclined

resin-rich regions	the openings in the Z-pinned and stitched laminates near the Z-pin and stitching yarn that are filled by resin.
stitch direction	the horizontal direction of the movement of the stitching yarn process during manufacturing, which is identical to the in-plane direction that is aligned with the continuity of the stitching yarn
unit-cell	the smallest unit representing the composite (having assumed periodicity of the manufacturing parameters)
warp, weft	the fiber-bundles in a woven composite that go along (warp) or across (weft) the length of the fabric (see Fig. 6.1a)
x- and y-direction	the (in-plane) periodicity directions of the unit-cell
z-direction	the through-the-thickness direction of the unit-cell
Z-crown	the top segment of the binder yarn which is located on top of the outer lamina surfaces in 3D woven composites (see Fig. 6.1a)

Chapter 1
Introduction

1.1 Background

In automative, aerospace and windturbine industry, fiber-reinforced composites are favored because of their high specific stiffness and strength [1–5]. These high-specific properties originate from the high stiffness and strength of the fibers and the low density of the matrix [6, 7]. The fibers are acting hereby as the main load bearing mechanisms while the matrix holds the fibers in place, protects the fibers against environmental conditions and acts as a medium distributing the load between the fibers. Carbon and glass fibers, and epoxy and polyester matrix are typically used as constitutive materials, but composites constructed from aramid and natural fibers, and other thermoset (e.g. vinyl ester) or thermoplastic resin matrix also exist [8–12].

Different types of fiber-reinforced composites have been manufactured during the last decades. The composites can be classified in prepreg-based and textile composites, according to how the matrix is introduced in the fibrous regions:

1. In prepreg-based composites, the fibers are pre-impregnated with semi-cured matrix [13]. The prepregs can be stacked manually or using automatic tape-laying machines [14] and are further consolidated and cured in auto-clave processes. The resulting consolidated laminates are characterised by a high quality (meaning a small void content) but are rather expensive and are characterised by low out-of-plane properties. The high costs of such composites is related to the use of an auto-clave, and refrigerators which are needed to delay the consolidation process of the thermoset matrix, while the low out-of-plane properties (for laminated prepreg-based composites) are mainly related to the lack of reinforcement in the out-of-plane direction.

2. In textile composites, the manufacturing process starts from a dry-preform which can be produced by different textile processing technologies as weaving, tufting knitting, braiding, etc [15]. The dry-preform is then injected by resin using resin injection techniques, which can be performed under atmospheric pressure and without the need to use an auto-clave The assembly can further be cured in standard ovens. Such composites are cheaper and have more design freedom for the reinforcement architecture than prepreg-based composites, but are more prone to void accumulation and further challenges the research community in their design and mechanical characterisation (due to the wide range of design parameters).

Composites may also be classified according to the architecture of the reinforcement. Typical categorisations are multi-directional laminates, non-crimp fabric composites, woven composites and 3D reinforced composites. The composite architecture for each category is described in more detail in the next chapter.

Mechanical characterisation of the fiber-reinforced composites is needed to obtain the basic input parameters which are necessary properties for the design of structural components. Depending on the complexity of the reinforcement architecture and due to the multi-scale nature of the material (see Fig. 1.1) this process may become quite tedious and complex. At micro-scale, fibers can be distinguished, as their diameters are typically in the range of 5 to $20\mu m$. At meso-scale, fibers are topologically grouped as fiber-bundles and laminae. At macro-scale, the reinforcement architecture can be considered as a homogenised medium. At structural-scale, the composite material can be used in the construction of several applications as wind turbine blades, airplanes, cars, etc. The multi-scale hierachical structure of fiber-reinforced composites results further in mechanisms taking place at different scales with (1) matrix cracking, interface debonding between the fiber and the matrix, and fiber-breakage taking place at the micro-scale; [16–22] and (2) transverse and shear cracking in the fiber-reinforced regions, interface debonding between the fiber-reinforced regions and the matrix, and cracking in the matrix taking place at the meso-scale [23–26]. The mesoscopic damage mechanisms can then evolve into mesoscopic failure, macroscopic failure and ultimately structural collapse upon increasing load or deformation levels.

Experimental techniques have been applied to study the mechanical behaviour of fiber-reinforced composites. Tensile and compression tests can be performed on a composite specimen to obtain its global mechanical properties while digitial image correlation, accoustic emission, fiber-optic sensors and X-ray experimental techniques can be used to assess the local strain levels on the specimen surface, local strain levels in the specimen, the amount of damage and the locations of damaged regions in the specimen respectively [27–32]. Imaging techniques such as optical and scanning electron microscopy, and micro-CT scans, can be used to assess the geometrical features of the reinforcement architecture, voids and crack patterns on 2D cross-section cuts of the specimen or in the whole specimen respectively [33–43]. Such investigations allow obtaining realistic geometrical and mechanical features but are time consuming, often expensive and inefficient to optimise the wide range of reinforcement parameters in an early design stage.

Unit-cell models have offered a powerful approach to help experimental investigations in the mechanical characterisation of fiber-reinforced composites [44–47] (as well as of other hetereogeneous materials [48–55]) and the further understanding of the correlation between geometrical and mechanical features at multiple scales:

1. **At micro-scale**, a square or hexagonal fiber distribution was initially assumed in unit-cell models [20, 45, 46, 56–58]. Random fiber distributions were considered afterwards to account for more realistic fiber distributions in the unit-cell models [59–66]. The size of the unit-cell with randomly-distributed fibers needs then to be determined from a convergence study on the stiffness or the local stress distribution characteristics of the unit-cell model [67–73].

2. **At meso-scale**, a unit-cell of fiber-bundles and lamina is often considered in which the reinforcement architecture is assumed periodic [44,45,74–76] The fiber-reinforced regions are hereby represented by their boundary and local fiber volume fractions and fiber direction distributions. The boundary of the region can be represented in the model using analytical and computational approaches. The local fiber volume fraction and fiber direction distribution are often modelled analytically in a post-processing applied on the constructed geometrical models [77, 78].

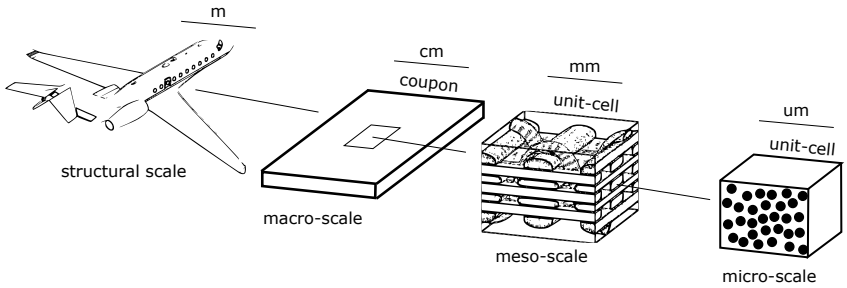

Fig. 1.1: Different scales in fiber-reinforced composites.

1.2 Problem statement

3D reinforced composites have been developed to increase effectively the delamination resistance of laminate composites [79–83]. Typically, Z-pinned laminates, structurally stitched non-crimp fabric composites and 3D woven composites are considered as the main types of 3D reinforced composites. A reinforcement (or binder) is inserted for this purpose through-the-thickness of the composites. The insertion of the binder has shown to increase the out-of-plane properties [84–90], but also to distort the in-plane reinforcement architecture, which may affect the in-plane mechanical behaviour [80]. Mesoscopic unit-cell models have then been presented to investigate the effect of these distortions on the in-plane mechanical behaviour. A brief description of the distortions and the approaches used in the literature to generate mesoscopic unit-cell models for each 3D reinforced composites type, are presented in the following. A more detailed description of the distortions and presented models for each 3D reinforced composite type can be found in the corresponding chapters.

1. **In Z-pinned laminates**, pins are inserted through-the-thickness of prepreg-based laminates. Resin-rich regions and local fiber distorted zones near the pins are present (see Fig. 1.2a). The shape and size of these features dependent on the pin parameters as pin diameter, content and inclination angle, and can further be affected by pin rotation during the manufacturing process. The pin can be assumed rigid.

   In the mesoscopic unit-cell models presented in [91–93], the distortions were modelled using analytical modelling approaches. The lamina were considered straight. The resin-rich regions were modelled by cosine or orthorhombic shapes.

The fiber-reinforced regions in each lamina were represented by a constant fiber volume fraction and local variations in the fiber misalignments near the pin. However, the models do not account for variations in local fiber volume fraction in each lamina, and do not account for shapes of resin-rich and fiber-reinforced distorted regions affected by pin rotation.

2. **In structurally stitched non-crimp fabric composites**, a stitching yarn is inserted through-thickness of non-crimp fabric composites. Resin-rich regions and fiber-reinforced distorted zones in the lamina are present near the stitching yarn, as well as out-of-plane undulations of the surface lamina caused by the continuity of the stitching yarn (see Fig. 1.2b). The shape and size of these features are affected by stitch content, diameter and stitch tensioning. The stitching yarn is assumed to be deformable. The shape of the stitching yarn is correlated with the shape of the resin-rich regions and out-of-plane undulations of the lamina, and is further affected by the stitching yarn tensioning. The term 'structurally' refers to the fact that the stitching yarn acts both as a binder (binding the plies together) and structural reinforcement (increasing the delamination resistance).

   In the mesoscopic unit-cell models presented in [94–99], the distortions were modelled using analytical modelling approaches for both the laminae and the stitching yarn. The lamina were often assumed straight with resin-rich regions being modelled by cosine or orthorhombic shapes. The stitching yarn was modelled using pre-assumed centerline and cross-section shapes. However, the models do not consider the out-of-plane undulations and the conformity of the deformable stitching yarn with the shapes of in-plane fibrous regions.

3. **In 3D woven non-crimp fabric composites**, a binder yarn is inserted through-the-thickness of in-plane positioned fiber-binders. The distortions of the fiber-reinforced regions are less severe, compared to pinned and stitched laminates, as the binder yarn is inserted inbetween the fiber-bundles. Small fiber-reinforced distorted zones and out-of-plane undulations in the surface layers can be present near the binder yarn (see Fig. 1.2c). These features further depend on binder content, diameter and pattern. The binder yarn is assumed to be deformable. The shape of the binder yarn is conform with the local undulated shapes of the in-plane fiber-bundles and is dependent on the binder yarn tensioning.

   In the mesoscopic unit-cell models presented in [100–105], the distortions were effectively modelled using more advanced modelling approaches (both analytical and computational), compared to the pinned and stitched laminates. The more advanced modelling approaches (which are described in more detail in the next chapter) allowed generating realistic 3D woven unit-cell models. However, a unified (computational) framework for the generation of pinned, stitched and 3D woven unit-cell models does not exist to the best knowledge of the author.

In summary, the mesoscopic unit-cell models for Z-pinned and stitched composites presented in literature do not include all features of the in-plane fibrous regions distortions. These features should therefore be included in the models, and their effect on the in-plane mechanical behaviour should be investigated to reach a predictive mechanical

model generation. Furthermore, a unified framework for an automated generation of pinned, stitched and 3D woven composites can be desirable in the design stage of 3D reinforced composites.

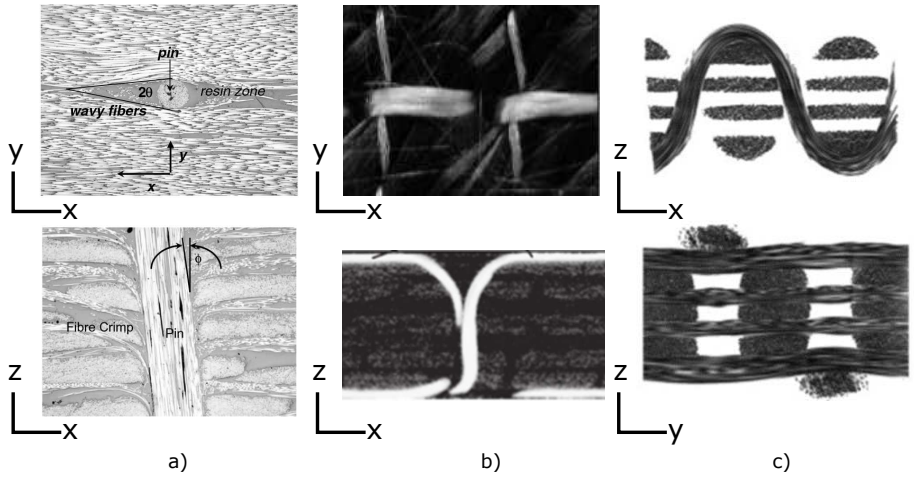

Fig. 1.2: Geometrical features present in 3D reinforced composites: (a) pinned laminate [106], (b) stitched non-crimp fabric composite [89], (c) 3D woven non-crimp fabric composite [107].

1.3 Objectives and contributions

In view of these informations and of the state-of-the art on each 3D reinforced composite presented in the corresponding chapters, the objectives are the following:

The first objective of the work is to generate realistic mesoscopic unit-cell models for Z-pinned and stitched composites. Combined with this, the wish is to present an automated and unified modelling framework for the unit-cell model generation for pinned, stitched and 3D woven composites. With respect to this objective, the following contributions have been made:

1. A novel approach is presented to generate in an automated way unit-cell models for Z-pinned and stitched laminates. The geometrical features of reinforcement distortions caused by binder insertion are shaped computationally, rather than analytically as adopted in current literature. The approach allows generating seamlessly the shapes of the reinforcement distortions corresponding to the different binder parameters, while accounting for additional geometrical features in the unit-cell models which may affect the mechanical behaviour.

2. A novel fiber-distorted zone model has been introduced to account for the local fiber-reinforced distortions in the Z-pinned and stitched laminates.

3. Unit-cell models including more (realistic) geometrical features for Z-pinned and stitched laminates have been generated. In Z-pinned laminates, pin rotation and the corresponding local fiber-reinforced distorted regions have been accounted for. In stitched laminates, the out-of-plane lamina undulations, a deformable stitching yarn conform with the shapes of the in-plane fiber-reinforced regions, and corresponding local fiber-reinforced distorted regions have been considered.

The second objective of the thesis is to study the effect of these geometrical features on the mechanical stiffness and damage initiation levels. The main focus is related to: (1) the effect of binder type and content, (2) the effect of pin rotation in Z-pinned laminates, out-of-plane undulations in stitched laminates and binder-yarn cross-section variations in 3D woven composites, and (3) the effect of local fiber volume fraction and fiber misalignment in each of the 3D reinforced composite types. The understanding of the effect of geometrical features on the mechanical behaviour complements the knowledge on the mechanical behaviour for fiber-reinforced composites (which is described in the next chapter). Note that the main focus of this study was to investigate the in-plane mechanical behaviour.

1.4 Outline

To address the topic in a progressive manner, the manuscript is organised in the following structure:

Chapter 2 provides a background in aspects which are needed to understand the state-of-the art in the generation of mesoscopic geometrical models for different types of fiber-reinforced composites. Different types of fiber-reinforced composites, different geometrical modelling approaches and the role of certain mesoscopic geometrical features on the stiffness and damage initiation mechanisms and stress levels are presented.

Chapter 3 presents the tools required to transform the geometrical models consisting of discretised lines into finite element models consisting of conforming tetrahedral meshes with in-plane periodic surface meshes. The implementation details of the (first-order) computational homogenisation framework, which is used to load the unit-cell and to extract the mechanical properties after simulation, are presented as well.

Chapter 4 presents the generation of geometrical unit-cell models and the results of mechanical simulations specific to Z-pinned laminates. It includes a state-of-the-art in the geometrical model generation for Z-pinned laminate, our geometrical model generation approach applied to Z-pinned laminates, a fiber-reinforced distorted zone model, an illustration on the shapes of the geometrical features which can be generated by the approach. It is complemented by mechanical simulations illustrating the effect of lamina orientation, fiber volume fraction, fiber misalignment and pin inclination on the stiffness, as well damage initiation mechanisms and stress levels for typical loading conditions.

Chapter 5 presents the application of the generation methodology to geometrical unit-cell models, as well as the results of mechanical simulations, for structurally stitched

non-crimp-fabric composites. It includes a state-of-the-art of the geometrical model generation for stitched laminates, our geometrical model generation approach for stitched laminates, an extension of fiber-reinforced distorted zone model of pinned laminates, an illustration on the shapes of the geometrical features that can be generated by the approach. Mechanical simulations are given, illustrating the effect of fiber volume fraction, fiber misalignment and model simplifications on the stiffness and damage initiation mechanisms and stress levels.

Chapter 6 presents the generation of geometrical unit-cell models and the results of the corresponding mechanical simulations for 3D woven non-crimp fabric composites. It includes a state-of-the-art related to geometrical model generation for 3D woven non-crimp fabric composites, our geometrical model generation approach for 3D woven composites, an illustration on the shapes of the geometrical features which can be generated by the approach, mechanical simulations illustrating the effect of cross-section variations in the binder and weft yarns on stiffness and damage initiation mechanisms and stress levels. A discussion on the different modelling approaches which are present to generate 3D woven models and on the role of local fiber-volume fraction in the 3D woven composite models.

Chapter 7 illustrates the further use of the framework by two case studies. In the first case study, the possibility of the geometrical modelling approach to generate simultaneously the contours and local fiber-reinforced distorted zones of a distorted lamina is investigated, using hereby an inner-line configuration for the lamina. In the second case study, the effect of binder content and type is illustrated on geometrical and mechanical features, using hereby the generated unit-cell models.

Chapter 8 presents the main conclusions and future perspectives in geometrical model generation and mechanical simulations.

Chapter 2
State of the art

This chapter provides a background on the main aspects which are required to understand geometrical model generation in fiber-reinforced composites. The main types of fiber-reinforced composites are shortly described, with the main mesoscopic geometrical model generation approaches for such fiber-reinforced composites. The main geometrical features of the fiber-reinforcement architecture affecting the stiffness and damage imitation for in-plane mechanical loading conditions are also addressed.

2.1 Different types of fiber-reinforced composites

Fiber-reinforced composites can be classified according to how the fibers are positioned. Different fiber-reinforcement architecture then result in different mechanical properties:

1. **Multi-directional laminates**: the fibers are positioned unidirectionally in laminae (prepregs) (Fig. 2.1a). The laminae can be stacked on each other to generate thicker composites. The stacking sequence can be controlled to optimise the mechanical properties in the different in-plane directions. The multi-directional laminates are often classified in unidirectional, orthogonal ($[0°/90°]$) and quasi-istropic ($[0°/60°/-60°]$) laminates, but dispersed stacking sequence laminates can also be present [108–110]. The undirectional orientation of fibers in a lamina in its in-plane direction results further in high in-plane properties, but low out-of-plane properties.

2. **2D woven composites**: fiber-bundles are orthogonally interwoven according to a certain weave pattern (Fig. 2.1b). The weave patterns differ in the number of fiber-bundles which are crossed by a perpendicular fiber-bundle before going to the other side. The 2D woven lamina can then be stacked on top of each other to generate thicker composites. Nesting of laminae can take place during transverse compaction (as the relative position of laminae during stacking is not controlled), wich further results in laminate thicknesses that are smaller than the sum of the thickness of their individual laminae [111]. The in-plane properties of 2D woven composites are reduced compared to multi-directional laminate while the out-of-plane properties are slightly increased but a rather small delamination resistance between the different lamina layers is still present due to a lack of through-the-thickness reinforcement.

3. **2D braided composites**: fiber-bundles are braided in two directions with an angle inbetween that can be different from $90°$ (Fig. 2.1c). Braid patterns can differ

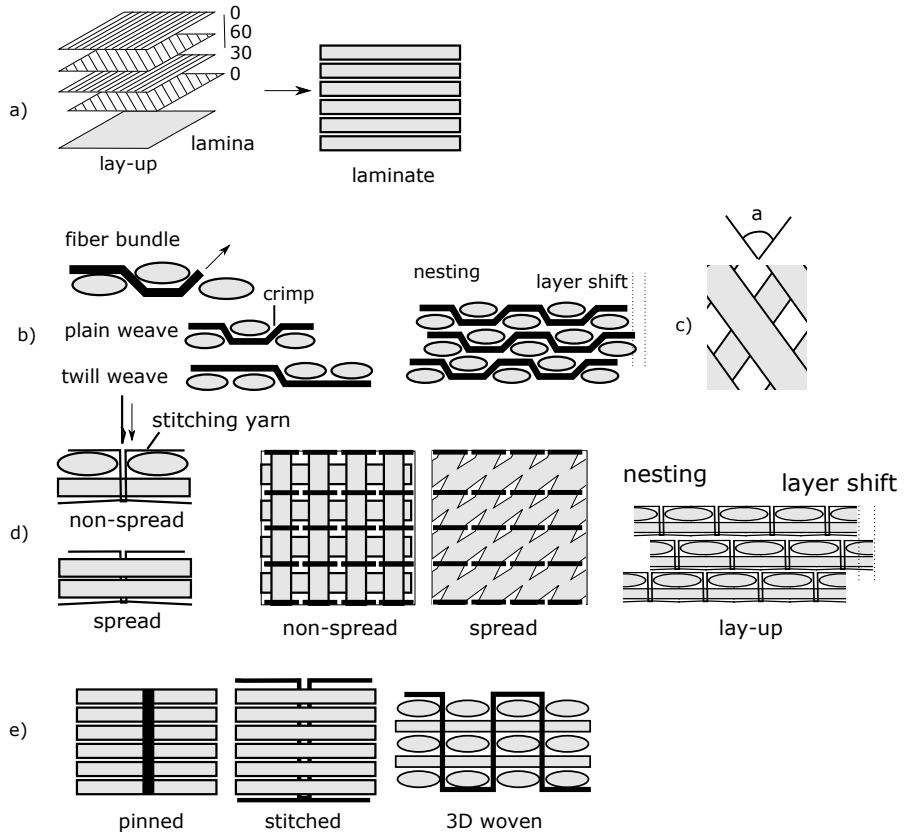

Fig. 2.1: Different types of fiber-reinforced composites: (a) multi-directional laminates, (b) 2D woven laminates, (c) 2D braided laminates, (d) non-crimp fabric laminates (non-spread and spread fiber-bundles), (e) 3D reinforced composites.

in the number of fiber-bundles that are crossed by a fiber-bundle, similarly to 2D woven composites. 2D braided composites are characterised by increased shear properties compared to 2D woven composites due to the presence of off-axis fiber-bundles [112, 113].

4. **Non-crimp fabric composites**: fiber-bundles are aligned in certain in-plane directions and subsequently stitched by a small binder yarn (Fig. 2.1d). The fiber-bundles can be positioned individually or can be spread using advanced air-flow technology into thin fiber-reinforced regions with the spread fiber-bundles having improved out-of-plane properties [114], and lower production cost [115,116] compared to the individually positioned fiber-bundles. Lamina of fiber-bundles can then be stacked, during which nesting of fiber-bundles of one lamina into resin-rich regions of the other lamina can take place (as also here the relative position of the lamina is not controlled during stacking). The in-plane and out-of-plane properties of these non-crimp fabric composites are, due to the non-structural stitching,

slightly decreased and increased respectively [87, 117–119]. This is also similar to the effect of structurally stitching of non-crimp fabric composites which will be addressed in this work.

5. **3D reinforced composites** (Z-pinned, structurally stitched and 3D woven composites): a through-the-thickness reinforcement is inserted in laminates to improve their out-of-plane properties and delamination resistance (Fig. 2.1e) [80, 120]. Metal or fibrous pins can be inserted in prepreg-based laminates to produce Z-pinned laminates [121]. A thick fiber-bundle can also be stitched through-the-thickness of non-crimp fabric composites to produce structurally stitched non-crimp fabric composites [95]. A thick fiber-bundle can be woven inbetween in-plane positioned fiber-bundles to produce 3D woven composites [122]. 3D braided composites also exist whereby the fiber-bundles are braided in both in-plane and out-of-plane directions [113]. Binder parameters such as binder content, diameter, tensioning, pattern can be tailored for each 3D reinforced composite to optimise their mechanical properties. The out-of-plane properties of 3D reinforced composites are significantly improved (pinned [123, 124], stitched [87, 125], 3D woven [126, 127]), while experimental results remain ambiguous on whether the binder insertion decraeses, increases or leaves unchanged the in-plane mechanical properties [80].

The types of composites can be used for a wide range of applications, dependent on the mechanical features in the in-plane and out-of-plane directions, the cost, the quality, the draping behaviour, and the requirement of the applications. Aersopace applications require high-quality products for which prepreg-based multi-directional laminates can be desired. Automotive applications require low cost and manufacturing time for which dry-preform solutions can be more ideal. 3D reinforced composites are desired for applications with out-of-plane loading conditions.

2.2 Approaches for mesoscopic geometrical model generation

Mesoscopic geometrical models have to be generated to represent the fiber-reinforcement architecture of the composite materials if one wants to resort to mechanical simulations. The fiber-reinforcement architecture can mostly be deconstructed in fiber-bundles and lamina (with openings) at the meso-scale. Fiber-bundles are often characterised by a center line and cross-sections while laminae (with openings) are often characterised by lines describing the openings or out-of-plane undulations. Three types of approaches can be distinguished to position and shape the lines and cross-section representing the fiber-bundles and laminae, and so to generate geometrical models including certain geometrical features: (1) descriptive approaches tend to describe explicitly the geometrical features of the reinforcement architecture; (2) predictive approaches tend to predict the position and the shapes of the features by modelling the mechanical behaviour of the dry fiber-reinforced regions and the load conditions during the different manufacturing stages; (3) kinematics approaches tend to position or shape the features by a computational approach, which is not necessarily predictive but can be used to ease the posi-

tioning and shaping of the geometrical features. The approaches are further classified in this work into analytical (descriptive), image-based (descriptive), energy-based (predictive), finite element based (predictive, kinematics), digital element (kinematics) and geometrical operations (kinematics) (see Table 2.1).

approach	type	advantage	main limitation
analytical	D	simple, fast	simplified models
image-based	D	realistic	cost, non-parametrised
energy-based	P	predictive	simplified models
FE-based	P	variable cross-sections	limited applicability
digital element	K	variable cross-sections	time consuming
geometrical operations	K	elegant	no mechanics involved

Table 2.1: A categorisation of the geometrical modelling approaches, whereby the approaches are classified into descriptive (D), predictive (P) and kinematics (K).

2.2.1 Analytical approach

In analytical modelling approaches, mathematical functions are used to represent the geometrical features in fiber-reinforced composites [101, 111, 128–130]. A cosine function can be adopted to represent the centerline of a fiber bundle or the waviness of fibers in a fiber-reinforced distorted zone in Z-pinned laminates for instance [131]. B-splines, or simply a collection of straight and circular segments, can be adopted to represent more complex-shaped centerlines of fiber-bundles (for example a stitching and binder yarns) [94]. Circular, elliptical or lenticular cross-sections are often adopted to represent symmetrical-shaped cross-sections of fiber-bundle or openings in laminae. More advanced cross-section shapes can be constructed by simply combining analytical functions in the plane of the cross-section [132, 133]. The shape of geometrical features in contacting fiber-reinforced regions further needs to be as realistic as possible to avoid interpenetrations that would make meshing impossible (see chapter 3). The analytically-determined shapes of the centerline and cross-section for a fiber-bundle, or a lamina, can then be combined into a parameterised surface representing the region [130].

2.2.2 Image-based approach

Images of composite materials can be obtained from optical or scanning electron microscopy or from micro-CT techniques. The obtained images consist of pixels that are positioned in a regular grid and to which a gray-value is assigned. The gray-level of each pixel represents the attenuation of X-rays or the reflection of electron waves upon their local interaction with the specimen material, which depends on certain physical properties of the analysed material. Differences in physical properties between the fibers and matrix, or fiber-reinforced regions and matrix (depending on the image resolution), results in different gray-values which can further be exploited in image segmentation processes that intend to separate both regions [134–136]. A grey-scale threshold, which can be set manually or automatically [137–139], is hereby used. The segmented images represent then the fibrous and matrix region by means of voxels (in 3D) which can be used

directly as a voxel mesh, or first be post-processed to smoothen the step-wise boundaries of the fibrous region which have been shown to act as artifical stress concentration regions [140, 141]. Image-based approaches have shown to be useful in the extraction of realistic geometrical models for fiber-reinforced composites [43, 142–148] (and other material types [42, 149–153]), and are further challenged by the limited contrast which can be present between fibers/fiber-reinforced regions and the matrix [144, 154–156].

2.2.3 Energy-based approach

In energy-based approaches as adopted in [157–160], the position of nodes controlling the centerline or cross-section shapes of fiber-bundles in 2D or 3D woven composites can be predicted for in-plane and out-of-plane loading conditions, by means of an energy integral equations that relate the geometry of an initial analytical model and the internal mechanisms with the externally applied load. The centerlines and cross-sections of fiber-bundles are represented by straight and circular segments, and elliptical-shaped cross-section, respectively. Stretching, bending and transverse compaction of the fiber-bundles, as well as friction between the fiber-bundles, are considered as internal mechanisms. In-plane tension and compression and transverse compaction can be considered as external loading conditions. Integral equations, representing the equality between internal and external work, are constructed and solved iteratively, whereby the position of the control nodes are the model parameters. Geometrical models can then automatically be generated, with the positions of the yarns and dimensions of the yarn cross-section being correlated with different externally applied load conditions, while the shape of the features remains the same as initially assumed. Such an approach can be done practically by (1) considering an initial analytical model of the woven composites, (2) implementing the integral expressions and (3) solving the integral equations, as being done in the sofware WiseTex [158].

2.2.4 Finite element-based approach

Finite-element based frameworks were adopted in the generation of geometrical models for 2D and 3D woven composites to include cross-section variations of the fiber-bundles. In [160–162], a simplified analytical 2D woven model is initially considered in which each fiber-bundle is represented by a single line with a constant cross-section. The fiber-bundles are then transformed into a finite element model with continuum elements representing the fibrous regions. The finite element model is then subjected to a transverse compaction while contact elements are introduced during the simulation to account for interactions between the fiber-bundles. Cross-section variations in fiber-bundles, which relate to different levels of transverse compaction, can automatically be obtained.
In [163, 164], an initial model of a 3D woven composite represents the fiber-bundle by a single line and a constant circular cross-section whereby local interpenetrations, which are present between the fiber-bundles, are resolved by means of FE simulations. For this purpose, the fiber-bundles are transformed into shell elements which are positioned along their contour. The contours of the fiber-bundles are then gradually inflated by a hydrostatic pressure, until a desired fiber-bundle volume fraction, while contact elements are introduced during the simulations to account for fiber-bundles interactions. The

cross-sections of the fiber-bundles which are conform with the shapes of neighbouring fiber-bundles and smoothly varying along the fiber-bundle direction can automatically be obtained.

In [165], a deformed digital element-based model of a 3D woven composites is transformed into a shell element-based model. The shell element based model was then used in draping simulations performed at structural-level.

2.2.5 Digital element approach

Frictionless connected rod or bar elements are used in [103, 165–167] to represent a fiber-bundle in 2D and 3D woven composites, on which then mechanical loading conditions can subsequently be applied during a finite element simulation to generate geometrical models. This approach differs from the previous described FE based approach in the fact that fiber-bundles are represented by rod or bar elements, rather than by a continuum finite elements. Originaly, a single-chain was used to represent a fiber-bundle and the kinematics of the weaving process were explicitly accounted for by explicit finite element simulations [168]. Later on, multi-chains representations of fiber-bundles were introduced to allow the deformation of fiber-bundle cross-sections [169] and an initial loose state configuration was considered to reduce the computational time [104, 170–172]. The multi-chain configurations of the fiber-bundles were then positioned in an initial loose state configuration, whereafter a thermal contraction on the binder yarn and a transverse compression on the unit-cell can be applied successively to mimic binder yarn tensioning and transverse compaction during the manufacturing stages respectively (see Fig. 2.2). Centerline deflections and cross-section variations in fiber-bundles, correlating with different binder yarn tensioning and transverse compaction load levels, can automatically be generated. The approach can further be adopted to predict the mechanical behaviour of fabric upon in-plane tension, compression and shear, transverse compaction and impact loading [173–178].

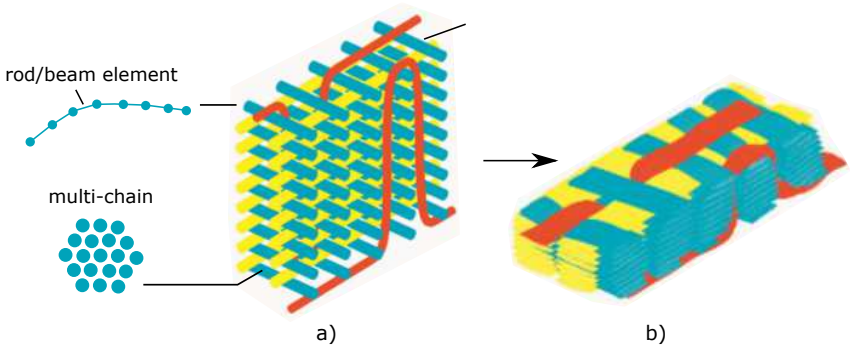

Fig. 2.2: Digital element framework: (a) initial loose configuration, (b) deformed configuration after thermal contraction of the binder yarn and transverse compaction applied on the unit-cell (the images of the 3D woven composites are reproduced from [103]).

2.2.6 Geometrical-based approach

A geometrical-based framework was adopted [105, 179] to generate geometrical models of 2D and 3D woven composites with fiber-bundles represented by constant cross-sections. Initially, discretised lines, representing the centerlines of the fiber-bundles, are positioned in a loose state configuration. A straightening operation is then applied successively on the discretised lines, while a contact treatment account for the interacterions between the yarns representations. The straightening operations are applied successively until a geometrical configuration is obtained with straight paths between the contacting points of interacting yarns. A contact parameter, which regulates the interactions between interpenetrating yarns, was adopted to generate geometries corresponding to different fiber-bundles tensioning levels. Models for different weave patterns and fiber-bundles tensioning levels can hereby be easily generated low computational cost.

2.2.7 Comparison

Each approach can be assessed based on its simplicity, its generality, its computational cost, etc.:

1. The analytical approach is the simplest, but it requires extensive experimental observations and generates models which are often simplified.

2. The image-based approaches allow generating realistic geometrical models, but it is rather expensive, requires experimental observations and produces geometrical models which are not parametrised and therefore not general for other reinforcement architectures.

3. The energy-based approach allows predicting the geometries for in-plane and out-of-plane loading conditions, but it has not been applied to Z-pinned (and stitched) laminates (and this works intends towards the presentation of an unified methodology for the 3D reinforced composites).

4. The finite element approaches allow including realistic cross-section variations in fiber-bundles for transverse compaction, but they are often complex to implement and time consuming, and require a detailed knowledge of complex FE simulations by the analyst.

5. The digital element approach offers a unique way to generate complex geometrical models including fiber-bundle deformations in 2D and 3D woven composites for different binder yarn tensioning and transverse compaction load levels. However, it remains computationally expensive, and was only adopted so far for the generation of 2D and 3D woven models.

6. The geometry-based approach carries the advantage of being computationally not expensive, but it is not predictive and only adopted for 2D and 3D woven composites so far, assuming in this last case constant cross-sections for the fiber-bundles.

The approach adopted in the generation of geometrical models for a given reinforcement architecture thus depends on the complexity of the reinforcement architecture, the need for a parametrised model, the computational cost.

2.3 Effect of mesoscopic features

The fiber-reinforcement architecture should be characterised, for use in unit-cell models, by geometrical features that can potentially affect the mechanical behaviour [128, 180–182]. Global fiber volume fraction, fiber misalignment distributions and composites thickness may affect mainly the stiffness. Local fiber volume fraction and fiber misalignment, composite thickness variations and neighbouring fiber-reinforced regions may affect more the local stress concentrations, which in turn may be determinant for damage initiation and strength levels. In the sequel based on the automated generation of unit-cell models, a more in-depth investigation is therefore presented on the effect of these geometrical features on the stiffness and damage initiation.

2.3.1 Global fiber volume fraction

The global fiber volume fraction represents the total amount of fibers present in the unit-cell (with possibly making a distinction between both in-plane directions). A larger global fiber volume fractions is mostly associated with larger stiffness of the components, but this statement should be treated cautiously as the level of reinforcement distortions for higher fiber volume fraction may increase, which has a detrimental effect on the stiffness for a given global fiber volume fraction [35, 160, 183–185].

2.3.2 Local fiber volume fraction

The local fiber volume fraction V_f represents the amount of fibers that is locally present in the fiber-reinforced regions inside a microscopic unit-cell. The effect of the local fiber volume fraction on local stress concentrations affecting damage initiation at the microscale is illustrated in the following (assuming everything remains linear until failure). Herefore, the Chamis equations [186] (see Eq. 2.1) and the emperical approximate formulae as presented in [187, 188] (see Eq. 2.2) are used to calculate the Young moduli E_{ij}, the shear moduli G_{ij} and the Poisson ratio ν_{ij}), and the strength components X_{ij}, respectively, as suggested in [44].

$$E_{11} = V_f.E_{f_{11}} + (1-V_f).E_m \tag{2.1a}$$

$$E_{22} = \frac{E_m}{(1-\sqrt{V_f}.(1-E_m/E_{f_{22}}))} \tag{2.1b}$$

$$G_{12} = \frac{G_m}{(1-\sqrt{V_f}.(1-G_m/G_{f_{12}}))} \tag{2.1c}$$

$$G_{23} = \frac{G_m}{(1-\sqrt{V_f}.(1-G_m/G_{f_{23}}))} \tag{2.1d}$$

$$\nu_{12} = V_f.\nu_{f_{12}} + (1-V_f).\nu_m \tag{2.1e}$$

$$\nu_{23} = (\frac{E_{22}}{2.G_{23}}) - 1 \tag{2.1f}$$

$$X_{11}^t = V_f + X_{f11}^t + (1 - V_f).X_m^t.\frac{E_m}{E_{f11}} \tag{2.2a}$$

$$X_{11}^c = \frac{G_m}{(1 - (V_f.(1 - G_m/G_{f12})))} \tag{2.2b}$$

$$X_{22}^t = (1 - V_f).X_m^t.E_t/E_m \tag{2.2c}$$

$$X_{22}^c = (1 - V_f).X_m^c.E_t/E_m \tag{2.2d}$$

$$X_{12}^s = X_{22}^c/2 \tag{2.2e}$$

Fig. 2.3 illustrates the effect of the local fiber volume fraction on the in-plane stiffness and strength components (using Eq. 2.1, Eq. 2.2), and on the in-plane failure strain components (obtained by dividing the corresponding strength component with the corresponding stiffness components) for a unidirectional lamina. The local fiber volume fractions were varied from 0.50 to 0.90 as being typical a range of values present in fiber-reinforced composites [35, 99, 189, 190]. The stiffness and strength components for the different fiber volume fractions were further normalised by the values of the parameters corresponding to a V_f equal to 0.50. The following can be observed (for increasing values of V_f): first, all in-plane stiffness components are increased, where the shear stiffness is increased the most (see Fig. 2.3a); secondly, the longitudinal strength X_{11} is increased while the transversal and shear strength (X_{22} and X_{12} respectively) are decreased (see Fig. 2.3b); thirdly, the failure strain in longitudinal direction ε_{11}^f is almost constant while a much larger decrease is present in the transversal and the shear direction (ε_{22}^f and ε_{12}^f respectively) (see Fig. 2.3c). Regions with a higher local fiber volume fraction are thus susceptible to early damage initiation in transverse and shear direction due to both an increased stiffness (which increase the stress concentrations) and a reduced strength (causing early damage initiation). Both effects should then be accounted for in the assessment of the criticality of local fiber volume fraction on damage initiation. Other contributions stating the effect of local fiber volume fractions in fiber-reinforced composites on local stress concentrations and damage initiation mechanisms can be found in [77, 78, 133, 191–193].

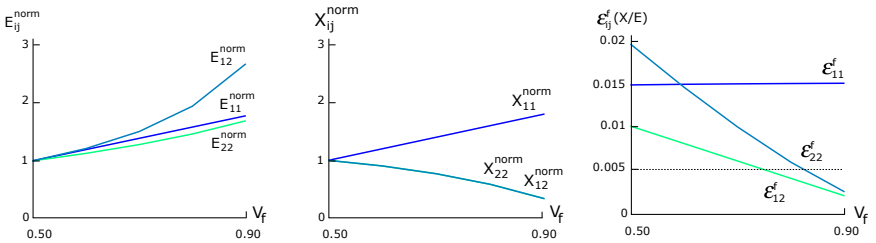

Fig. 2.3: An illustration on the effect of the local fiber volume fraction V_f on the local normalised stiffness, the strength and the failure strain in uni-directional fiber-reinforced regions (having used hereby the Chamis-formulae [186]).

2.3.3 Local fiber misalignment

Local fiber misalignment which affects the in-plane mechanical behaviour can be defined as the angle between the local fiber direction and the in-plane loading direction. In unidirectional lamina, the local fiber direction can be determined from the main fiber direction and variations of a local fiber direction to this main fiber direction. In textile composites, the local fiber direction in a fiber-bundle can be determined from the local tangent to the fiber-bundle centerline and local variations to this tangent. The number of crimp regions (defined as the regions with the most inclined segment of the fiber-bundle, see Fig. 2.1b) can further be used in 2D woven composites to represent the level of fiber misalignment inherent to the weave pattern (for in-plane loading).

Effect on the stiffness

Fig. 2.4 illustrates the effect of the main fiber misalignment in a unidirectional lamina on the stiffness. The graph was obtained using Eq. 2.3a ([194]) in which the stiffness of each lamina was further normalised by the stiffness of the lamina with fibers aligned in the load direction. It can be seen that the stiffness is drastically reduced for small fiber misalignments, while the further reduction in stiffness is much smaller for even larger fiber misalignments. For undirectional laminae with non-uniform fiber misalignment distributions, the stiffness can be determined from the weighted mean of the stiffness components corresponding to certain fiber misalignments (see Eq. 2.3a).

$$E_p(\theta) = [\frac{\cos^4\theta}{E_{0(x)}} + \frac{\sin^4\theta}{E_{0(y)}} + (\frac{1}{G_{0(xy)}} - \frac{2\nu_{0((xy)}}{E_{0(x)}})\sin^2\theta\cos^2\theta]^{-1} \tag{2.3a}$$

$$E_{p(x)} = V_p.E_p(\theta) + (1-V_p).E_{0(x)}) \tag{2.3b}$$

where V_p is the volume fraction of the lamina with fibers aligned in the direction defined by θ and E_p is the stiffness of the lamina in the horizontal direction (being the x-direction in Fig. 2.4). $E_{0(x)}$, $E_{0(y)}$ and $G_{0(xy)}$, and $\nu_{0(xy)}$, are the in-plane stiffness components and Poisson coefficient of the lamina with fibers aligned in the load direction respectively. The formulae will be used to help explaining qualitatively the effect of reinforcement distortions on the stiffness in the 3D reinforced composites (see corresponding chapters).

In 2D woven composites, the crimped regions are responsible for a reduction in the in-plane stiffness [195] and this reduction enlarges for more crimped regions [196]. For example, plain weaves have a larger reduction in stiffness compared to twill or satin weaves, while non-crimp fabric composites, in which no crimped regions are present, have a higher stiffness compared to woven composites. Cross-section variations in fiber-bundle, and their corresponding in-plane and out-of-plane fiber misalignment, can also cause a reduction in the stiffness. For example, the binder yarn in 3D woven non-crimp fabric composites causes cross-section distortions and corresponding fiber misalignments which have been shown to affect the stiffness.

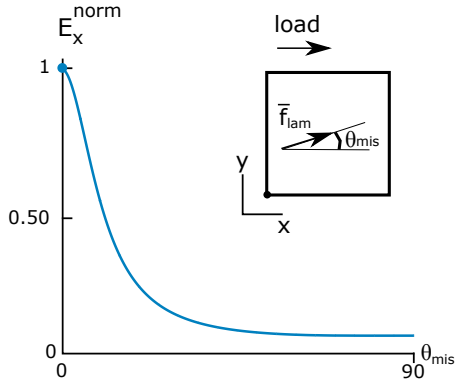

Fig. 2.4: An illustration on the effect of the local fiber misalignment θ_{mis} on the local stiffness E (having used hereby Eq. 2.3a).

Effect on local stress concentrations

Locally misaligned fibers cause local stress concentrations on the neighbouring matrix and on the interface between the fiber and the matrix. The level of the stress concentrations depends on fiber misalignment distribution characteristics.

For a undirectional lamina, the maximum fiber misalignment is often considered as the geometrical feature determining the strength of the lamina [197]. The size, the position in the lamina and the fiber waviness distribution characteristics (uniform, gradual, random) of the region with fiber-misalignment can also affect the strength [131, 198–203]. The local fiber misalignment can further change the damage initiation mechanisms in fiber-reinforced regions that are transversally loaded from transverse cracking to shear cracking and longitudinal splitting [23].

For textile composites, the crimped regions have been observed to act as critical stress concentrations region [204–207], which is directly explained from their correlation with the observed maximum fiber misalignment. Transverse cracking in fiber-bundles neighbouring crimped regions, longitudinal splitting and local kinking have been observed in fiber-bundles [25, 90, 205, 206, 208, 209] (indicating further the presence of fiber misalignments in the fiber-bundles).

2.3.4 Composite thickness

Physically, the composite thickness can be affected during the transverse compaction. A reduced thickness correlates with an increase in global fiber volume fraction (which then correlates with a potential increase in stiffness). Local variations of the laminate thickness can also be present (in fiber-reinforced composites which are manufactured out-of-clave using vaccuum bag), in which the local variations have been shown to affect the stress and strain distributions in the surface lamina of the laminates [210, 211].

Numerically, differences in thickness between models of fiber-reinforced composites can be caused due to modelling simplifications. For example, a (simplified) constant cross-section for the surface weft yarn and binder yarn in 3D woven models can results in different model thickness compared to more realistic model which include cross-section variations of the surface weft and binder yarn, with the matrix assumed to fully surround the reinforcement. The differences in thickness results in a decrease of stiffness.

2.3.5 Neighbouring fiber-reinforced regions

The stress distribution in a fiber-reinforced region also depends on its surrounding. A lamina in multi-directional laminates experiences a different stress distribution dependent on its position in the lamina stack (inner or surface), and on the main fiber direction in the neighbouring laminae [212–216]. A fiber-bundle in a textile composites experiences a different stress distributions depending on the position (inner or surface) of the lamina to which it belongs, and on the fabric layer shifts in a multi-layers woven composites which can happen during nesting (see Fig. 2.1b) [133, 162, 217–219]. The (undesired) effect of isolating a lamina depends on the reinforcement architecture inside the lamina, which is different for unidirectional and 2D woven lamina [217].

2.4 Reflection on the use of geometrical experimental data

The geometrical data of the reinforcement architecture relies mostly on the use of experimental data, as mechanical modelling simulations of the manufacturing processing are still in their infancy (and not yet fully predictive). Cross-sections can hereby be taken and analysed by optical or scanning electron microscope, or micro-CT scans can be performed to obtain a 3D representation of the reinforcement architecture in a non-destructive way [33,35,94,220–226]. Other non-image based techniques, which exploits for example the electrical properties of carbon fibers to investigate fiber waviness in a lamina [227–229], can be adopted as well, but their use remains limited. However, the extraction of realistic geometrical features using experimental techniques is expensive and time-consuming (especially looking at the wide range of composites specimens to be examined). This has resulted in a limited availability of experimental data on more complex geometrical features and the need to make assumptions on these features in modelling approaches.

Parametric studies can then be used to provide a first insight on the effect of geometrical features due to which the mechanical properties may vary. These studies will then provide information on which geometrical features are important to incorporate in realistic models and for which experimental geometrical data is needed. Unit-cell models that include the main features and in which the presence of features and their dimensions are parameterised, are then advantageous. Such models can further be used in stochastic simulations [74, 220, 230–232] to understand partly the scatter in mechanical results (caused by geometrical variations), and so to reduce the large safety factors being applied [233, 234].

2.5 Conclusion

A brief overview has been presented on the main aspects important to understand mesoscopic geometrical model generation in fiber-reinforced composites. The following main conclusions can be drawn:

1. Differences in topology between fiber-bundles and lamina with openings resulted in the introduction of different types of mesoscopic geometrical modelling approaches adopted in different types of reinforced composites.

2. Analytical modelling approaches have been adopted for all composite types but are time-consuming and the need to assume certain shapes of features a priori which often results in simplified models. Computational approaches have been proposed to obtain automatically and to even predict certain geometrical features of reinforcement architecture for fiber-bundles, but no unified computational approach exist for lamina distortions or interaction of lamina with fiber-bundles

3. The global fiber volume fraction is the main driver for the stiffness. Variations in the local fiber volume fraction increase the stress concentrations and reduces the strength in transverse and shear direction, making regions with increased fiber volume fraction susceptible for early damage initiation. Fiber misalignment distribution characteristics affects the stiffness and local stress concentrations. Local thickness variations and neighbourhood characteristics of fiber-reinforced regions should be properly accounted for.

A unified computational framework to generate unit-cell models for all types of fiber-reinforced composites is desired. To do so, the gap between the different topologies of fiber-bundles and lamina with openings during geometrical model generation should first be bridged, and tools should be proposed to allow an automatic transformation of geometrical models into finite element models for all types of topologies present in the geometrical models.

Chapter 3
Tools

This chapter presents the tools that are used to transform the geometrical models into finite element models for use in mechanical simulations. These tools are presented here as they are common to all subsequent chapters. During the transformation, discretised lines, which represent the fiber-bundles and laminae in the geometrical model, are first contoured into closed triangulated surfaces. Interpenetrations between the fiber-reinforced regions are then suppressed while a gap is generated simultaneously. A conforming tetrahedral mesh with in-plane periodic surface meshes and local mesh refinement is further generated from the closed surface representations of the fiber-reinforced regions using the free mesh generation software GMSH. A first-order computational homogenisation framework is finally adopted to define a boundary value problem on the unit-cell during mechanical simulations. A brief introduction and the implementation details on each described post-processing steps on the generated geometry are presented in the following.

3.1 Introduction

The geometrical model generation approach uses discretised lines to represent the geometrical features of lamina and fiber-bundles in unit-cell models (Fig. 3.1a). Lamina can be represented by discretised lines which are positioned near potential opening locations and out-of-plane undulations or at its interior to represent its fibrous nature (as will defined in chapter 4,5 and 7) (Fig. 3.1b) while fiber-bundles can be represented by either a single line and cross-sections defined on this line, or by lines positioned at their boundaries or at their interior (as will defined in chapter 6) (Fig. 3.1c). The discretised lines, representing a fiber-bundle or a lamina, need to be transformed, after geometrical model generation, in cross-sections (on which the local fiber volume fraction and fiber direction are modelled); and subsequently in finite element models for use in mechanical simulations. Different approaches have been adopted in fiber-reinforced composite literature to transform geometrical models into finite element models [235–244].

In a mesh sweep approach [245], fiber-reinforced regions are assumed to be represented by a cross-section and a centerline. A 2D mesh is then generated on the cross-section and swept along the centerline to form a hexahedral mesh. Fiber-bundles and laminae are often meshed using such an approach [95,246], but the matrix region (which is often complex-shaped) requires more advanced approaches.

In a voxel-based meshing, the domain of the geometrical unit-cell model is divided into

a grid of cuboids [143, 166, 247, 248]. For fiber-reinforced composites, a cuboid belongs either to the fiber-reinforced regions or the matrix, to which corresponding material properties can be attributed after assignment. A voxel-based representation is then obtained for fiber-reinforced region and the matrix. The staircase like discretisation border of the fiber-reinforced regions in such a voxel-based representation was shown, however, to cause artificial stress concentrations which do not converge upon mesh refinement [141, 166]. Complex geometrical models can easily be transformed into such voxel-based models, but the staircase discretisation border of the fiber-reinforced regions should first be smoothened for models intending to predict local stress concentrations or to model damage development.

In a tetrahedral mesh approach, a closed surface representation of the region is required. Mesh nodes are then positioned in the region and connected by tetrahedral elements [249]. Optimisation techniques are furter adopted to increase the quality of the tetrahedral mesh, conform the requirements on the shape and the size of the elements imposed by the finite element method [250–258]. The approach is able to mesh complex shaped fiber-reinforced and matrix regions and, assuming smooth borders of the fiber-reinforced regions at meso-scale, the approach is also able to represent these smooth boundaries while voxel-based geometries would anyway not be physically meaningful for damage initiation. However, some further adaptations are still needed to combine the fiber-reinforced regions and matrix meshes into a solid finite element model. First, the meshes of the fiber-reinforced and matrix region should be conforming at their interface. This can be done in an approximate way by connecting the mesh nodes of separately meshed regions with connector elements (non-conforming meshes) [133, 259]; or by directly generating volumetric meshes of both regions sharing the same mesh nodes at the boundaries (to form a conforming mesh) [243, 244]. Second, contacting fiber-reinforced regions should share the same mesh nodes on contacting surfaces (to form a consistent mesh) [260]; or a gap should be inserted between fiber-reinforced regions before meshing in order to allow a high-quality matrix mesh in these contacting regions. Potential interpenetrations between fiber-reinforced regions should further be suppressed a priori to well-define the matrix region.

Mesh superposition techniques, or embedded element techniques, can be used to facilitate the meshing process [97, 261–264]. The meshes of the fiber-reinforced region, and of the matrix which is considered as an effective medium (filling the entire unit-cell), are generated separately and connected afterwards to obtain a solid model. Matrix meshing is simplified, and interpenetration suppression and gap insertion are not required, but the approach does not allow modelling explicitly the boundary between the fiber-reinforced region and the matrix, while this can be desired to account for interface debonding during mechanical simulations.

In an extended finite element aproach, a regular grid of finite elements is considered whereby the geometry is accounted for by enriching the finite element discretisation itself [179, 265, 266]. Complex shapes of geometries can be accounted for, but the approach does not allow the use of commercially available finite element simulation software.

Boundary conditions are further imposed on the finite element model to account for the effect of neighbouring material and to subject the unit-cell model to certain macroscopic or average load conditions during finite element simulations. Uniform displacement, uniform traction and periodic boundary conditions at the boundary of the unit-cell are used in literature to account for the presence of neighbouring material. Periodic boundary conditions have been illustrated to provide the best estimate of stiffness and local stresses for the smallest unit-cell size. [67, 71, 267–269]. The periodic boundary conditions can be directly applied on matching mesh nodes located on opposite unit-cell boundaries (which requires periodic surface meshes) or by means of more advanced interpolation schemes [270, 271] (which do not require periodic surface meshes). The global strain (or stress) can then, for periodic boundary conditions, be applied using the displacement or the reaction force components of the corner controlling nodes only, from which, after the simulation, the stiffness and global stress (or strain) can be deduced [55]. The expressions which relate the displacement or reaction forces at the control nodes to the global stress or strain applied on the unit-cell further depend on the type of applied loading (first-order, shell-behaviour or general second-order loading, etc.) [51–53, 55, 272–276].

In this work, conforming tetrahedral meshes with in-plane periodic surfaces will be generated for unit-cell models. First, the discretised lines representing a lamina or fiber-bundle have to be transformed into closed surface representations. Second, potential interpenetrations are suppressed and a gap is inserted between the fiber-reinforced regions. Third, the closed triangular surface representations are transformed into conforming meshes using the meshing software GMSH [277]. Periodic boundary conditions can then be applied on the in-plane periodic surface meshes in a first-order computational homogenisation setting. The tools to transform the discretised line models into finite element models for use in mechanical simulations are introduced in the following.

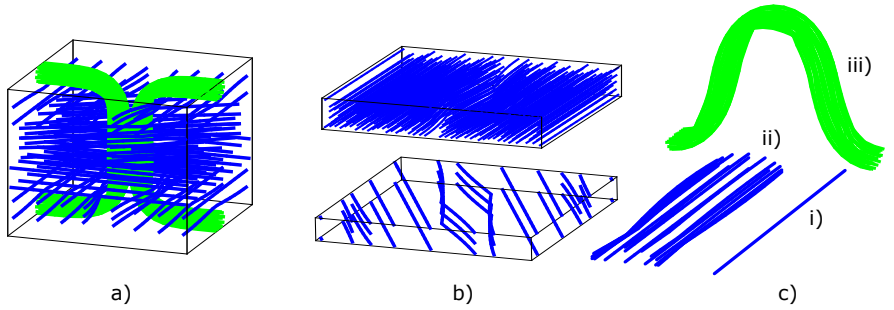

Fig. 3.1: Different line-configurations of lamina and fiber-bundles as adopted by the generation approach: (a) line representation of lamina and fiber-bundles in an unit-cell model (the green lines represent the binder yarn), (b) lines positioned at the interior or at the boundaries of the lamina, (c) a single-line (i) and multi-line configuration with lines positioned at either the boundaries (ii) or at the interior (iii) of a fiber-bundle.

3.2 Elementary tools

The distance to and normal onto a discretised line or triangulated surface starting from a point are often used during the unit-cell model generation process. Coordinate system transformations are also used to transform the coordinates of a point between the global coordinate system of the unit-cell to the local coordinate system of a cross-section of a fiber-reinforced region. The determination of the distance and normal direction for discretised lines and triangulated surfaces is not as uniquely defined as is the case for analytically-defined lines or surfaces, for which the distance and the normal direction(s) can easily be obtained from the gradient of the analytical function. The implementation details for computing such quantities on discretised lines and triangulated surfaces and the coordinate system transformations are therefore described in the following.

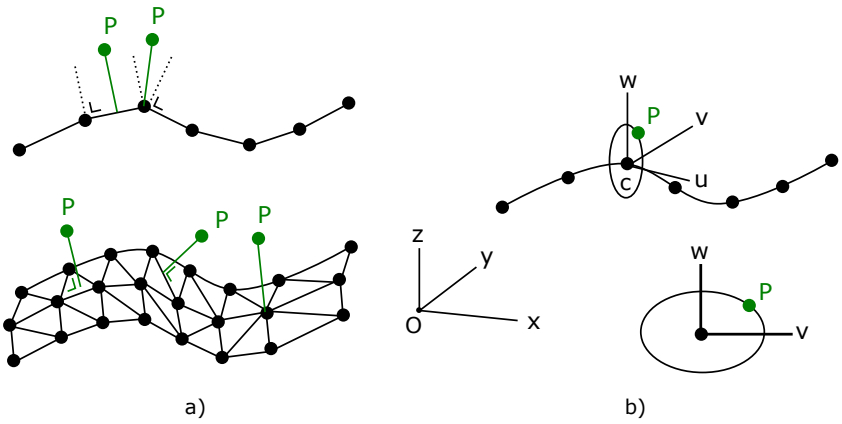

Fig. 3.2: Basic tools: (a) the distance of a point P to a discretised line or triangulated surface, (b) coordinate system transformation between a global coordinate axis system (x,y,z) and a local coordinate axis system (u,v,w).

3.2.1 Distances and normals

The distance from a point to a discretised line or triangulated surface (see Fig. 3.2a) can be defined as the minimum of the distances between the point and all the vertices, line segments or triangular surface patches belonging to the discretised line or triangulated surface [278, 279]. The distance of a point to a line segment or triangular surface path is defined as the length of the orthogonal projection on the line segment or triangular surface patch.

The normal from a point onto a discretised line is defined separately on the line segments and in the vertices of the discretised line. On a line segment, the normal is defined from the analytical expression of the line segment and the plane passing through the line segment and the considered point. In a vertex, the normal can be defined from the average of the normals on its neighbouring line segments. It can further be weighted by

the length of the corresponding line segments.

The normal on a triangulated surface is defined separately on the triangular facets, on the line segments and in the vertices of the triangulated surface. On a triangular facet, the normal is defined from its analytical expression. On a line segment, the normal can be obtained from the mean of the normals on neighbouring facets. In a vertex, the normal can be obtained from the average of the normals on its adjacant triangular facets which should further be weighted by the angle in each corresponding triangle neighbouring the vertix [54, 278].

Signed distances can be computed for closed triangulated surfaces by combining the unsigned distance calculations with the local normal on the surface [54, 280].

3.2.2 Coordinate system transformations

Consider a global coordinate system with orthogonal unit vectors $(\bar{e}_x, \bar{e}_y, \bar{e}_z)$ and origin $O(0,0,0)$, and a local coordinate system with orthogonal unit vectors $(\bar{e}_u, \bar{e}_v, \bar{e}_z)$ and origin C with global coordinates $\vec{C_{xyz}}$ (see Fig. 3.2b). The global coordinates of a point P ($\vec{P_{xyz}}$) can be transformed into local coordinates ($\vec{P_{uvw}}$), and conversely, by:

$$\bar{P}_{uvw} = (\bar{P}_{xyz} - \bar{C}_{xyz}).\bar{\bar{M}}^t_{rot} \tag{3.1a}$$

$$\bar{P}_{xyz} = (\bar{P}_{uvw}.\bar{\bar{M}}_{rot}) + \bar{C}_{xyz} \tag{3.1b}$$

where M_{rot} is the transformation matrix defined by:

$$\bar{\bar{M}}_{rot} = \begin{bmatrix} (\bar{e}_u.\bar{e}_x) & (\bar{e}_u.\bar{e}_y) & (\bar{e}_u.\bar{e}_z) \\ (\bar{e}_v.\bar{e}_x) & (\bar{e}_v.\bar{e}_y) & (\bar{e}_v.\bar{e}_z) \\ (\bar{e}_w.\bar{e}_x) & (\bar{e}_w.\bar{e}_y) & (\bar{e}_w.\bar{e}_z) \end{bmatrix} \tag{3.2}$$

Note that the considered orthogonality of the unit vectors is a prerequisite for such coordinate system transformations.

3.3 Contouring

Cross-sections and closed surface representations need to be generated from the discretised lines. The discretised lines, representing a fiber-bundle or a lamina, are hereby intersected by planes perpendicular to a local main fiber direction. The intersection points on each plane are then contoured, after which the generated contour lines undergo an offset to account for the line radius. The cross-sections are then transformed into closed triangulated surfaces representing the fiber-reinforced regions. In the following, the approaches adopted to generate a contour around points in 2D and to transform the obtained cross-sections into closed triangulated surfaces are presented.

3.3.1 Contouring a 2D point set

The problem of contouring points in 2D or 3D by a line or a surface respectively is well known in research fields related to object recognition [281–284] and surface reconstruction [285–297]. In these fields, points, which represent the surface of an object, are obtained from imaging techniques or simulations results. These points can be characterised by the level of scatter, their density, the availability of extra information on geometrical features of the object represented by the points, etc. Techniques to reconstruct the surface starting from the points then differ whether the point set represents the surface approximately (for point sets with scatter) or whether the points should be embedded in the surface (for point sets with no scatter). The points in this work, which are intersections of the lines that are shaped during the generation process, should be embedded in the contour.

The contour of a convex-shaped set of points can easily be obtained from a Delaunay triangulation (Fig. 3.3a) [298–300], while the contour of a concave-shaped set of points requires other strategies (as a delaunay triangulation would result in undesired elements, see Fig. 3.3b). In [166, 167, 301, 302], concave sets of points are contoured starting from a circle attached to one of the points. The circle is rotated around the point until it touches another point whereafter a line connecting both points is generated. The circle is then positioned at the obtained point and the approach is repeated until a closed contour is obtained. In [303], an adapted Delaunay-based approach is used to generate contours around concave-shaped sets of points. A Delaunay triangulation is first constructed from the points. Tetrahedral elements with an circumsphere radius larger than $1/\alpha$ are then removed. Different α-shapes (or concave geometries) of the points can be generated by adopting different α's. In [290, 304–306], additional auxialiry points are added to the points, and a Delaunay triangulation is then applied on all points. Tetrahedral elements connecting one of the auxiliary added points are subsequently suppressed. In [298], Voronoi vertices, which are the vertices of the Voronoi diagram constructed from the initial points, were considered as additional points. A similar approach is adopted in this work, but where the additional points are simply positioned on a rectangle surrounding the initial set of points to be contoured. Such an approach is chosen as it allows to obtain in a straight-forward way contours around convex and concave shaped set of points.

Fig. 3.3c illustrates the approach used in this work to generate a contour around sets of points of arbitrary convexity. First, additional auxiliary points are added to the problem, with these points being positioned on a rectangle surrounding the initial set of points. Second, a Delaunay triangulation is performed on all points whereafter the triangles that connect at least one auxliary point are removed. Third, the free-boundary of the triangular mesh is extracted and the vertices of the free-boundary are moved along a local normal with a distance equal to the line radius used in the generation procedure (see subsequent chapters). The parameter a (see Fig. 3.3c), which controls the position of the rectangle on which the points are added, is set to $0.10\mu m$. Examples of generated contours around convex- and concave-shaped points sets using this parameters are illustrated in Fig. 3.3d.

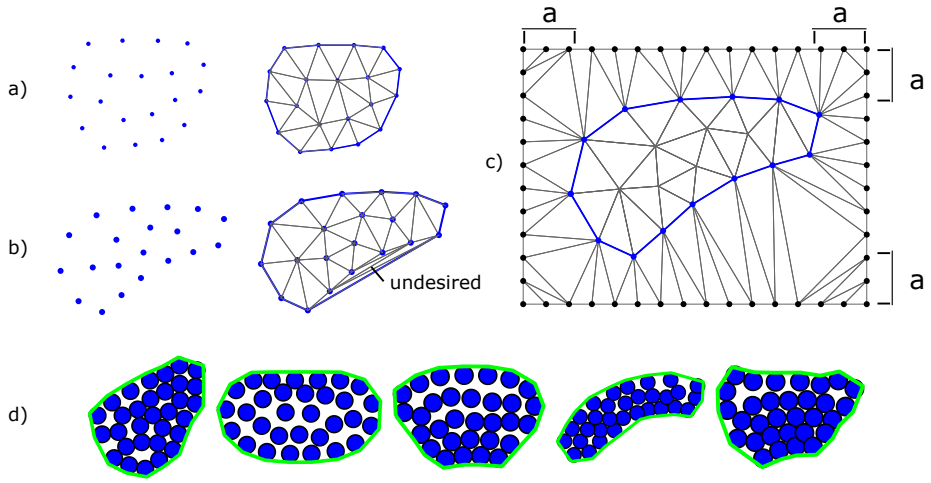

Fig. 3.3: Contouring a 2D point set: (a) the convex hull of the point set, (b) undesired elements which arise in a default delaunay triangulation of a concave-shaped point set, (c) points added before triangulation on rectangle surrounded to the point set to suppress the undesired elements (distance a regulates the position of the rectangle and is added extra to the dimension of the point set), (d) examples of generated contours around line intersections.

3.3.2 An automated approach to connect cross-sections

Two approaches can be used to transform (discretised or parametrised) cross-sections into closed surface representations. In one approach, the cross-sections are parametrised and interpolated between each other, hereby creating a parameterised surface (as adopted in TexGen [130]). In another approach, the cross-sections are discretised and connected by triangles (either manually or automatically) [307, 308]. Here an automated approach is used to generate triangles between discretised cross-sections of both fiber-bundles and laminae with openings, as it will allow to seamlessly connect cross-sections of different shapes.

Fig. 3.4 illustrates the approach used to connect cross-sections of fiber-bundles, considering the cross-sections of a fiber-bundle as presented in Fig. 3.4a. First, each cross-section is replaced (see Fig. 3.4b) by a set of points representing the cross-section (blue points) and additional points that are added in the cross-section plane (green points). The additional points are positioned in each cross-section plane along a local normal with a distance a. The cross-sections are hereby reused from previous contouring operations (see section 3.3.1), which will be used to model the fiber volume fraction in the fiber-reinforced regions. Second, a delaunay triangulation is applied on all the points. Finally, the tetrahedral elements connecting at least one of the added points are removed and the free boundary of the triangular mesh, representing the contour, is extracted. The distance a should be chosen to avoid cuts and the presence of undesired elements in locally curved regions and will be in function of the local curvatures of the fiber-bundle. The

resulting triangulated surface around the fiber-reinforced regions is depicted in Fig. 3.4c.

Fig. 3.5 illustrates the approach used to connect the cross-sections of a lamina with openings. The cross-sections of the lamina (as presented in Fig. 3.5a) should hereby be merged at places where the lines which represent the boundaries of resin-rich regions (see Chapter 4, section 4.2.3) are locally not moved during the model generation process. First, each cross-section is replaced (see Fig. 3.5b) by points (blue points) and additional auxiliary points to be suppressed after a triangulation (green points). The additional points are positioned in each cross-section plane along a local normal, and are removed at places where the distance between cross-sections (see plane 2 in Fig. 3.5b) are less than a tolerance distance. Second, a Delaunay triangulation is applied on all the points. Third, the tetrahedral elements connecting one of the added points are removed and the free boundary of the triangular mesh, representing the contour, is extracted. The distance on which the additional points are positioned in each cross-section plane should be small enough to avoid interpenetrations of the additional points in neighbouring cross-sections. The approach allows then generating automatically closed triangulated surfaces of complex-shaped lamina with openings (Fig. 3.5c).

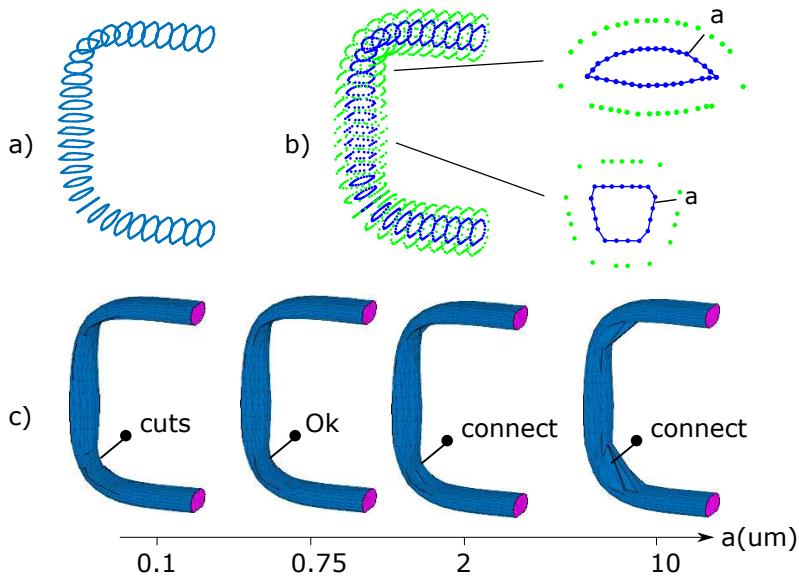

Fig. 3.4: An automated approach to connect cross-sections representing a fiber-bundle: (a) cross-sections of a fiber-bundle, (b) points representing the cross-sections (blue points) and auxiliary points to suppress undesired elements (green points)(a indicates the distance between an auxilary point and the cross-section), (c) triangulated surfaces controlled by parameter *a*.

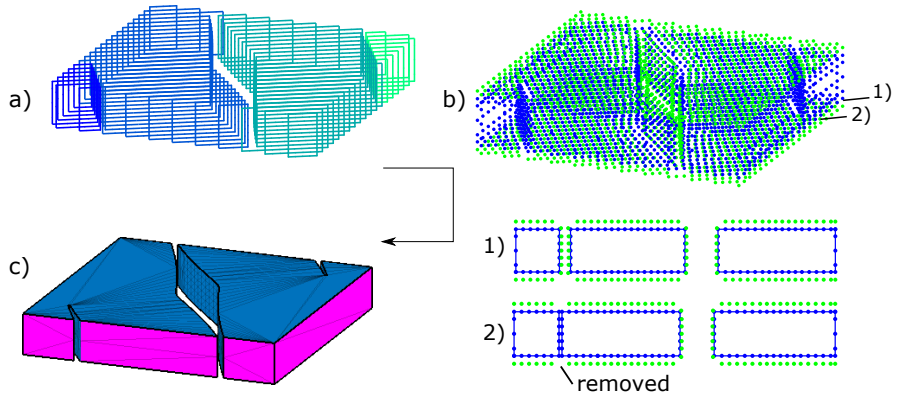

Fig. 3.5: An automated approach to connect cross-sections representing a lamina (with openings): (a) cross-sections of the lamina, (b) points representing the cross-sections (blue points) and auxiliary points to suppress undesired elements (green points), (c) the generated triangulated surface.

3.4 Interpenetration suppression and gap generation

Interpenetrations between fiber-reinforced regions can arise in analytical modelling approaches due to simplified modelling and in computational modelling approaches due to discretisation errors (allowance on the maximum residual interpenetration distance, limitation on the maximum iteration number, etc.) Interpenetrations are here defined as occurring when representations of fiber-reinforced regions occupy locally the same position. The interpenetrations can partly be avoided by considering more advanced shapes of the presented geometrial features [132, 133] (for analytical modelling approaches) or by adopting a multi-line configuration for fiber-bundles [103, 169, 173], smaller discretisation, an increased number of maximum iterations, a zero tolerance on residual interpenetrations, etc. (for computational approaches). Residual interpenetrations are however often still present in models of more complex-shaped fiber-reinforced regions, which then need to be suppressed in a post-processing stage before meshing. At the same time, a gap is often introduced between fiber-reinforced regions at their contacting regions to allow and facilitate matrix meshing

The simplest approach to suppress potential interpenetration and to insert a gap between fiber-bundles is by decreasing the dimensions of the cross-section dimension of the fiber-bundles [309]. The decrease in cross-section dimensions then correlates, however, with an increase in local fiber volume fraction and corresponding artificial stress concentrations which should be avoided in models aiming at local stress level predictions. Cross-sections can be rotated to preserve the cross-section area while suppressing the interpenetrations [105, 310], but such cross-section rotations are rather difficult to perform and not always possible, for example in textile composites with high fiber-bundle volume fractions.

Another approach relies on the local modification of cross-section shapes by means of the finite element method, as performed in [44,163,164] to suppress interpenetrations between fiber-bundles in 2D and 3D woven composites. In [44], the part of the composite with interpenetrating fiber-bundles is first extracted out of the model. The interpenetrated fiber-bundles are then separated from each other and transformed into a continuum finite element representation. The fiber-bundles are brought back to their original positions during a finite element simulation, while contact elements between the fiber-bundles are used to account for fiber-bundle interaction and subsequent local cross-section shape modifications which suppresses the initial interpenetrations. In [163, 164], the initial model was assumed to consist of interpenetrating fiber-bundles which are represented by their centerline and a circular cross-section. The fiber-bundles boundaries are then transformed into a shell elements representation with the shell elements positioned along the contour of the fiber-bundle. A hydrostatic pressure is then gradually applied inside of the fiber-bundle to inflate them, while contact elements are introduced. This allows generating locally deformed shapes of cross-sections, which are more compacted in contact regions and gradually smoothed along the bundle, but the computational cost complexity of such methods is high.

Local modifications of cross-section shapes could also be obtained using a geometrical-based framework. Sonon introduced a level-set based approach to suppress interpenentrations [179], while in Texgen [130,311], the interpenetrations are suppressed by simply moving the points of triangulated surfaces. The level-set based approach allows to easily suppress interpenetration by means of analytical expressions applied on a distance field representation of each fiber-reinforced region, but requires additional implementation to preserve automatically sharp features of triangulated surfaces upon their transformation into distance field representations. The point-movement-approach can be applied directly on the generated triangulated surfaces of the fiber-reinforced regions after the contouring operation, and preserves automatically sharp features of the triangulated surfaces as no transformation into distance field is needed.

Both approaches have been implemented in the model generation framework from which, in the end, the moving point approach was adopted for interpenetration suppression and gap generation because of its simplicity and lower computational cost compared to the level-set based approach. The implementation details of both approaches are presented in the following.

3.4.1 Level-set based approach

The approach starts from a distance field representation DS_i of each fiber-bundle (see Fig. 3.6a), the zero level-set of which represents the surface of the fiber-bundle:

$$DS_i(\bar{x}) = 0 \tag{3.3}$$

The representation of each fiber-bundle can be further modified (O_i) by means of analytical expressions [105, 179], to suppress interpenetration and to simultaneously insert a gap g between the fiber-bundles (see Fig. 3.6b). This can be achieved by taking the

zero level of the function $O_i(\bar{x})$ defined by

$$O_i(\bar{x}) = max(DS_i(\bar{x}) - e, (DS_i(\bar{x}) - DO_i(\bar{x})) + g) \tag{3.4}$$

with $DO_i(\bar{x}) = min(DS_j(\bar{x}))(i \neq j)$. An inflation e of the cross-section area opposite to the interpenetration can be calculated to preserve the cross-section area of the fiber-bundles (see Fig. 3.6c). The modified level set function O_i for each fiber-bundle can then be transformed (back) into a triangulated surface representation using marching cubes algorithms ([312, 313]) (where the triagulated surface can be input in default meshing software) or directly be used in more advanced meshing approaches [314, 315].

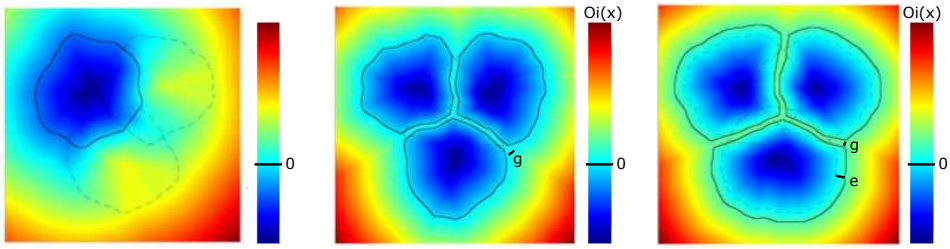

Fig. 3.6: The level-set based approach to suppress interpenetration and to insert a gap: (a) 2D representation of the function $DS_i(\bar{x}) - DO_i(\bar{x})$, (b) modified distance field representations of the inclusions with interpentrations being suppressed and a gap g generated simultaneously ($e = 0$), (c) an inflation e added to the cross-section shape to preserve the cross-section area (the images were taken from [179]).

3.4.2 Moving points of triangulated surfaces

The approach starts from a triangulated surface representation of each fiber-bundle. Interpenetrations between the triangulated surfaces can be detected locally in the points of the triangulated surface using the point-to-surface distance calculations presented in section 2. A point of a triangulated surface which interpenetrates another triangulated surface is then moved along a local normal $\vec{D}_P$ (from point P on the triangulated surface) (see Fig. 3.7a) with a distance that combines both a fraction q of the interpenetration distance d_{int} and a desired gap g (see Eq. 3.5).

$$\vec{x}_P = q.(d_{int} + g).\vec{D}_P \tag{3.5}$$

The movement of points located on the in-plane unit-cell borders is controlled by constraining equations on corresponding points on opposite unit-cell borders to preserve the periodicity of the unit-cell. The fiber volume fraction in each cross-section is further modified to account for potential changes in the cross-section area. The fraction q can be further used to control the type of fiber-reinforced region in which the distortions during this interpenetration suppression are taking place. Note hereby that the fraction q does not have any physical meaning and is merely be used to control the artificial distortions taking place in the fiber-reinforced regions during interpenetration suppression.

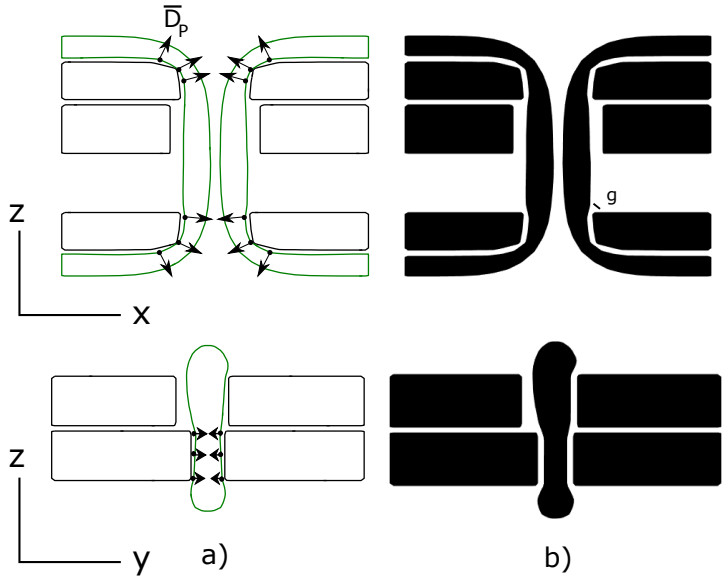

Fig. 3.7: The point movement approach to suppress interpenetration and to insert a gap: (a) before interpenetration suppression and gap insertion, (b) after interpenetration suppression and gap insertion (note that most of the interpenetration in this example have been avoided by enlarging and reducing the cross-section dimensions of the stitching yarn prior and after simulation respectively and that the point movement approach was still needed to effectively introduce a gap between the regions for matrix meshing purposes).

3.5 Tetrahedral mesh generation

The closed triangulated surface representation of the fiber-reinforced regions are transformed into a conforming tetrahedral mesh model using GMSH [277]. The transformation is taking place in the following four steps (which will further be elaborated upon in the following sub sections): first, the triangulated surface representation of the matrix is obtained from the triangulated surface representations of the fiber-reinforced regions (Fig. 3.8a); second, the triangulated surfaces are partitioned in surface patches on which parametrisation techniques will be applied, during the mesh generation, to obtain high quality surface meshes (Fig. 3.8b); third, to reduce the number of degrees of freedom, the mesh size is refined near narrow and sharp features which allows a coarser mesh size away from these features; fourth, periodic surface patches (on which periodic surface meshes will be generated) are assigned on opposite unit-cell borders. The software GMSH was chosen as it is free to use and is able to generate straightforwardly conforming tetrahedral meshes of complex-shaped composite geometries in reasonable computational time. An illustration of a generated mesh can be found in Fig. 3.8c.

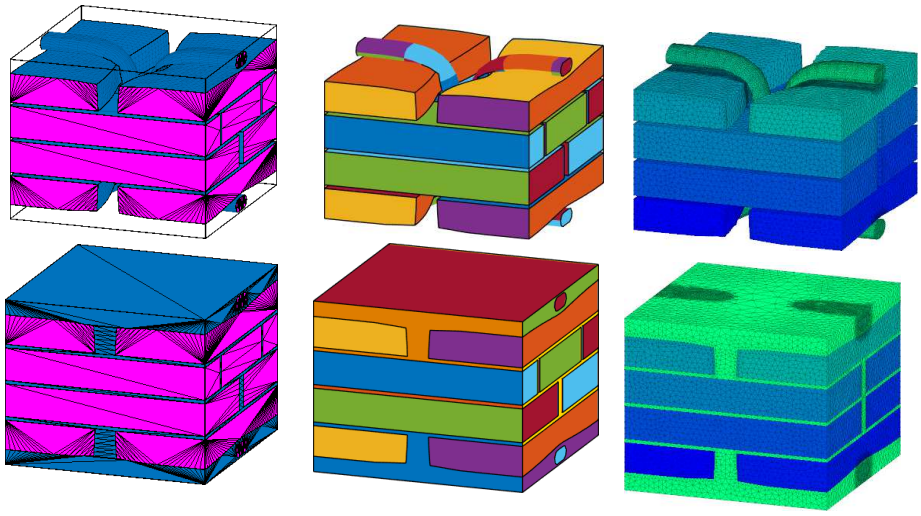

Fig. 3.8: Meshing approach: (a) triangulated surface representations of fiber-reinforced regions and matrix (obtained from the contouring operations), (b) the triangulated surfaces partitioned in patches (each patch given different color), (c) conforming meshes with local mesh refinements near geometrical features.

3.5.1 Matrix representation

The matrix is defined as the space in the unit-cell which lies outside the fiber-reinforced regions. The triangulated surface of the matrix can be defined by the triangles of the fiber-reinforced region lying inside the unit-cell, added with triangles constructed on the unit-cell borders to close the matrix region. A problem arises when fiber-reinforced regions crosses the unit-cell borders (see chapter 5, the stitching yarn), as the triangulated surfaces obtained from the Delaunay-based contouring operations for these regions are not automatically conform with the unit-cell borders, and conformity is required to allow the separation of triangles of the fiber-reinforced region in inner and outer triangles to define the matrix.

One approach to have triangles conforming with the boundaries consists in intersecting the triangles at the unit-cell boundaries and in retriangulating the surface afterwards. Another approach consists in transforming the triangulated surface representation in a level-set based geometry whereby the grid is chosen to be aligned with the unit-cell borders. The latter approach is adopted in this work for stitched composite models in which the stitching yarn extended the unit-cell boundaries (see chapter 5), while in the Z-pinned and 3D woven composites models the pin and the binder yarn, respectively, are assumed to be fully located in the unit-cell boundaries.

3.5.2 Parametrised surface partitions

Badly-shaped or badly-sized triangles are often present in the Delaunay-based or level-set based triangulated surfaces of the fiber-reinforced regions. Parametrisation techniques can then be applied on the triangulated surfaces to generate high-quality surface meshes. The triangulated surfaces should therefore be partitioned first in surface patches. The partitions should hereby meet the geometrical requirements that are imposed on the surface patches by the build-in parametrisation techniques in GMSH (see [316, 317]).

Fig. 3.9 illustrates the generated partitions of a lamina, and a fiber-bundle with its triangulated surface obtained (1) from the Delaunay-based contouring operations (section 3.3.2) and (2) from a level-set based geometry (the edges of triangles are not depicted in Fig. 3.9). For a lamina (Fig. 3.9a), sharp edges of the triangulated surfaces (indicated by the black lines in Fig. 3.9a) are detected first and the triangulated surface is partioned with the sharp edges as the boundaries of the partitions. For a Delaunay-based fiber-bundle (Fig. 3.9b), triangles connecting identical cross-sections are grouped into a partition, whereafter each partition can further be split to account for sharp features in the fiber-bundle geometry. For a level-set based fiber-bundle (Fig. 3.9c), the triangles were grouped using horizontal and vertical cuts inbetween the unit-cell borders (see Fig. 3.9c). The level-set based geometries are used hereby to facilitate the seperation of triangles of fiber-bundles, but not to suppress the interpenetrations (as indicated in the previous section). For the matrix (see previous Fig. 3.8b), the triangles of its surface representation which are located on the unit-cell border can further be grouped individually on each side and into patches of connected triangles.

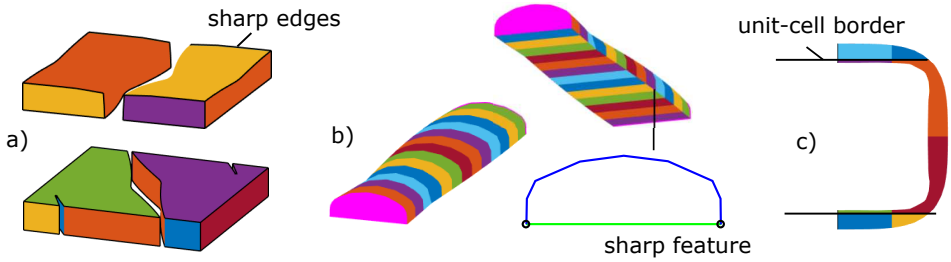

Fig. 3.9: Partioned triangulated surfaces for: (a) lamina (inner and surface), (b) Delaunay-based triangulated fiber-bundle respecting sharp features, (c) level set-based triangulated fiber-bundle conform with the out-of-plane unit-cell borders.

3.5.3 Local mesh refinement

A local mesh size field around a geometrical feature can be defined by:

$$m_i(d) = \begin{cases} m_1 & \text{for} \quad d < d_1 \\ (\frac{d-d_1}{d_2-d_1}).(m_2-m_1)+m_1 & \text{for} \quad d_1 < d < d_2 \\ m_2 & \text{for} \quad d_2 < d \end{cases} \tag{3.6}$$

where d is the distance to the geometrical feature (represented by vertices, lines or surface patches). m_1 and m_2 are the mesh sizes which are adopted in the region that is closer than d_1 or further than d_2, respectively, around a geometrical feature. Hereby, m_1 can be determined by the characteristics of the geometrical feature (local curvature, gap) and m_2 can be a desired coarse mesh size away from critical geometrical features, the parameters being evaluated by a mesh comparison study in Chapter 4. d_1 and d_2 are set in this work to $75\mu m$ and $150\mu m$, respectively, as a certain multiplication factor of the gap $30\mu m$ which will be introduced between fiber-reinforced regions for facilitating the matrix meshing. The global mesh size field is then calculated as the minimum of the local mesh size fields.

3.6 Computational homogenisation

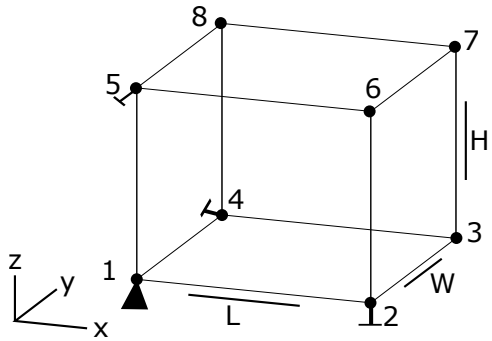

Fig. 3.10: A schematic illustration of a unit-cell with an indication of the dimensions and control nodes used by the computational homogenisation framework (the z-axis being the thickness direction).

3.6.1 Averaging relations

The computational homogenisation framework is build around the strain, stress and energy averaging theorems applied on the unit-cell model (this work uses the classical infinitesimal strain setting):

The strain averaging states that the average of the local microscopic infinitesimal strain tensor ε in the volume of the unit-cell equals the macroscopic strain tensor E (see Eq. 3.7). By assuming periodicity of the unit-cell boundaries, the macroscopic strain tensor can be enforced on the unit-cell by the displacement components of controlling nodes of the unit-cell (being nodes 1,2,3 and 5 in Fig. 3.10) only.

$$\mathrm{E} = \frac{1}{V}\int_V \varepsilon dV \tag{3.7}$$

where V is the volume of the unit-cell.

The energy averaging (also known as the Hill-Mandel relation) states that the macroscopic mechanical work equals the average of the local microscopic work components (see Eq. 3.8):

$$\Sigma : \mathrm{E} = \frac{1}{V} \int_V \sigma : \varepsilon dV \tag{3.8}$$

where Σ and σ are the macroscopic and microscopic stress tensor, respectively.

The stress averaging, which enforces the macroscopic stress tensor to be the average of the microscopic stress tensor, can then be automatically obtained from the strain and energy theorems (for more details, see [55]).

3.6.2 Periodic boundary conditions

Periodic boundary conditions can be applied on the unit-cell boundaries to account for the presence of neighbouring unit-cells. These conditions indicate that the displacement components on opposite unit-cell boundaries/faces are allowed to periodically fluctuate with respect to a displacement corresponding to a uniform homogeneous local strain level ($\bar{\bar{E}}.\bar{x}$):

$$\bar{u}(\bar{x}) = \bar{\bar{E}}.\bar{x} + \bar{u}_p(\bar{x}) \tag{3.9a}$$
$$\bar{u}_p(\bar{x}) = \bar{u}_p(\bar{x} + \bar{V}) \tag{3.9b}$$

where $\bar{V}$ are the periodicity vectors of the unit-cell and $\bar{u}_p$ is the periodic fluctuation field. The position of nodes on opposite unit-cell boundaries/faces can further be related to the position of the controlling nodes of the unit-cell (which are node 1,2,4 and 5 in the illustration presented in Fig. 3.10).

$$\bar{x}_R = \bar{x}_L + (\bar{x}_2 - \bar{x}_1) \tag{3.10a}$$
$$\bar{x}_B = \bar{x}_F + (\bar{x}_4 - \bar{x}_1) \tag{3.10b}$$

where L, R, F, B indicates the left, right, front and back side of the unit-cell respectively. The bottom and top will not be considered periodic in this work. Eq. 3.10a and Eq. 3.10b are then used to prescribe periodic boundary conditions on corresponding mesh nodes located on the opposite unit-cell boundaries.

3.6.3 Loading conditions

The displacement components u_i of the units cell control nodes are used to apply the global strain components E_{ij} and to prevent rigid body motions of the unit-cell model:

$$u_x^1 = u_y^1 = u_z^1 = u_z^2 = u_x^4 = u_1^5 = 0 \tag{3.11a}$$

$$u_x^1 = E_{xx}.L \tag{3.11b}$$

$$u_y^4 = E_{yy}.W \tag{3.11c}$$

$$u_y^1 = E_{xy}.L \tag{3.11d}$$

Node 5 is allowed to move freely. Only in-plane loading conditions are considered in this work, but the set of equations can be easily extended to consider out-of-plane loading conditions (for future work).

The reaction forces component f_i of the units cell control nodes are then used to extract the global stress components Σ_{ij}:

$$\Sigma_{xx} = f_x^1/(LH) \tag{3.12a}$$

$$\Sigma_{yy} = f_y^3/(WH) \tag{3.12b}$$

$$\Sigma_{xy} = f_y^1/(LH) \tag{3.12c}$$

In the subsequent chapters, the simulations will be performed by imposing E_{ij} on the unit-cell. The stiffness components can further be calculated from the global strain and stress components.

3.7 Conclusion

Tools are here presented to transform the geometrical models consisting of discretised lines representing fiber-bundles and lamina (with openings) into conforming tetrahedral meshes with in-plane periodic surfaces and local mesh refinement for use in mechanical simulations:

1. An approach has been introduced to contour convex and concave-shaped 2D point sets and to connect automatically discretised cross-sections of fiber-bundles and lamina (with openings) into triangulated surfaces.

2. The implementation details of a (geometrical) level-set based and point movement approach to suppress interpentration have been given.

3. An approach is presented to generate conforming tetrahedral meshes of fiber-reinforced composites using the free meshing software GMSH. The triangulated surface representations of the fiber-reinforced region and matrix are partitioned in patches which are transformed in parametrical surfaces during mesh generation to allow high quality surface meshes by GMSH. Periodic surface meshes on opposite

in-plane unit-cell faces and local mesh size fields around geometrical features are adopted.

4. The implementation details of the first-order computational homogenisation are described.

The tools do not pose any restriction on geometrical model input type and can therefore be directly used to transform automatically the geometrical unit-cell models of pinned, stitched and 3D woven composites generated in subsequent chapters into finite element models.

Chapter 4

Z-pinned laminates

This chapter presents a computational approach to generate unit-cell models of Z-pinned laminates [1]. The unit-cell models intend to embed the main mechanisms responsible for a potential reduction of in-plane mechanical properties, being a local change in fiber content, fiber distortions, and the inclusion of resin-rich regions near the Z-pin. The shape of these geometrical features strongly depends strongly on the laminate stacking sequence and on pin parameters such as pin diameter, pin content (defined in glossary), and initial pin inclination angle. In the approach, resin-rich regions are modelled by initially straight discretized lines which are gradually shaped by a set of geometrical operations mimicking pin insertion, pin rotation and fiber deflection. Fiber distortion is modelled in a post-processing stage in cross-sections accounting for the preservation of the amount of fibers. These models are then transformed into finite element mechanical models in order to investigate how local fiber volume fraction changes, fiber misalignment, or distortions in reinforcement due to pin rotation, affect the global stiffness and local stress concentrations.

Contributions:

1. A novel approach to generate unit-cell models of Z-pinned laminates, in which discretised lines are shaped by geometrical operations and for which different shapes of resin-rich regions corresponding to different pin content, diameter can automatically be generated.
2. The presentation of unit-cell models which include the effects of pin rotation and variations in local fiber volume fractions.

Novelty:

1. Straightening operation to shape the lines representing the resin-rich regions.
2. Fiber-reinforced distorted zone model for rectangular cross-sections.
3. Local failure indicators for transverse and shear failure initiation in fiber-reinforced region and matrix failure.

[1] This chapter is inspired on: G Pierreux, L Wu, D Van Hemelrijck, and TJ Massart. Evaluation of microdamage initiation in z-pinned laminates by means of automated rve computations. Composite Structures, 2018.

4.1 Introduction

Z-pins are used in the through-thickness direction of laminates to increase their delamination resistance [84–86, 123, 124, 318, 319]. Various methods have been proposed for inserting such pins. The most widespread technique, used both in industry and research, consists of pushing the pins from a foam bed into the laminate by applying a pressure combined with ultrasonic vibration [121, 320]. The part of the pins not embedded in the laminate is removed afterwards by chamfering, followed by a further consolidation and curing process in an autoclave (see Fig.4.1a). Apart from the intended increase in delamination resistance, experimental results have shown a reduction of the in-plane mechanical properties, with an extent dependent on pin parameters such as their spacing, diameter and insertion pattern [80, 106, 228, 321, 322]. The reduction is caused by reinforcement distortions, which take place during pin insertion and further processing, and can be characterized by resin-rich regions and fiber distortions near the pin [228, 323–325]. The effect of these geometrical features on the in-plane mechanical properties needs to be understood in order to optimize the design. A computational homogenization approach that uses a periodic mesoscopic unit-cell model has shown positive results in understanding and even predicting the mechanical behavior of fiber-reinforced composites with other geometrical arrangements [44, 95, 133, 162, 166, 208, 326–328]. Such an approach requires however the generation of mesoscopic geometrical models that include the main geometrical features affecting the in-plane mechanical behavior.

Resin-rich regions and fiber distortions or reorientations around the pin are gradually shaped during pin-insertion (during which the fibers are pushed aside) and further processing (during which the pin rotates), as illustrated in Fig. 4.1a. A small pin content results in eyelet-shaped regions, Fig. 4.1b, while larger pin contents result in channel-shaped resin-rich regions that form due to distortions from neighboring pins. Upon further processing, pin rotation can take place during the pin chamfering process and laminate consolidation, whereby the fibers are pushed more to one side of the resin-rich region, which results in distortion of its symmetrical shape (see Fig. 4.1c). The extent of these asymmetrical distortions in a lamina depends on the vertical position of the lamina relative to the pin rotation center, and on the main fiber direction in the lamina relative to the direction of pin rotation. The fiber-reinforced distorted zone around a pin is mostly assumed to be rectangular with a width related to the pin-diameter. Coupled with these issues, an out-of-plane component, known as fiber crimp, can also arise during pin-insertion and pin-rotation. Furthermore, swelling of the laminate, fiber-breakage, and fiber-weaving in irregular pin patterns (see Fig. 4.1d), upon pin insertion, and interfacial cracking between the pins and composites caused by thermal shrinkage of the pin after curing, can also be present. Experimental observations of the different features are presented in Fig. 4.2, while experimental data on variations in local fiber volume fraction and local fiber direction inside this region are, to the best knowledge of the author, rather scarce in the literature. All these geometrical features can alter the local stress distribution and consequently need to be included in the RVE geometries used in simulations.

In the literature, an analytical approach was developed to include these geometrical fea-

tures in a mesoscopic geometrical model [91–93]. In these contributions, symmetrical eyelet-shaped resin-rich regions are represented either by a cosine shape, an orthorhombic shape, or a diamond-shape, whereas for channel-shaped regions a rectangular shape is used. The fiber distorted zone is mostly represented as a rectangular area around the pin. Local fiber misalignment reduces linearly from a maximum at the resin-rich region boundary to zero outside the fiber distorted area (see Fig. 4.1e). The local fiber volume fraction is mostly assumed constant in each lamina. However, no existing model can provide the asymmetrical shape of a resin-rich region due to pin rotation or can ensure a seamless transition between eyelet- and channel shaped resin-rich regions.

Therefore, in the present contribution, a computational approach capable of generating geometries for all of these geometrical features in laminates is presented. Resin-rich regions are represented by discretized lines, which are initially straight and are then gradually shaped using a set of geometrical operations (see Fig. 4.3), with concepts similar to [105, 179]. The pin is assumed rigid with constant cross-section. The fiber-reinforced distorted zone is obtained in a post- processing step from these deformed discretized lines and is modelled in cross-sections perpendicular to the main fiber direction of the considered lamina. Preservation of the amount of fibers in a cross-section is used to calculate the model parameters. The generated RVE geometrical model is then transformed into a finite element model in order to investigate to what extent geometrical features affect the global stiffness and local stress distributions within laminates given a prescribed stacking sequence.

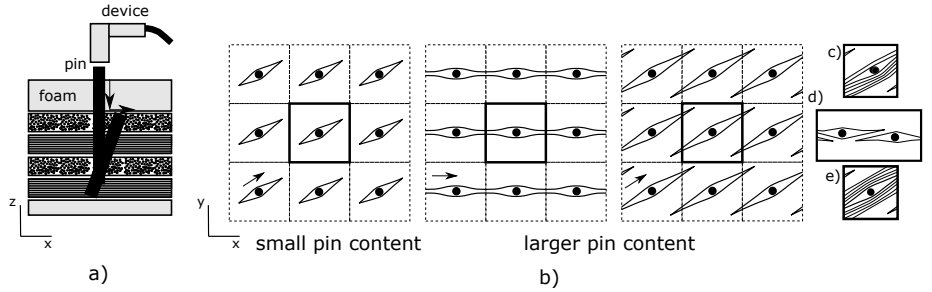

Fig. 4.1: Z-pinned laminates: (a) pin insertion and pin chamfering, (b) eyelet- and channel-shaped resin-rich regions for small and large pin content, (c) asymmetrical-shaped resin-rich region and fiber-reinforced distorted zone (due to pin rotation), (d) fiber weaving (due pin pattern imperfections) and (e) local fiber-reinforced distorted zones near the pin.

4.2 Geometrical model generation

Unit-cell models with a single pin can be inserted vertically or initially inclined are generated. A regular pin pattern, a mesoscopic initially homogeneous fiber volume fraction (before pin insertion) and fiber direction in each undistorted lamina, and a straight and rigid pin are hereby assumed. Fiber-breakage, localised through-thickness crimping of

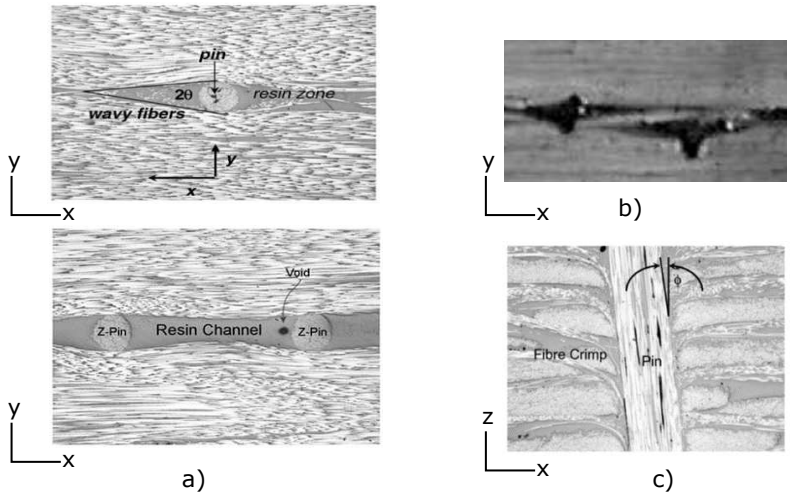

Fig. 4.2: Experimentally observed geometrical features in Z-pinned laminates: (a) eyelet- and channel-shaped resin-rich regions (images taken from [324]), (b) fiber-weaving between pins (image taken from [121]), (c) pin rotation (image taken from [324])

the in-plane fibers, and interfacial cracking between pins composite are not considered in the modelling.

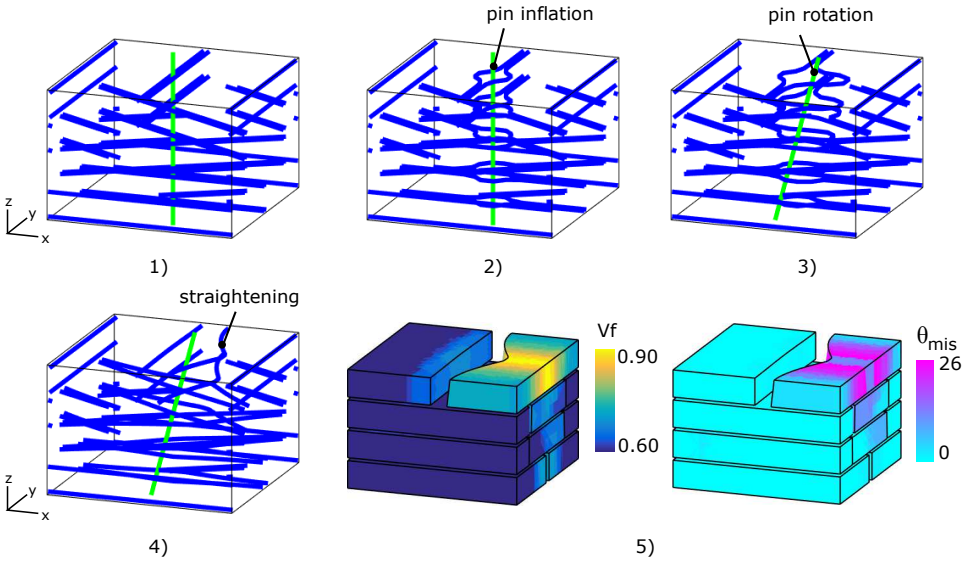

Fig. 4.3: Step-wise generation process: (1) initial model, (2) pin inflation, (3) pin rotation, (4) lamina straightening, (5) fiber volume fraction (V_f) and fiber misalignment (θ_{mis}) distributions in a post-processing step.

4.2.1 Initial model

The initial model accounts for potential resin-rich regions, which are caused by pin insertion, and the presence of an initially inclined pin. Lines are used to represent these geometrical features. They are discretized and a line radius is assigned to enable the shaping of the fibers and the detection of interpenetrations between the inserted pin and the reinforcement. The line configuration can be regarded as a boundary-line configuration of the lamina (see Chapter 3), as the fibers at the interior of the lamina are not modelled.

The pin is positioned at the center of the unit-cell and can be initially inclined. A single line is used to represent the pin. Its position is determined by a rotation center, an angle of inclination plane and an initial pin inclination angle, as illustrated in Fig. 4.4. The line radius is taken as the pin radius and the line representing the pin is not further discretized.

The resin-rich regions in a lamina are aligned with the main fiber direction $\vec{f}_{lam}$. They originate either from the insertion of a pin within the unit-cell or from neighboring pins for larger pin contents in lamina with fibers which are not aligned with one of the pin pattern directions (which are the x- and y-direction in Fig. 4.1). Straight lines are used to represent the boundaries of resin-rich regions. These lines are aligned to the main fiber direction of the considered lamina and are positioned through its thickness at the bottom and the of the lamina and at both sides of potential opening locations. The position of the lines for both a 0°-lamina and 30°-lamina is illustrated in Fig. 4.4. For the 30°-lamina, the presence of potential resin-rich regions caused by pins belonging to neighboring unit-cells is accounted for. The positioning of lines (see Fig. 4.4b) can easily be achieved by considering a cross-section that is perpendicular to the main fiber direction. For inclined pins, the lines at the top and bottom of a lamina are displaced. The lines are uniformly discretized into line segments described by nodes (not to be confused with FE discretisation nodes). The line segment length equals one third of a standard pin diameter ($280\mu m$) as having shown a good compromise between the obtained shape of the resin-rich regions and the computational cost of the geometrical model generation.

4.2.2 Geometrical shaping operations

The discretized lines of the initial model are next shaped by a set of geometrical operations that are applied sequentially and mimic the pin and fiber kinematics taking place during the manufacturing process (see Fig. 4.3), while no mechanics are incorporated in the generation process. For instance, the pin insertion is mimicked geometrical by an inflation operation applied on an embedded pin. The chamfering process applied in order to remove the excess length of the pins after insertion and the transverse compaction during laminate consolidation as part of the cure process causes the pin rotation which is represented geometrically by a rotation operation. The locally deformed shape of the lines near the pin are smoothed by a straightening operation. Upon inflation, the interaction between the fibers and the pin is accounted for by a geometrical contact treatment. Furthermore, the inflation and rotation operations are applied incrementally to prevent lines from crossing over each other before interpenetration is detected by the contact treatment. The nodes used in the line description can then be constrained to the

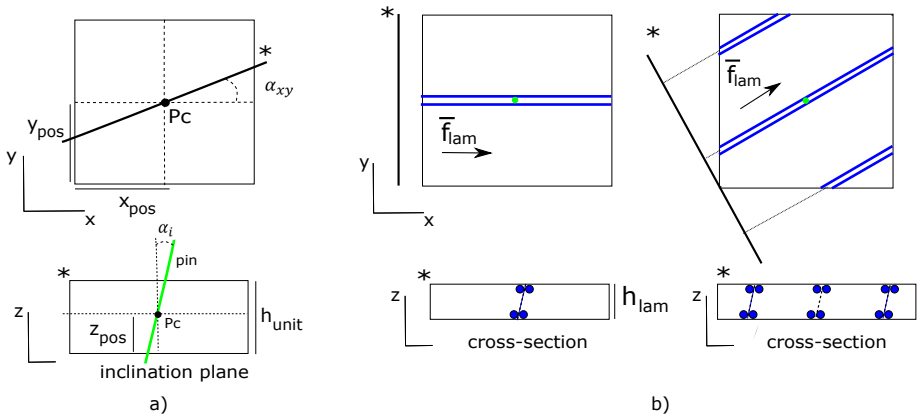

Fig. 4.4: Initial model: (a) pin, (b) lamina with fiber aligned and not aligned with a pin pattern direction (left and right respectively).

lamina boundaries for an easier control of the final geometrical model. The geometrical operations are governed by the following equations.

Inflation operation

The inflation operation incrementally increases a line radius R_{line} from zero to a final radius:

$$R^n_{line} = R^{n-1}_{line} + \frac{R_{line}}{n_{infl}} \qquad (4.1)$$
$$R^0_{line} = 0 \text{ and } n : 1 \rightarrow n_{infl}$$

where n_{infl} is the number of inflation increments. n_{infl} is calculated (in this chapter) by dividing R_{pin} with R_{line} (the radius of the lines representing the resin-rich regions).

Rotation operation

The rotation operation rotates a line in a certain inclination plane, around a rotation center, and with an inclination angle α_n that is incrementally increased from α_i to a final value α_f:

$$\alpha^n = \alpha^{n-1} + \left(\frac{(\alpha_f - \alpha_i)}{n_{rot}} \right) \qquad (4.2)$$
$$\alpha^0 = \alpha^i \text{ and } n : 1 \rightarrow n_{rot}$$

where n_{rot} is the number of rotation increments. n_{rot} is calculated (in this chapter) by guarantying that the horizontal displacement of the point near the unit-cell boundaries does not exceed the radius of the lines representing the resin-rich regions.

Straightening operation

The straightening operation repositions the nodes of a line after local displacements induced by inflation or a rotation of the pin. Each node i of a line is moved to the middle of the segment connecting the neighboring nodes (see Eq. 5.2 and Fig. 4.5a). This operation mimics the fact that a fiber under tension moves transversally with the largest movement taking place in regions with the highest curvature (so a purely geometrical operation).

$$\vec{x}_i = (1/2).(\vec{x}_{i-1} + \vec{x}_{i+1}) \tag{4.3}$$

This operation is applied to shape the lines near the pin of the unit-cell and is extended to account for the effect of potential resin-rich regions from neighboring unit-cells on the geometry of the considered unit-cell. Before applying the straightening operation, the lines near the unit-cell pin (master lines) are extended, as illustrated in Fig. 4.5b for both channel-shaped (0°-lamina) and eyelet-shaped (30°-lamina) resin-rich regions. After straightening, the extended part can be removed (0°-lamina) or used to shape the additional eyelet-shaped regions (30°-lamina). By applying this operation a number of times (defining parameter s) (typically in between 1 to 100 times, dependent on the length of the resin-rich region), a desired length of a resin-rich region can be generated. Note that no convergence of the geometry for an increased number of straightening operations is achieved as no mechanics are involved in the generation approach.

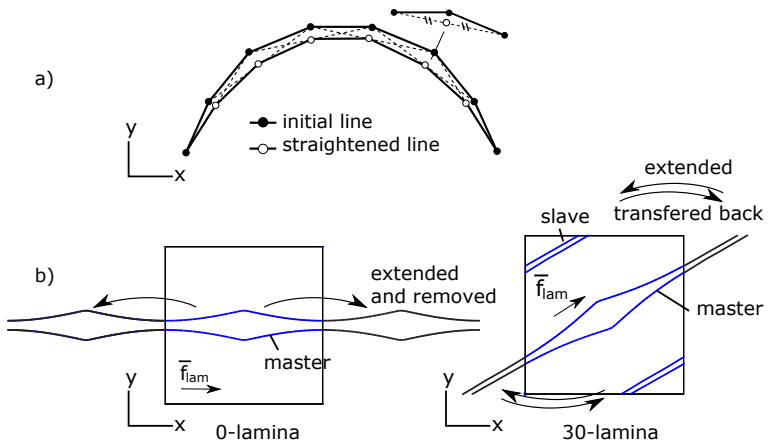

Fig. 4.5: Straightening operation: (a) concept inspired from [179], (b) periodic line straightening.

Contact treatment

The contact treatment detects interpenetrations locally between two discretized lines, based on their attributed radius and by evaluating the distance between a node on a line and all other lines. When interpenetration is detected, the concerned nodes are moved in the opposite direction as illustrated by Fig. 4.6:

$$d^P_{\text{int}} = \min[(d^P - (R_1 + R_2)), 0] \tag{4.4a}$$

$$\vec{x}^P_{\text{mov}} = q.d^P_{\text{int}}.\vec{D}_P \tag{4.4b}$$

where d^P_{int} is the distance between lines at node P, and R_1 and R_2 are the line radii. The control of the movement of node P, $\vec{x}^P_{mov}$, is defined by Eq. 4.4b in an interpenetration resolving step that uses the normal from the node on the pin, $\vec{D}_P$, multiplied by a fraction, q, and the local interpenetration distance or the overlap between both lines. q is a numerical parameter which controls the movement of lines upon contact. As the pin is not discretized and is considered to be rigid, only the nodes belonging to the boundaries of the resin-rich region are moved (by setting q equal to 1 for the resin-rich region boundaries and to 0 for the pin) such that dissimilar lines are not interpenetrated.

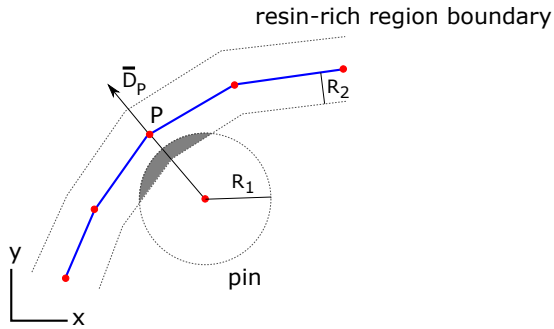

Fig. 4.6: Contact treatment.

Boundary conditions

The position of nodes can be constrained during generation by simply moving the nodes back to their desired location after each contact treatment. This procedure is implemented to constrain the nodes on the unit-cell border during generation, and to have a control over the bottom and top surface of a lamina in the final geometrical model.

4.2.3 Fiber-reinforced distorted zone modelling

Discretised lines into cross-sections

The deformed lines, which represent the boundary of potential resin-rich regions, are used to create cross-sections representing the fiber-reinforced region. Additional lines are added to represent the in-plane borders of the lamina (or unit-cell) which are positioned on the in-plane borders and through-the-thickness (see Fig. 4.7a). All the lines are then intersected by planes perpendicular to the main fiber direction that are defined at regular intervals along a diagonal of the unit-cell (see Fig. 4.7a). On each plane, a contour-line is generated around each set of intersection points that belong to a certain

part (see Fig. 4.7b). Adjacent contour-lines for which the opening between them is less than an opening distance are then merged.

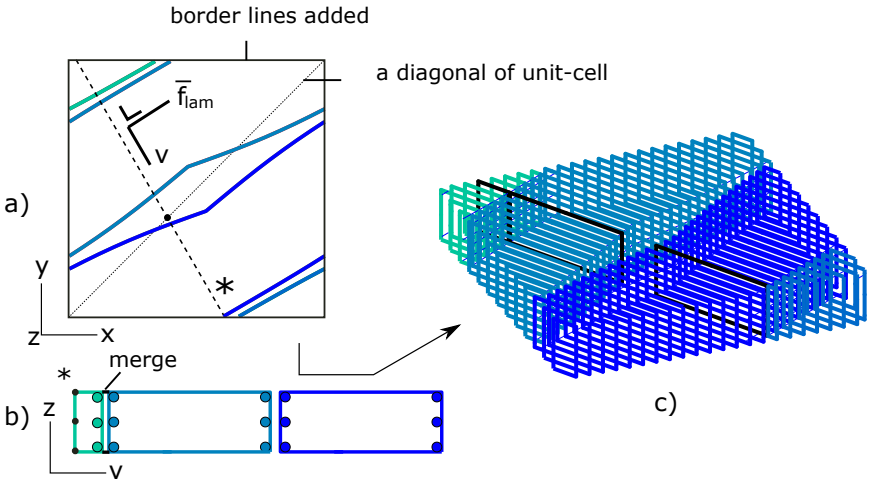

Fig. 4.7: Contouring the discretised lines of a lamina with openings into cross-sections: (a) additional lines added on the in-plane lamina borders, (b) cross-sections generated around individual point set, (c) a 3D representation of the generated cross-sections.

Fiber volume fraction and fiber direction

Fig. 4.8a depicts an arbitrary cross-section at position u, with the origin of the local coordinate axis system positioned at the center of the pin and the u-axis aligned with the main fiber direction. The area within the considered cross-section, next to the resin-rich zone, is the area where the fibers are distorted due to pin insertion. The cross-section is deformed only at the sides adjacent to the resin-rich region and the shape of the cross-section can be considered to be rectangular or trapezoidal, for a vertical or inclined pin respectively. A distorted zone with a width that is constant along the lamina thickness is assumed and is assumed to consist of two regions with differing fiber volume fraction and fiber direction profiles, as illustrated in Fig. 4.8b. The first region, which is the closest to the resin-rich region, is characterized in our model by a constant but increased fiber volume fraction $V_{f,c}(u)$ and a constant fiber direction $\vec{f}_{loc}(u)$ that is identical to the local tangent at the boundary of the resin-rich region $\vec{f}_{bound}(u)$. The second region, which is located between the first region and the undistorted zone, is characterized in our model by a fiber volume fraction and fiber direction that are linearly varying between the values in these two regions. The supposed linear interpolation in fiber volume fraction and fiber direction is similar to experimental observations [78] and to assumed fiber-reinforced distorted zone models in unit-cell models of Z-pinned and stitched laminates presented in [93, 95]. The width of each region is represented respectively by $d_1(u)$ and $d_2(u)$. The fiber-reinforced distorted model in a cross-section at position u is then defined by the parameters $d_1(u)$, $d_2(u)$ and $V_{f,c}(u)$.

The value of these parameters is obtained by considering the preservation of the amount of fibers in the cross-section during the model generation. An amount of fibers equivalent to the area $A_{df}(u)$ multiplied by the volume fraction, $V_{f,lam}$, is redistributed locally in a distorted zone of the cross-section according to the assumed fiber volume fraction profile, which gives rise to the following relation:

$$A_{\mathrm{df}}(u).V_{f,\mathrm{lam}} = (A_{d1}(u) + \frac{A_{d2}(u)}{2}).(V_{f,\mathrm{c}}(u) - V_{f,\mathrm{lam}}) \tag{4.5}$$

where the areas $A_{df}(u)$, $A_{d1}(u)$ and $A_{d2}(u)$ are illustrated in Fig. 4.8a. Since these areas can be considered rectangular or trapezoidal, Eq. (4.5) can be altered to define:

$$v_0(u).V_{f,\mathrm{lam}} = d_1(u) + d_2(u).(V_{f,c}(u) - V_{f,\mathrm{lam}}) \tag{4.6}$$

where $v_0(u)$ is the local position of the resin-rich region boundary.

For the parameters $d_1(u)$, $d_2(u)$ and $V_{f,c}(u)$ additional assumptions are required to fully describe the fiber distribution in each cross-section. First, the distorted zone parameters $d_1(u)$ and $d_2(u)$ are assumed to be constant in each cross-section. Secondly, d_2 is considered a multiplication of d_1:

$$d_2 = k.d_1 \tag{4.7}$$

where k is further called the distorted zone parameter and can be chosen to have models with a distorted zone width conform experimental observations (hereby using Fig. 4.11). Thirdly, a value of $V_{f,c}(0)$ near the pin is assumed, which takes into account a maximum threshold and corresponds to the maximum fiber volume fraction $V_{f,max}$ present in the fiber-reinforced region. These assumptions then allow the subsequent calculation of d_1 in the cross-section near the pin, d_2 as a multiplication of d_1, and finally $V_{f,c}(u)$ in each other cross-section, such as to determine the model parameters for both the assumed fiber volume fraction and fiber direction models.

The assumed fiber volume fraction $V_f(u,v)$ and fiber direction $\vec{f}_{loc}(u,v)$ in a cross-sections are thus defined as follows for the generation of geometrical features:

$$V_f(u,v) = \begin{cases} V_{f,lam} & \text{for } d_2 \leq v \\ V_{f,lam} + (\frac{v-d_1}{d_2-d_1}).(V_{f,c}(u) - V_{f,lam}) & \text{for } d_1 \leq v \leq d_2 \\ V_{f,c}(u) & \text{for } v \leq d_1 \end{cases} \tag{4.8}$$

$$\vec{f}_{loc}(u,v) = \begin{cases} \vec{f}_{lam} & \text{for } d_2 \leq v \\ \vec{f}_{lam} + (\frac{v-d_1}{d_2-d_1}).(\vec{f}_{bound}(u) - \vec{f}_{lam}) & \text{for } d_1 \leq v \leq d_2 \\ \vec{f}_{bound}(u) & \text{for } v_o \leq v \leq d_1 \end{cases} \tag{4.9}$$

The local fiber volume fraction and fiber direction are assigned to grid points positioned in the cross-sections. The values assigned to the grid points are then linearly interpolated and used to assign the local fiber volume and fiber direction to the Gauss points of the

finite elements and subsequently the material properties.

The fiber misalignment $\theta_{mis}(u,v)$ with respect to $\vec{f}_{lam}$ is often used to represent the local fiber direction in a lamina and is defined as the angle between $\vec{f}_{loc}(u,v)$ and $\vec{f}_{lam}$.

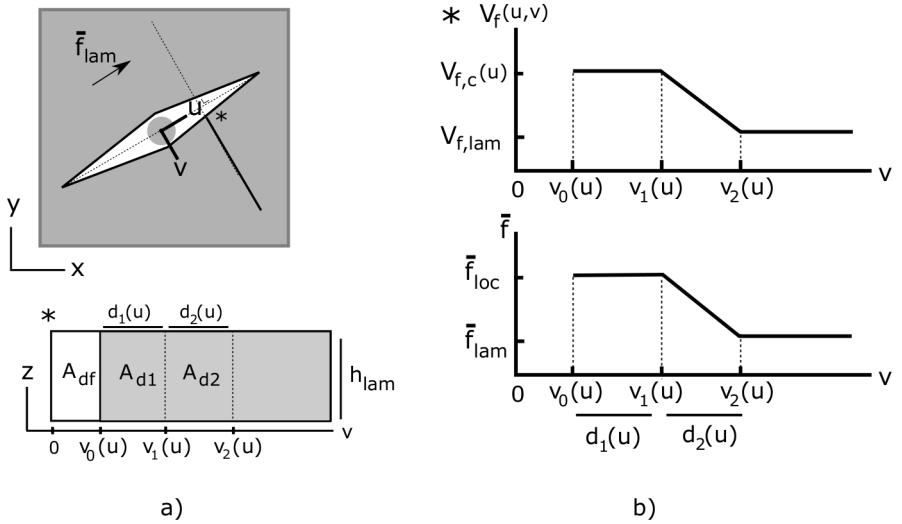

Fig. 4.8: Fiber-reinforced distorted zone model: (a) a cross-section indicating the model parameters, (b) the assumed fiber volume fraction and fiber direction distribution in the cross-section.

4.3 Generated geometrical features

4.3.1 Shapes

In Fig. 4.9, the computational approach proposed here is compared with the analytical approaches that use orthorhombic and cosine functions [93,95], for a pin diameter equal to $280\mu m$ and a resin-rich region length of $2000\mu m$ considering an opening distance of $4\mu m$. As can be observed in Fig. 4.9, the model parameters used in the generation process resulted in a resin-rich region shape that has a smaller area and a larger maximum misalignment at the boundaries (Fig. 4.9b) compared to the analytical models. By increasing the number of straightening operations, and by allowing a larger opening distance, both the area and maximum misalignment can be satisfactorily recovered as from the functional representations. It can be concluded that the straightening operation, applied on locally deformed lines, is able to generate realistic shapes of resin-rich regions in comparison to the analytical modelling approach based on experimental observations [323,324].

An illustration of the possibility of the modelling approach to generate different shapes of resin-rich regions and fiber-reinforced distorted zones in a flexible manner for differ-

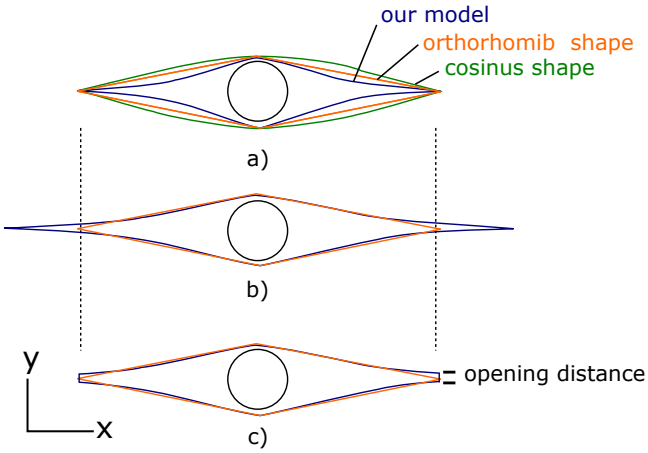

Fig. 4.9: Setting the tolerance opening distance and comparing the shaped of generated resin-rich regions with functional representations, hereby having used in the generation: (a) a tolerance opening distance of $4\mu m$, (b) an increased number of straightening operations, (c) and an increased tolerance opening distance.

ent pin parameters and stacking sequences is presented in Fig. 4.10. Pins with diameter $280\mu m$ are considered in the models. Different pin contents are obtained by changing the in-plane dimensions of the unit-cell models while keeping the pin diameter constant. The models are constructed using the generation process described in Table 4.1. As can be seen in Fig. 4.10, the modeling approach can account for the transition from eyelet to channel shapes for increasing pin content (Fig. 4.10a), the fiber weaving shape for irregularly positioned pins in a 0°-lamina (Fig. 4.10b), the symmetrical shapes for initially inclined pins and asymmetrical shapes for a pin inclined due to pin rotation in different lamina orientations (Fig. 4.10c), and the possibility to control the out-of-plane position of the top boundary of a lamina that accounts for fiber crimp due to pin rotation (Fig. 4.10d).

step	operations	id line	parameter	value	introduced geometrical feature
1	inflation	pin	-	-	width of resin-rich region
2	rotation	pin	α_f	0° - 15°	pin inclination
3	straighening	lamina	s	17	length of resin-rich region
4	post-processing	-	k	1	distorted zone width

Table 4.1: Different steps during the generation, represented by the applied geometrical operation, a corresponding parameter and its value for the generated models, the type of line on which the operation is applied, and the geometrical feature which can be used from experimental observations to set the corresponding parameter.

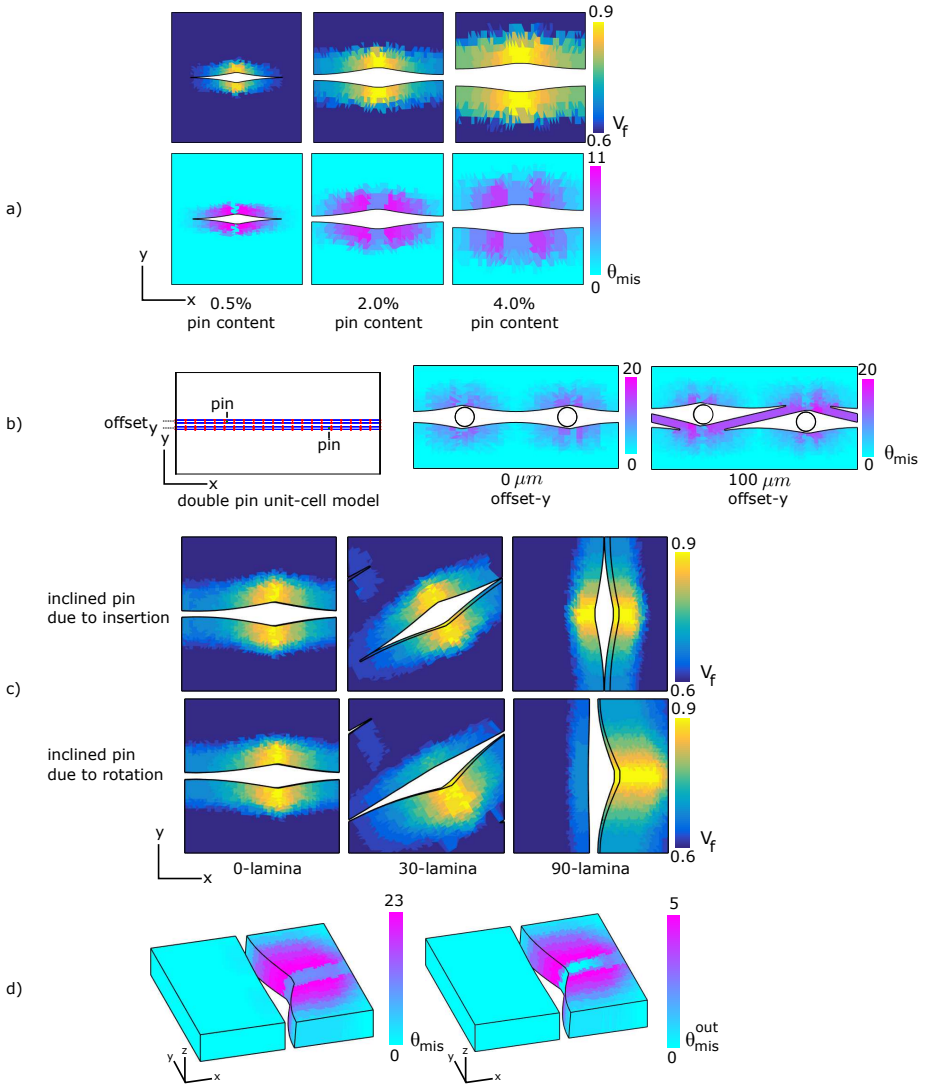

Fig. 4.10: Shapes of resin-rich regions and corresponding fiber volume fraction V_f and fiber misalignment θ_{mis} distributions: (a) eyelet- and channel-shaped resin-rich regions corresponding to a pin content $0.5-4\%$ (pin diameter $280\mu m$), (b) fiber weaving for an irregular pin pattern, (c) symmetrical- and asymmetrical- resin-rich regions for an inclined pin configuration upon pin insertion or due to pin rotation respectively, (d) out-of-plane fiber misalignment θ^{out}_{mis} or fiber-crimp due to pin rotation.

4.3.2 Dimensions

The resin-rich region can be characterized by its width and length. The width is similar to the pin diameter, which is automatically obtained during generation. The length

(which controls the addition of the eyelet shape or channel shape) can be regulated by the number of straightening operations.

The fiber-reinforced distorted zone can be characterized by its width, length, maximum fiber volume fraction, and out-of- plane fiber waviness. Its width is obtained automatically in the model by considering the amount of fibers contained in a cross-section and can be further regulated by adapting the distorted zone parameter k (see Eq. 4.7). As can be seen in Fig. 4.11, the smallest distorted zone width is obtained for $k = 0$, while for $k = 20+$ larger distorted zone widths are obtained, representing a step-wise constant and linear varying fiber volume fraction or fiber misalignment profile respectively. Its length is equal to the resin-rich region length, as local distortions start emerging as soon as lines are moved locally. A value of 1 for the parameter k is adopted in subsequent simulations and can easily be modified to generate models with a distorted zone width equal to experimental observation. The maximum fiber volume fraction near the pin is a direct input parameter in the fiber-reinforced distorted zone model and was assumed equal to 0.900 which represents near the pin a fully compacted fiber-reinforced zone [94]. The out-of-plane fiber waviness that can be present due to pin chamfering can be controlled by constraining or un-constraining the positions of nodes on the bottom and top of lamina during generation which is directly related to presence of fiber crimping.

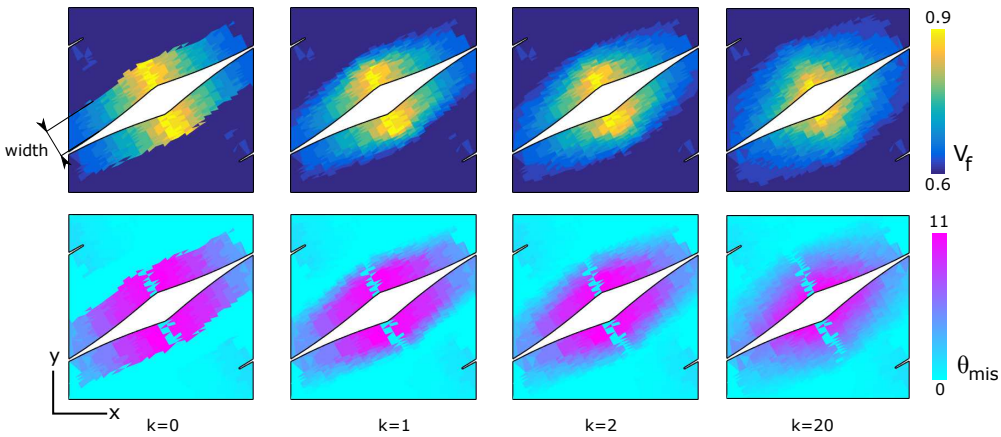

Fig. 4.11: The effect of the distorted zone parameter k on the fiber volume fraction V_f and fiber misalignment distribution θ_{mis} in lamina.

4.3.3 Comparing geometries with experimental observations

The results from Fig. 4.10 can be compared with the experimental observations presented in Fig. 4.2. Qualitatively, it can be seen that geometrical models represent satisfactory the eyelet- and the smooth channel- shaped resin-rich regions, as well as the fiber-weaving between imperfectly positioned pins. Quantitatively, the dimensions of the resin-rich region, fiber-reinforced distorted width and pin inclination angle can be compared between experiments and simulations, but are implicitly an input of the model

via the geometrical parameters. Indeed, the resin-rich region length can be controlled by the parameter s while the distorted zone width can be controlled by the parameter k. It suffices then to map out a relation which links the values of geometrical operation parameters with the geometrical characteristics in order generate explicitly unit-cell model with certain dimensions of geometrical features.

4.4 Mechanical simulations

Using the computationally built geometrical models developed here, finite element models can be generated automatically, hereby using the free 3D finite element mesh generation procedure GMSH [277, 316, 317]. A small matrix layer was inserted between the laminae to ease meshing (see Fig. 4.12). Tetrahedral elements were adopted because of the free-form shape of the fiber-reinforced regions and matrix for which a high-quality hexahedral mesh would be difficult to construct. Linear elastic simulations with periodic boundary conditions are performed for the purpose of analysing the effect of the detailed geometrical features associated with pinning. The effect of the stacking sequence on the reduction in global stiffness and the presence of stress concentrations that can explain early damage initiation for different pin contents [99, 329] are investigated on a lamina-level, by considering a single lamina with different fiber orientations and pin contents. The effect of the local fiber volume fraction as well as local fiber direction in a lamina, and the effect of the reinforcement distortions caused by pin rotation in a laminate are also investigated. Such effects are finally investigated at the scale of a laminate. The anisotropy of the fiber-reinforced regions is taken into account by means of analytical mechanical models, while the mechanical simulations are performed using Abaqus.

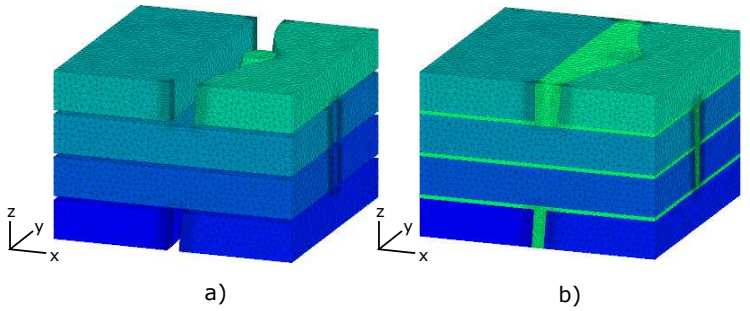

Fig. 4.12: Generated mesh: (a) without matrix, (b) with matrix.

4.4.1 Models

Pinned lamina models are now generated with fibers in lamina oriented 0°, 30° and 90° from the tensile direction and different pin diameters (a horizontal tensile direction is assumed in the sequel). For each lamina configuration, the pin content, pin radius and fiber-reinforced region representation are varied as presented in Table 4.2. The intend of this study is to evaluate the effect of different lamina orientations by means of a para-

metric study, irrespective of available experimental data.

model	description	V_f^{max}	θ_{mis}^{max}	$V_{distzone}/V_{lam}$	pin content(%)	$R_{pin}(um)$
1	equivalent	0.60	0	0	-	-
2	const V_f / const $\vec{f}_{loc}$	0.66	0	0.00	2	140
3	var V_f / const $\vec{f}_{loc}$	0.90	0	0.48	2	140
4	const V_f / var $\vec{f}_{loc}$	0.66	10	0.48	2	140
5	var V_f / var $\vec{f}_{loc}$	0.90	10	0.48	2	140
6	pin content 0.50	0.76	6	0.27	0.50	70
7	pin content 4	0.90	14	0.80	4	200

Table 4.2: The lamina models with their geometrical characteristsics ($V_{distzone}/V_{lam}$ indicates the percentage of waviness region inside the lamina). V_f^{max},θ_{mis}^{max} and $V_{distzone}/V_{lam}$ are obtained/calculated from the models, while R_{pin} and pin content (via the unit-cell dimensions) are input of the models.

Pinned laminate models with a stacking sequence [0°/90°/90°/0°] and a pin diameter $280\mu m$ are then generated. The pin is considered to be vertical, or inclined due to pin rotation in the x-direction (x-direction is clarified in Fig. 4.12), for which an inclined pin angle of 15 degrees is used (conform experimental observations [323]). The model parameters that describe the position of the vertical and inclined pin, are given in Table 4.3. The results of these models are compared with experimental observations.

	α_i	α_f	α_{xy}
vertical pin	0	0	0
inclined pin	0	15	0

Table 4.3: The pin parameters for the pinned laminate models.

For each configuration, equivalent lamina/laminate models are also generated. The same lamina dimensions are then considered in the equivalent configuration, hereby not accounting for laminate swelling that may be present upon pin insertion.

4.4.2 Boundary conditions and mechanical analysis methodology

The unit-cell model is constrained on its in-plane borders by periodic boundary conditions with the bottom and top surfaces of the unit-cell left free. Displacements are applied on the corner nodes to control the equivalent strain value [55]. A strain of 0.5% is applied on the unit-cell, which would cause local failure to take place inside the distorted zone but not outside the distorted zone [99, 329].

The materials used in this analyses consists of carbon fibers, an epoxy matrix, and a metal pin, with properties as defined in Table 4.4. Material properties for the fiber-reinforced region, as function of local fiber volume fraction, are calculated using the analytical mechanical model of Chamis [186] (for stiffness) and the emperical formula

presented in [187, 188] (for strength), using the previously defined properties; and are assigned afterwards in the local material system that is prescribed by the local fiber direction.

	carbon fiber	epoxy matrix	metal pin		carbon fiber	epoxy matrix
$E_{11}(GPa)$	231	3.45	200	$X_{11,t}(MPa)$	3500	70
$E_{22}(GPa)$	15	-	-	$X_{11,c}(MPa)$	3000	130
$E_{33}(GPa)$	15	-	-	$X_{12}(MPa)$	-	57
ν_{12}	0.20	0.35	0.30			
ν_{13}	0.20	-	-			
ν_{23}	0.20	-	-			
$G_{12}(GPa)$	15	1.28	143			
$G_{13}(GPa)$	7	-	-			
$G_{23}(GPa)$	7	-	-			

Table 4.4: The stiffness and strength properties of carbon fiber (AS4 carbon [330]), epoxy matrix (5260 epoxy [330]) and pin.

The mechanical models are analyzed in terms of global stiffness and local stresses. The global stiffness of a pinned laminate is normalized by the global stiffness of its equivalent unpinned laminate. Local stress levels are evaluated for the risk of local transverse and shear failure in the fiber-reinforced region, and matrix failure in the resin-rich region. Maximum stress criteria are used to evaluate the potential damage initiation in the elements in each region (see Eq. 4.10). The maximum stress criteria are used by means of simplification to more elaborted models that takes into account the shear coupling, as the shear coupling coefficient were not directly available. The results obtained would therefore underestimate the presence of potential local failure initiated regions.

$$\text{transverse failure: } f_{22} = \frac{\sigma_{22}}{X_{22}(V_f)} \geq 1 \tag{4.10a}$$

$$\text{shear failure: } f_{12} = \frac{\sigma_{12}}{X_{12}(V_f)} \geq 1 \tag{4.10b}$$

$$\text{matrix failure: } f_m = \frac{\sigma_p}{X_t} \geq 1 \tag{4.10c}$$

were X_t is the matrix tensile strength, and X_{22} and X_{12} the local transverse strength and local shear strength of the fiber-reinforced region respectively in function of the local fiber volume fraction (see chapter 2). σ_p is the maximum principle stress, with f_m and f_{ij} being defined as the local failure indicator for the different local damaging modes, and that indicate damage initiation. The transverse and shear strength are calculated as a function of local fiber volume fraction and were obtained by the emperical formulae proposed in [187, 188].

Stress concentrations in a certain region are represented by a 97-percentile of the local failure indicators in this region (see Eq. 4.11. The local failure indicator in an element k ($f_{ij,k}$) is hereby weighted by the volume of the element k ($V_{elem,k}$) to remove any mesh

size dependency on $f_{ij}^{97\%}$.

$$f_{ij}^{97\%} = 97perc(w_k.f_{ij,k}) \quad \text{with} \quad w_k = \frac{V_{elem,k}}{\Sigma V_{elem,k}} \tag{4.11}$$

where the summation is taken over all finite elements of the considered region (the matrix, the surface lamina, all laminae with fibers in a given direction). The 97 percentile was taken to remove any artificial high values which can be due to small numbers of badly-shaped elements. However, this default 97-percentile for the local failure indicators has been observed to not converge during mesh comparison study that only modified the mesh size near critical geometrical features while the coarse mesh size remained the same (see next paragraph). This non-convergence could be related to the fact that the number of elements near the critical regions are increased and that as such the average number of potential badly-shaped elements was increased, then increasing the 97-percentile values. To counteract this effect, a weighted percentile has been taken for each local failure indicator with the weights being the volume of each element over the total volume of a considered region. By doing so, the increase of badly-shaped elements upon mesh reduction would be counteracted by a reduced assigned weight (being the volume of the element) which eventually would results (and has observed to be) a convergence in the mesh comparison study.

Before analysis, a mesh refinement analysis was performed to analyze the effect of discretisation parameters on the global stiffness and local stresses. For a single lamina and with different fiber directions, a coarse and finer mesh were analyzed, with the finer mesh constructed by decreasing the mesh parameters belonging to the local mesh size fields. The mesh size parameters for the coarse and fine mesh, according to the mesh model definition presented in chapter 3, are given in Table 4.4.2 The results of the mesh comparison study are presented in Table 4.6. It can be seen that the results for the fine and coarse mesh are relatively similar with no large deviations, hereby having ensured that mesh resolution is sufficient to represent local fiber direction variations. It was concluded that the coarse mesh could be used in further mechanical analyses.

	$m_1(\mu m)$	$m_2(\mu m)$
fine mesh	15	100
coarse mesh	30	100

Table 4.5: The mesh size parameters of the coarse and fine mesh, hereby having used the mesh model presented in chapter 3.

4.4.3 Results

Single lamina

The global stiffness of pinned laminae with different fiber orientations and pin contents is presented in Table 4.4.3. It can be seen that the 0°-lamina has a reduction in stiffness, while for the 30°- and 90°-laminae an increase in stiffness is observed with the change

	0°-lamina			30°-lamina			90°-lamina		
	E_x^{norm}	$f_{22}^{97\%}$	$f_{12}^{97\%}$	E_x^{norm}	$f_{22}^{97\%}$	$f_{12}^{97\%}$	E_x^{norm}	$f_{22}^{97\%}$	$f_{12}^{97\%}$
fine mesh	0.97	0.59	1.70	1.05	0.88	1.41	1.02	1.61	0.16
coarse mesh	0.97	0.59	1.60	1.05	0.90	1.43	1.02	1.62	0.16

Table 4.6: The normalised stiffness and the 97-percentile of the transverse and shear cracking failure indicators of the pinned lamina which is meshed by two different meshs sizes.

in stiffness depending on the pin content. These trends can be explained, for example, by considering the analytical mechanical model which relates the local fiber misalignment with respect to a loading direction to the local stiffness (e.g. Piggott [194]) and by accounting for the presence of the pin. As illustrated in Fig. 4.13, a fiber misalignment in the distorted zone in a lamina for different lamina orientations can either decrease or increase the local stiffness, dependent on whether the fiber misalignments tends to make the fibers become more aligned or less aligned with the loading direction. For off-axis laminae, the presence of a pin acts as a stiffness enhancing medium. The combined effect of fiber misalignment and pin inclusion can either decrease or increase the global stiffness. These results can then help explaining the differences in reduction of global stiffness of pinned laminates for different stacking sequences and pin contents [80].

model	description	0^o-lamina	30^o-lamina	90^o-lamina
5	pin content 0.5%	0.99	1.02	1.01
6	pin content 2.0%	0.97	1.05	1.02
7	pin content 4.0%	0.90	1.12	1.06

Table 4.7: The normalised stiffness of a pinned lamina for different orientations of the main lamina's fiber direction in the lamina (models 5-7 as presented in Table 4.2).

The local stresses are analyzed in terms of their location within the lamina, with the contributing effects of local fiber volume fraction and fiber direction on these values being assessed. From the contour plots of local failure indicators as presented in Fig. 4.14, it can be seen that the stress concentrations are taking place in the fiber-reinforced distorted zone and, that for the applied strain, local damage is initiated inside the distorted zone but not in the undistorted zone. The stress components that are causing these stress concentrations are either the shear stress for a 0°-lamina and a 30°-lamina, or the transverse stress for a 90°-lamina. The local failure indicator concentrations can be increased by a factor 2 or 3 with respect to the values in an equivalent unpinned lamina (see Table 4.8). This is further correlated with the pin content as depicted in Fig. 4.16. The effect of local fiber volume fraction and fiber direction on the local failure indicators is illustrated in Fig. 4.15 by plotting the results from the different models as described in Table 4.2. It can be seen that the increase of fiber volume fraction in the distorted region has the largest contribution to the local stress concentrations compared to fiber misalignment. These results confirm that, for pinned laminates, earlier damage initiation may indeed take place. The results also demonstrate the importance of a proper evaluation

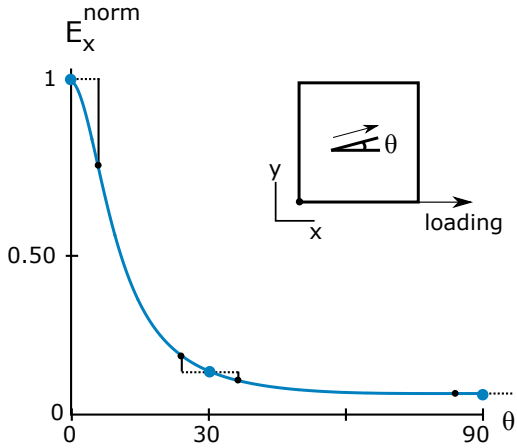

Fig. 4.13: A graph illustrating the effect of fiber misalignment θ_{mis} on the stiffness E whereby the dashed lines show that the fiber misalignment θ_{mis} can either decrease or increase the stiffness (having used hereby the analytical model presented in for example [194]).

of the local fiber volume fraction for a relevant evaluation of local stress concentrations in computational models, and their potential in partly explaining the observed scatter in global strength [80].

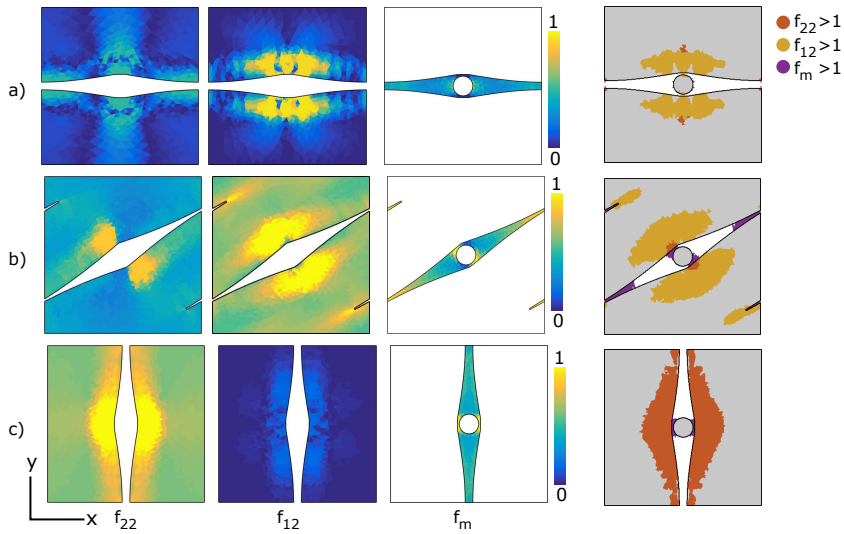

Fig. 4.14: Transverse, shear and matrix cracking local failure indicator distributions for a lamina with fibers aligned in different directions: (a) 0°-lamina, (b) 30°-lamina, (c) 90°-lamina.

	0^o-lamina		30^o-lamina		90^o-lamina	
	$f_{22}^{97\%}$	$f_{12}^{97\%}$	$f_{22}^{97\%}$	$f_{12}^{97\%}$	$f_{22}^{97\%}$	$f_{12}^{97\%}$
equivalent	0.00	0.00	0.34	0.63	0.62	0.00
var V_f / var $\vec{f}_{loc}$	0.59	1.60	0.90	1.43	1.62	0.16

Table 4.8: The 97-percentile of the transverse and shear failure indicators in an equivalent and pinned lamina with different orientations of their main fiber direction.

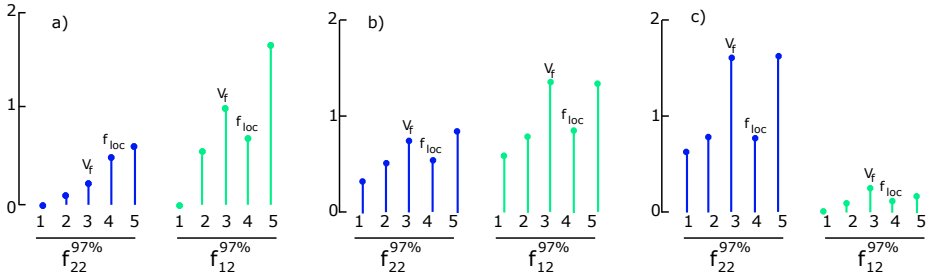

Fig. 4.15: Graphs showing the role of fiber volume fraction V_f and fiber misalignment θ_{mis} on the 97-percentile of the transverse and shear cracking local failure indicators (above 1 indicates local failure) for lamina with fibers aligned in different directions (1-5 are the models presented in Table 4.2): (a) 0°-lamina, (b) 30°-lamina and (c) 90°-lamina.

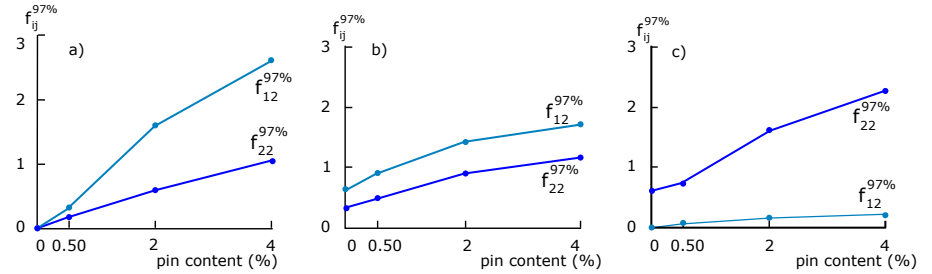

Fig. 4.16: Graphs indicating the effect of pin content on the 97-percentile of the transverse and shear cracking local failure indicators in a lamina with fibers aligned in different directions: (a) 0°-lamina, (b) 30°-lamina and (c) 90°.

Laminate

The global stiffness of the [0°/90°/90°/0°] laminate for both a vertical and inclined pin (see section 4.4.1) is presented in Table 4.9 for both x- and y-direction loading. It can be seen that a reduction in global stiffness is present for all cases and that the reduction is larger for the inclined pinned laminate when loaded transversally to the inclination direction. This enlarged reduction for y-loading (see Fig. 4.17a) can be explained by the larger fiber distortion region that are present in the main load-bearing lamina (90°-lamina), while in the case of x-loading, the main load-bearing lamina 0°-lamina) are only slightly distorted. These results indicate that the geometrical distortions due to pin

rotations can affect the global stiffness, which can partly explain the scatter in global stiffness as observed in experimental results and need to be included in geometrical models.

Local stress distributions for values of $f_{ij} > 1$ are illustrated by contour plots of the local failure indicators in Fig. 4.17b. It can be seen that the stress concentration are correlated with the fiber-reinforced distorted zone (see Fig. 4.17a) and that both transverse, shear, matrix damage initiation may be present. Mechanisms accounting for these local degradation should therefore be included for strength modelling of Z-pinned laminates.

	E_x^{norm}	E_y^{norm}
vertical pin	0.98	0.98
inclined pin	0.98	0.84

Table 4.9: The normalised stiffness of the pinned laminate models in both in-plane directions.

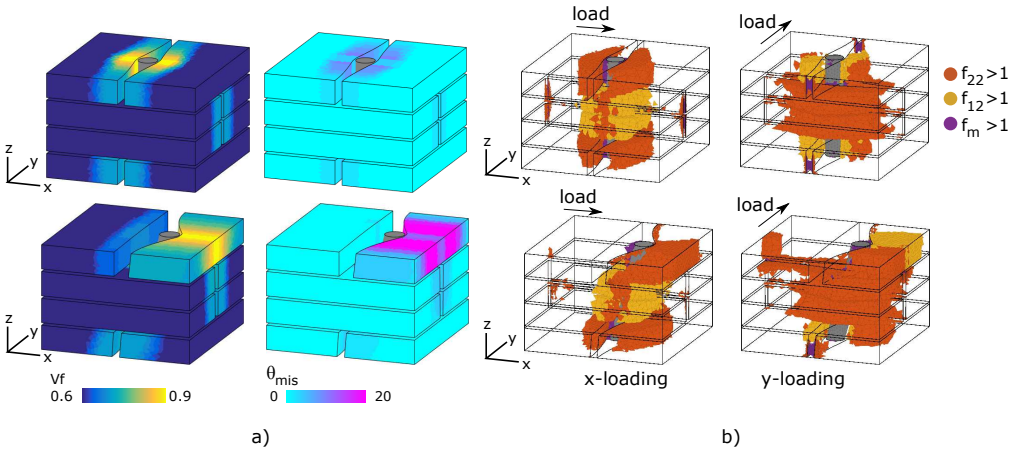

Fig. 4.17: Geometrical and mechanical features of the vertical and inclined pinned laminate model: (a) fiber volume fraction V_f and fiber misalignment θ_{mis} distributions, (b) regions with potential local failure initiation.

4.4.4 Comparison with experimental data

The simulations result are now compared with experimental data presented in [80] that show the stiffness of unidirectional [0°], cross-ply [0°/90°] and quasi-isotropic 0°/45°/−45°/90°] pinned laminates (normalised by the stiffness of an equivalent unpinned laminate) for different pin contents. The normalised stiffness of the unidirectional, cross-ply and quasi-isotropic pinned laminates for pin contents of 2% is hereby approximately 0.87, 0.94 and 1.00, respectively, while a linear trend is observed for increasing pin content.

Lamina

The experimental results indicate that distortions in the 0°-lamina reduce the stiffness to a larger degree compared to distortions in the 45°- and 90°-lamina, and that the distortions in the 45°-lamina reduce the stiffness the least and may even increase the stiffness. Similar trends can be observed from the simulation results (presented in Table 4.4.3) that show that the distortions in the 0°-lamina, 90°-lamina and 30°-lamina are more negatively affecting the stiffness in a successive order respectively. The larger stiffness reduction in the experimental observations, compared to the simulation results, can be explained by not having considered lamina swelling, pin inclination, secondary geometrical features (broken fibers, fiber-crimp, interface cracking, etc.), which may further reduce the stiffness in the lamina modelling.

Laminate

The normalised stiffness of the cross-ply laminates with a pin content of 2% from the experimental observations (0.94) and the simulations (being 0.98 and 0.84 for an inclined pin laminate models with pin inclination due to pin insertion and pin rotation respectively, see Table 4.9) can be compared. The difference between the physical and numerical model values can be explained by differences in geometrical features similar to as presented in section 4.4.4 including some further remarks on pin inclination angle and loading direction:

1. Physically, the pin inclination angle is characterised by a Gaussian distribution with a mean for pin diameters of $280\mu m$ which gradually evolves from 2° on average after pin insertion to approximately 15° on average after consolidation [323]. Numerically, the pin inclination angle was considered as 15° and either obtained from pin insertion or from pin rotation (see Table 4.3). The considered 0°-value for the pin inclination angle upon pin insertion can then be considered as a worst case scenario whereby variations in pin inclination angles (which can be up to 20°) can further affect the results.

2. The stiffness component of Z-pin inclined laminate in a in-plane direction (x- or y- direction) can dependent on the angle between this direction and the pin inclination direction (see Table 4.9), but experimental observations do not make a distinction between the in-plane direction and consequently average out the effect of different pin inclination directions. Averaging the simulation results (0.98 and 0.84) would then lead to a closer estimate compared the experimentally observed value 0.94.

A parametric study including variations in pin inclination angle and direction, and laminate swelling, should then be performed to understand in a quantitative manner the differences between the experimental data and simulations results.

4.5 Discussion

The computation of fiber-reinforced distorted zone model parameters vs. experimental observations

Fiber-reinforced distorted zone model characteristics vs. experimental observations:

1. d_1 **and** d_2 are computed based on (1) assuming their values to be constant in each cross-section, (2) considering d_1 as a multiplication of d_2 ($d_1 = k.d_2$) and (3) using the preservation of the amount of fibers in a cross-section before and after the shaping process by geometrical operations. The fiber-reinforced distorted zone model then depends only on the parameter k which further regulates the distorted zone width. The parameter k can be set by comparing the distorted zone width for different parameters k (see Fig. 4.11) with experimentally observed distorted zone widths. By lack of experimental data, this parameter k is set equal to 1 in all simulations, which means that the width of the constant but increased fiber volume fraction region (determined by d_1) is equal to the width of the linear interpolated region (determined by d_2).

2. **The supposed linear interpolation** between the constant but increased and the undistorted region is consistent with the linear variation of fiber volume fraction distribution in other fiber-reinforced composites near compacted regions [78]. Moreover, a supposed linear interpolation for the fiber direction distribution was also considered in analytical models of Z-pinned and stitched laminates presented in the works [93, 95] to which our models (with $k = +20$) may be compared with.

Fiber-reinforced distorted zone model characteristics vs. multi-fiber model:

1. **The multi-fiber model** presented in Chapter 7 has predicted rather two regions with constant fiber volume fraction and fiber direction, and with a negligible linear interpolation in between the regions. It is believed the assumptions made in the multi-fiber model (no mechanics involved, no matrix, no friction, no physical fiber radius for the lines) are too rough and therefore make a comparison in terms of supposed linear interpolation with the analytical models not worthwhile. An overview of the different aspects which may limit the predictability of the multi-fiber approach are discussed in the manuscript (see section 7.1.5).

Implications of the periodic boundary condition assumption

Single Z-pin unit-cell models have been constructed whereby (1) the periodicity of the mesoscopic geometrical features (being the resin-rich regions) have been taken into account (via the periodic straightening operation) and (2) the fiber-reinforced distorted zones are modelled separately around each resin-rich region (not taking potential interactions). The models assume thus the fiber-reinforced distorted zone around resin-rich regions to not interact with each other and the pin inclination to be equal in all neighbouring unit-cells. These assumptions are indeed not always valid:

1. Fiber-reinforced distorted zones can interact with neigbouring fiber-reinforced distorted zone for higher pin content and inclination angles

2. The pin inclination angle can be different in neighbouring unit-cells following a certain distribution.

Moreover, applying periodic boundary conditions on microscopic non-periodic unit-cell may have certain implications. The potential implications for each assumption are as follows:

1. **For the non-periodic fiber-reinforced distorted zone:** Ideally, the model (depicted in Fig. 3.17a at bottom) should have yellow regions at both sides of the unit-cell. This would indicate stiff regions near the unit-cell boundaries on both sides and relative small deformations locally in the fiber-reinforced regions near the unit-cell borders. For the non-periodic model, yellow regions are not present at both sides. The deformations locally in the fiber-reinforced regions at both sides are therefore probably be larger (due to the less stiff blue region and applied periodic boundary conditions). This would result in a larger load applied on the yellow and blue region, and corresponding higher stress concentrations and earlier local damage near the unit-cell boundaries for the non-periodic model. Additionally, as the distorted zone is not translated to the other side, the non-periodic model may slightly over predict the stiffness and under predict the presence of regions with potential local failure initiation. Still a few remarks should be mentioned:

   (a) The non-periodicity is only present for larger pin content and inclination angles, while in the other cases the fiber-reinforced distorted regions are not interacting with each other and periodicity of the model is preserved.

   (b) While the stress concentrations near the unit-cell boundaries may increase, the main stress concentrations are situated near the pin location and no additional damage locations has been observed near the unit-cell boundaries.

   (c) The difference in relative displacements at the opposite unit-cell boundaries caused by the periodicity assumption might be small as the fibers are aligned with these boundaries.

2. **For the single Z-pin unit-cell model:**

   (a) For Z-pins positioned in a perfect Z-pin pattern (no fiber-weaving), the effect of the single Z-pin assumption (compared with double Z-pin unit-cell models with different Z-pin inclination angles) is considered to be small as the fiber-reinforced distorted zones characteristics for slight differences in Z-pin inclination angle would only cause very slight difference in fiber-reinforced distorted zones.

   (b) For Z-pins that are not perfectly positioned (so fiber-weaving is present, see Fig. 4.2 b), the effects of the single Z-pin model assumption may be much larger. Indeed, (1) the single Z-pin models cannot represent fiber-weaving and (2) as the fiber-weaving itself is characaterised by maximum fiber-misalignment, the fact of not including fiber-weaving may affect the stiffness and local failure initiation levels. The single Z-pin models may underestimate the maximum of the local failure indicators and overestimate the stiffness. A comparison between the single Z-pin model and a double Z-pin

unit-cell model that can include fiber-weaving (illustrated in Fig. 4.10 b) should be performed quantitatively to investigate the effect.

Future work consists in:

1. Extending the fiber-reinforced distorted zone model by accounting for periodicity in the local fiber volume fraction and fiber misalignment distributions for higher pin content and inclination angles. It would suffice to translate the fiber-reinforced distorted zone that extends the unit-cell borders to the opposite side of the unit-cell.

2. Assessing the effect of the applied periodic BC assumption for current models with larger pin content and inclination angle on the stress concentrations and stiffness by comparing the current and extended models in mechanical simulations.

3. Assessing the effect of different pin inclination angles in neighbouring unit-cell models (as well as fiber-weaving) by using the double Z-pin unit-cell models and comparing the results from the single and double Z-pinned models.

The maximum fiber volume fraction

The maximum local fiber volume fraction in the fiber-reinforced distorted zone model was taken as 0.900. The value represent the fiber volume fraction for a closed-packed hexagonal fiber configuration. Such stacking may indeed be difficult to achieve in practice, as such that the assumed maximum fiber volume fraction may be indeed too high. Potential implications of a too-high maximum fiber volume fraction on the modelling results are the following:

1. The stress concentrations may be overestimated while the distorted zone width, which is obtained by the preservation of the amount of fibers, is underestimated. The underestimation of the distorted zone width can further cause an underestimation of both the stiffness and the extent of regions with potential local failure initiation.

2. The closed-form expressions that relate the stiffness and strength components of unidirectional laminates may not be valid for such high fiber volume fractions. A verification of the adopted closed-form expression for the considered range of fiber-volume fraction $[0.50 - 0.90]$ was already performed in [44]. It was shown that most of the stiffness components (except G12) matches well with FE models predictions (even for higher fiber volume fraction) and mentioned that a verification for the strength components was limited by lack of experimental data. In the reference work [44], closed-form expressions for the strength components were taken by lack of better for the range of fiber volume fractions considered.

In future work, more realistic unit-cell models should be generated by lowering the maximum fiber volume fraction. A potential maximum fiber volume fraction can lie in a range $0.75 - 0.80$ (which are potential maximum fiber volume fraction as observed in a woven composite), but should ideally be determined by an in-depth experimental investigation for Z-pinned and stitched composites individually.

The use of linear elasticity for estimating regions with potential local failure initiation

In our approach, linear elastic computations have been used to evaluate both the stiffness and regions where potential damage initiation are to be expected. A global strain of 0.50% is hereby applied. The finite elements in which a local failure indicator exceeded unity are then marked as positions in the RVE were damage initiation is likely to occur. In reality, the behaviour up to 0.50% can be not linear elastic as for example early damage initiation has observed to taken place near 0.30% in 3D reinforced composites. The linear computations were performed because of simplicity, but do have indeed some implications on the estimation of these potential locally damage initiated regions for the globally applied strain compared to full nonlinear simulations.

A non-linear simulation would ideally include local failure initiation mechanisms, damage constitutive laws and damage propagation mechanisms, and be performed with incremental-iterative procedures. Stiffness degradation and/or crack propagation mechanisms, which cause a redistribution of stress, can then take place before the global applied load level, altering hereby the final estimation of the local failure initiated regions. The locally failure initiated regions should therefore simply be seen as an indication of the most critical regions where local failure can take place.

Maximum stress criteria

The maximum stress criteria were used by simplification due to lack of clear data on the coefficient that couples the transverse and shear behaviour in function of the local fiber volume fraction (in for example the Hashin formula). Such an approach was used in the recent contribution [190]. By not accounting for the shear contribution, the obtained results underestimate or overestimate the local failure initiation levels, depending on the ratio of the normal to shear component stress. More elaborated models as Hashin [331], Puck [332] should be used in future work to predict local failure initiation, especially for strength model prediction where an accurate prediction of the local failure initiation may significantly affect the outcome.

4.6 Conclusion

A computational approach was presented for a fully automated generation of mesoscopic geometrical unit-cell models of pinned laminates. The resin-rich regions are modelled by initial straight discretized lines that are gradually shaped using geometrical operations mimicking pin-insertion, pin rotation, and fiber deflections. The fiber-reinforced distorted zone is modelled in a post-processing stage in cross-sections perpendicular to the main fiber direction and on which a certain fiber volume fraction is assumed based on the preservation of the amount of fibers in the cross-section during generation. The shapes of the geometrical features are obtained computationally and in an automated way without the need to be set a priori as for analytical modelling approaches. The ability of the defined approach to obtain shapes computationally and to generate shapes of the main geometrical features belonging to a range of pin parameters and stacking

sequences was also presented.

The geometrical models can be automatically transformed into FE mechanical models, based on which the effect of distortions on global stiffness and local stress distribution can be investigated. The following was observed:

1. The global stiffness of a pinned lamina can both be decreased and increased, depending on the main fiber direction with respect to the tensile direction.
2. The geometrical distortions caused by pin rotation can have a large effect on the global stiffness when loaded transversally to the inclination direction.
3. The fiber-reinforced distorted zone is acting as a stress concentration regions and both transverse, shear, and matrix damage initiation can be present at early strain values.
4. The fiber volume fraction is the main geometrical feature affecting the stress concentration. The results can help explaining the effect of the stacking sequence and the experimentally observed scatter on global stiffness and strength of Z-pinned laminates.

These results emphasize the importance of properly incorporating geometrical features of reinforcement distortions caused by pin rotations and variations in fiber volume fraction in mesoscopic models for Z-pinned laminates. These features have been only partly accounted for by past geometrical models [91–93] and have clearly been shown to affect the material properties of the laminates modelled here.

In the next chapter, the presented computational approach for geometrical model generation will be adopted and extended to generate geometrical unit-cell models for stitched composites, in which geometrical features of local distortions of the reinforcement caused by the stitching yarn need to be accounted for.

Chapter 5

Stitched non-crimp fabric composites

This chapter presents an approach to generate unit-cell models of stitched non-crimp fabric composites. Resin-rich regions and out-of-plane undulations caused by the stitching yarn are represented by initially straight discretised lines, while the stitching yarn is represented initially by a single discretised line which can be transformed into a multi-line configuration to model stitch cross-section variations. The discretised lines are shaped by geometrical operations while a contact treatment and boundary conditions can be used to account for line interactions and to control the bottom and top surface of each lamina respectively. A fiber-reinforced distorted zone with local variations in fiber volume fraction and fiber direction is modelled in cross-sections in a post-processing step. Different shapes of the geometrical features, dependent on the stacking sequences and stitch parameters (stitch diameter, content, tensioning), can be automatically generated. The models are further transformed into finite element based mechanical models to assess how stitching, local fiber volume fraction and fiber misalignment changes, and simplifications made in current geometrical models, affect the global stiffness and damage initiation stress levels.

Contributions:

1. A novel approach to generate unit-cell models of stitched laminates, including an inner-line configuration for fiber-bundles to account for cross-section deformations.
2. The generation of unit-cell models including out-of-plane undulations in surface lamina, variations of local fiber-reinforcement distortions near the stitching yarn and a deformable stitching yarn which is conform with the neighbouring lamina.

Novelty:

1. Deformable stitching yarn.
2. A fiber-reinforced distorted zone model for generally shaped cross-sections.
3. Analysis of out-of-plane undulations, the presence of the stitching yarn and matrix boundary layer.

5.1 Introduction

Stitching is a technique by which a high-strength stitching yarn can be inserted through-the-thickness of non-crimp fabric laminate to increase their out-of-plane properties [87–89]. The out-of-plane properties can be tailored by stitch parameters as stitch content, diameter, pattern and tensioning [333–336]. However, the insertion of the stitching yarn distorts the in-plane fiber-reinforced regions. Experimental investigations have been ambiguous on whether the in-plane mechanical properties are increased, decreased, or remain unchanged by these distortions [34, 80, 89, 99, 337–339]. On the other hand, it is generally accepted that stitching sites are acting as stress concentrations regions which causes early damage initation. [34, 99, 329, 340–343]. Unit-cell models have been shown a valuable approach to help understanding trends from experimental observations as a function of the underlying reinforcement geometry [44, 55]. The main geometrical features of the reinforcement architecture should then be characterised and be included in these models [181, 344].

Resin-rich regions, local fiber-reinforced distorted zones, out-of-plane undulations in the surface lamina and a deformable stitching yarn are the main features present in stitched non-crimp fabrics composites. Their shape and size depend further on the stitch parameters and on the main fiber direction in each lamina, with respect to the stitch direction (Fig. 5.1a) [94, 181, 344, 345]. Eyelet shaped resin-rich regions arise for small stitch content and can evolve into channel-shaped resin-rich regions for larger stitch content in laminae whereby its fibers are aligned in one of the stitch pattern directions (Fig. 5.1b). The width of the resin-rich region in a lamina depends on the angle between the main fiber direction in the lamina and the stitch direction (Fig. 5.1b) and is larger in a surface lamina compared to an inner lamina (Fig. 5.1c). Asymmetrically shaped resin-rich regions are present in laminae with fibers not aligned in one of the stitch pattern directions [34]. Local variations in fiber volume fraction and fiber misalignment are present in the fiber-reinforced distortions zone [346]. Centerline deflections and cross-section shape variations of the stitching yarn should be conform with the neighbouring lamina distortions and are further affected by stitching yarn tensioning, transverse compaction processes. Non-crimp fabric composites have further comparable (but smaller) geometrical features [119, 129, 212, 347, 348] while stitching imperfections can also results in certain geometrical features of the reinforcement architecture (as fiber-weaving [349–351], an inclined through-the-thickness segment of the stitching yarn [94], crimp of the through-the-thickness segment [344], or fiber breakage due to stitch insertion [80]. The main geometrical features of the resin-rich regions and deformable stitching yarn as taken experimental observations are illustrated in Fig. 5.2, while more rigorous data on distorted zones in the fiber-reinforced regions remains state-of-the art.

Analytical modelling approaches have been adopted in the literature to include the presented features in geometrical unit-cell models whereby the laminae were often assumed straight [94–99]. The resin-rich regions are then represented by a cosine-, orthorhombic- or rectangular shape. The fiber-reinforced distorted zone has been modelled by a rectangular region in which the fiber direction [95, 96] and the fiber volume fraction [346] are

assumed to linearly evolve between the resin-rich region boundaries and the undistorted zone. The out-of-plane undulations (in non-crimp fabrics), which are present due to the small binder yarn, have been modelled by either introducing a locally curved region at the corresponding locations underneath the binder yarn in [352], or by considering a straight lamina with changes in the local material axis system representing the fiber waviness as in [353, 354]. The stitching yarn is modelled in [94, 97–99] by straight and circular segments with a circular cross-section in the through-the-thickness segment and an elliptical cross-section in the top segment, and a full fiber compacted state for each cross-section. The simplified modelling for both stitching yarn and lamina resulted in interpenetrations, which were resolved in the finite element model construction by the adoption of a mesh superposition techniques. An example of a stitching yarn geometry obtained from a micro-CT scan can be found in [355]. The models presented here can only partially account for the main geometrical features which further highlights the difficulty of using an analytical modelling approach for describing the geometry of deformable stitching yarns incorporating the lamina distortions and the complex shapes of the reins-rich regions that arise for different stitch parameters and stacking sequences.

A computational approach has been presented in Chapter 4 to generate unit-cell models of Z-pinned laminates [356]. The resin-rich regions and the pin were represented by initially straight discretised lines. The discretised lines were shaped by geometrical inflation, rotation and straightening operations while a contact treatment and boundary conditions accounted for line interactions and control of the bottom and top surface of the lamina respectively. The fiber-reinforced distorted zone was modelled on cross-sections of the laminae in a post-processing step, accounting for local variations in the fiber volume fraction and the fiber direction on the cross-sections.

Here, this computational approach [356] is adopted and further extended for the generation of stitched non-crimp fabric composite unit-cell models. An inner-line configuration is hereby introduced to account for stitching yarn cross-sections (similar to the multi-chain digital element configuration adopted in [165,166,169,171,173,176] for the generation of 3D woven models) as well as a multi-line inflation and flattening operation to introduce the multi-line configuration in a unit-cell model and to mimic transverse compaction respectively. Extensions to the fiber-reinforced distorted zone model presented in [356] are proposed to account for local variations of the distorted zone width in the surface lamina where both in-plane and out-of-plane undulations are present. The framework is illustrated by the generation of unit-cell models for different values of the geometrical operations parameters. The effect of geometrical features on stiffness and damage initiation levels in unit-cell models is afterwards assessed using FE-based mechanical simulations.

5.2 Geometrical model genereration

A unit-cell model of a stitched non-crimp fabric laminate is generated. A modified lock stitch pattern, consisting of a continuous fiber-bundle located on bottom and top of the laminate, and a stitch direction along the x-direction (as illustrated in Fig. 5.1a)

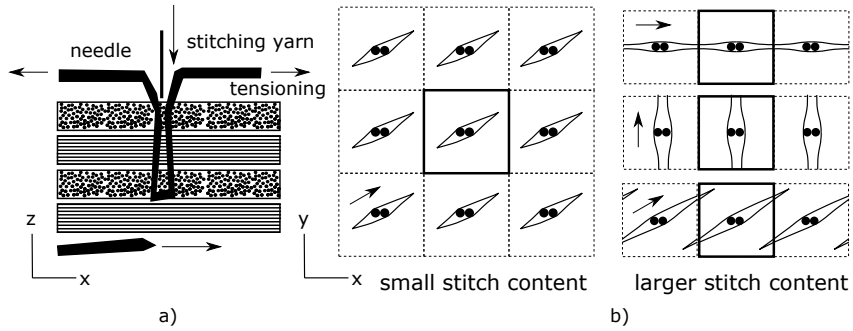

Fig. 5.1: Stitched non-crimp fabric composites: (a) stitching yarn insertion, locking, and tensioning, (b) resin-rich regions in a lamina for small and large stitch content and different fiber orientations, (c) widening of resin-rich regions, out-of-plane undulations in the surface lamina and the modified lock stitch pattern.

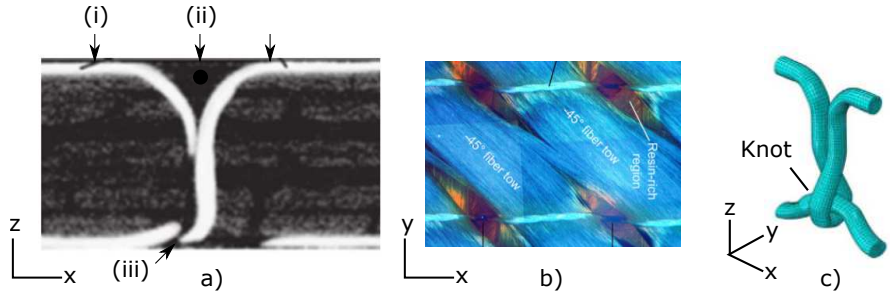

Fig. 5.2: Experimentally observed geometrical features in stitched non-crimp fabric composites: (a) (i) out-of-plane undulations, (ii) widening of resin-rich regions and (iii) the knot structure of a modified lock stitch pattern (image taken from [89]), (b) asymmetrically shaped resin-rich regions (image taken from [34], (c) a post-processed micro-CT obtained modified lock stitch (image taken from [355].

are considered. The modified lock stitch pattern is simplified by two unconnected U-shaped fiber-bundles (see Fig. 5.3a). This assumption, in what respect it may affect the results presented, and to what extent the approach can be modified to accout for it, will be discussed in section 6.5. The non-crimp fabric laminae are further assumed to be initially straight and homogeneous in fiber volume fraction and fiber direction. The minor geometrical features of the binder yarn distortions in the non-crimp fabric laminate, crimping and inclination of the through-thickness segment of the stitching yarn, fiber-weaving for irregular stitch patterns and broken fibers are not considered in the modelling.

5.2.1 Initial model

The stitching yarn (corresponding to a modified lock stitch pattern) is represented by two U-shaped lines and an initial constant circular cross-section (see Fig. 5.3a). The

U-shaped lines are aligned in the stitch direction (x-direction). Their through-thickness segments are positioned near the unit cell center P_C on a very small distance x_{small} from each other and their horizontal parts are positioned at a distance z_1 from the bottom or top of the unit cell. The lines are further discretised in segments with a length equal to one third of a typical stitching yarn diameter ($120\mu m$) [94].

Laminae are represented by initially straight lines that are aligned in their main fiber direction $\vec{f}_{lam}$ (see Fig. 5.3b-c). The lines are positioned near the through-thickness segment of the stitching yarn to represent potential resin-rich regions that arise upon the insertion of the stitching yarn belonging to the unit-cell itself. For inner laminae with fibers not aligned to the main stitch pattern directions, lines are additionally introduced to account for potential resin-rich regions caused by neighbouring stitching yarns (see Fig. 5.3b). The length of the potential resin-rich regions is hereby limited to the length of the lines that are currently employed to represent the resin-rich regions, where this length can easily be enlarged by adding more lines at corresponding opening locations. For the surface laminae (see Fig. 5.3c), lines are additionally positioned near the out-of-plane borders of the lamina to account for potential out-of-plane undulations caused by stitching yarn tensioning. A small line-radius is further attributed to each line (for contact treatment) and the lines are discretised in line segments with a length of $120\mu m$ (similar to the length of the stitching yarn line segments).

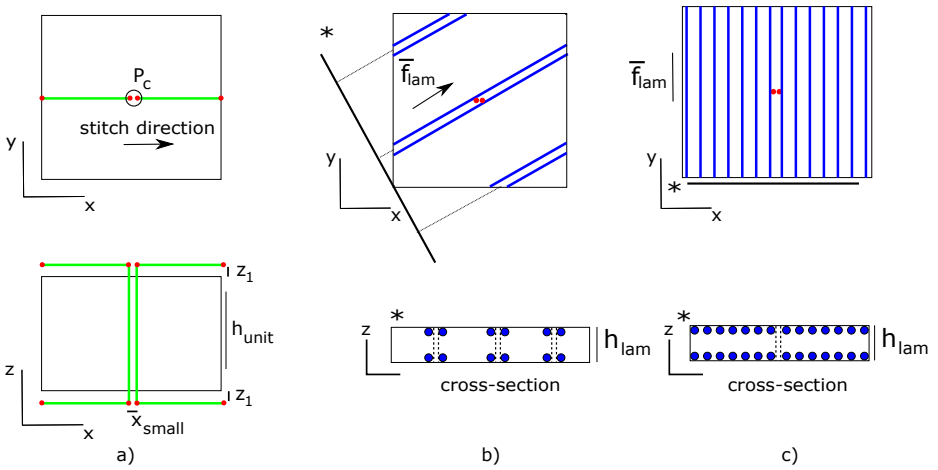

Fig. 5.3: Initial model: (a) stitching yarn model, (b) inner lamina model (lines representing potential resin-rich regions), (c) surface lamina model (lines representing potential resin-rich regions and out-of-plane undulations).

5.2.2 Geometrical tools

The discretised lines are shaped by geometrical operations in subsequent steps while a contact treatment accounts for line interactions (see Fig. 5.4). A straightening, a single-line inflation, a multi-line inflation and a flattening operations are considered here as ge-

ometrical operations. Each step intends to introduce a geometrical features in the model or simply transforms the single-line configuration of the stitching yarn into a multi-line configuration (see Table 5.1). The parameter q_{sl}, which controls the interaction between the stitch lines and lamina lines (see section 5.2.2), is adopted in each step to constrain either the shape of the stitch lines or the lamina lines ($q_{sl} = 0$ and $q_{sl} = 1$ respectively. The constraining allows to preserve the geometry of previously generated features, as such to have a larger control over the introduced features. The step-wise generation process is described in the sequel, followed by a description of the adopted geometrical operation.

Step 1, the stitch lines are inflated by the single-line inflation operation, hereby moving down potentially the lamina lines to account for out-of-plane undulations of the surface lamina in the generated unit-cell model (the out-of-plane undulations are controlled by parameter z_1 in Fig. 5.3a). The initial circular cross-sections of partially inflated stitching yarns can be transformed into elliptical cross-sections to account for deformable stitching yarns. During the stitch cross-section transformation, interpenetrations can arise between the stitching yarn and laminae with fibers not aligned transverse on the stitch direction (see Fig. 5.5). The interpenetrations will further be resolved in step 4 by transforming the single line representation of the stitching yarns into a multi-line representation and by introducing the multi-line representation gradually in the interprenetrated configuration using a multi-line inflation operation.

Step 2, the stitch lines are shaped by the straightening operation to account for different shapes of the stitching yarn centerline due to stitching yarn tensioning

Step 3, the lamina lines are straightened by the same straightening operation to locally smoothen their deformed shapes near the stitching yarn (hereby having constrained the stitch lines).

Step 4, the single-line configuration of the stitching yarn is transformed into a multi-line configuration (see section 5.2.2) to account for further cross-section variations of the stitching yarn. The multi-line configuration is further introduced in the model by a multi-line inflation operation to account for the potential interpenetration arising in step 1 and to generate shapes of the stitching yarn conforming with the resin-rich region boundaries (hereby having constrained the lamina lines).

Step 5, a flattening operation is applied on the unit-cell model to mimic the effect of transverse compaction on the cross-section shapes of the stitching yarn. The lamina-lines are hereby constrained as their geometries were shaped during the previous generation steps.

Step 6, the multi-line configuration of the stitching yarn is tensioned by the straightening operation to account for different cross-section shapes due to stitching yarn tensioning (hereby having constrained the lamina lines).

Step 7, the bottom and top surface of the unit-cell can be adjusted to generate models

with a stitching yarn that is fully embedded in the matrix rather than floating on top of the unit-cell.

Step 8, the local fiber volume fraction and fiber direction inside the laminae and the stitching yarn are obtained in a post-processing step.

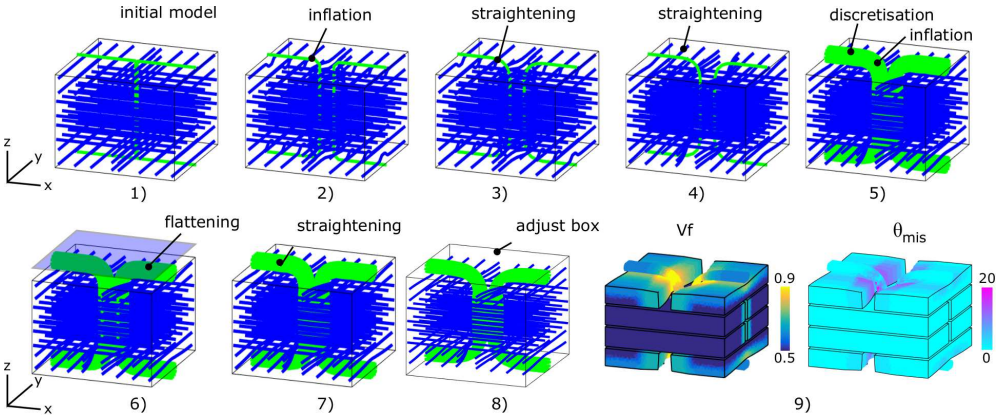

Fig. 5.4: Step-wise generation process: (1) initial model, (2) stitch inflation, (3) stitch straightening, (4) lamina straightening, (5) transformation stitch into multi-line configuration, (6) flattening, (7) stitch straightening, (8) adjusting bottom and top surface of unit-cell box, (9) fiber volume fraction V_f and fiber misalignment θ_{mis} distributions in a post-processing step.

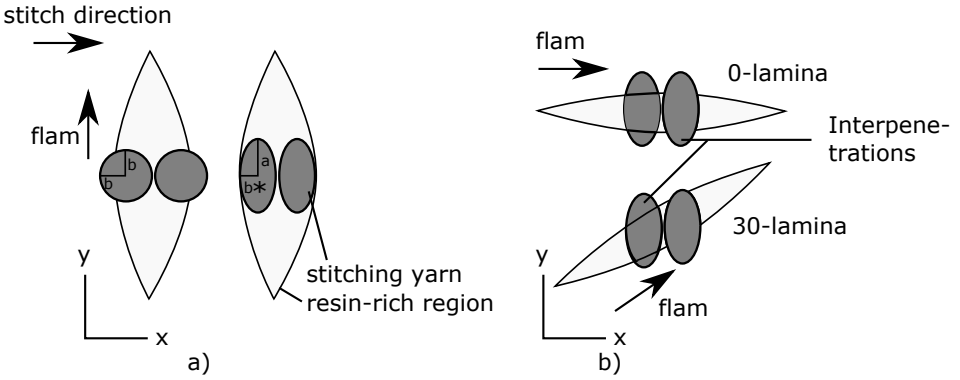

Fig. 5.5: Inflation operation: (a) initial cross-sections transformed into elliptical cross-section for partially inflated stitching yarns, (b) residual interpenetrations in laminae with fibers not aligned in the direction transversal on the stitch direction.

step	operations	id line	q_{sl}	parameter	introduced geometrical feature
1	single-line inflation	stitch	0	f	width of resin-rich region
2	straightening	stitch	0	s_1	centerline of stitching yarn
3	straighening	lamina	1	s_2	length of resin-rich region
4a	multi-line representation	stitch	0	c	deformablility of stitching yarn
4b	multi-line inflation	stitch	0	-	cross-sections of stitching yarn
5	flattening	-	0	z_{limit}^{final}	cross-sections of stitching yarn
6	straightening	stitch	0	s_3	cross-sections of stitching yarn
7	adjust box	-	-	no-yes	matrix

Table 5.1: Different steps during the generation, represented by the applied geometrical operation, a corresponding parameter, the type of line on which the operation is applied, the contact parameter q_{sl} and the geometrical feature which can be used from experimental observations to set the corresponding parameter.

Contact treatment

The distance of a line node P to all other lines is evaluated (see Fig. 5.6). When local interpenetration is detected, the line node P is moved along a direction $\vec{D}_P$ by a fraction q of the interpenetrated distance d_{int} (Eq. 5.1b). The direction $\vec{D}_P$ in which the node P is moved is the normal from node P onto the other interpenetrated line. The full interpenetration is suppressed by the movement of line node Q which belongs to the other line (see Eq. 5.1c)). The position of all nodes is updated once all the movements are computed. This procedure is applied iteratively until the maximum interpenetration is below an allowable residual interpenetration distance.

$$d_{int}^{i} = d^{i} - (R_1 + R_2) \tag{5.1a}$$

$$\vec{x}_{mov}^{P} = q.d_{int}^{P}.\vec{D}_P \tag{5.1b}$$

$$\vec{x}_{mov}^{Q} = (1-q).d_{int}^{Q}.\vec{D}^{Q} \tag{5.1c}$$

where R_1 and R_2 are the radii of the interacting lines, d_i is the distance of point i to the other line, and $\vec{x}_{mov}^{Q}$ and $\vec{x}_{mov}^{P}$ are the movements of point P and point Q respectively.

The fraction q, which determines how lines are moved upon interpenetration, is set to be dependent on the type of the interacting lines (see Table 5.2). Two stitch lines are considered to interact symmetrically with each other ($q = 0.50$). Lamina lines are allowed to remain interpenetrated ($q = 0$). The interaction between the stitch and the lamina lines is regulated by the fraction q_{sl} which can be set during each generation step to constrain the position of certain types of lines.

	stitch	lamina
stitch	0.50	q_{sl}
lamina	(1-q_{sl})	0

Table 5.2: Different contact parameters q dependent on the types of interaction lines.

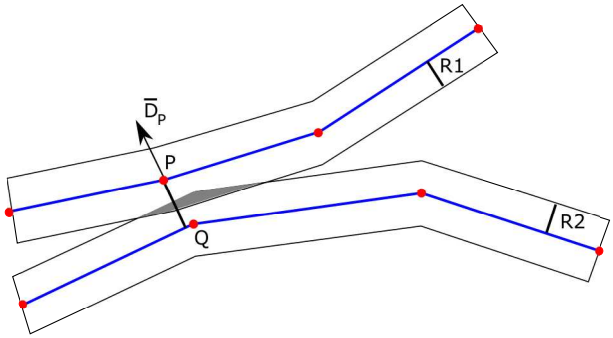

Fig. 5.6: Contact treatment.

Straightening operation

Lines are straightened by redefining the position of each of their nodes $\vec{x}_i$ according to:

$$\vec{x}_i = \frac{1}{2}(\vec{x}_{i-1} + \vec{x}_{i+1}) \tag{5.2}$$

The operation mimicks the kinematics of a fiber upon tensioning [105,357]. Small extensions to its implementation are needed to account potentially for the effect of distortions in neighbouring unit-cells on the geometry of the lamina and stitch lines. The lines on which the straightening operation will be applied (indicated by master in Fig. 5.7) are herefore, before straightening, extended at both sides by a corresponding part (indicated by slave) as illustrated in Fig. 5.7. After straightening, the extended part is used to update the geometry of slave-lines (see Fig. 5.7a-b) or simply removed from the unit-cell model (see Fig. 5.7c).

Inflation operation

The inflation operation incrementally increases a line radius R_{line} from 0 to a final radius R_{line}^{final} (Eq. 5.3a). The final radius is considered as a fraction f of an initial stitching yarn radius R_{line}^{init} (Eq. 5.3b).

$$R_{line}^{n} = R_{line}^{n-1} + \frac{R_{line}^{init}}{n_{infl}} \tag{5.3a}$$

$$R_{line}^{final} = f.R_{line}^{init} \tag{5.3b}$$

where n_{infl} is the number of increments which is needed to prevent the stitch lines from jumping over the lamina-lines during the inflation operation. The initial circular cross-sections of partially inflated stitching yarns are subsequently transformed into elliptical cross-sections by extending their transversal dimension on the stitch direction, and by preserving the cross-section area (as was indicated on Fig. 5.5a).

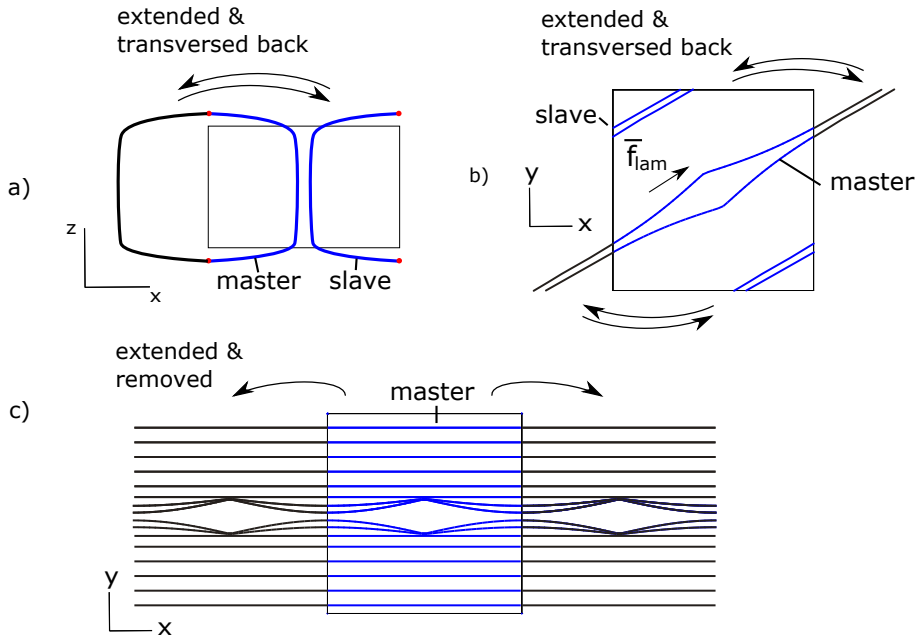

Fig. 5.7: Accounting for the effect of neighbouring unit-cell: (a) the stitching yarn, (b) an inner lamina with fibers not aligned with a stitch pattern direction, (c) a surface lamina.

Inner-line configuration

Fig. 5.8 illustrates the transformation of the single line configuration of the stitching yarn into a multi-line configuration. The initial cross-sections of the stitching yarn are discretised in circles which are defined by their center points and line radius. The center points are considered as the nodes of a uniform 2D mesh, whereby the number of nodes can be regulated by adjusting the uniform mesh size. The line radius R_{line} is determined by the number of lines c and the initial fiber volume fraction $V_{f,stitch}$ of the stitching yarn:

$$R_{line} = \sqrt{\frac{V_{f,stitch}.\pi ab}{\pi c}} \tag{5.4}$$

where a and b are the long and short axis dimensions of the elliptical cross-section (of the stitching yarn) respectively. The cross-sections are then transformed from the 2D plane configuration into their a local coordinate systems attached to the stitching yarn centerline (see Fig. 5.8a), whereafter the center nodes of the circles between adjacent cross-sections are connected to obtain the multi-line configuration (see Fig. 5.8b).

Multi-line inflation

The multi-line inflation gradually inflates the cross-sections of a multi-line configuration from a reduced size to its original dimensions. It hereby gradually moves the position

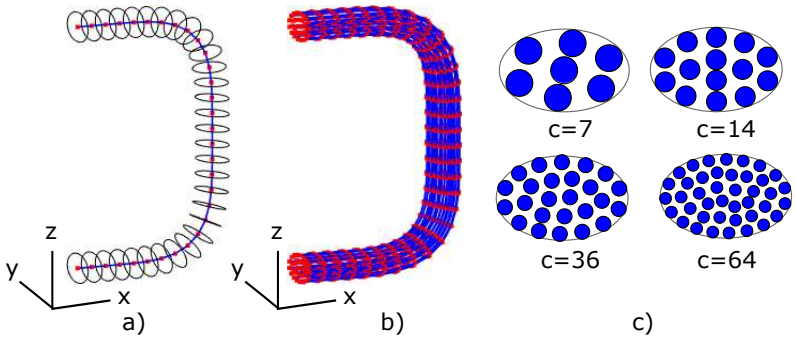

Fig. 5.8: The construction of an inner-line configuration for the stiching yarn: (a) the initial single-line configuration, (b) the multi-line configuration, (c) different cross-section discretisations (c indicates the number of lines.

of the center nodes in each cross-section away from the stitching yarn centerline and adjusts the radii of the lines. The distance d_{node} of a center node in each cross-section to the cross-section center C, and the corresponding direction $\vec{D}_{node}$ (see Fig. 5.9a), are first determined:

$$d_{node} = ||\vec{x}_{node} - \vec{x}_C|| \tag{5.5a}$$

$$\vec{D}_{node} = (\vec{x}_{node} - \vec{x}_C)/d_{node} \tag{5.5b}$$

The position of each center node $\vec{x}_{node}$ and the radius R_{line} of each lines can then be incrementally updated according to:

$$\vec{x}^i_{node} = \vec{x}_C + \left(\frac{i}{n}\right).d_{node}.\vec{D}_{node} \tag{5.6a}$$

$$R^i_{line} = \left(\frac{i}{n}\right).R_{line} \tag{5.6b}$$

where i is the increment number. The number of increments n should be large enough to prevent the crossing of the stitch lines over the lamina lines during the multi-line inflation operation:

$$\left(\frac{max(d_{node})}{n}\right) < (R^{lam}_{line} + R^{stitch}_{line}) \tag{5.7}$$

where R^{lam}_{line} and R^{stitch}_{line} are the radius of the lamina lines and stitch lines, respectively. An example of the stitching yarn and its cross-section at different stages during the multi-line inflation operation are illustrated in Fig. 5.9b.

Flattening operation

A top boundary vertical position is gradually decreased from z^{init}_{limit} to z^{final}_{limit} while lines coming into contact with this border are moved downwards (see Fig. 5.10). The self-

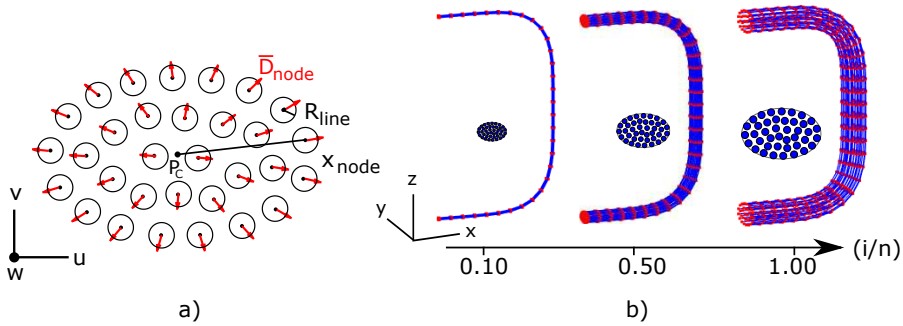

Fig. 5.9: Multi-line inflation operation: (a) a discretised cross-section indicating the operation parameters (b) an illustration of progressively inflated stitching yarns, during which the contact between the stitch lines, as well as with neighbouring lamina lines, is controlled by the parameter q_{sl}.

contact between the lines is processed by the contact treatment.

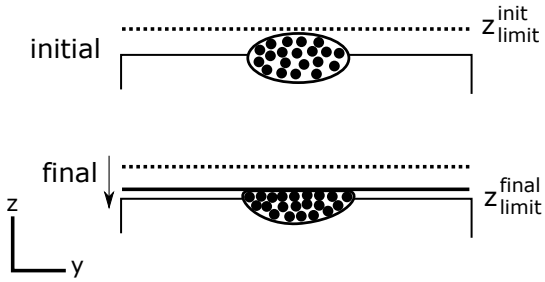

Fig. 5.10: Flattening operation whereby a vertical limit z_{limit} is gradually lowered.

Boundary conditions

In-plane periodicity of the unit-cell borders is enforced by tying constraints between initially periodic line nodes located on the in-plane unit-cell borders (see Fig. 5.11a). The bottom and top surface of laminae can be forced to remain straight by moving the line nodes back to corresponding locations (see Fig. 5.11b). The update of node positions is performed during the contact treatment procedures.

5.2.3 Fiber-reinforced distorted zone model

The fiber-reinforced distorted zone and corresponding local fiber volume fraction and fiber direction are modelled on cross-sections in the lamina (as illustrated in Fig. 5.12a). The cross-sections are obtained from the discretised lines by intersections perpendicular to the main fiber direction in the lamina and by accounting afterwards for the line radius of the lamina lines. The fiber-reinforced distorted zone in each cross-sections is assumed to take place only in a limited region near the deformed border of the cross-section. The

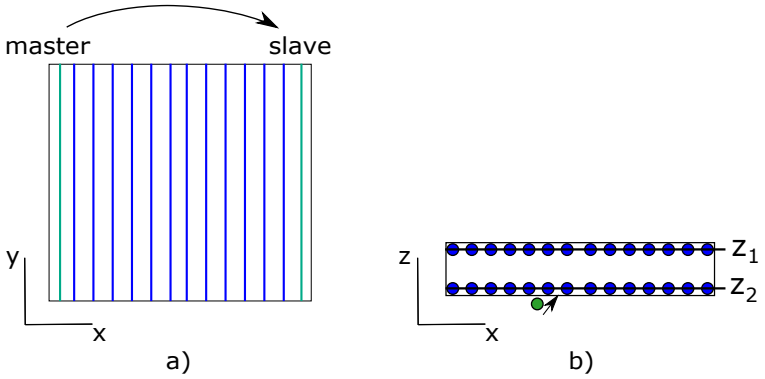

Fig. 5.11: Boundary conditions: (a) applied on the in-plane borders of the surface lamina for periodic model generation, (b) applied on the bottom or top surface of lamina to allow the generation of a straight lamina surface.

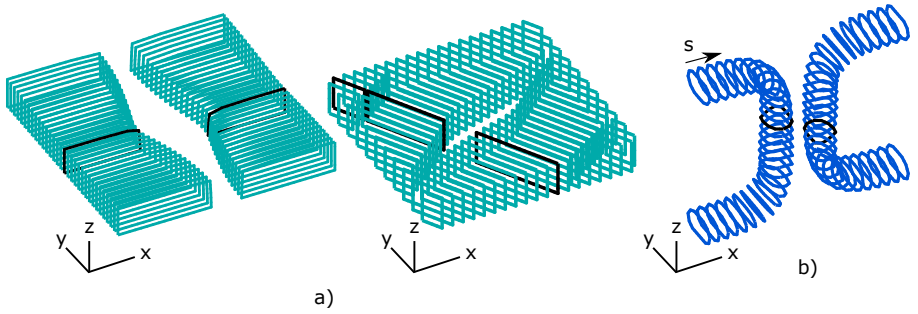

Fig. 5.12: Generated cross-sections for: (a) surface and inner laminae, (b) the stitching yarn.

width of the fiber-reinforced distorted zone in each cross-section is further considered to be dependent on the local movement of the border (see Fig. 5.13a). Local distorted zones near each line in a cross-section will therefore first be constructed and then combined into a global distorted zone.

Local distorted zone near a line in a cross-section

The local distorted zone near a line i in a cross-section at position u (see Fig. 5.13a) can be characterised by two regions with different fiber volume fractions and fiber direction distribution, similar to concepts presented in [356]. The first region, which is the closest to the deformed border, is characterised by a constant but increased fiber volume fraction $V_{f,c,i}(u)$ and a constant fiber direction $\vec{f}_{loc}(u,i)$ that is tangent to the boundary of the resin-rich regions or at the top surface of the lamina. The second region, which is located between the first region and the undistorted zone, is characterised by a fiber volume fraction and a fiber direction linearly evolving between both regions. The width of this first and second region in a cross-section at position u near a line i is represented

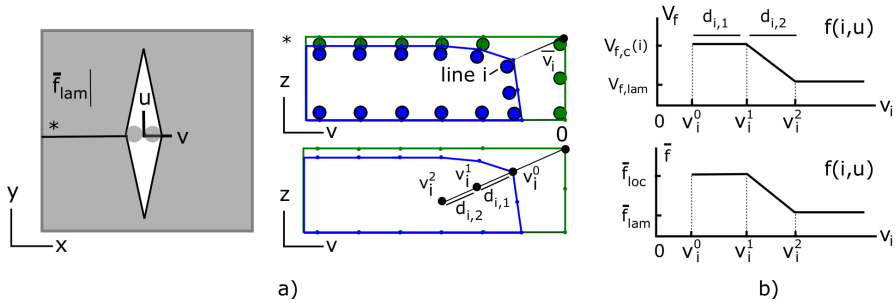

Fig. 5.13: Local distorted zone model near a line in a cross-section: (a) an undeformed and deformed cross-section (green and blue respectively) indicating the model parameters (the circles in the top cross-section represent the intersections of the discretised lines at the cross-section location), (b) the assumed fiber volume fraction V_f and fiber direction $\vec{f}$ distribution near a line in cross-section along a local axis v_i.

by $d_{i,1}(u)$ and $d_{i,2}(u)$ respectively.

The parameters $d_{i,1}(u)$,$d_{i,2}(u)$ and $V_{f,c}(u,i)$ are computed based on the following assumptions. First, an amount of fibers that is equivalent to $v_i(u).V_{f,\text{lam}}$ is assumed to be redistributed locally according to [356]:

$$v_i(u).V_{f,\text{lam}} = (d_{i,1}(u) + \frac{d_{i,2}(u)}{2}).(V_{f,c,i}(u) - V_{f,\text{lam}}) \tag{5.8}$$

where $v_i(u)$ is the movement of the line i at position u and $V_{f,\text{lam}}$ is the initial fiber volume fraction in the lamina. Secondly, $d_{i,1}(u)$ and $d_{i,2}(u)$ are assumed constant along each line i. Thirdly, $d_{i,1}$ is considered a multiplication of $d_{i,2}$:

$$d_{i,1} = k.d_{i,2} \tag{5.9}$$

where k is considered equal for each line.
The local fiber volume fraction in the lamina near the stitching yarn is assumed to depend linearly on the local movement of the stitching yarn and is assumed to be equal to the maximum fiber volume fraction $V_{f,max}$ for local movements of the stitching yarn larger than d_{max}:

$$V_{f,i} = V_{f,lam} + \frac{v_{i,max}}{d_{max}}.(V_{f,max} - V_{f,lam}) \quad \leq V_{f,max} \tag{5.10}$$

where $v_{i,max}$ represents the local movement of the stitching yarn locally near a line i and is determined from the maximum displacement v of the line i. The maximum local fiber volume fraction $V_{f,max}$ is considered to be 0.900, representing the fiber volume fraction of a fully packed hexagonal fiber-configuration [158]. The distance d_{max} is considered $100\mu m$, being approximately 10 times a carbon fiber diameter. The system of equations is then solved by first computing the increased fiber volume fraction $V_{f,c,i}(u)$ in the cross-section underneath the stitching yarn (using Eq. 5.10), followed by the calculation

of $d_{i,1}$ and $d_{i,2}$ using Eq. 5.9-5.8, from which afterwards $V_{f,c,i}(u)$ can be computed for each line i at each cross-section position u.

The values of the distorted zone parameters are then assigned to circular-shaped distorted zones as illustrated in Fig. 5.14a. The fiber volume fraction $V_{f,i}$ and the fiber direction $\vec{f}_{loc,i}$ distributions near a line i in a cross-section at position u for such circular-shaped distorted zones can be described as:

$$V_{f,i}(r,u) = \begin{cases} V_{f,lam} & (d_{2,i} \leq r) \\ V_{f,lam} + (\frac{r-d_{1,i}}{d_{2,i}-d_{1,i}})(V_{f,c,i}(u) - V_{f,lam}) & (d_{1,i} \leq r \leq d_{2,i}) \\ V_{f,c,i}(u) & (r \leq d_{1,i}) \end{cases} \tag{5.11}$$

$$\vec{f}_{loc,i}(r,u) = \begin{cases} \vec{f}_{lam} & (d_{2,i} \leq r) \\ \vec{f}_{lam} + (\frac{r-d_{1,i}}{d_{2,i}-d_{1,i}})(\vec{f}_{border,i}(u) - \vec{f}_{lam}) & (d_{1,i} \leq r \leq d_{2,i}) \\ \vec{f}_{border,i}(u) & (r \leq d_{1,i}) \end{cases} \tag{5.12}$$

where r is the distance from a point to the point center C_i corresponding to line i.

Global distorted zone in a cross-section

The global fiber volume fraction field $V_f(u,v,z)$ is determined in each cross-section by taking locally the maximum of the local fiber volume fraction fields $V_{f,i}$:

$$V_f(u,v,z) = max(V_{f,i}(r,u))$$

The global fiber direction field $\vec{f}_{loc}(u,v,w)$ is defined in each point of a cross-section as the local fiber direction belonging to the line i from which the fiber volume fraction was obtained:

$$\vec{f}_{loc}(u,v,z) = \vec{f}_{loc,i}(u,v,z) \quad \text{with } i \text{ satisfying} \quad V_f(u,v,z) = V_{f,i}(u,v,z)$$

The fiber misalignment θ_{mis}, which is often used in the illustrations to represent the fiber direction in a lamina, is defined by the angle between a local fiber direction and the main fiber direction in the lamina. Examples of obtained fiber volume fraction, and in-plane, out-of-plane and total fiber misalignment distribution in a cross-section are illustrated in Fig. 5.14b.

Discussion

The circular field assumption near a line has been introduced as a tool to construct varying fiber volume fraction and fiber directions distributions in a cross-sections correlated with the local movements of cross-section boundaries. The obtained results and the models should ideally be further validated by experimental observations on the microstructure of the distorted fiber-reinforced regions which are currently not available in the literature.

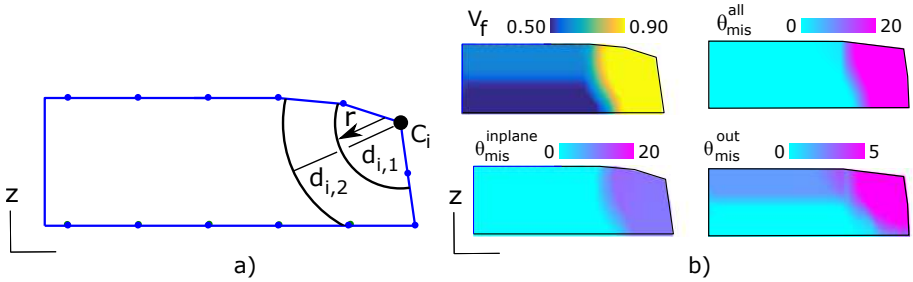

Fig. 5.14: Global distorted zone model in a cross-section: (a) a circular-shaped local distorted zone near each line, (b) the obtained fiber volume fraction V_f and fiber misalignment θ_{mis} distribution, as well as the in-plane and out-of-plane fiber misalignment distribution (θ^{in}_{mis} and θ^{out}_{mis} respectively).

5.2.4 The fiber volume fraction and fiber direction in the stitching yarn

A constant fiber volume fraction and fiber direction are assumed in each cross-section of the stitching yarn (which are illustrated in Fig. 5.12b). The constant fiber volume fraction in a cross-section at position s along the stitching yarn is determined as:

$$V_f(s) = \frac{A_{init}}{A_{deform}(s)}.V_{f,stitch} \tag{5.13}$$

where A_{init} and A_{deform} are the initial and deformed area of the cross-section, respectively, and $V_{f,stitch}$ is the initial local fiber volume fraction of the stitching yarn. The constant fiber direction in each cross-section is taken as the local tangent to the centerline at the cross-section position.

5.3 Generated geometrical features

Different shapes of certain geometrical features which can be generated by the approach are illustrated in this section. The geometrical models are generated using the generation strategy described in Table 5.1. The presented results can then be used to select the values of the parameters of the geometrical operations with the intent to match experimental observations.

5.3.1 Centerline of the stitching yarn

Different shapes of the stitching yarn's centerline can be obtained by varying the number of straigthening operations s_1 or the contact parameter q_{sl} in generation step 3. In Fig. 5.15a, the parameter s_1 is varied while having set q_{sl} to 0. In Fig. 5.15b, the parameter q_{sl} is varied while having set s to 10. The parameter s_1 increases the main deflections of the centerline while the parameters q_{sl} fine-tunes its shape in the highest curved region.

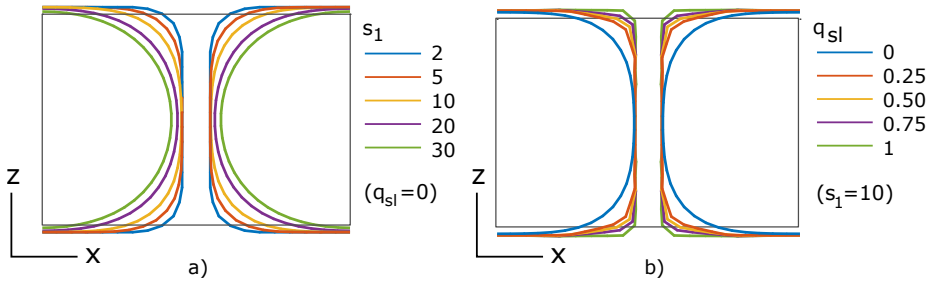

Fig. 5.15: Different shapes of the stitching yarn centerline by varying: (a) the straightening parameter s_1 and (b) the contact parameter q_{sl}.

5.3.2 Shapes of the resin-rich regions

The complexity in shapes of the resin-rich regions for different laminate stacking sequences and stitch content, which can automatically be generated in step 2, is illustrated in the following (Fig. 5.16). A [90°/0°/30°/90°] stitched laminate with a stitching yarn initial radius of $100\mu m$ is considered. The unit-cell size is taken as either $3550\mu m$ or $1770\mu m$ for a stitch content of 0.5% or 2% respectively. In Fig. 5.16, the transition from eyelet-shaped into smooth channel shaped resin-rich region for increased stitch content can seamlessly be obtained. The width of the resin-rich regions that depends on the angle between the fiber direction in the lamina and the stitch direction is also captured; and the assymmetrical shapes of the resin-rich region and fiber misalignment distributions in lamina with fibers not aligned in stitch pattern direction are also obtained.

5.3.3 Cross-section shapes of the stitching yarn

First, the number of lines in the multi-line configuration (parameter c in Eq. 5.7) is determined by a convergence study on the geometry of a stitching yarn on which a certain number of straightening operations were applied. Afterwards, the cross-section shapes of the stitching yarn for a different number of straightening operations applied on the stitching yarn mimicking different stitching yarn tensioning stages, are illustrated.

Convergence study on the number of lines

Fig. 5.17 illustrates the effect of using a different number of lines c (in generation step 4) on the geometry of a tensioned stitching yarn. Cross-section discretisations with 7, 14, 36, and 64 lines were hereby analysed and the effect of the number of lines was investigated on the deformed shapes and area of the cross-sections located at given positions along the stitching yarn (see Fig. 5.17a). It can be seen that the shape and area of the considered cross-sections converges and that this convergence is already taking place for a number of lines equal to 14. So, c equal to 14 is used in further model generations (see Table 5.1).

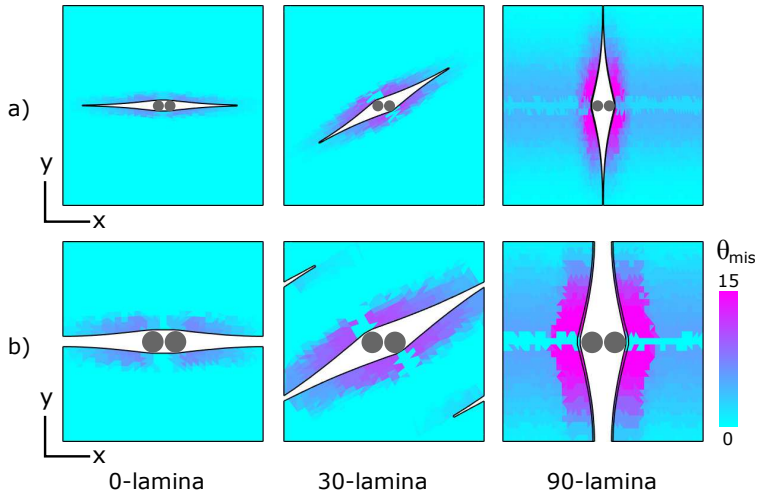

Fig. 5.16: An illustration of the shapes of resin-rich regions and fiber misalignment distributions θ_{mis} in stitched laminae for different orientations of the main fiber direction (0°, 30° and 90°) in the lamina and different stitch content: (a) a stitch content of 0.50%, (b) a stitch content of 2.00% (the stitching yarn is here simplifed represented by two circular cross-sections).

Mimicking different binder yarn tensioning

Cross-section shape variations in the stitching yarn corresponding to different stitching yarn tensioning states can be generated in step 5 by setting a different number of straightening operations s_3, as illustrated in Fig. 5.18a. The cross-sections in the most curved region (plane 2) are the most affected by increasing values of s_3 whereby the cross-sections are first widened and then flattened while being conform with the slight out-of-plane undulations of the underlying surface lamina. The cross-sections in the through-thickness (plane 4) are barely affected by s_3, which is explained from the highly compacted states of the multi-line configuration in the through-thickness segment of the stitching yarn as caused by the multi-line inflation process (see Fig. 5.17). Note that a fully compacted state in the through-the-thickness segment of the stitching yarn is also considered in the analytical models presented in [158]. The cross-sections in the top segment start flattening only for larger values of s_3 and can further be straightened at their top border by a subsequent flattening operation as performed in step 5. More compacted states of the stitching yarn can further be observed from the fiber volume fraction distribution contour plots presented in Fig. 5.18b for increasing values of s_3.

5.3.4 Comparing with experimental observations

The shapes of the geometrical features illustrated in Fig. 5.15, Fig. 5.16) can be compared with the experimental observations presented in Fig. 5.2. Qualitatively, it can be seen that the modelling approach is able to account for asymmetrically shapes of resin-rich regions, deformable stitching yarn and out-of-plane undulations, whereby the knot

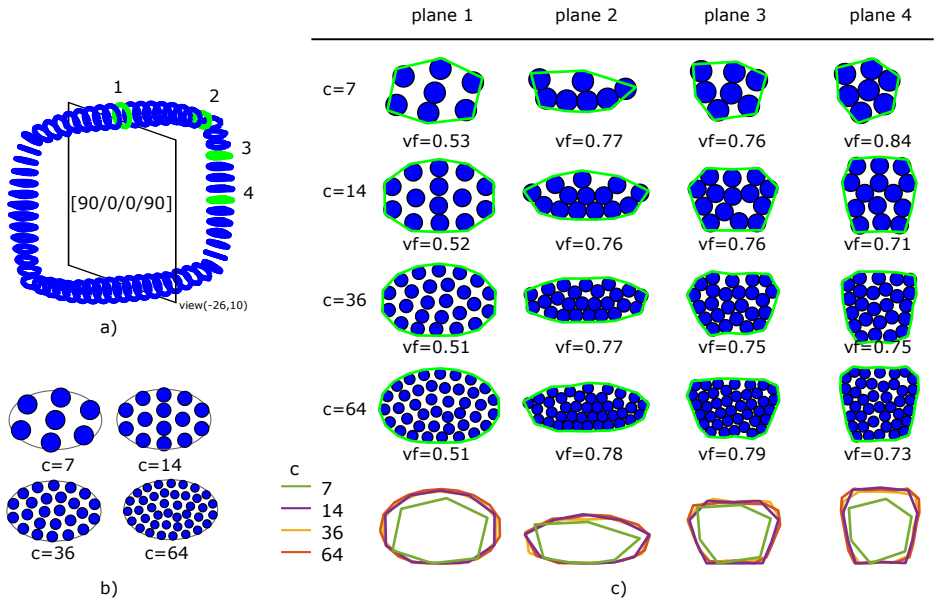

Fig. 5.17: Convergence study for the number of lines c on the geometry of a tensioned stitching yarn: (a) the cross-section locations, (b) the initial cross-sections corresponding to different lines, (c) the deformed cross-section shapes and local fiber volume fraction.

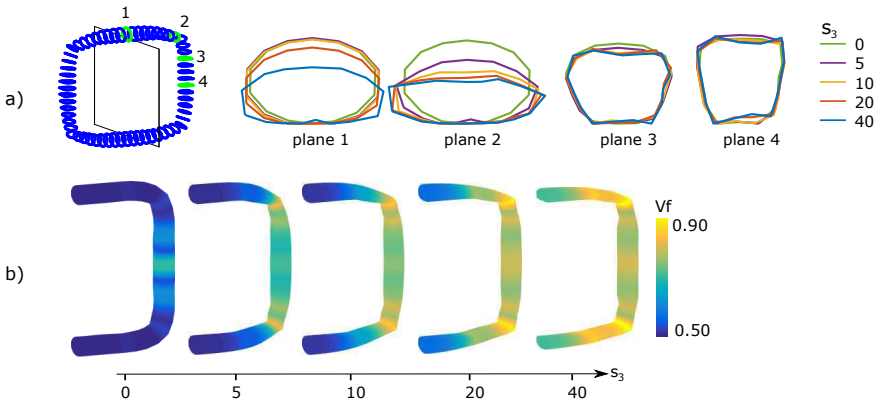

Fig. 5.18: Shapes of a tensioned stitching yarn for varying straightening parameter s_3: (a) cross-section shapes and (b) fiber volume fraction V_f distribution.

structure of the stitching and the asymmetrical fiber-reinforced region distortions on the bottom and top of the laminate could be accounted for by the simplified stitching yarn model. Quantitatively, the parameters of the geometrical operations can be regulate to potentially match exact dimensions and shape of geometrical features (which need to be validated in future work).

5.4 Mechanical simulations

The geometrical models can next be transformed into a conforming tetrahedral mesh with in-plane periodic surface meshes for further use in mechanical simulations with computational homogenisation (mechanical simulations are performed in Abaqus). First, the cross-sections of the laminae and the stitching yarn are transformed into closed triangular surfaces which are then used to define the triangulated surface of the matrix. Secondly, potential interpentrations between the stitching yarn and the lamina are first partly avoided by increasing the initial dimensions of the stitching yarn prior to geometrical model generation and removing the offset after the generation process. Residual interpenetrations are further resolved in a post-processing by simply moving the points of the stitching yarn which interpenetrate the lamina to the outside, while a gap between the regions can be inserted simultaneously. Thirdly, the resulting closed triangulated surface representation of the laminate, the stitching yarn and the matrix are used as input for the meshing software GMSH [316]. An example of a generated mesh of a geometrical model for which the stitching yarn floats on top of the unit-cell is illustrated in Fig. 5.19.

laminate	stacking sequence	$[0°/90°/90°/0°]$
	$V_{f,lam}$	0.500
	unit-cell dimensions	$1750x1750x1200\mu m^3$
	ply thickness	$300\mu m$
stitching yarn	radius	$100\mu m^*$
	$V_{f,stitch}$	0.500
	content	2%
	spacing	$1750\mu m$
generation parameters	$f = 0.80$, $s_1 = 7$, $s_2 = 50$, $s_3 = 7$, $k = 1$, adjust box = no	

Table 5.3: The initial model and generation parameters for the stitched laminate model. The radius of the stitching yarn is calculated from the stitching yarn spacing, the stitch content and an assumed initial circular cross-section of the stitching yarn.

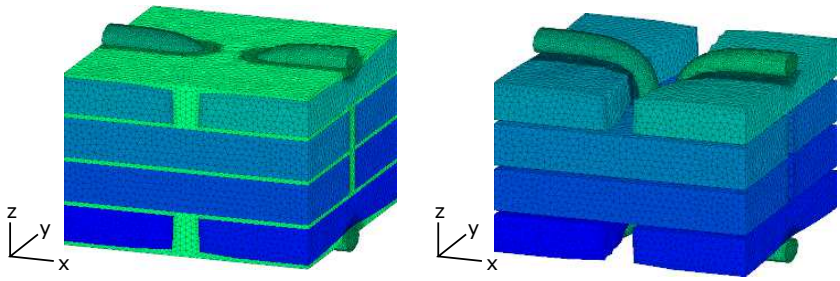

Fig. 5.19: Generated mesh of a stitched laminate model whereby the matrix is conform with the initial unit-cell box dimensions: (a) with matrix, (b) without matrix.

5.4.1 Models

The effect of stitching, the role of local fiber volume fraction distribution and fiber misalignment, and the effect of simplifications made in geometrical models presented in the literature on the stiffness and local stress concentrations is present in three following cases.

Case 1, the effect of stitching is investigated by comparing a stitched laminate model with an equivalent unstitched laminate model. The stitched laminate model is generated using the generation procedures and parameters as described in Table 5.1 and Table 5.3 respectively. The mesh size parameters are taken equal as for the Z-pinned laminates (see chapter 4). A constant overall fiber volume fraction in the unit-cell is ensured by considering the bottom and top of the unit-cell (which encloses the in-plane fiber-reinforced region) to be independent of the stitching yarn (see Fig. 5.19). This causes additional complexity in defining the matrix region (as explained in chapter 3). The effects of adding a matrix boundary layer (which simplifies the model generation) are analysed in case 3. The unstitched laminate model is taken as the initial model without the stitching yarn and the corresponding distortions on the reinforcement architecture.

Case 2, the influence of fiber volume fraction and fiber direction variations is investigated by means of the models presented in Table 5.4 in which a constant or variable fiber volume fraction or fiber direction distributions can be considered for the laminae.

1. The constant fiber volume fraction $V_{f,const}^{lam}$ in each lamina is obtained by:

$$V_{f,const}^{lam} = \frac{V_{f,lam}.H_{lam}^{init}}{H_{lam}^{deform}}$$

   where H_{lam}^{init} and H_{lam}^{deform} are the volume of the undistorted and distorted lamina respectively.

2. The constant fiber direction $\vec{f}_{loc}$ in each lamina is the main fiber direction $\vec{f}_{lam}$ in the lamina.

3. The in-plane and out-of-plane fiber direction distribution ($\vec{f}_{loc,xy}$ and $\vec{f}_{,loc,z}$ respectively) are obtained from the variable fiber-direction by considering only the in-plane or out-of-plane component of the fiber direction respectively.

Case 3, the effect of simplified features in geometrical models is investigated by comparing the stitched laminate model with three simplified geometrical models. The stitched laminate model itself (see Fig. 5.20a) considers both out-of-plane undulations in the surface lamina, the stitching yarn and a matrix region which is conform with the lamina. A simplified model 1 (the straight border model, see Fig. 5.20b) does not consider the out-of-plane undulations and the presence of the stitching yarn. A simplified model 2 (the no stitch model, see Fig. 5.20c) does not consider the presence of the stitching yarn. A simplified model 3 (the box around model, see Fig. 5.20d) considers a matrix region which fully embeds the stitching yarn. The simplified models were generated using the same generation procedures and parameters as for the generation of the stitched laminate

model, in which the straight borders were obtained by constraining the top border of the surface lamina.

The fiber volume fraction and fiber misalignment characteristics for each generated model are further presented in Table 5.4.

model	description	$V_f^{lam,xy}$	$V_{f,surf}^{max}$	$(\theta_{mis} > 0)_{surf}^{vol\%}$	$\theta_{mis,xy}^{max}$	$\theta_{mis,z}^{max}$	θ_{mis}^{max}
model 1	equivalent	0.46	0.50	0.00	0	0	0
model 2	const V_f / const $\vec{f}_{loc}$	0.46	0.72	0.00	0	0	0
model 3	var V_f / const $\vec{f}_{loc}$	0.44	0.90	0.00	0	0	0
model 4	const V_f / var $\vec{f}_{loc,xy}$	0.46	0.72	0.37	12	0	12
model 5	const V_f / var $\vec{f}_{loc,z}$	0.46	0.72	0.57	0	6	6
model 6	var V_f / var $\vec{f}_{loc}$	0.44	0.90	0.64	12	6	13
model 7	no stitch	0.44	0.90	0.64	12	6	13
model 8	box around	0.36	0.90	0.65	12	6	13
model 9	straight border	0.46	0.90	0.37	12	0	12

Table 5.4: The in-plane fiber volume fraction V_f, and certain fiber volume fraction V_f and fiber misalignment θ_{mis} characteristics in the surface lamina, for the models presented in Table 1.

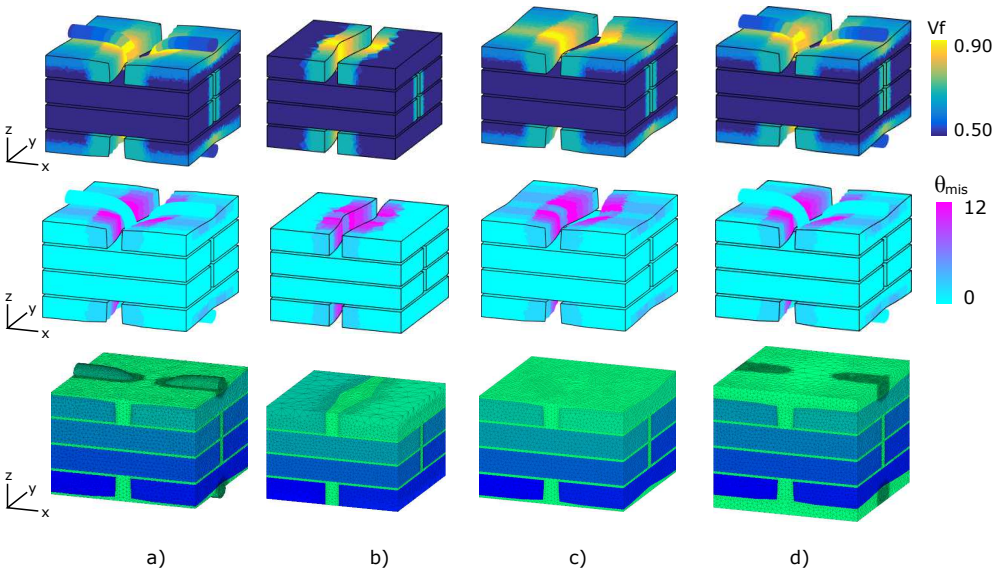

Fig. 5.20: The models 6-9 (presented in section 5.4.1) illustrated by means of the fiber volume fraction V_f and fiber misalignment θ_{mis} distribution, and the generated mesh: (a) stitched laminate model (model 6), (b) straight border model (model 9), (c) no stitching yarn model (model 7), (d) box around model (model 8).

5.4.2 Boundary conditions, material properties and mechanical analysis methodology

The unit-cell models are subjected to periodic boundary conditions on their in-plane borders while their bottom and top surfaces remain free. Carbon fibers and epoxy matrix are considered as constitutive materials for which properties are presented in Table 5.5. The properties of the fiber-reinforced region in function of the local fiber volume fraction are obtained using the Chamis-formulae [186] (for stiffness) and emperical formulae presented in [187, 188] (for strength) in which the local fiber direction is used to define the local material axis-system in which these properties are assigned. A global strain of 0.50% is then applied on the unit-cell model, a straining level that has been shown experimentally to cause early damage initiation in stitched laminates [99, 329].

The stiffness of the unit-cell models is computed and normalised by the stiffness of the equivalent unstitched laminate model. The local stress levels in each finite element are evaluated based on their potential to initiate damage. Transverse cracking (via f_{22}) and shear cracking (via f_{12}) in the fiber-reinforced regions, debonding at the interface between the fiber-reinforced regions and the matrix (via f_{int}) and matrix cracking (via f_m) are experimentally observed [34, 182, 340, 342] as damage initiation mechanisms in fiber-reinforced composites, and are therefore further considered in this work. Each damage initiation mechanisms is evaluated by a local failure indicator f_{ij} defined by:

$$f_{22} = \frac{\sigma_{22}}{X_{22}(V_f)} \geq 1$$
$$f_{12} = \frac{\sigma_{12}}{X_{12}(V_f)} \geq 1$$
$$f_m = \frac{\sigma_p}{X_t} \geq 1$$

where σ_p is the maximum tensile principle stress, X_t is the tensile strength of the matrix, and X_{22} and X_{12} are transerve and shear strength, respectively, of the fiber-reinforced regions. The strength properties X_{22} and X_{12} in function of the fiber volume fraction are computed using the Chamis formulae. Interface debonding is evaluated by Ye's criterion [358]:

$$f_{int} = \sqrt{(\frac{< \sigma_{nn} >}{X_{nn}})^2 + (\frac{\sigma_{nt}}{X_{nt}})^2} \geq 1$$

where $< . >$ is the MacAuley bracket defined as $< x >= \frac{1}{2}(x + |x|)$, σ_{nn} and σ_{tn} are the normal and tangential stress component, respectively, and X_{nn} and X_{tn} are the corresponding mode-1 and mode-2 interfacial strengths (see Table 5.5). A 97-percentile of each failure indicator [356] will further be used to compare the local failure indicator distribution between the different models.

Stiffness	carbon fiber	epoxy matrix	strength	carbon fiber	epoxy matrix	interface
$E_{11}(GPa)$	231	3.45	$X_{11,t}(MPa)$	3500	70	-
$E_{22}(GPa)$	15	-	$X_{11,c}(MPa)$	3000	130	-
$E_{33}(GPa)$	15	-	$X_{12}(MPa)$	-	57	-
v_{12}	0.20	0.35	$\varepsilon^f_{11,t}(\%)$	1.51	4.5	-
v_{13}	0.20	-	$\varepsilon^f_{11,c}(\%)$	1.30	8	-
v_{23}	0.20	-	$\gamma^f_{12}(\%)$	-	5	-
$G_{12}(GPa)$	15	1.28	$X_{nn}(MPa)$	-	-	80
$G_{13}(GPa)$	7	-	$X_{nt}(MPa)$	-	-	100
$G_{23}(GPa)$	7	-				

Table 5.5: The stiffness and strength properties of carbon fiber (type AS4 [330]) and epoxy matrix (type 5260 [330]), and the strength properties of the interface between the fiber-reinforced regions and the matrix [359].

5.4.3 Results

The effect of stitching (case 1)

E^x_{norm}	1.01
E^y_{norm}	0.85

Table 5.6: The normalised stiffness components of the stitched laminate model (the x- and y-direction are clarified in Fig. 5.19).

The normalised stiffness of the stitched laminate model in the x- and y-direction is presented in Table 5.6. The stiffness in the x-direction is slightly increased, while the stiffness in the y-direction is largely decreased. The decrease in stiffness can be attributed to the fiber misalignments (similar to the discussion presented in chapter 4), that are larger in the fiber-reinforced regions aligned in the y-direction, where the slight increase in stiffness can be attributed to the presence of the stitching yarn. These results compare with the experimental data presented in [80] which show the normalised stiffness to vary in between 0.80 and 1.20. The effects of geometrical simplifications as fiber-crimp fiber-breakage, and neglecting of the continuity of the stitching yarn are further assumed to lie in this experimental range.

The local failure indicator distributions in the stitched laminate model for x- and y- loading are illustrated in Fig. 5.21 and summarised by their 97-percentile value in Table 5.7. The 97-percentile of the local failure indicators is increased by a factor 2 to 3 in the lamina, indicating early damage initiation. Transverse cracking in the surface lamina is present for the x-loading, and shear cracking in the surface lamina and transverse cracking in the stitching yarn are present for the y-loading, whereby the regions with potential for local failure initiation (see Fig. 5.22) are situated near the stitching yarn. The stitching yarn experiences hereby damage for y-direction loading but not for x-direction loading. Note that the damage initiation regions are symmetrically on bottom and top of the laminate, while in physical models, the knot configuration of the stitching yarn may cause increased levels of distortions and corresponding damage initiated regions at the

bottom of the laminate. The role of local fiber volume fraction and fiber direction on the failure indicator mechanisms is investigated in the next subsection.

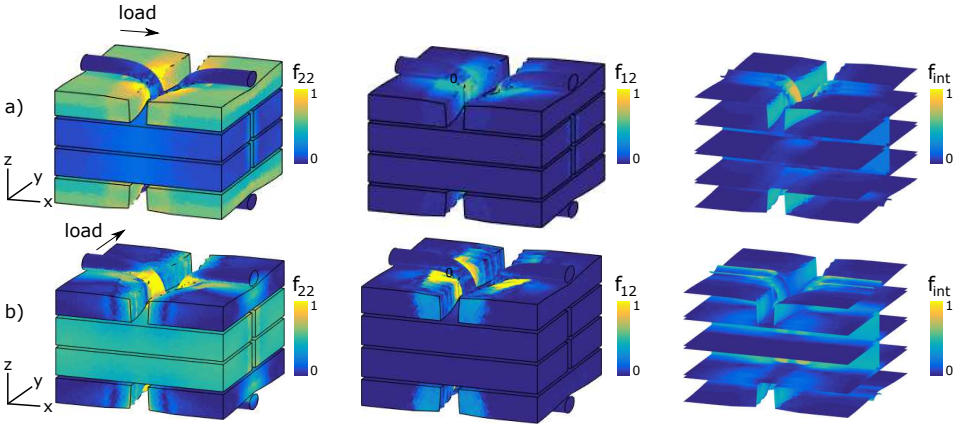

Fig. 5.21: Failure indicator distributions for the stitched laminate model for different load direction: (a) in the stitch direction, (b) transverse on the stitch direction.

		stitch			surface lamina		inner lamina		interface	matrix
		$f_{22}^{97\%}$	$f_{12}^{97\%}$	$f_{int}^{97\%}$	$f_{22}^{97\%}$	$f_{12}^{97\%}$	$f_{22}^{97\%}$	$f_{12}^{97\%}$	$f_{int}^{97\%}$	$f_{m}^{97\%}$
x-load	equivalent	-	-	-	0.49	0.00	0.12	0.00	0.00	0.28
	var V_f/var $\vec{f}_{loc}$	0.30	0.38	0.75	0.94	0.49	0.25	0.27	0.13	0.63
y-load	equivalent	-	-	-	0.12	0.00	0.49	0.00	0.00	0.28
	var V_f/var $\vec{f}_{loc}$	1.85	0.12	0.64	0.85	1.70	0.84	0.08	0.38	0.56

Table 5.7: A 97-percentile of the local failure indicator distributions in the stitching yarn, the surface and inner lamina, the matrix and at the bottom interface of the surface lamina, for the equivalent unstitched and stitched laminate model.

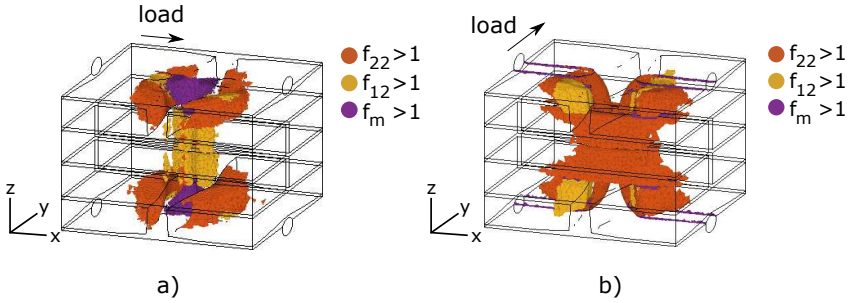

Fig. 5.22: Regions with potential for local failure initiation in the stitched laminate model for different load direction:(a) in the stitch direction, (b) transverse to the stitch direction.

The role of fiber volume fraction and fiber misalignment (case 2)

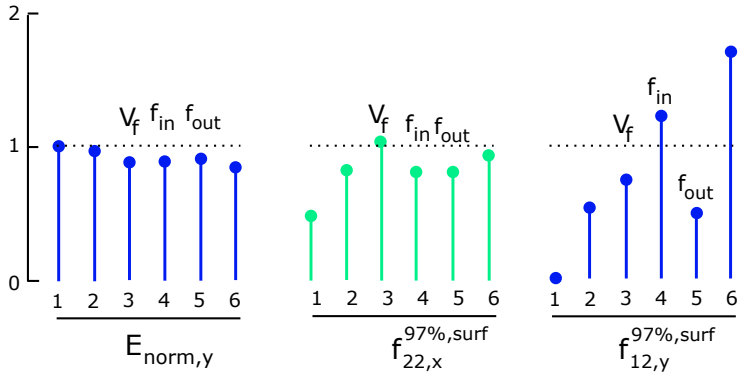

Fig. 5.23: The role of local fiber volume fraction V_f, in-plane fiber misalignment f_{in} and out-of-plane fiber misalignment f_{out} on the stiffness and the transverse and shear cracking failure indicator in the surface lamina for different load directions, using hereby the models presented in Table 5.4.

The influence of fiber volume fraction and fiber misalignment variations on the normalised stiffness and damage initiation for the stitched laminate model is illustrated in Fig. 5.23. The normalised stiffness in the y-direction $E_{norm,y}$, and the local failure indicators $f_{22}^{97\%}$ and $f_{12}^{97\%}$ in the surface lamina for x- and y-loading respectively, are considered in the analyses, as these parameters have been shown to be the most affected by stitching (see case 1). The following can be observed (see Fig. 5.23): The normalised stiffness in the y-direction is evenly affected by both fiber volume fraction and fiber misalignment variations. Transverse cracking in the surface lamina $f_{22}^{97\%}$ is mainly affected by the fiber volume fraction (as similar to experimental observations reported in [342]). Shear cracking in the surface lamina $f_{12}^{97\%}$ is mainly affected by the (in-plane) fiber misalignment. The local fiber volume fraction and the fiber misalignment are therefore shown to be important to include in models aiming at damage initiation prediction.

The effect of geometrical simplifications (case 3)

The role of simplified geometrical features on the stiffness and local failure indicators in the surface lamina of the simplified models for x- and y-loading is illustrated in Fig. 5.24. The stiffness and local failure indicators of the simplified models are here normalised by corresponding parameters of the stitched laminate model. The following can be observed (see Fig. 5.24). A model which does not include the stitching yarn (model 7 in Table 5.4) can provide a good estimate for the stiffness but underestimates or overestimates the local failure indicators in the surface lamina (Fig. 5.24a). A model which does neither include the stitching yarn or the out-of-plane undulations in the surface lamina (model 8 in Table 5.4) overestimates the stiffness in the y-direction, and underestimate and overestimate even more the local failure indicators compared to a model which does not include the stitching yarn (Fig. 5.24b). A model which embeds fully the stitching

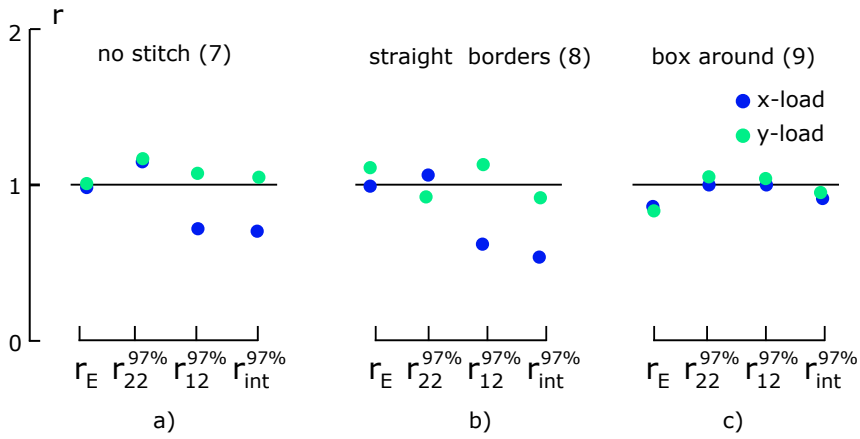

Fig. 5.24: The effect of geometrical simplifications in the models (as presented in Table 5.4) on the stiffness and the transverse and shear cracking, and interface debonding, failure indicators in the surface lamina, whereby the stiffness and the failure indicators of each (simplified) model were normalised by the corresponding parameters of the full stitched model (which are represented by parameter *r*): (a) no stitching yarn model, (b) straight border model and (c) box around model.

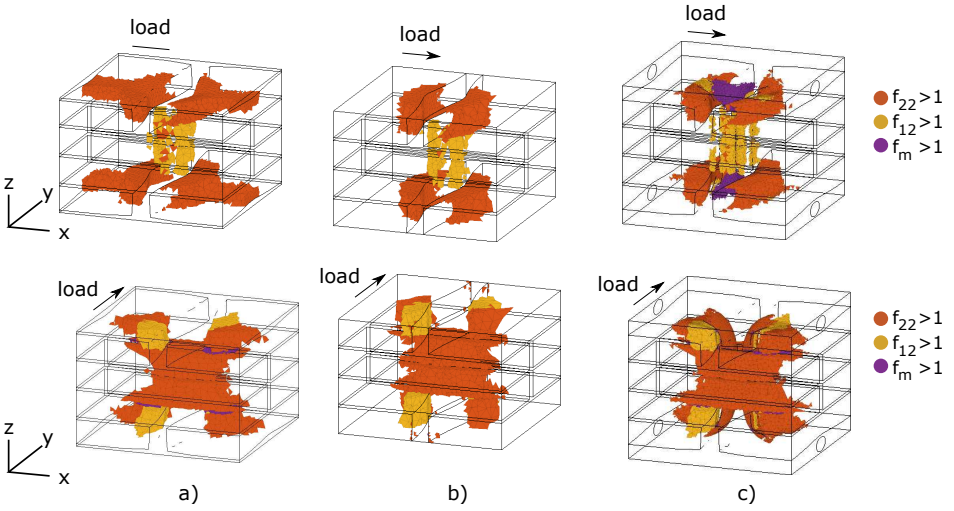

Fig. 5.25: Regions with potential for local failure initiation in the simplified models with an indication of the main local damage initiation mechanisms, for a load applied both in and transverse on the stitch direction: (a) no stitching yarn model, (b) straight borders model and (c) box around model.

yarn (model 9 in Table 5.4) underestimates the stiffness (due to the added matrix boundary layer) but can still provide a satisfactory estimation of the local failure indicator with respect to the full laminate model (Fig. 5.24c). The regions undergoing damage initia-

tion are further also affected by the geometrical features as can be observed in Fig. 5.25. The out-of-plane undulations resulted in an enlargement of the regions with potential local failure initiation in the surface lamina while the stitching yarn was responsible for local regions of matrix cracking. Both stitching yarn, out-of-plane undulations and a matrix region which surrounds only the in-plane fiber-reinforce regions should therefore be considered in models aiming at an accurate prediction of both stiffness and damage initiation stress levels.

5.5 Discussion

5.5.1 Simplified stitch yarn model

The modified lock stitch pattern was simplified represented by two unconnected U-shaped line-bundles,. The continuity of the fiber-bundles at bottom and top of the laminate and the knot structure of the stitching yarns are not considered.

1. By not considering the continuity of the stitching yarns, the generated models may slightly underestimate the stiffness in the stitch direction. The underestimation of the stiffness may however be limited due to the fact that (1) the stitching yarn is only a small fraction of the in-plane fiber-volume fraction in the stitch direction and (2) that it was shown that the presence of the stitching yarn affected barely the stiffness (see Fig. 5.24a).

2. By not considering the knot in the stitch pattern, the generated models may underestimate the reinforcement distortions and the corresponding stress concentration levels at the bottom of the laminate. It is assumed that the effect of such simplifications are in the same range as other simplifications assumed in the model (being no fiber-breakage, asymmetry of stitching yarn, fiber-weaving between stitch positions).

The approach presented in this work can further be modified to account for these features. The initial model of the stitching yarn should hereby be modified while the same geometrical operations can be adopted, but it should still be investigated whether such an approach would generate realistic geometries of the knot structures.

5.5.2 Comparison with experimental results

The results of the models can be qualitatively compared with experimental data present in [80]. The data are a summary of a substantial amount of published data on the stiffness of stitched laminates (normalised by an equivalent unstitched laminate) for different stitch content. It is show that the normalised stiffness could vary in between 0.80 to 1.20 and that it remained ambiguous whether the normalised stiffness decreases or increases for larger stitch content. Comparing these data with the simulation results presented in Table 5.6, it can be seen that the generated models are able to predict a stiffness lying in the same range. The geometrical simplifications in the models are then assumed to have an effect on the stiffnes which lies in the experimental range. Note that the models are not constructed based on quantitative geometrical data, but that such data, specially

for complex features as binder yarn, are not available. The presented framework offers a unique approach to assess the effect of geometrical features which are difficult to measure experimentally.

5.6 Conclusion

An approach was presented for the automated generation of mesoscopic unit-cell models for stitched non-crimp fabric composites. Potential resin-rich regions and out-of-plane undulations in the lamina are represented initially by straight discretised lines, while the stitching yarn is initially represented by a single discretised line. The disccretised lines are shaped by geometrical operations while a contact treatment accounts for line interactions. Boundary conditions can be imposed to control the out-of-plane undulations of the surfaces of the lamina. The single-line configuration of the stitching yarn can be transformed into a multi-line configuration to account for cross-section variations of the stitching yarn during the generation process. The fiber volume fraction and fiber direction in the laminae are modelled based on cross-sections of these in a post-processing stage, allowing to account for a local fiber-reinforced distorted zone in the lamina with variations in fiber volume fraction and fiber misalignment. The shape of the centerline and cross-section of the stitching yarn corresponding to different stitching yarn tension states can be set by the parameters of geometrical operations, as well as the length of the resin-rich regions and out-of-plane undulations, the shape of which are automatically conform with the shape of the stitching yarn.

The effect of the reinforcement distortions caused by the stiching yarn insertion on the stiffness and damage initiation levels of the stitched laminate unit-cell models is assessed by means of elastic computations:

1. The stiffness is largely reduced transversal to the stitching direction, while the stiffness is slightly increased in the stitching direction.

2. Early damage initiation is taking place in the stitched models in regions located near the stitching sites.

3. Transverse and shear cracking in the surface lamina, and transverse cracking in the stitching yarn are the main critical damage initiation mechanisms in a [0/90/90/0] stitched laminate model.

4. Fiber volume fraction and fiber misalignment variations affect the prediction of transverse and shear cracking.

5. Out-of-plane undulations and a matrix which surrounds the stitching yarn affect the stiffness, while the presence of the stitching yarn and out-of-plane undulations affect damage initiation levels. Unit-cell models including such geometrical features can provide further insights in stiffness and damage initation results with respect to earlier works [95, 96].

Fiber volume fraction and fiber misalignment variations in the lamina, the stitching yarn, the out-of-plane undulations in the surface lamina and a matrix which surrounds only the

in-plane fiber-reinforced regions should therefore be properly accounted for in models aiming at a correct estimation of the stiffness and damage initiation levels. A comparison of the mechanical performance to the Z-pinned laminates is done in Chapter 7.

In the next chapter, 3D woven non-crimp fabric unit-cells models, including cross-section variations in the surface weft yarns and binder yarns, could be generated using the proposed framework for geometrical operations combined with the multi-line configuration presented here to represent the binder yarn.

Chapter 6
3D woven non-crimp fabric composites

This chapter presents an approach to generate unit-cell models of 3D woven non-crimp fabric composites with the ability to incorporate cross-section variations in the weft and binder yarns. The approach starts from an initial loose-state configuration of the fiber-bundles, in which each fiber-bundle is represented by a discretised line. The discretised lines are shaped in a step-wise generation process by geometrical operations, while the single line configuration of the weft and binder yarns can be transformed into a multi-line configuration to account for their cross-section variation in subsequent generation steps. The fiber volume fraction and fiber direction are modelled on cross-sections in a post-processing step. The shape of the surface weft yarn cross-section and binder yarn cross-sections and centerline for different binder content, diameter and tensioning can be automatically accounted for. The geometrical models are then transformed into finite element models to investigate how the binder yarn, and cross-section variations in the surface weft and binder yarns alter the stiffness and damage initiation levels.

Contributions:

1. An unified model generation approach for 3D reinforced composites (pinned, stitched, 3D woven).
2. A boundary-line configuration to account for cross-section variations in fiber-bundles.

Novelty:

1. Deformable weft and binder yarns.

6.1 Introduction

3D woven non-crimp fabric composites consist of in-plane fiber-bundles which are straight and interwoven by a binder yarn (see Fig. 6.1) to increase their delamination resistance [360–362]. The in-plane and out-of-plane mechanical properties of these composites have shown to be larger than 2D woven composites [90, 363, 364], showing their potential to replace the widely-adopted 2D woven composites. The properties of the 3D woven composites can further be tailored by binder parameters as binder content, diameter, length, tension, pattern, etc. [80, 126, 196, 365–367]. However, the insertion of the binder yarn distorts the reinforcement architecture of the in-plane fiber-bundles.

Experimental studies remain ambiguous whether the in-plane mechanical properties are reduced, increased or left unchanged by the distortions [80, 122, 368, 369], but are clear on the fact that binder locations are acting as stress concentration regions that cause early damage initiation [24, 196, 363]. Unit-cell models have therefore shown to be a valuable approach to help understanding experimental observations or to even predict the mechanical behaviour of 3D woven composites. [44, 328, 370]. The main geometrical features of the reinforcement architecture therefore need to be characterised and included in the models.

Centerline deflection and cross-section variations in the surface weft yarn and the binder yarn, as well as the warp yarn for larger binder yarn tensioning and transverse compaction, are the main geometrical characteristics that are present in 3D orthogonally woven composites (see Fig. 6.2). Their shape and size further depend on the binder parameters and manufacturing conditions [33, 35, 101]. The binder content affects the cross-section variations and corresponding fiber waviness in the surface weft yarn [196]. The binder yarn tensioning can cause deflections of the surface weft yarn centerlines, and corresponding distortions in the underlying warp yarns, and generates higher compacted stages of the binder yarn itself. The cross-section in the top segment of the binder yarn (Z-crown, indicated in Fig. 6.1a) are hereby more compacted than the cross-sections in the through-the-thickness segment [35, 371]. Transverse compaction can further cause the sinking of Z-crown into the surface weft yarn [182,372] and the flattening and widening of the warp and weft yarns. Assymmetrical shapes of the binder yarn [190], crimping of the through-thickness segment of the binder yarn [373,374] and fiber-breakage during 3D weaving [375] can also arise.

Analytical modelling approaches have been adopted in [100–102] to include the main features in geometrical models. In earlier models, the warp and weft yarns are considered straight with constant cross-sections along their centerline. In more advanced models, centerline deflections and cross-section shape variations in the warp, weft and binder yarn have been accounted for [100]. Energy-based approaches could then be used on analytical models to predict the centerline position and the cross-section dimensions of the fiber-bundles for different in-plane and compaction loading stages [158, 159, 376], while elliptical-shaped cross-sections of the fiber-bundles were assumed.

Image-based approaches were adopted in [190, 372] to generate realistic geometrical models of 3D woven composites. To this end, the images of micro-CT scans were transformed into a voxel-based mesh representation [190] or into a tetrahedral mesh representation [372].

A digital element approach was adopted in [103,104,165–168,170–172,176,177] to generate 3D woven composite models, in which the shape of centerlines and cross-sections of the fiber-bundles are obtained computationally during a finite element simulation. Initially, a loose-state configuration of the binder yarn inbetween the warp and weft yarn is assumed. The fiber-bundles can then be transformed into a single- or a multi-line configuration of frictionless connected bar or rod elements. A thermal contraction is further applied on the binder yarn, followed by a global compaction on the unit-cell model,

while contact elements account for fiber-bundle interaction to generate the geometrical model. Stig adopted also a finite element framework to generate 3D woven composite models [163, 164] in which the fiber-bundles are assumed to initially interpenetrate each other. The fiber-bundles are then transformed into a shell element representation with the shell elements being positioned along their contour resulting in a tube structure. A hydrodynamic pressure is further applied on the shell-element representation to gradually inflate the fiber-bundles until a desired fiber-bundle volume fraction, while contact elements accounting for fiber-bundle interactions at initial intepenetrating locations causes deformable cross-section shape variations of the fiber-bundles.

Recently, a geometry-based framework to generate 3D woven unit-cell models was used in [105, 357]. The fiber-bundles are represented by a single discretised line and constant cross-section. The discretised lines are shaped by straightening operations until an equilibrium between fiber-bundle movements is obtained, with a contact treatment accounting for the line interactions. The geometry-based framework was adopted later on to generate Z-pinned and stitched laminate unit-cell models [356, 377]. Potential resin-rich regions and out-of-plane undulations in the laminae are hereby represented by initial straight discretised lines while the pin and stitching yarn are represented initially by a single discretised line. The discretised lines are shaped in step-wise manner by geometrical operations while the contact treatment accounts for line interactions. The initial single-line configuration of the stitching yarn could hereby be transformed in a generation step into a multi-line configuration to account in subsequent steps for its cross-section variations.

Here, 3D orthogonally woven non-crimp fabric composites unit-cell models which include cross-sections variations in the weft and binder yarns are generated by the geometry-based framework. The cross-section variations for the weft and binder yarns are accounted for by a boundary- and inner-line procedure respectively (as defined in section 6.2.2). The originality of the approach is the ability to represent cross-section variations in a geometry-based framework (so no mechanics induced) and the presentation of a unified approach to generate all morphologies of 3D reinforced composites (pinned, stitched, 3D woven) with the same tool. The geometrical models are then transformed into finite element models to investigate how the 3D weaving, cross-section variations in the weft and binder yarn affect the stiffness and damage initiation stress levels.

6.2 Geometric model generation

Unit-cell models of a 3D orthogonally woven non-cimp fabric composites are generated. The warp yarns are assumed (by means of simplification) to remain straight with constant cross-section while the weft yarns are assumed to remain straight but with cross-section that are allowed to deform upon binder insertion. The binder yarn is allowed to vary in centerline and cross-section shapes correspond to different binder yarn tensioning states. Fiber-breakage, asymmetrically-shaped binder yarn profile, crimping of the through-thickness segment of the binder yarn are not considered in the modelling. The simplified assumption of straight warp yarns with constant cross-sections is justi-

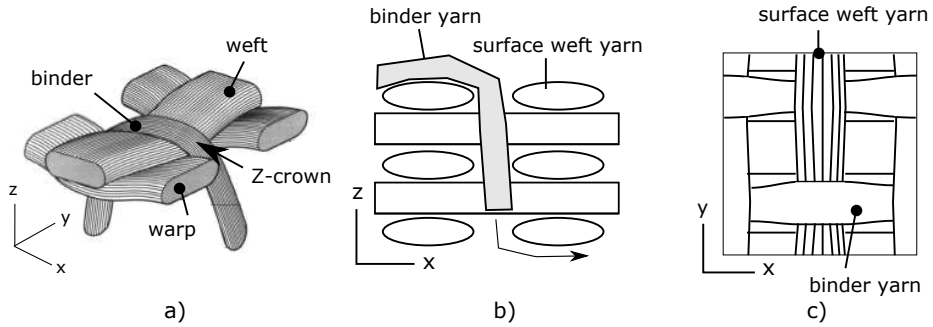

Fig. 6.1: 3D orthogonally woven non-crimp fabric composite: (a) a schematic 3D view (taken from [378]), (b) side view, (c) top view.

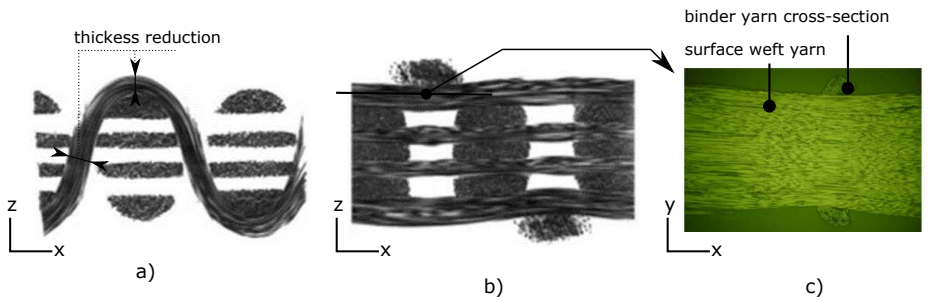

Fig. 6.2: Experimentally observed main geometrical features in 3D woven non-crimp fabric composites: (a) cross-section variations in binder yarn (image taken from [190]), (b) center-line deflection of surface weft yarns (image taken from [190]), (c) cross-section variations in surface weft yarn.

fied for small binder yarn tensioning and low transverse compaction levels, while larger binder yarn tensioning and compaction levels may require additional implementation to account for deformable warp yarns (see future work).

6.2.1 Initial model

Each yarn is initially represented by a single line and constant cross-section (see Fig. 6.3). The lines representing the warp and weft yarns are straight, while the line representing a binder yarn is S-shaped, mimicking a loose state configuration of the binder yarn around the warp and weft yarns. Elliptical, power ellipse and rectangular cross-sections are considered for the binder yarn, the inner weft and warp yarns, and the surface weft yarns, respectively (as indicated in Fig. 6.3). The rectangular cross-section shape of the surface weft yarns will subsequently be shaped during the generation process. The lines are further discretised in line segments with a length e_{line} of $100\mu m$ (that has shown a good compromise between geometrical accuracy and computational cost). The unit-cell dimensions itself (L,B,H in Fig. 6.3) depend on the dimensions of the warp, weft and binder yarn, the number of fiber-reinforcement layers and the amount

of transverse compaction during the manufacturing process.

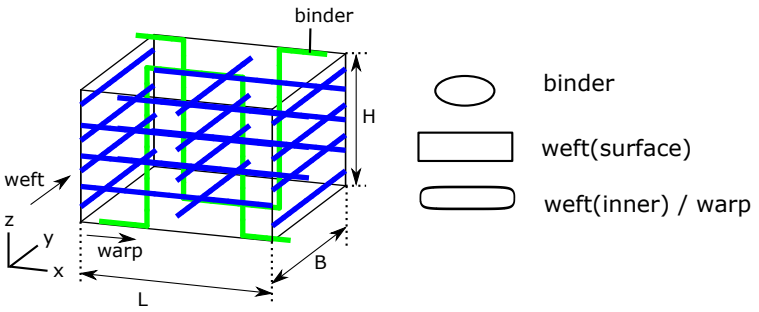

Fig. 6.3: Initial model with a fiber-bundle represented by a single line and constant cross-section.

6.2.2 Boundary-line and inner-line configuration for fiber-bundles

A boundary-line and an inner-line configuration are used for the weft and binder yarns, respectively, to account for their cross-section variations.

1. In a boundary-line configuration, the lines are positioned near the boundaries of the fiber-bundles (see Fig. 6.4a). The cross-sections of an initial single-line configuration are discretised using circles. The circles can be positioned uniformly along the cross-section boundary or can be positioned dependent on the local curvature of the cross-section boundary. A radius is assigned to the circles to facilitate contact treatment. However it can be chosen to vanish, as the boundary-lines do not represent anything physically and contact treatment, between the boundary-lines and the binder, can still be resolved by the binder yarn radius itself. The number of circles defines the geometrical accuracy of the cross-section shape variations in a post-processing at the expense of a higher computational cost.

2. In an inner-line configuration, lines are positioned at the interior of a fiber-bundles (as introduced in the work [377]). The cross-sections of the initial single-line configurations are discretised in circles positioned inside the cross-section. The circles can be defined as the nodes of a 2D mesh generated on the cross-section. The radius of circles is related to the number of circles and the initial fiber volume fraction in the binder yarn. The number of circles (represented by parameter c) is assessed by means of a convergence study on the cross-section variations of a tensioned binder yarn (see section 6.3.3).

A boundary-line configuration is favored to account accurately for local cross-section shape distortions at a reduced computation cost, but the centerline of the fiber-bundles should remain straight. An inner-line configuration can then be used to account for cross-section variations in fibers-bundles with centerlines that does not need to remain straight, but at the expense of a reduced control over the final cross-section. Note that a special attention needs to be given for a boundary-line configuration to not exceed locally the

maximum fiber volume fraction, while this conditions is automatically satisfied for an inner-line configuration.

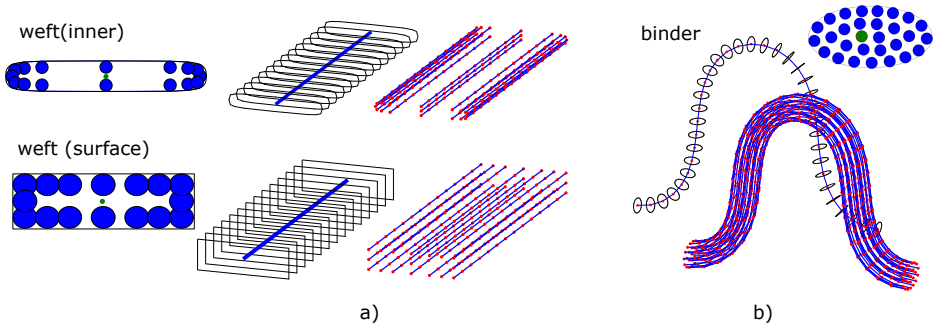

Fig. 6.4: Different line configurations for a fiber-bundle: (a) a boundary-line configuration for the weft yarns, (b) an inner-line configuration for the binder yarn.

6.2.3 Geometrical tools

The geometrical operations are applied on the discretised lines in a step-wise manner, with a straightening operation as the only operation adopted in the presented generation process. Each step intends to introduce a geometrical feature in the model or to transform the single-line configuration of the weft or binder yarns into a multi-line configuration (see Table 6.2). The contact parameter q, which regulates the relative movement between two lines upon contact, can be used to constrain certain types of lines during a generation step (see section 6.2.3). Boundary conditions can be enforced on the bottom and top of the surface weft yarns to keep them straight (as explained in chapter 4). The generation stages are illustrated in Fig. 6.5 and described in the sequel, followed by a short description of the adopted geometrical operations.

Step 1, the weft yarns are transformed in a boundary-line configuration.

Step 2, the binder lines (representing a single line configuration of the binders at this stage) are first made conform with the shape of the surface weft yarns by an applied straightening operation, in order to have a binder yarn shape independent of its initial position (the weft lines are constrained during this operation).

Step 3, the binder lines are then further subjected the same straightening operation, but whereby the weft lines are unconstrained this time. The center-line of the binder yarn, and simultaneously the cross-sections of the surface weft yarns underneath the binder yarn, can hereby be shaped to account for different binder yarn tensioning levels.

Step 4, the boundary-lines of the weft yarns are straightened to smooth their locally distorted shape near the binder yarn (the binder lines are hereby constrained during this operation).

Step 5, the binder yarn is transformed into a multi-line configuration to account for its cross-section variations in subsequent steps.

Step 6, the binder-lines are tensioned by the straightening operations to generate cross-section variations of the binder yarn which can correspond to different binder-yarn tensioning (the weft lines are hereby constrained).

Step 7, the bottom and the top of the unit-cell box, which surrounded initially only the warp and weft yarns, can be adjusted to generate models wherein the binder yarn is fully embedded in the matrix.

Step 8, the local fiber volume fraction and fiber direction in each fiber-bundle are obtained in a post-processing step.

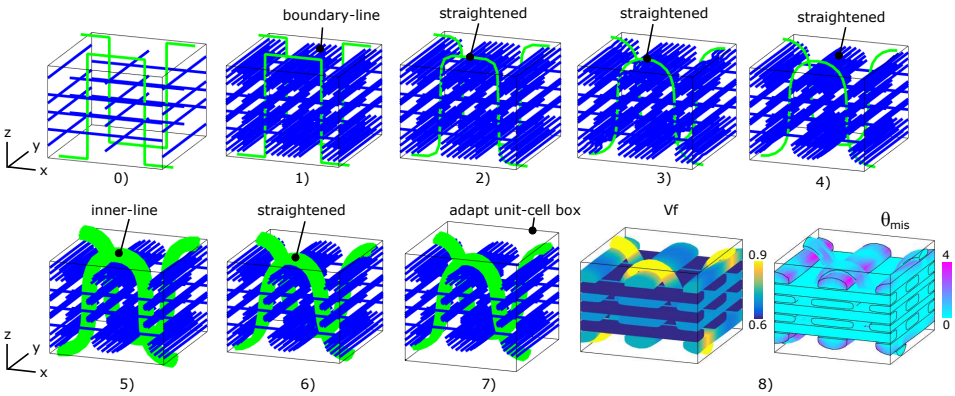

Fig. 6.5: Step-wise generation process: (0) initial model, (1) transformation weft into boundary-line configuration, (2) binder straightening, (3) binder straightening, (4) weft straightening, (5) transformation binder into multi-line configuration, (6) binder straightening, (7) adjusting bottom and top surface of unit-cell box, (8) calculating the fiber volume fraction V_f and fiber misalignment θ_{mis} in post-processing step with θ_{mis} corrected from the local normal orientation for each fiber-bundle.

Straightening operation

The straightening operation repositions the nodes of a line according to [357]:

$$\vec{x}_i = (1/2).(\vec{x}_{i-1} + \vec{x}_{i+1}) \tag{6.1}$$

To further account for the potential effect of neighbouring unit-cells on the shape of the lines of the considered unit-cell, the lines of the unit-cell are extended first, before straightening, at their sides by their replicates (actually generating the neighbouring unit-cell models in this step), where, after straightening, the extended parts are removed (Fig. 6.6). The shape of the lines is hereby controlled by the number of applied straightening operations (represented by parameter s) during the generation step .

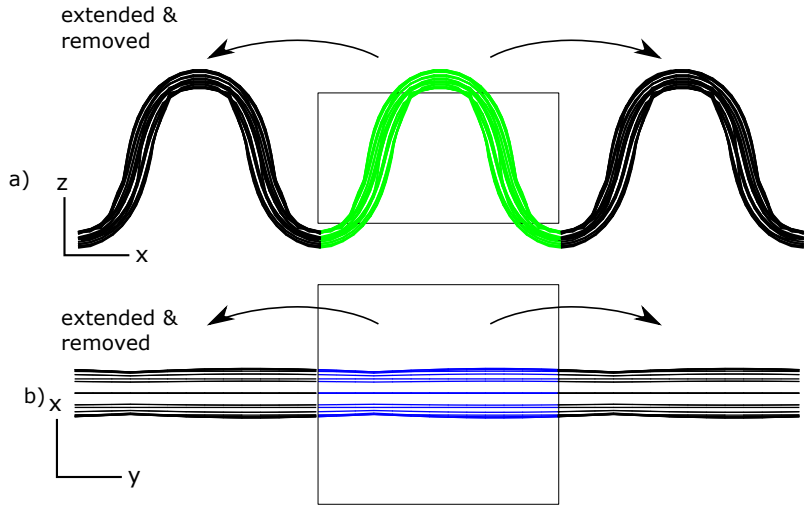

Fig. 6.6: Extending the lines prior to straightening for: (a) binder yarn and (b) weft yarns.

Contact treatment

The contact treatment in this chapter is similar to the contact treatment presented in chapter 5. A node P of a line i (see Fig. 6.7) which interpenetrates a line j is to be moved along its normal $\vec{D}_P$ on the line j to suppress the interpenetration [357,377]. The movement $\vec{x}_P$ of the node P can further be regulated by a parameter q :

$$\vec{x}_P = q.d_{int}.\vec{D}_P \tag{6.2}$$

where d_{int} is the interpenetration distance. The parameter q is set dependent on the type of lines interacting with each other (see Table 6.1). A 0-value is considered for interacting boundary-lines of the weft yarns. A 0.50-value is considered for interacting binder-lines. The parameter q_{bw} controls the interaction between a weft-line and a binder-line, which can be set to 0 or 1 to constrain the position of either the weft lines or the binder lines upon their interaction, respectively.

	binder	weft
binder	0.50	q_{bw}
weft	(1-q_{bw})	0

Table 6.1: Different contact parameter q dependent on the type of interacting lines.

6.2.4 Fiber volume fraction and fiber direction

A constant fiber volume fraction and linear fiber direction distributions are modelled on the cross-section of the fiber-bundles. The cross-sections are obtained by intersecting the

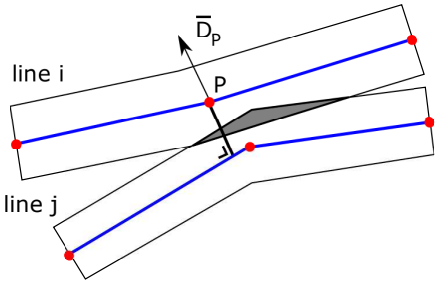

Fig. 6.7: Contact treatment.

multi-line configuration perpendicular to a local tangent to the centerline, whereby the centerline of the boundary-line configuration is a straight line positioned in the center of the initial cross-section and the centerline of the inner-line configurations is the line connecting the center point in the initial inner-line configuration. An example of generated cross-section for a binder yarn and a surface weft yarns are illustrated in Fig.6.8.

The uniform fiber volume fraction $V_f(s)$ in each cross-section is obtained by:

$$V_{f,deform}(s) = \frac{A_{init}}{A_{deform}(s)}.V_{f,init} \tag{6.3}$$

where A_{deform} is the deformed cross-section area and $V_{f,init}$ is the initial fiber volume fraction in the yarn. A_{init} represents the initial cross-section area, except for the surface weft yarns which have an enlarged cross-section due to their rectangular shape. For these yarns, the initial cross-section area of the inner weft yarns is considered. An example of obtained fiber volume fraction distribution for the binder and surface weft yarns is illustrated in Fig. 6.8b.

The linear fiber direction in each cross-section can be obtained from a linear interpolation between the local tangent of the lines which are positioned near the boundary of the cross-sections. The fiber misalignment θ_{mis}, as often used to visualize the local fiber direction inside yarns, is defined in each cross-section as the angle between the local fiber direction and the local tangent of the centerline of the yarn. An example of the fiber misalignment distribution obtained for the binder and surface weft yarns is illustrated in Fig. 6.8c.

6.2.5 Interpenetration suppression and gap generation

Interpenetrations can take place between the binder and weft yarns. These interpenetrations are first partly avoided by increasing the initial dimensions of the binder yarn prior to geometrical model generation and removing the offset after the generation process, as such that during the generation, lines upon contact with the binder yarn are moved aside more than necessary. Residual interpenetration between the binder and weft yarns are suppressed by moving points of a triangulated binder yarn surface that interpenterates

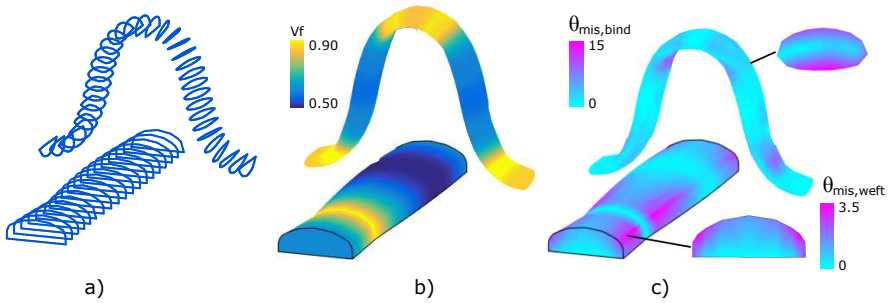

Fig. 6.8: Surface weft and binder yarn after post-processing: (a) generated cross-sections, (b) fiber volume fraction distribution (V_f), (c) fiber misalignment distribution (θ_{mis}).

the weft yarns along a local normal on the binder yarn surface external (see Fig. 6.9), while a gap can be inserted simultaneously. The fiber volume fraction in each cross-section of the binder yarn is afterwards systematically adapted to account for the (small) cross-section area changes taking place during this post-processing treatment.

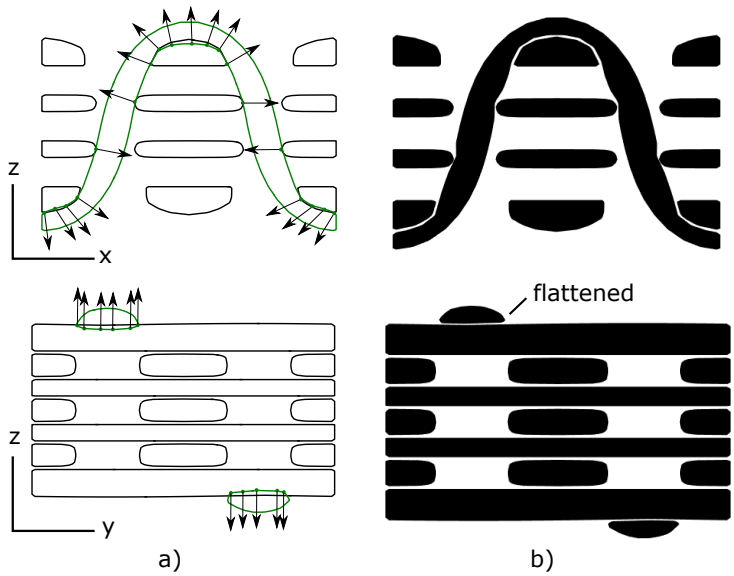

Fig. 6.9: Interpenetration suppression and gap insertion methodology: (a) before post-processsing, (b) after post-processing.

6.3 Generated geometrical features

First, the shape of introduced geometrical features in the surface weft and binder yarns for different values of the geometrical operation parameters is illustrated. The geometri-

cal models are hereby generated using the generation strategy and parameters presented in Table 6.2 and Table 6.3, respectively. The cross-section shapes and dimensions of the fiber-bundles are taken from the experimental geometrical data presented in [190]. The illustration can then be used to generate the shape of geometrical features conform to experimental observations. Second, models for different binder content are generated and illustrated to showcase the generality of the approach.

step	operations	id line	q_{bw}	parameter	geometrical feature
1	boundary-line configuration	weft	-	-	-
2	straightening	binder	0	-	-
3	straightening	binder	1	s_1	centerline of binder yarn
4	straightening	weft	1	s_2	cross-sections of weft yarn
5	inner-line configuration	binder	0	c	-
6	straightening	binder	0	s_3	cross-sections of binder yarn
7	adjusting box	-	-	(no-yes)	matrix

Table 6.2: A description of the step-wise generation process in terms of geometrical operations, corresponding parameters, the types of lines on which the geometrical operation are applied in each step, the contact parameter in each step and the geometrical features for which experimental observations can be used to set the corresponding parameters (s_1, s_2, s_3 represent the straightening parameter s in step 3,4 and 6, respectively).

initial model	yarn	shape	a(μm)	b(μm)	n	V_f^{init}	$A_{init}(\mu m^2)$
	weft surface	rectangle	525	130	-	0.700	156.50
	weft inner	super ellipse	525	80	5	0.700	156.50
	warp	super ellipse	430	110	5	0.700	176.25
	binder	ellipse	280	150	-	0.500	136.00
generation	$s_1 = 7$,	$s_2 = 50$,	$c = 15$,	$s_3 = 5$,	adjust box = no		

Table 6.3: Initial model and generation parameters for the 3D woven model.

6.3.1 Centerline of the binder yarn and corresponding cross-section of the surface weft yarn underneath the binder yarn

The centerline of the binder yarn can be shaped in generation step 3 by the parameters s_1 and q_{bw}, while the cross-section of the surface weft yarns are shaped simultaneously (due to the contact treatment). Shapes for different values of s_1 and q_{bw} are illustrated in Fig. 6.10a and Fig. 6.10b respectively. A wide range of possible positions of the centerline of the binder yarn can be generated while the shape of cross-sections of the surface tends towards lenticular shapes that is often used in analytical modelling approaches [190].

6.3.2 Cross-section variations in the surface weft yarns

The cross-sections variations in the surface weft yarns are controlled in generation step 4 by the parameter s_2 (which is the number of straightening operations in step 4). The shape of the surface weft yarns for different values of s_3 are illustrated in Fig. 6.11 by

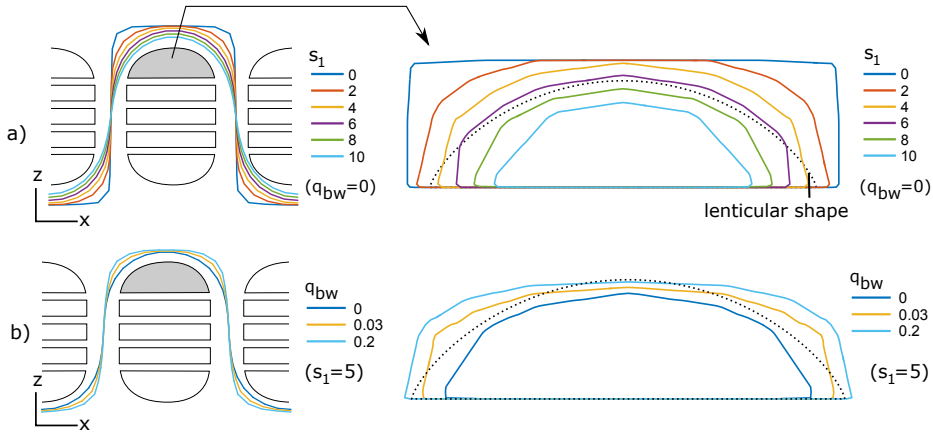

Fig. 6.10: Different shapes of the binder yarn centerline and surface weft yarn cross-section underneath the binder yarn for varying: (a) straightening parameter s_1 and (b) contact parameter q_{wb}.

means of the fiber volume fraction and fiber misalignment distributions in the surface weft yarns. The parameter s_2 can then be set by comparing for example the maximum in-plane fiber misalignment in the model with the maximum in-plane fiber mislaignment in experimental observations which is dependent on the binder content and tensioning. A fully straight configuration of the surface weft yarns can be obtained in the limit ($s_2 = +100$).

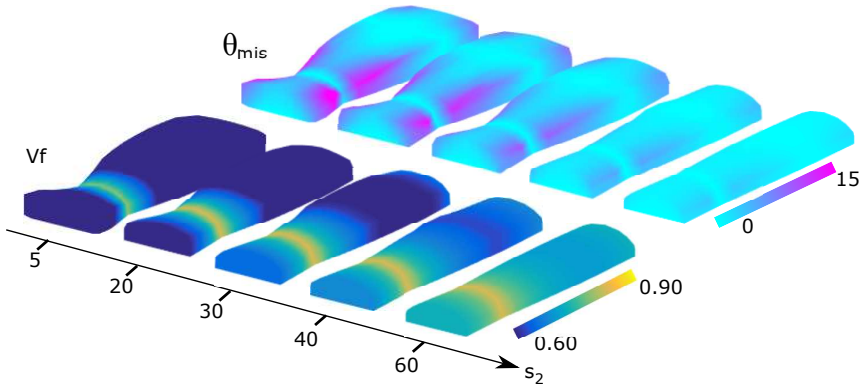

Fig. 6.11: Cross-section variations in the surface weft yarn for varying straightening parameter s_2, illustrated by the fiber volume fraction V_f and fiber misalignment θ_{mis} distribution.

6.3.3 Cross-section variations in the binder yarn

Convergence study on the number of lines

The number of lines (c) present in the multi-line configuration of the binder yarn is set (in generation step 5) to have converged tensioned binder yarn geometries. The effect of the number of lines on the cross-section shapes and on the fiber volume fraction distributions in the binder yarn is illustrated in Fig. 6.12. A convergence in cross-sections shapes and corresponding fiber volume fraction distributions of the binder yarn is taking place and this for a number of lines equal to 15 which will further be used in the generation process (see Table 6.2).

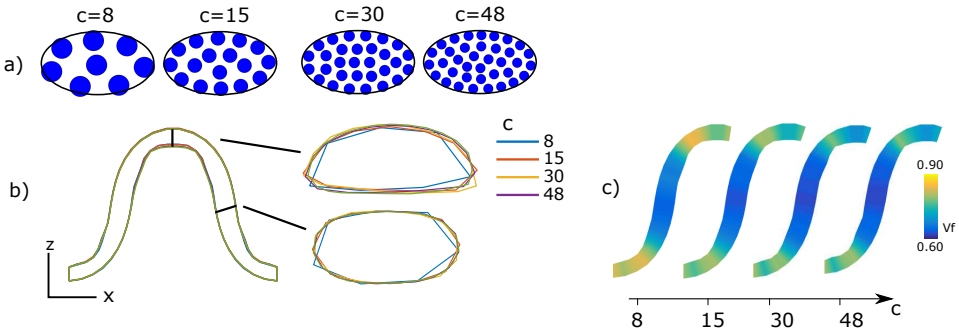

Fig. 6.12: Convergence study on the number of lines c for a tensioned binder yarn: (a) different cross-section discretisations, (b) cross-section shape variations, (c) fiber volume fraction V_f distribution.

Mimicking different binder yarn tensioning

Cross-section shape variations in the binder yarn for different binder yarn tensioning states can be regulated in generation step 6 by means of parameter s_3 (which is the number of straightening operations in step 6). The cross-section shapes and corresponding fiber volume fraction distributions for different values of s_3 are illustrated in Fig. 6.13. The cross-section shapes in the top segment are flattened first and then widened for increasing values of s_3, while the cross-section shapes in the middle of the through-the-thickness segments of the binder yarn are barely changed. A binder yarn configuration which is conform with a physical observation can then be generated by setting first the initial cross-sections of the binder yarn to a cross-section located in the middle of the through-the-thickness segment of the physical binder yarn, whereafter parameter s_3 should be set by comparing for example the thickness of the cross-section at top segment. Typical cross-section thickness reductions in the top segment of the binder yarn lie between 0.30 and 0.70 [33, 100, 101, 196, 376].

6.3.4 Geometerical models for different binder content

Models for different binder content are generated and illustrated in Fig. 6.14. The binder content is varied from 0.5% to 4% by changing the unit-cell dimensions (which

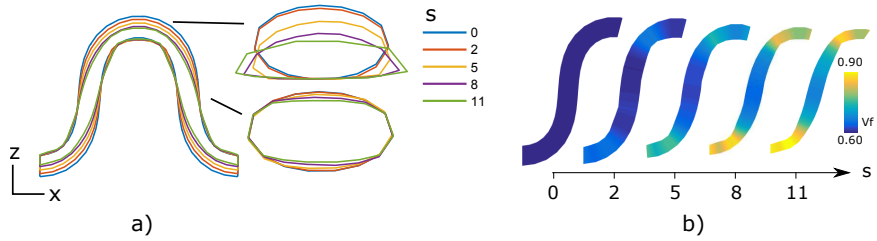

Fig. 6.13: Shapes of a tensioned binder yarn for varying parameter s_3: (a) cross-section shapes of the binder yarn, (b) fiber volume fraction V_f distribution in the binder yarn.

corresponds to changing the binder yarn spacing during manufacturing) while the binder diameter remained constant. It can be seen that the approach accounts automatically for different shapes of the surface weft yarns corresponding to the different binder content.

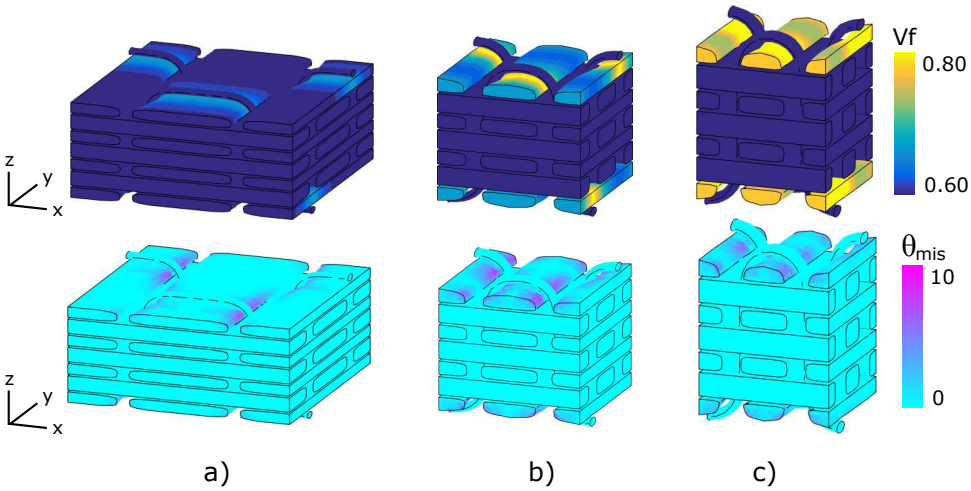

Fig. 6.14: 3D woven models for different binder content (represented by their fiber volume fraction V_f and fiber misalignment θ_{mis} distribution): (a) binder content of 0.50%, (b) binder content of 2%, (c) binder content of 4%.

6.4 Mechanical simulations

The geometrical models are transformed into finite element models using the meshing software GMSH. The mesh size parameters m_1 and m_2, which are used in the mesh model described in chapter 3, are $40\mu m$ and $100\mu m$ respectivelly. Periodic boundary conditions are applied on the in-plane unit-cell borders while the bottom and top of the unit-cell are left free. Carbon fibers and epoxy matrix are considered as constituent materials with mechanicals properties presented in Table 4 of [377]. The mechanical properties of the fiber-reinforced region are obtained, in function of the local fiber volume

fraction, by means of the Chamis-formulae [186] (for stiffness) and emperical formulae presented in [187,188] (for strength). A global strain of 0.50% is applied on the unit-cell models in the warp-, weft- and bias(45°)-direction, a straining level that has been shown experimentally to cause early damage initiation in 3D woven composites [24, 363].

The stiffness of the unit-cell model is then computed and normalised by the stiffness of an equivalent non 3D-woven composites (described in section 6.4.1). The local stress-levels are evaluated based on their risk to locally initiate damage, using the local failure indicators f_{22}, f_{12}, f_m and f_{int} as defined in chapter 5. Transverse and shear damage in the fiber-bundles (via f_{22} and f_{12} respectively), interface debonding between the fiber-bundles and the matrix (via f_{int}), and matrix damage (via f_m) are considered in the analysis, as being the ones which can potentially arise in 3D woven composites (stated by the experimental observations presented in [24, 363]). The local failure indicators (f_{ij}, f_{int}, f_m) are calculated using similar criteria as presented in [377]. A 97-percentile of the local failure indicators f_{ij} is used to compare the failure distribution in a region between different models.

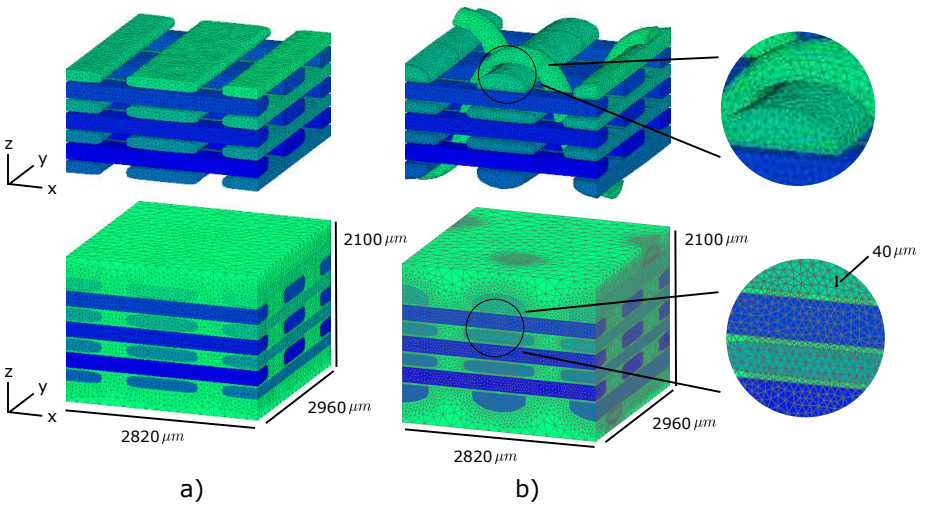

Fig. 6.15: Generated mesh models for: (a) the non 3D woven model, (b) the 3D woven model.

6.4.1 Models

The effect of 3D weaving, cross-section variations in the surface weft yarns and cross-section variations in the binder yarn on the stiffness and damage initiation is evaluated by the following three cases:

Case 1, the effect of 3D weaving is investigated by comparing the results of a 3D woven model with an equivalent non 3D-woven composite model. The 3D woven model is obtained using the generation procedures and parameters presented in Table 6.2 and

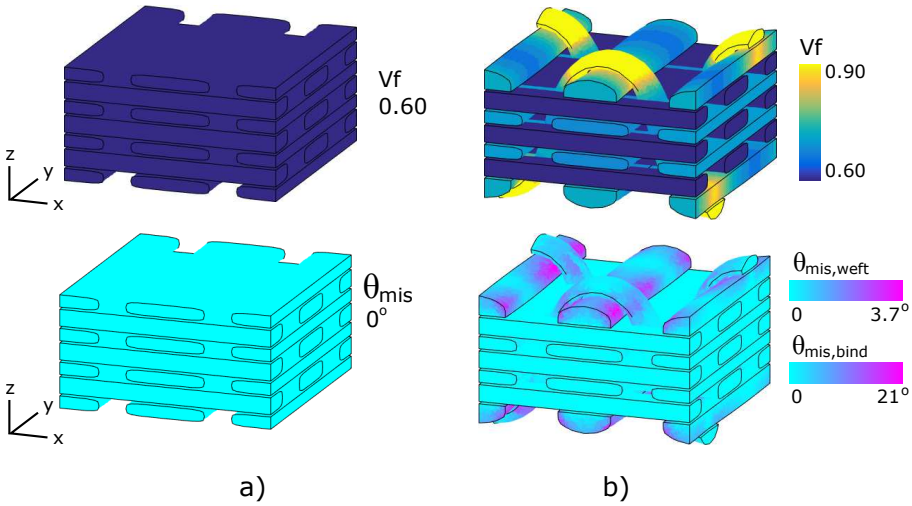

Fig. 6.16: An illustration of the fiber volume fraction V_f and the fiber misalignment θ_{mis} distribution present in: (a) the non 3D woven model and (b) the 3D woven model.

Table 6.3 respectively. The equivalent non 3D woven model is considered in this work as the initial configuration of the 3D woven model but without the binder yarn and with the cross-sections of the surface weft yarns been taken equal to the cross-sections of the inner weft yarns. The mesh models, and the fiber volume fraction and fiber direction distribution, for both configurations are illustrated in Fig. 6.15 in Fig. 6.16 respectively.

Case 2, the effect of cross-section variations in the surface weft yarn is investigated by generating 3D woven models whereby the parameter s_2 in generation step 4 is varied (see Table 6.2). Surface weft yarn geometries for the different parameters s_2 are similar to the illustrations presented in Fig. 6.11.

Case 3, the effect of cross-section variations in the binder yarn is investigated by generating 3D woven models in which the parameter s_3 in generation step 6 (see Table 6.2) is varied. Binder yarn geometries for the different values of the parameter s_3 are similar to the illustrations presented in Fig. 6.13.

6.4.2 Results

The effect of 3D weaving (case 1)

The normalized stiffness components of the 3D woven model are presented in Table 6.4. The stiffness in the warp direction is slightly increased (2%) while the stiffness in the weft- and bias-direction are in larger proportion increased (12% and 14% respectively). The stiffness in the bias-direction is approximately 10 times lower than the stiffness in the warp and weft direction. The stiffness components fall in the range of experimental observations which has shown to be between 0.80 and 1.20 (thus remained ambiguous

whether 3D weaving increases or decrease the stiffness).

The failure indicator distributions in the 3D woven model for warp-, weft- and bias-loading are presented in Fig. 6.17 and summarized by their 97-percentile in Table 6.5. The 97-percentile of the local failure indicators in the fiber-reinforced regions and matrix are increased, which indicate early damage initiation. Transverse damage in the surface weft yarn, transverse damage in the binder yarn, and shear damage in the surface weft and binder yarn are the main damage initiation mechanisms taking place for warp-, weft- and bias-loading respectively. The warp- and bias- direction experience more damage with respect the weft-direction, making them the most critical directions to be looked after in the design of the 3D woven composites. The potential local failure initiated regions (see Fig. 6.18) correlate hereby with the most distorted fiber-reinforced regions (see Fig. 6.16) which are taking place near the binder locations.

The damage initiation characteristics from the simulations results substantiate further be compared with experimental observation. Early damage initiation and stress concentrations near binder locations, as observed in the simulation results, have also been observed experimentally in the works [24, 196, 363]. For warp-loading, the very small damage appeared first near the middle section of the Z-crown crossover with the adjacent surface weft yarns, which is then followed by transverse damage in the weft yarns under increasing load [363]. For weft-loading, the damage is initiated in the form of transverse damage in the warp and binder yarns [363]. For the bias direction, the damage starts at the Z-crowns (defined in Fig. 6.1) [363]. Similar trends can be observed in the simulation results presented in Fig. 6.18.

E_{norm}^{warp}	1.02
E_{norm}^{weft}	1.12
E_{norm}^{shear}	1.14

Table 6.4: The normalised stiffness components of the 3D woven model.

		binder			inner weft		surface weft			matrix
		$f_{22}^{97\%}$	$f_{12}^{97\%}$	$f_{int}^{97\%}$	$f_{22}^{97\%}$	$f_{12}^{97\%}$	$f_{22}^{97\%}$	$f_{12}^{97\%}$	$f_{int}^{97\%}$	$f_{m}^{97\%}$
warp-load	equivalent	-	-	-	0.52	0.01	0.51	0.01	0.30	0.36
	3D woven	0.16	0.22	0.41	0.71	0.05	0.80	0.11	0.34	0.43
weft-load	equivalent	-	-	-	0.13	0.01	0.12	0.01	0.08	0.35
	3D woven	1.82	0.18	0.45	0.16	0.02	0.41	0.21	0.17	0.39
shear-load	equivalent	-	-	-	0.04	0.75	0.03	0.69	0.26	0.33
	3D woven	0.25	1.77	0.45	0.08	0.97	0.10	1.55	0.29	0.41

Table 6.5: The 97-percentile of the local failure indicators in the binder, the inner and surface weft yarns, and the matrix.

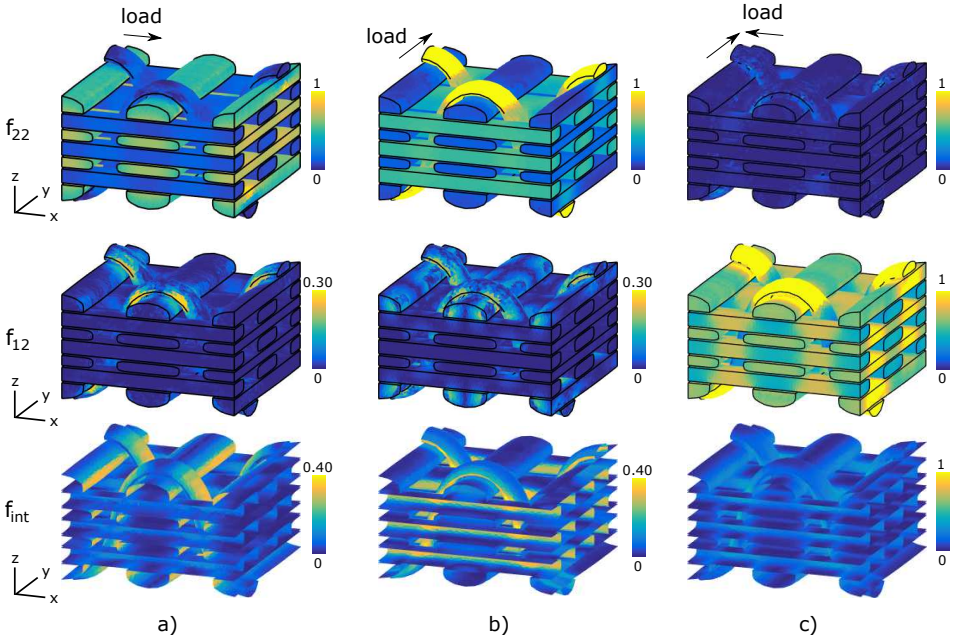

Fig. 6.17: An illustration of the transverse and shear damage, and interface debonding, failure indicator distribution in the 3D woven model for different loading directions: (a) warp-direction, (b) weft-direction and (c) shear-direction.

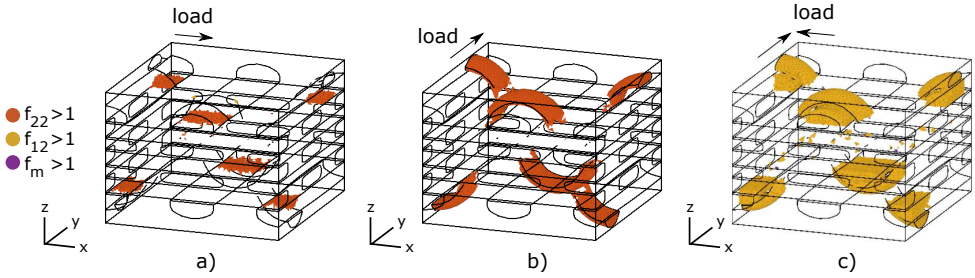

Fig. 6.18: An illustration of the potential local failure initiated regions in the 3D woven model, with an indication of the main local damage initation mechanisms, for different loading directions: (a) warp-direction, (b) weft-direction and (c) shear-direction.

The effect of cross-section variations in the surface weft yarns (case 2)

The effect of cross-sections variations in the surface weft yarns is investigated (Fig. 6.19a) on the stiffness of the 3D woven model and on transverse and shear failure indicators in the surface weft yarns for warp- and bias-loading (as being the most critical, see Table 6.5) respectively. The stiffness components of the 3D woven models are normalised by the stiffness of the 3D woven model in which the surface weft yarns are fully straight (setup corresponding to $s_2 = 100$). The considered failure indicator are

presented in the fiber-bundles by their average. An increased average would then indicate an increased probability of early damage initation in regions with a failure indicator lower than the maximum failure indicator as well as a faster propagation of cracks after their initiation at the most critical location [342]. Cross-section variations in a fiber-bundle that can be considered as realistic are the ones with a value of s_2 being between 20 and 100, as these values corresponds to experimentally observed maximum in-plane fiber misalignment that lie in between 0° and 10° [80].

It can be seen (in Fig. 6.19a) that a small s_2-value (corresponding to a large maximum in-plane fiber misalignment) can result in lower stiffness components and in a lower average of the transverse and shear damage indicators than a large s_2-value (corresponding to a small maximum in-plane fiber misalignment). 3D woven models which adopt straight weft yarn (as adopted in [57,379–381]) may then overestimate the risk for damage initiation.

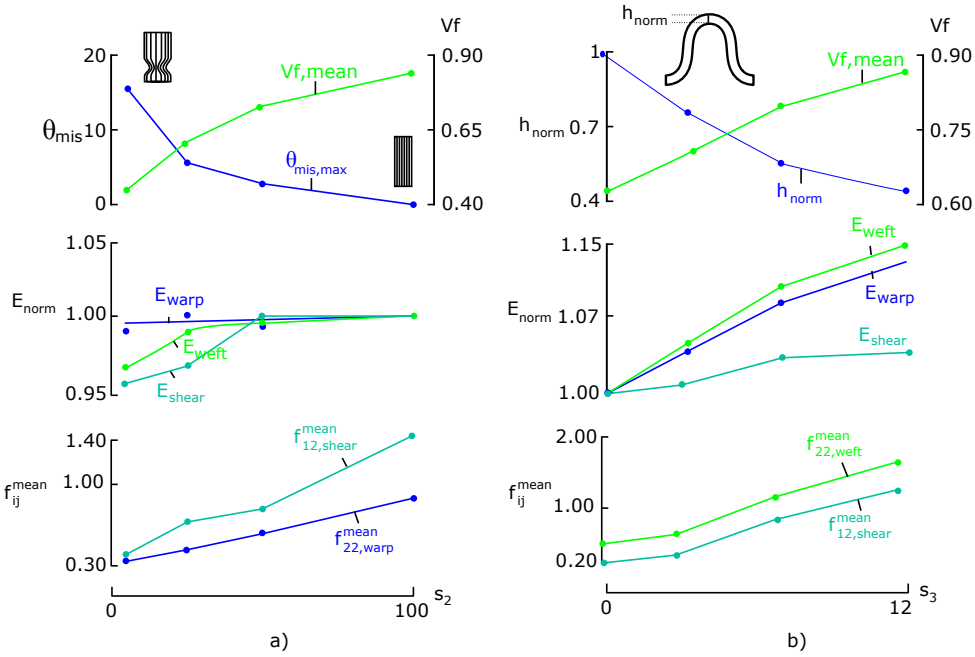

Fig. 6.19: Graphs showing the effect of cross-section variations in surface weft yarn and binder yarn: (a) the maximum in-plane fiber misalignment and the mean of the fiber volume fraction in the surface weft yarns, the stiffness components, and the mean of transverse damage failure indicators (for warp-loading) and shear damage failure indicator (for shear-loading) in the surface weft yarns are presented for varying parameters s_2 - (b) the normalised thickness of the cross-section in the top segment of the binder yarn and the mean of the fiber volume fraction in the binder yarn, the stiffness components, and the mean of the transverse damage failure indicators (for weft-loading) and the shear damage failure indicators (for warp-loading) are presented for varying parameters s_3.

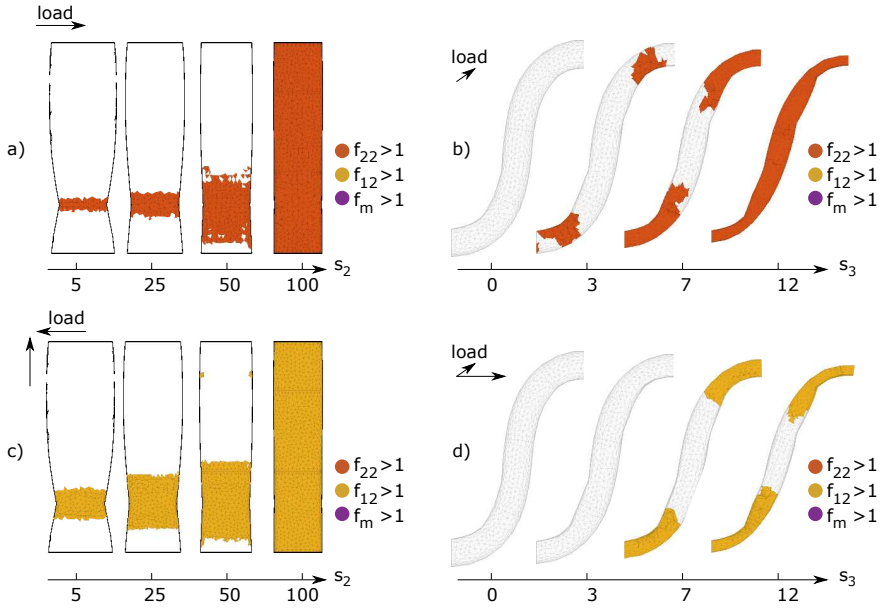

Fig. 6.20: The corresponding potential local failure initiated regions in the surface or binder yarn for the different cross-section variations configurations analysed in section 6.3.2 and section 6.3.3: (a) transverse damage in surface weft yarn for warp-loading, (b) transverse damage in binder yarn for weft-loading, (c) shear damage in surface weft yarn for shear-loading, (d) shear damage in binder yarn for shear-loading

The effect cross-section variations in binder yarn (case 3)

The effect of cross-section variations in the binder yarn is investigated (Fig. 6.19b) on the stiffness of the 3D woven model, and on the transverse and shear damage indicators in the binder yarn for weft- and shear-loading respectively (as being the main critical damage indicators in the binder yarn, see Table 6.5). The thickness of the cross-section in the top segment of the binder yarn, normalised by the thickness of the initial cross-section of the binder yarn, and the average of the fiber volume fraction distribution in the binder yarns are presented as well. The stiffness components of the 3D woven models are further normalised by the stiffness of the 3D woven model with constant cross-sections for the binder yarn ($s_3 = 0$) and the mean for the considered failure indicators is considered. Realistic values of s_3 would lie inbetween 4 and 12 (dependent on binder content and tensioning), which corresponds to experimentally observed values of the normalised thickness which typically lie inbetween $0.30 - 0.70$ (as can be deduced from experimental figures presented in [33, 100, 101, 196, 376]).

It can be seen (in Fig. 6.19b) that a small s_3 value (corresponding to small binder yarn cross-section variations), results in a lower stiffness and a lower mean of the local failure indicators than a large s_3 value (corresponding to large binder yarn cross-section variations). 3D woven models with a constant assumed cross-section for the binder yarn and

with a matrix which fully embeds the binder yarn (as adopted in [57, 379–381] would then underestimate the stiffness and the mean of the local failure indicators with a level of underestimation dependent on the binder content. The increase in stiffness of 3D woven model embedding a binder yarn with large cross-section variations is related to the fact that the matrix is defined around the binder yarn, which can easily be resolved by considering a matrix that only surrounds in the in-plane fiber-reinforced regions (as done in [377]).

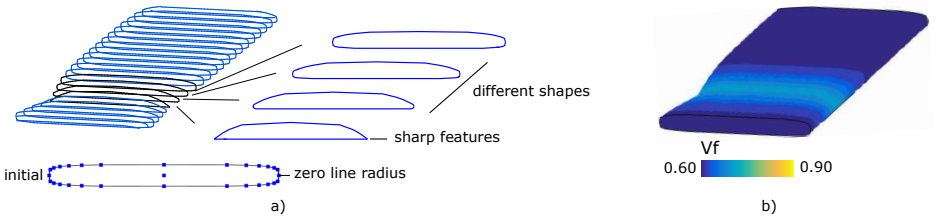

Fig. 6.21: A reflection on some features of the geometrical model generation approach: (a) smooth cross-section shape variations caused by binder insertion in the surface weft can be generated by adopting a zero line-radius in the boundary-lines configuration, (b) the constant assumed fiber volume fraction V_f in cross-section may not correctly represent the V_f-distribution in a cross-section of the surface weft yarns for small binder content.

6.5 Discussion

6.5.1 Comparing geometrical modelling approaches

The centerline and cross-sections of fiber-bundles in 3D woven models can be shaped using analytical, digital element and geometrical-based modelling approaches.

1. Analytical modelling approaches shape the fiber-bundles in 3D woven composites manually by means of functional representations. Different functional representations need to be adopted each time the shape of geometrical features changes, as for example due to binder content and binder tensioning, making analytical models not general to include the main geometrical for a wide range of binder parameters, but a full control over the shape of geometrical features is present.

2. Digital element approaches shape the fiber-bundles in 3D woven composites by means of an inner-line configuration for each fiber-bundle which are positioned initially in a loose-state configuration, using a binder yarn tensioning and transverse compaction during finite element simulations. The shape of fiber-bundles which are conform with each other and correlated with a binder yarn tensioning and transverse compaction loading can hereby be automatically generated, but the approach is computationally expensive.

3. The geometrical-based approach as presented in this work shape the fiber-bundles by means of a boundary-line and inner-line configuration (for weft and binder

yarn respectively), and geometrical operations. The boundary-line configuration allows hereby to accurately model small changes in the cross-sections shapes in fiber-bundle with straight centerlines, as illustrated in Fig. 6.8a). The inner-line configuration allows to automatically account for cross-section variations in fiber-bundle due to different stages of binder yarn tensioning (similar to the digital element approach). The geometrical-based framework does not require expensive finite element simulations, but the predictive behaviour is limited as no mechanisms are induced during generation. The combination of an inner-line configuration and a geometrical-based framework to shape cross-section variations in fiber-bundles for transverse compression loading should still be investigated.

The modelling approach adopted in the generation of 3D woven models can then depend on a desired generality, simplicity, computational time, control over the obtained shape of the geometrical features, etc.

6.5.2 The role of local fiber volume fraction

Local fiber volume fraction have already been shown in fiber-reinforced composites to act as stress concentration and damage initiation regions [133, 191, 342, 356, 377]. A similar trend can also be observed in this work, by comparing the contour plots of the regions of stress concentrations in the surface weft and binder yarns illustrated in Fig. 6.20 with the corresponding fiber volume fraction distributions presented in Fig. 6.11 and Fig. 6.13 for the surface weft and binder yarn respectively. The location of the stress concentration regions are observed to be correlated with the locations of increasesd fiber-volume fraction. The positive correlation further indicates the importance to include the local fiber volume fraction correctly in the models. Still, a uniform fiber volume fraction in each cross-section of the fiber-bundles is assumed in this work, but may be unrealistic in 3D woven models with a smaller binder content or tensioning (see Fig. 6.8b) whereby the distortions should only take place near the borders. A locally distorted zone in the surface weft yarns should then be adopted to account more properly for fiber volume fraction variations. Local fiber-reinforced distorted zone models similar to [356, 377] for Z-pinned and stitched laminates can therefore be adopted.

6.5.3 Comparison different software

Different software exist for the generation of 3D reinforced composites:

1. **In WiseTex** [382]: stitched models can be generated with orthorhomic-shapes resin-rich region, straight lamina and a stitching yarn which consists of straight and circular centerline segments and circular and elliptical cross-sections. 3D woven models can be generated with each fiber-bundle initially represented by a functional representation and a circular initial cross-section, and an energy based approach to compute the position of nodes controlling the shape of the centerline and cross-sections for different in-plane and out-of-plane loading conditions. A constant fiber volume fraction and fiber direction in the laminae of the stitched models are assumed while different fiber volume fraction distributions in the cross-section of the fiber-bundles can be chosen for 3D woven models. Meshing techniques are

further built in the software to transform the geometrical model into finite element models, whereby a mesh sweep approach is adopted for fiber-bundles and straight lamina and mesh superposition techniques are adopted for the stitched models (hereby resolving the interpenerations which have been present between the lamina and stitching yarn due to analytical model simplifications). Geometrical models corresponding to binder parameters (pattern, content, diameter, tensioning) can automatically be generated, but the models remain simplified.

2. **In TexGen** [130, 311]: functional representation are used to generate the geometrical model. Symmetrical and assymmetrical-shapes (as ellipse, power ellipse and lenticular) can be used to represent cross-sections, while cosine- and B-spline shapes can be used to represent the fiber-bundle centerline. [130]. Parametrised and triangulated surface representations can be obtained from the analytical expression of the centerlines and cross-sections. Interpenetrations between fiber-bundles can be suppressed by the point-movement-based approach applied on the triangulated surfaces. Mesh sweep and voxel-based meshing approaches are further build-in functionalities to transform the generated models into finite element models. Models of any reinforcement architecture complexity can theoretically be generated using such an analytical-based toolbox, but the geometrical features of these models are often simplified.

3. **In Wintibas model**: the fiber-bundles are represented by single discretised lines with constant elliptical cross-sections and using the geometrical straightening operation to shape the discretised lines towards a tensioned equilibrated configuration. The fiber-bundles are then transformed into level-set representation, and the level-set representations are modified by analytical expression, to suppress interpenetration and to insert a gap simultaneously.

4. **In our approach**: discretised lines are used to shape both lamina (with openings) and fiber-bundles by means of geometrical operations. Triangulated surfaces can be generated from the distorted line models and further automatically be transformed into tetrahedral based meshes. Local fiber-reinforced distorted zones can be accounted for in cross-section of both laminae and fiber-bundles. The approach allows to generate automatically different shapes of geometrical features in the unit-cell models (discretised lines are used for both lamina and fiber-bundle, and independent of the binder parameters), which may make the framework more general and simpler to use compared to current software. The framework can easily be used and further extended to generate unit-cell models for other fiber-reinforced composite types, with more realistic geometrical features and for other loading conditions (see Chapter 8). A comparison between the different framework boils down to similar conclusions as presented in section 2.2.7.

6.5.4 The robustness, performance, advantages, disadvantages of the framework

On the robustness:

1. The approach is able to generate in most cases finite element models from the initial unshaped line model by one push on the button. The finite element models are hereby automatically translated into an .inp file as input for Abaqus. The .inp file is loaded in Abaqus in which the mechanical simulations are performed. After the simulations, data is automatically extracted from the .out file fro, Abaqus and used in further post-processing in the Matlab environment.

2. The mesh generation in GMSH was observed to be the most crucial part. The implementation adopted in this work sometimes failed to automatically generate meshes of more complex geometrical models as the stitched laminate models. It was observed to be related (in the current implementation) to the discretisation of the triangulated surfaces, for which it sufficed to adjust the discretisation parameters of the contouring operations by trial and error.

3. The contouring operation fully automatically connects cross-sections of fiber-bundles and lamina with openings. However, sometimes it may happen, in the contouring of lamina with out-of-plane undulations, that the auxiliary points suppress tetrahedral elements which are not allowed to be removed. In such cases, it sufficed to adjust manually the discretisation parameters of the contouring operations.

On the performance: The generation time of the 3D reinforced unit-cell models and the performed mechanical simulations are in the order of several minutes. The short time, due to the use of the analytical fiber-reinforced distorted zone model compared to the multi-fiber model, allows for an efficient evaluation of different binder parameters via parametric studies.

Advantages of the approach:

1. It is general: shapes of geometrical features corresponding to different binder parameters can automatically be obtained, while analytical modelling approaches would need different models for each different shape.

2. It is fast: unit-cell models can be generated in order of several minutes, related to fact that only geometrical operations are used to shape the lines. Such a geometrical-based approach may be faster compared to the finite element method, as in the later a system of equations should be solved by increment-iterative procedures, but a quantitatively investigation should further be performed to test this statement.

3. It is simple: geometrical model generation approach can be implemented in any programming language and easily be extended using other initial models or geometrical operations to generate unit-cell models including for example voids or micro-vascular networks and their corresponding fiber-reinforced distorted zones.

4. It is automated and integrated with meshing and mechanical simulation frameworks: with one push on the button, initial unshaped lines can be transformed in finite element models for which an inp.file is created for input in Abaqus. With a second push on the button, the mechanical simulations are run and an output file is generated. With a third push on the button, relevant data is extracted from

the output file and automatically post-processed for stiffness computation and the generation of potential local failure initiated regions maps.

Disadvantages of the approach:

1. It is non-predictive: the shape of the features can automatically be obtained, but the size of the geometrical features (controlled by the geometrical operations parameters) should ideally still rely on experimental input data.

2. It has been used to generate unit-cell models for local geometrical distortions but not yet to generate unit-cell models including local effects of fabric compaction.

Capabilities: it is able to generate unit-cell models for in-plane and out-of-plane mechanical simulations.

6.6 Conclusion

An approach is presented to generate automatically mesoscopic unit-cell models of 3D orthogonal woven non-crimp fabric composites which include cross-section variations in the surface weft and the binder yarns. A boundary-line and inner-line configuration are considered for the weft and binder yarns respectively to account for the cross-section shapes variations. Geometrical operations are applied to shape the discretised lines. Shapes of the binder and surface weft yarn corresponding to different binder contents and tensioning can be automatically obtained.

The geometrical models are then transformed into FE mechanical models, based on which the effect of distortions on the stiffness and damage initiation levels is investigated. The following can be observed:

1. The stiffness in the warp direction is slightly increased (2%) while the stiffness in the weft- and bias-direction are larger increased (12% and 14% respectively).

2. Early damage initiation is observed with the stress concentration regions located near the binder locations.

3. Transverse cracking in the surface weft yarns, transverse cracking in the binder yarn, and shear cracking in the binder and surface weft yarn, have been initiated in 3D woven models subjected to a load applied in warp-, weft- and bias-direction respectively (global strain of 0.50).

4. A constant cross-section for the surface weft yarn would overestimate the extent of stress concentration region in the surface weft for warp and bias loading, while a constant cross-section for the binder yarn in a 3D woven model would underestimate the stiffness and overstimate the extent of potential local failure initiated regions in the binder yarn.

5. The local fiber volume fraction is a main driver of transverse and shear damage in the weft, warp and binder yarns.

The results emphasize the importance to account for cross-section variations in the weft and binder yarns as well as a proper modelling of the fiber volume fraction distribution in each cross-section.

In future works, geometrical models of 3D orthogonally woven composites including centerline deflections of the warp yarns (by considering an inner-line configurations for the warp yarns) and more elaborated fiber-reinforced distorted zones (see chapter 4 and 5), as well as geometrical models of other types of 3D woven composites, can be generated using the geometry-based framework. The geometry models for the different types of composites can then further be compared with the in-house 3D woven model generator (presented in [105]) which uses also geometry-based framework but in which the cross-sections of the fiber-bundles were assumed constant.

Chapter 7
Framework illustrations

This chapter presents two case studies with the intend to extend the use of the framework. In a first case study, a lamina is modelled by an inner-line configuration and the geometrical-based framework is used to model the effect of a pin-insertion on both the resin-rich region geometry and the distortions inside the fiber-reinforced regions simultaneously. In a second case study, unit-cells models of both pinned, stitched and 3D woven composites, and different binder content, are first generated. Then, the geometrical and mechanical characteristics of the models are compared and related to trends in binder type and content.

7.1 Fiber-reinforced distorted zone modelling

In a first stage of this research, an inner-line configuration of a lamina was adopted to model the distortions of the fiber-reinforced regions upon pin insertion. The distorted inner-line configuration was afterwards used to extract the local fiber volume fraction and fiber distribution in each lamina. Later on, a boundary-line configuration of a lamina was adopted and distance fields on generated cross-sections were used to model the fiber volume fraction and fiber direction distribution in the lamina (see chapter 4). The boundary-line configuration was introduced to drastically decrease the computational cost of model generation (which is favored in parametrical studies) and to have a parameterised fiber-reinforced distorted zone model for which its distorted zone width can be modified to match experimental observations (rather than being an outcome of the simulation process itself). Nevertheless, the inner-line configuration has attempt to model the fiber-reinforced distorted zones in the Z-pinned laminates in a novel way and can also be seen as an extension of the analytical model which can be used but at a larger generation cost. The presented inner-line configuration can also potentially be used as lamina representation in Z-pinned and stitched laminates to account for lamina interactions that can take place for larger pin inclination angles and stitching yarn tensioning. Therefore, the adopted inner-line configuration of a lamina and the results of the initially performed investigation, to whether the inner-line configuration and the geometrical-based framework is able to model satisfactory the fiber-reinforced distorted zone in a single pinned lamina, are presented in the sequel.

7.1.1 Initial model

The pin is represented by a single line and a constant circular cross-section. The line is positioned at the center of the lamina in the direction perpendicular to the lamina plane

and is not further discretised in line segments.

The inner-line configuration of the lamina is constructed as follows: First, lines are positioned on a cross-section (see Fig. 7.1a) near the border (border-lines), near potential opening location (opening-lines) and at the interior (inner-lines), respectively, (1) to account for smooth lamina surfaces in a post-processing, (2) to detect potential resin-rich regions and (3) to represent the fibrous nature of the lamina. The radius of the lines is determined from the number of lines and the initial fiber volume fraction in the lamina, with the effect of the number of lines that will be assessed by a convergence study on the generated distorted zone width (see section 7.1.4). A square, a hexagonal and a random inner-line distribution can be considered initially, but their effect on the obtained distortions will be assessed further in section 7.1.4. The random distribution of the lines can hereby be obtained using the level-set based micro-RVE generator presented in [357]. Potential initial interpenetrations between the lines in the cross-section are further suppressed by the contact treatment, in which the border and opening lines are constrained and the movement of inner-lines accounts for the full interpenetration suppression. Afterwards, the lines are extended in the main fiber direction to obtain the inner-line configuration (see Fig. 7.1b).

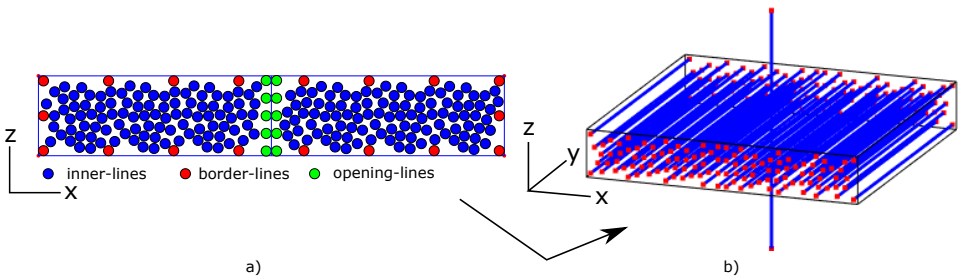

Fig. 7.1: An inner-line configuration of a lamina: (a) the cross-section with circles representing line intersections, (b) 3D model.

7.1.2 Geometrical model generation

Geometrical operations are applied on the pin and lamina lines while the contact treatment accounts for interaction between the lines (Fig. 7.2). The interaction between the lamina lines is considered symmetrically ($q = 0.50$) while a lamina line is fully moved upon contact with the pin. Boundary conditions can be enforced on the bottom and top surface of the lamina to keep the borders straight.

Step 1: the pin is inflated from zero to its final radius using the inflation operation.

Step 2: the lamina lines are straightened using the straightening operation.

An optimisation for the contact search algorithm is further implemented, through which only lines having the potential to interpenetrate other lines are considered. Initially, the

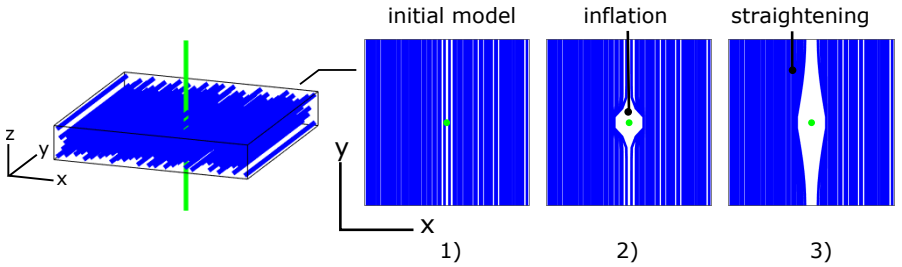

Fig. 7.2: Step-wise generation proces: (1) initial model, (2) pin inflation, (3) lamina straightening.

pin and the boundaries of the resin-rich regions (see Fig. 7.3a) are the only lines that are included in the contact search. Upon pin inflation, other lines will be gradually introduced in the contact search when one of their neighbours started to move in a previous iteration. The neighbour for each line (Fig. 7.3b) can hereby be easily deduced from a Delaunay triangulation applied on the initial cross-section. Finally, only a limited number of lines will have been included in the contact search (see Fig. 7.3c).

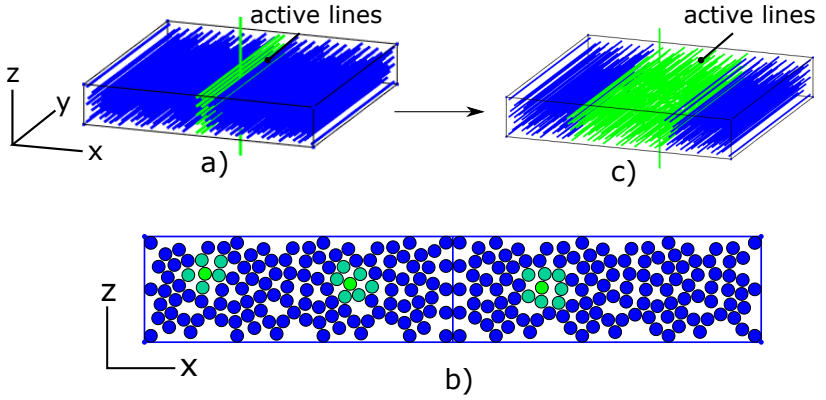

Fig. 7.3: An optimisation of the contact treatment to reduce the computational time: (a) lines which are present in the contact search initially (indicated in green), (b) neighbours for certain lines detected by a Delaunay triangulation (indicated in green), (c) lines which are present in the contact search after generation (green)

7.1.3 Fiber volume fraction and fiber direction in the lamina

The local fiber-volume fraction is evaluated on cross-sections which are obtained from intersections of the distorted inner-line configuration (see Fig. 7.4a-b). The distorted lines in each cross-section (red lines) (see Fig. 7.4b) are hereby distributed rather uniformly in a limited region near the pin. A distorted zone with rectangular shape and constant fiber volume fraction ($V_{f,c}(u)$) in each cross-section (see Fig. 7.4c) can then be assumed. The constant fiber volume fraction $V_{f,c}(u)$ in the distorted zone of each

cross-section is determined by:

$$V_{f,c}(u) = \frac{A^{init}_{cross}(u) - (A^{deform}_{cross}(u) - A_{dist}(u))}{A_{dist}(u)} . V_{f,lam} \tag{7.1}$$

where $V_{f,lam}$ is the initial fiber volume fraction in the lamina, and A_{dist}, A^{init}_{cross} and A^{deform}_{cross} are the area of the distorted zone, the initial cross-section and the deformed cross-section, respectively. The resulting fiber volume fraction V_f distribution is illustrated in Fig. 7.5a.

The fiber direction distribution in the lamina is directly obtained from the local tangents to the inner-lines. The fiber misalignment f_{mis}, often used to illustrate the local fiber direction in a lamina, is defined as the angle between the main fiber direction in the lamina and the local fiber direction. The resulting fiber misalignment f_{mis} distribution is illustrated in Fig. 7.5b.

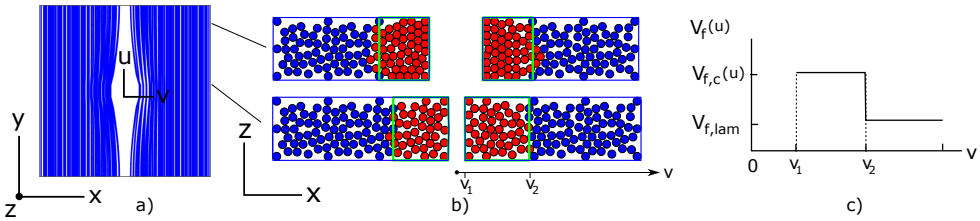

Fig. 7.4: Fiber volume fraction modelling: (a) the deformed inner-lines, (b) cross-section of the deformed inner-lines, (c) the assumed fiber volume fraction V_f distribution in a cross-section.

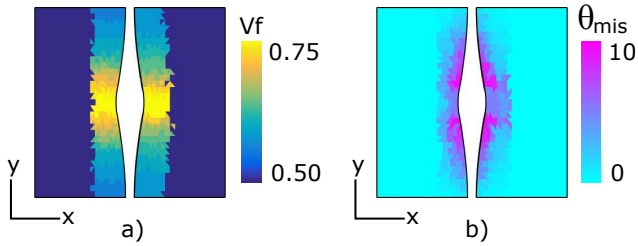

Fig. 7.5: The resulting fiber volume fraction V_f and fiber misalignment f_{mis} distribution in the lamina.

7.1.4 Illustration on the effect of different model parameters

The next illustrations will be performed on 2D models representing approximately the cross-section near the pin location in the 3D models. The initial cross-section of the inner-line configuration (see Fig. 7.1a) is considered here, and a pin is positioned vertically in the center of the cross-section. The pin is inflated, while the contact treatment accounts for line interaction and, to keep the lamina borders straight, boundary conditions are imposed on the bottom and top of the cross-section to keep the lamina borders

straight. The cross-section models represent approximately what is happening in a cross-section near the pin in 3D models, but with the main difference that compaction effects due to line straightening in the 3D models are not considered.

Inner-line distribution

Fig. 7.6 illustrates the effect of the inner-line distribution on the distortions taking place (indicated by the red lines) in the cross-section models. A square, a hexagonal and a random inner-line distribution are considered. The line radius for each configuration is approximately 4 times a carbon fiber radius $R_{fiber}(3.5\mu m)$ while the initial fiber volume fraction in the cross-section is 0.5 (as typically observed in prepregs). It can be seen that a square and hexagonal configuration for the inner-lines results in less compacted distorted zones, and to a larger distorted zone width compared to the random configuration.

SEM-images were then taken (by the author) from cross-section cuts of a non-crimp fabric composite to investigate the fiber-distribution in assumed undistorted and distorted regions caused by the binder (Fig. 7.7). The undistorted region was considered at the center of a fiber-reinforced region while the distorted region was considered near the binder yarn (see Fig. 7.7a). The fibers are rather randomly positioned in the undistorted region (see Fig. 7.7b) and have a closely-packed configuration in the distorted region (see Fig. 7.7c), conform to other experimental observations [220, 224, 383]. A random initial inner-line distribution should therefore probably be considered in the models, rather than to a square or hexagonal initial inner-line distribution (and so will be adopted in further simulations).

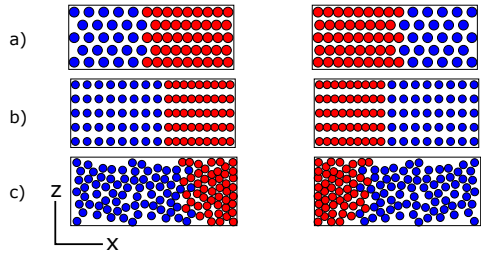

Fig. 7.6: Distorted inner-lines in a cross-section for different initial line distributions: (a) a hexagonal distribution, (b) a square distribution, (c) a random distribution (note that a line configuration can have a different numbers of lines and as such a different radii for its lines).

Number of lines

Fig. 7.8 illustrates the effect of the number of lines on the distorted zone width with a 2D model. The number of lines is deduced from the line radius and initial fiber volume fraction in the lamina, with a line radius chosen as the multiplication of a parameter f and a default fiber radius $R_{fiber} = 3.5\mu m$. The width of the distorted zone for each cross-section is normalised by the radius of the pin. Three random-distributed inner-line configurations have further been generated for each number of lines. The average

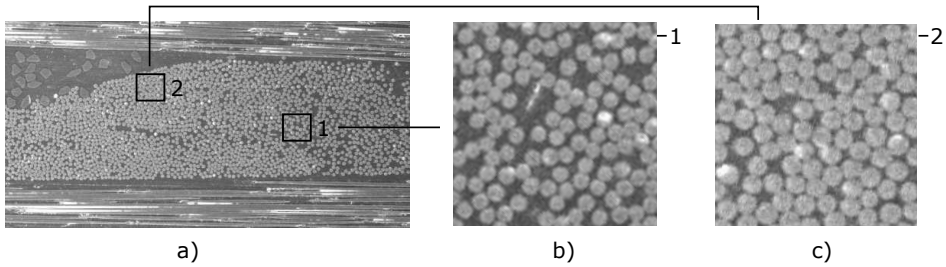

Fig. 7.7: SEM-images made from a [0/90/90/0] non-crimp fabric composite: (a) 2D view, (b) a zoom on the fiber-reinforced region away from the binder yarn (undistorted zone), (c) a zoom on the fiber-reinforced region near the binder yarn (distorted zone)

of these results was considered in the graphs presenting the distorted zone width and computational time in function of the number of lines. It can be seen that the distorted zone width decreases for an increasing number of lines and that no convergence is taking place for the distorted zone width for decreasing line radii (see Fig. 7.8). The lack of convergence can be explained from the presence of residual interpenetrations which arise from a limit imposed on the maximum number of contact iterations to obtain results in reasonable time. The distorted zone width further depended on the pin inflation increment as illustrated in Fig. 7.9. Both the lack of convergence and the distorted zone width dependency on the pin inflation increment questions the predictability (and so the benefits) of the approach (as disucssed in section 7.1.5).

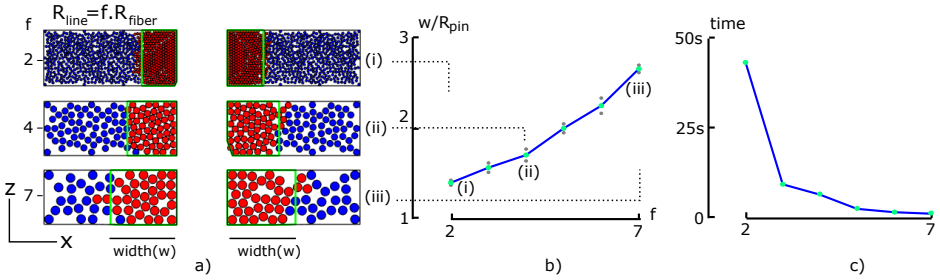

Fig. 7.8: Convergence study on the number of lines: (a) distorted inner-lines in a cross-section, (b) the distorted zone width in function of the number of lines, (c) the generation time in function of the number of lines. ($R_{pin} = 140\mu m$, $R_{fiber} = 3.50\mu m$)

Boundary conditions on lamina surfaces

Fig. 7.10a illustrates the effect of boundary conditions that can be applied on the bottom and top of the lamina (as described in chapter 4). For unconstrained lamina, lines can locally move beyond the lamina borders. For constrained lamina, the lamina borders remain straight and the width of the distorted zone is observed to be slightly larger compared the unconstrained configuration. The application of boundary conditions would then allow to account in an advantageous manner for lamina interactions in laminate

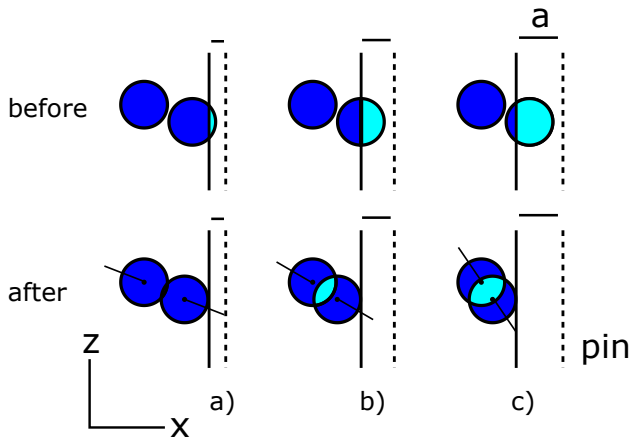

Fig. 7.9: The dependency of a pin inflation increment a on the movement of lines during contact treatment: (a) $a = 0.10R_{line}$, (b) $a = 0.50R_{line}$, (c) $a = 0.90R_{line}$. The small inflation increment ($a = 0.10R_{line}$) gives the most realistic results, but the corresponding increase in the number of inflation increments makes such small inflation increment computationally expensive.

models, without the need to model explicitly lamina interactions (reducing hereby the computational time).

Pin radius

Fig. 7.10b illustrates the effect of different pin radii on the distorted inner-line configuration (red lines). It can be seen that the inner-line configuration is able to account for distorted zone widths which increase with the pin radius, as experimentally observed in [324].

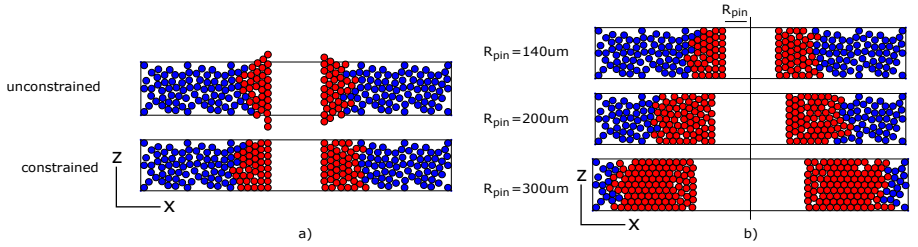

Fig. 7.10: Distorted inner-lines in cross-sections illustrating the effect of different model parameters: (a) the boundary conditions which can be applied on the bottom and top surface of the lamina, (b) the pin radius.

Initial fiber volume fraction in the lamina

Fig. 7.11 illustrates the effect of different fiber volume fraction of the lamina $V_{f,lam}$ on the final local fiber-volume fraction and fiber misalignment distributions in the lamina, and on cross-sections of the distorted inner-line configuration. It can be seen that the inner-line methodology indicates a correlation between the distorted zone width and the initial fiber volume fraction in the lamina. The maximum fiber volume fraction in the lamina is hereby lower than the theoretical maximum 0.90 that corresponds to a closely-packed hexagonal fiber configuration.

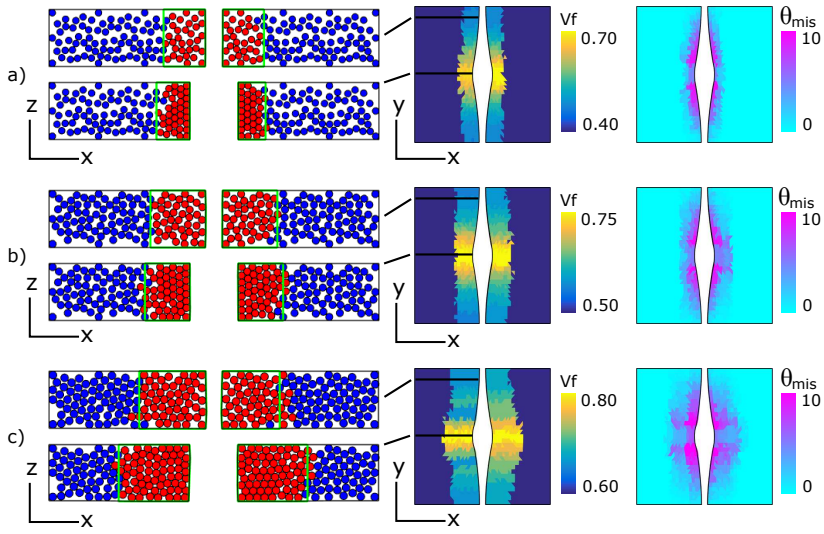

Fig. 7.11: Distorted inner-lines in cross-sections and the fiber volume fraction V_f and fiber misalignment θ_{mis} distribution in the lamina for different initial fiber volume fraction V_f^{init} in the lamina: (a) $V_f^{init} = 0.40$, (b) $V_f^{init} = 0.50$, (c) $V_f^{init} = 0.60$.

7.1.5 Reflection on the predictability of the approach

The predictive behaviour of the approach is challenged by following aspects:

1. Straight lines are considered in the inner-line configuration, while fibers in undistorted configuration are characteristed by microscopic waviness which can affect transverse compaction [43, 384–386].

2. The line radius is taken larger than a fiber radius, as such that lines geometrically do not represent fibers.

3. Initial interpenetration are allowed during the contact treatment, which are not physical and causes the model outcome to be dependent on the pin inflation increment.

4. The distorted zone width does not converge for a reduced number of lines (hereby having set a maximum number of iterations to make the problem computationally feasible).

5. No mechanics are involved in the contact treatment and straightening operation, where, experimentally, friction between the fibers, fiber bending stiffness and the presence of semi-cured matrix upon pin insertion may affect the outcome.

Model parameters should therefore be calibrated with experimental observation for use in predictive mechanical simulations.

7.1.6 Conclusion

The framework developed previously was extended to model the fiber-reinforced distorted zones in pinned lamina computationally. An inner-line configuration of the lamina was adopted and geometrical operations were applied on the pin and the lamina lines, while a contact treatment accounted for line interactions. The fiber volume fraction distribution in the lamina was deduced from cross-section of the distorted inner-line configuration in a post-processing stage, while the fiber direction distribution in the lamina was obtained as the local tangent to the inner-lines.

The approach allows obtaining automatically correlations of the distorted zone width with the initial fiber volume fraction in the lamina and the pin radius, but is computationally expensive. The approach is challenged in its predictability and in its ability to fit geometrical features as distorted zone width, fiber-volume fraction and fiber direction distributions to experimental data (contrary to the analytical fiber-reinforced distorted zone model for which the distorted zone width can be regulated and the profile of fiber volume fraction and fiber direction can theoretically be chosen). The analytical-based fiber-reinforced distorted zone model (as presented in the pinned and stitched laminate chapters) was therefore seen as a better and more efficient alternative for fiber-reinforced distorted zone modelling the fiber volume fraction and the fiber-direction in pinned, stitched and even 3D woven models.

7.2 Models with different binder content and binder type

The framework allows the generation of 3D reinforced composite unit-cell models corresponding to different binder type, content, diameter, tensioning, etc. The generation process (summarised in Fig. 7.12) starts from an initial model on which geometrical operations are applied. The shaped lines are transformed into cross-sections on which fiber-reinforced models are afterwards assigned. The geometrical models are subsequently meshed and further used in mechanical simulations. The generation process for each 3D reinforced composite differs in the initial model configuration, the applied geometrical operations (and corresponding parameters) and the selected fiber-reinforced distorted zone model, while interpenetration suppression, meshing and mechanical simulations are general applicable among the 3D reinforced composite types. The differences in the adopted geometrical operations and their corresponding parameters can be

found in Table 4.1, Table 5.1 and Table 6.2 for the Z-pin, stitched and 3D woven composites respectively. An illustration of the framework, accompanied by the geometrical and mechanical characteristics of generated models corresponding the different binder types and binder content, are presented in this section.

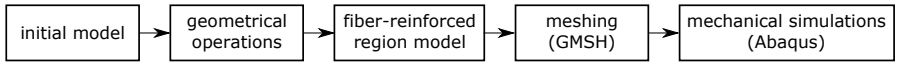

Fig. 7.12: Flowchart: generation process similar for each 3D reinforced composite.

7.2.1 Models

For illustration, pinned, stitched and 3D woven unit-cell models for binder content of 0.5, 2 and 4% are generated using the presented framework and subsequently compared.

Table 7.1 presents the initial model parameters for the different binder type models. A stacking sequence of [0/90/90/0] is considered for the pinned and stitched laminates, while the in-plane fiber-bundles of the 3D woven model are automatically aligned in the 0 and 90-direction. The initial fiber volume fraction in the in-plane fiber-reinforced regions is $0.6, 0.5, 0.6$ for pinned, stitched and 3D woven composites respectively, comparable to experimental observations [35,99,189,190]. A circular and an elliptical cross-sections are considered for the pin and stitching yarn, and the binder yarn, respectively. Their dimensions are determined by considering a unit-cell model with sides $1750\mu m$ and a binder content of 2%. The in-plane unit-cell dimensions are adapted to generate unit-cell models for different binder content while the binder yarn dimensions remain constant.

Table 7.2 presents the step-wise generation process for the different binder type models. The single-line configuration of the binders is not transformed into multi-line configuration in this section. The matrix in the generated unit-cell model will be considered to fully embed the stitching and binder yarn (as illustrated by the mesh models presented in Fig. 7.13). The same generation parameters are used for the different binder contents.

Finite element models are then generated from the geometrical models. A global strain of 0.50% is applied on the unit-cell models, a straining level for which early damage initation have experimentally shown to take place in 3D reinforced composites [24,99,329]. The stiffnesses of the models (E) for different binder content are normalised by the stiffness of the model with a binder content of 0.50% and the corresponding binder type (this normalised stiffness is indicated by E_{norm^*}). Local stresses are evalualated based on the local damage indicators for transverse and shear damage (f_{22} and f_{12} respectively) in the fiber-reinforced regions and matrix damage (f_m) using the criteria presented in [377](see also chapter 4). The x-direction and y-direction are further defined along the 0- and 90-direction of the fiber-reinforced regions, respectively.

pinned (inclined)	laminate	stacking sequence	0/90/90/0
		$V_{f,init}$	0.600
	pin	cross-section(R)	circular(280μm)
	(inclined)	α_{final}	15°
stitched	laminate	stacking sequence	0/90/90/0
		$V_{f,init}$	0.500
	stitch	cross-section(R)	circular(100μm)
		$V_{f,init}$	0.500
3D woven	warp,weft,binder	$V_{f,init}$	0.600
	binder	cross-section (a-b)	ellipse(100-50μm)
		$V_{f,init}$	0.500

Table 7.1: Initial model parameters for the vertically pinned, inclined pinned, stitched and 3D woven models.

	step	operation	id line	q_{bl}	parameter	value	experimental data
pinned	1	single-line inflation	pin	0	f	1	width of resin region
(inclined)	(2)	rotation	pin	0	α_f	15	final pin inclination
	3	straightening	lamina	0	s	23	length of resin region
	4	distorted zone	-	-	k	1	width of distorted zone
stitched	0	initial model	-	-	z_{out}	-	out-of-plane undulation
	1	single-line inflation	stitch	0	f	0.80	width of resin region
	2	straightening	stitch	0	s	2	centerline stitching yarn
	3	straighening	lamina	1	s	30	length of resin region
	4	distorted zone	-	-	k	1	width of distorted zone
3D woven	1	border-line	weft	-	R_{line}	0	-
	2	straightening	binder	0	s	10	-
	3	straightening	binder	0	s	5	centerline binder
	4	straightening	weft	1	s	50	fiber misalignment weft

Table 7.2: Generation strategy and parameters for the vertically pinned, inclined pinned, stitched and 3D woven models.

7.2.2 Geometrical characteristics

The percentage of in-plane fiber-reinforced region with a local fiber volume fraction V_f larger than 0.7 ($V_f^{>0.70}$), the percentage of in-plane fiber-reinforced region with a fiber misalignment f_{mis} larger than 0 ($f_{mis}^{>0}$) and the maximum misalignment in the in-plane fiber-reinforced region (f_{mis}^{max}) are considered as the main geometrical characteristics which may potentially explain trends of stiffness (using $f_{mis}^{>0}$) and stress concetrations (using $V_f^{>0.70}$ and f_{mis}^{max}). A distinction in geometrical features is further made between fiber-reinforced regions which are aligned to or transverse to the stitching direction (x- and y- direction respectively).

Fig. 7.14 presents the geometrical characteristics of the generated models, from which the following trends on binder content, binder type and in-plane direction can be observed (a comparison with experimental observations is given thereafter):

1. An increase in binder content increases the relative amount of distortions in the in-plane fiber-reinforced regions (see $V_f^{>0.7}$, $f_{mis}^{>0}$) and leaves unchanged the max-

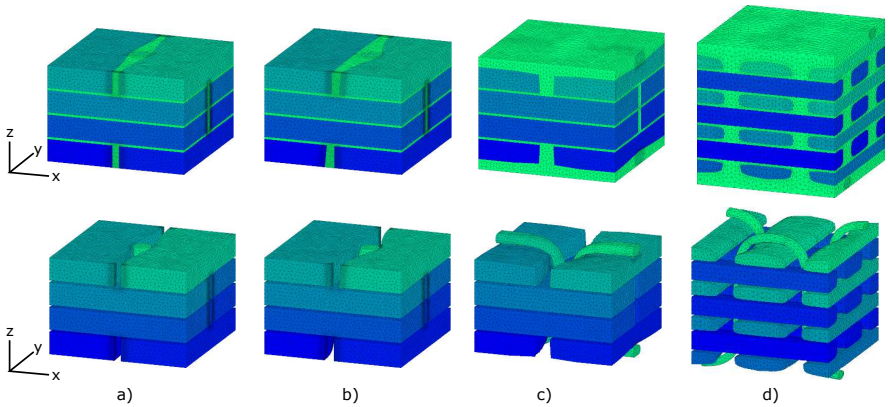

Fig. 7.13: Generated mesh models (with and without matrix) for different binder configurations: (a) vertical pin, (b) inclined pin, (c) stitching yarn, (d) binder yarn (binder content 2%).

imum fiber misalignment for relatively small binder content. The slope of the increase in fiber-waviness region and the maximum fiber misalignment in the fiber-reinforced region decreases for large binder contents, which can directly be explained from the interactions between distortions in neighbouring unit-cells that can take place for larger binder content (see Fig. 7.15).

2. Inclined pinned and stitched laminates are the highest distorted, while 3D woven composites are the lowest distorted, upon binder insertion. The largest distortions for the inclined pin and stitching yarn are due to the pin rotation and the continuity of the stitching yarn respectively. The smaller distortions for the 3D woven composites can be due to the fact that in the 3D woven model the binder yarn is inserted between the fiber-bundles, compared to pinned and stitched models in which the binder is inserted through the fiber-reinforced regions.

3. The fiber-reinforced regions aligned in the binder direction are less distorted compared to the fiber-reinforced regions with fiber aligned transversal on the binder direction. Note also the zero distortions in the fiber-reinforced regions of the 3D woven model aligned in the binder direction, that are due to modelling assumptions through which the warp yarns were assumed to not interact with the weft and binder yarns. The effect of this assumption, especially for larger binder yarn tensioning and transverse compaction levels, should be investigated in future work.

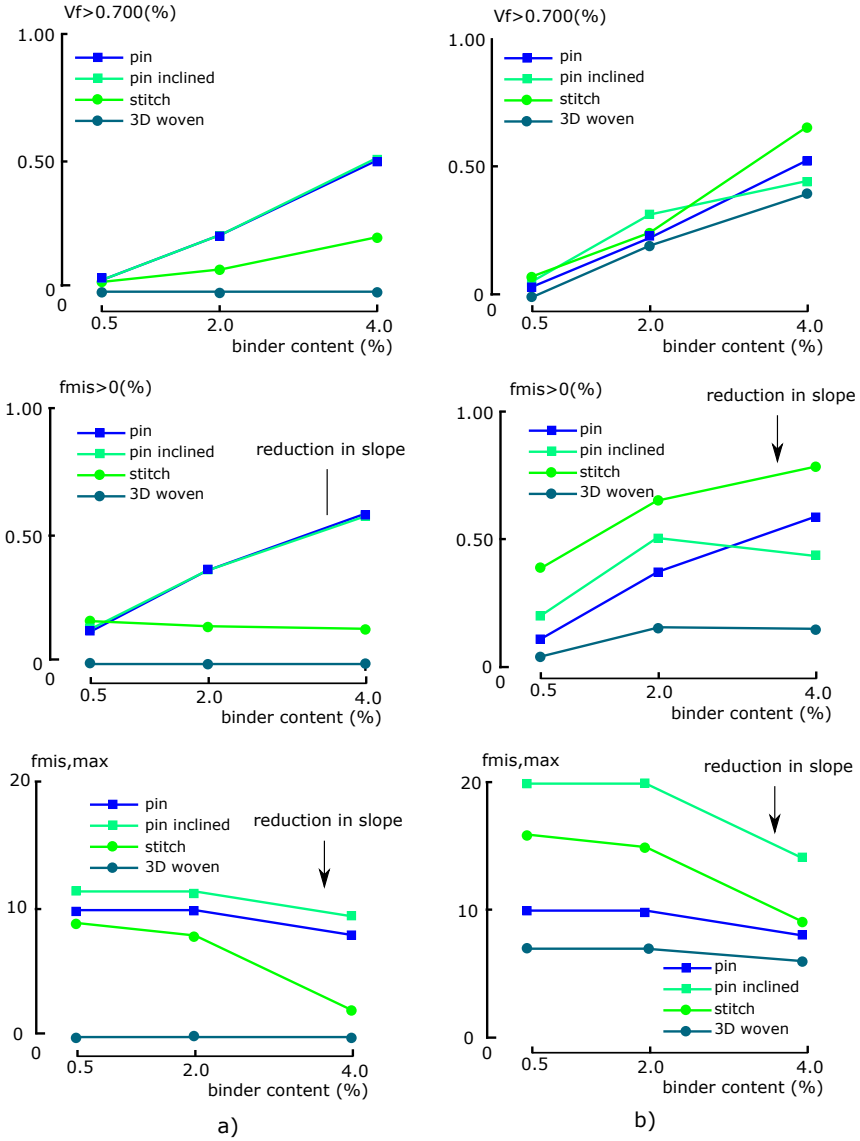

Fig. 7.14: Graphs illustrating the effect of the binder content and binder type on the percentage of fiber-reinforced region with a fiber volume fraction larger than 0.700 ($V_f^{>0.700}$) or with a fiber misalignment larger than 0 ($\theta_{mis}^{>0}$), and on the maximum fiber misalignment in the fiber-reinforced region, in the models, whereby a distinction is made between the fiber-reinforced regions which are aligned in the x- or y-direction (illustrated in (a) and (b) respectively).

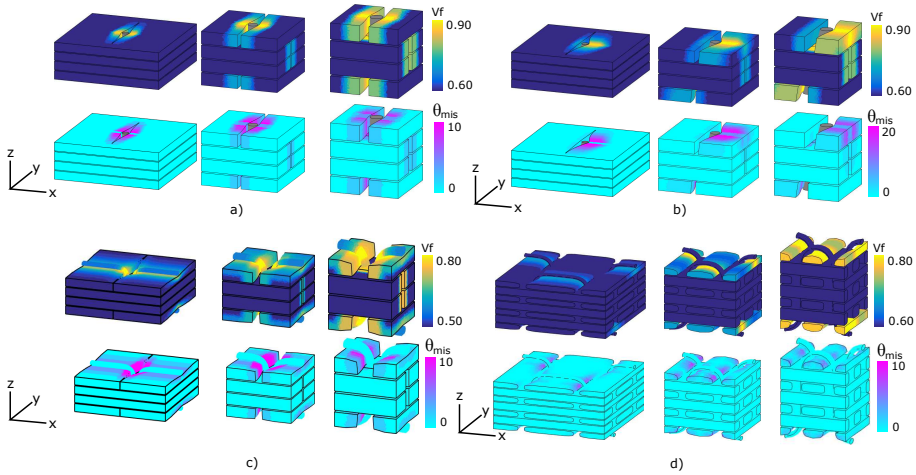

Fig. 7.15: Fiber volume fraction V_f and fiber misalignment θ_{mis} distributions for different binder type models corresponding to binder content 0.5,2 and 4%: (a) vertically pinned models, (b) inclined pinned models, (c) stitched models, (d) 3D woven models.

7.2.3 Mechanical characteristics

The stiffness components E_{ij} (which will be for our case the ratio between the macroscopic stress and strain in the direction of the loading) and the percentage of damage initiated in-plane fiber-reinforced region (indicated by $f_{ij}^{>1}$) of the unit-cell model are considered in the mechanical characterisation, in which the unit-cell models were subjected to a global strain of 0.5% along both directions in and transversal to the binder direction (x- and y-loading respectively). The stiffness of each model was further normalised by stiffness of the model with a binder content of 0.5% and the same binder type (this normalised stiffness is indicated by E_{norm^*}).

Fig. 7.16 presents the mechanical characteristics of the generated models, for which the following trends in terms of binder content, binder type and loading direction can be observed:

1. An increased binder content decreases the stiffness and increases the percentage of damage initiation indicator in the fiber-reinforced regions. The slope in the stiffness reduction of the models loaded in the y-direction diminishes for large binder content (conform to f_{mis}) while the slope of the region percentage that undergoes damage initiation $f_{ij}^{>1}$ remains approximately linear (conform to V_f, rather than f_{mis}).

2. Vertical pinned laminates are characterised by the smallest reduction in stiffness, while 3D woven models are characterised by the largest reduction in stiffness (taking place transversal to the binder direction). The large stiffness reduction of the 3D woven models is explained by the decrease of the in-plane fiber volume fraction caused by the fact that the gaps between the fiber-bundles remain constant and the fiber-bundle dimensions are changed to accommodate larger binder

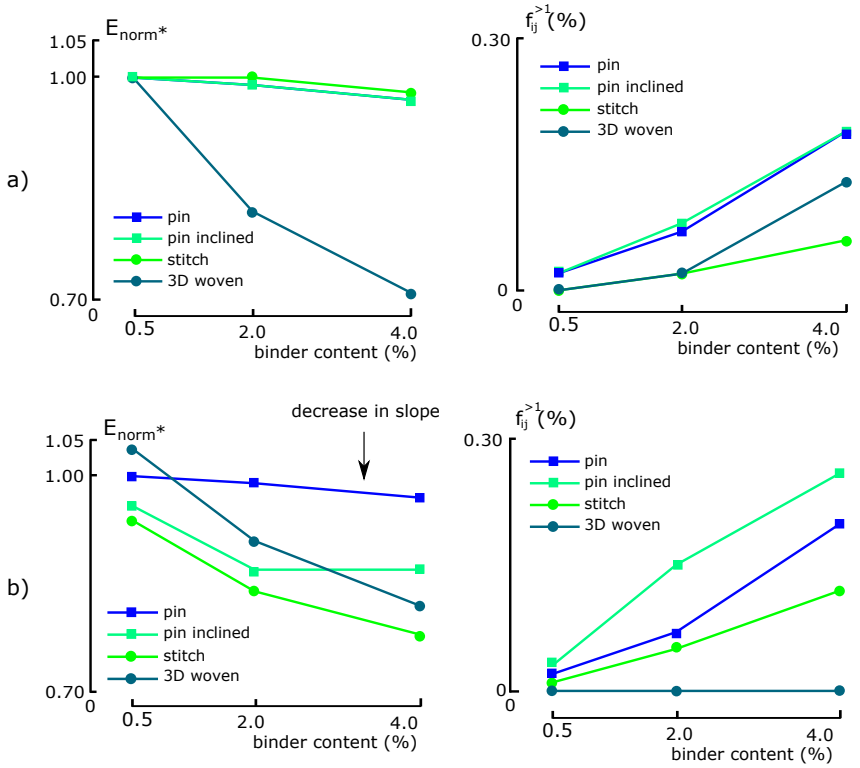

Fig. 7.16: Graphs illustrating the effect of the binder content and binder type on a normalised stiffness E_{norm^*} (defined in section 7.2.3) and on the percentage of locally damaged regions ($f_{ij}^{>1}$), for the models loaded in different directions: (a) x-direction loading, (b) y-direction loading.

content (openings between fiber-bundles are not present in pinned and stitched laminates). 3D woven models experience further the least local damage initiation regions, as can also be observed from Fig. 7.18.

3. The stiffness transverse to the binder direction (meaning pinned, stitched and 3D weaving direction) is much larger decreased than the stiffness in the binder direction (correlating with the trends in the percentage of fiber-reinforced waviness region $\theta_{mis}^{>0}$), while the percentage of regions subject to damage initiation in both directions are approximately similar.

A comparison can further be made between experimental observations presented in [80] (see also Fig. 7.17 for a reproduction) and the simulations results. The experimental data showed that the stiffness of pinned laminates was reduced for increasing binder content, while it remained ambiguous whether the stiffness of stitched and 3D woven composites increases, decreases or remains unchanged for increased binder content. The simulation results, for which a reduction in stiffness was observed for each binder type, then suggest that other features such as an increased in-plane fiber volume fraction due

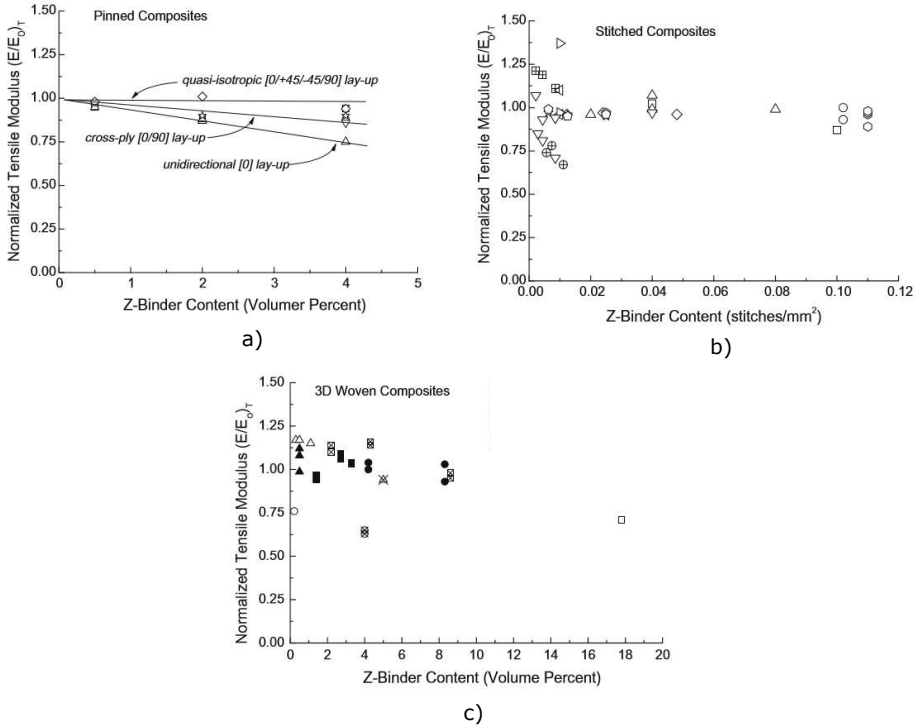

Fig. 7.17: Effect of z-binder content on the normalized tensile modulus of (a) 3D woven (b) stitched and (c) pinned composites (reproduced from [80])

to consolidation processes caused by stitching and 3D weaving, should be present (or accounted for) to reproduce the experimental observation (as was also proposed in [80] by means of mechanistic interpretations).

7.2.4 Conclusion

Models are generated for different binder types and binder contents. They are generated and characterised geometrically and mechanically using the presented framework. Binder content and binder type seem to generate different geometrical characteristics which then correlate with mechanical characteristics. The potential of the framework for an automated generation of unit-cell models for 3D reinforced composites, integrated with existing finite element software and developed post-processing tools, have hereby been illustrated.

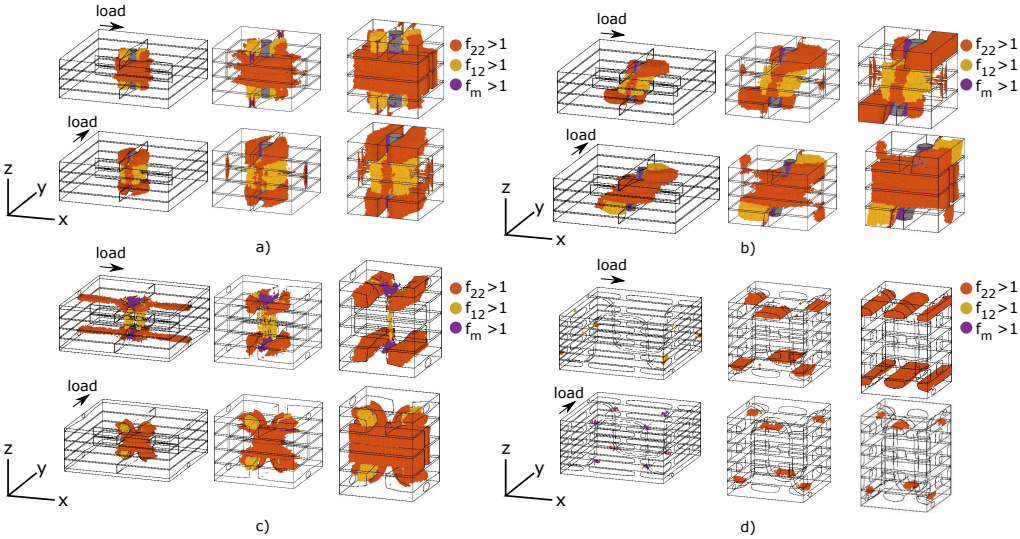

Fig. 7.18: Potential local failure initiated regions, with an indication of the main local damage initiation mechanism, for different binder type models corresponding to the binder content 0.5, 2 and 4%: (a) vertical pinned model, (b) inclined pinned model, (c) stitched model, (d) 3D woven model.

Chapter 8
Conclusions and future work

This chapter present the conclusions and future work in geometrical model generation and mechanical simulations.

8.1 Conclusions

8.1.1 Geometrical modelling approach

An approach was presented to generate unit-cell models of pinned, stitched and 3D woven composites. Discretised lines, which are used to represent the geometrical features in the lamina and fiber-bundles, are positioned in an initial undistorted loose-state configuration and are then gradually shaped by geometrical operations, while the interactions between the lines are accounted for by a geometrical contact treatment. The fiber volume fraction and fiber direction in the lamina and fiber-bundles are modelled on cross-sections in a post-processing step, hereby having included a local fiber-reinforced distorted zone in the cross-sections of the pinned and stitched lamina. The shapes of the geometrical features corresponding to different laminate stacking sequences and binder parameters (content, diameter, tensioning) can automatically be generated while the dimensions of the geometrical features can be regulated by the parameters of the geometrical operations. The implemented geometrical features for each binder type are the following:

1. For pinned laminates, a rectangular pin pattern is considered. Resin-rich regions, local fiber-reinforced distorted zones and pin inclination (due to pin insertion and pin chamfering) can be included in the unit-cell models. The length of the resin-rich regions, the width of the local distorted zone, the initial and final pin inclination angle and the fiber crimp during pin chamfering can be controlled. The laminae are assumed not to interact with each other as matter of simplification.

2. For structurally stitched non-crimp fabric composites, a modified lock stitch pattern is considered. Resin-rich regions, out-of-plane undulations in the surface laminae, a deformable stitching yarn and local fiber-reinforced distorted zones can be included in the unit-cell models. The width and length of the resin-rich regions, the extent of the out-of-plane undulations in the surface laminae, the local distorted zone width and the shape of the stitching yarn (discretised) centerline and cross-sections corresponding to different stitching yarn tensioning can be controlled by the parameters corresponding to the geometrical operations. The lamina

are assumed not to interact with each other and the modified lock stitch is represented by two unconnected U-shaped arm, both as matter of simplification.

3. For 3D woven non-crimp fabric composites, a 3D orthogonal weave pattern is considered. Cross-section variations for the weft yarns and cross-section variations and different centerline positions for the binder yarns can be included in the unit-cell models, which can further be controlled to account for different binder content and tensioning. The in-plane fiber-bundles are assumed to not interact with each other by means of simplification.

The geometrical models can then be automatically transformed into conforming tetrahedral meshes with in-plane periodic surface meshes by the tools presented in this work.

8.1.2 Mechanical simulations

The effect of geometrical features on the stiffness and local damage initiation was investigated. A normalised stiffness is considered to state the effect of binder insertion compared to an undistorted configuration that does not include the binder neither its distortions. The following observations could be made:

1. The normalised stiffness of a pinned lamina is either decreased or increased, depending on the main fiber direction in the lamina. A lamina with fibers aligned in the load direction experienced a reduction in stiffness (3%) while a lamina with fibers oriented in 30° or 90° from the load direction experienced an increase in stiffness (5% and 2% respectively) (for a pin content of 2%). The decrease and increase in stiffness for each binder type enlarges for larger binder content.

2. The normalised stiffness of a laminate depends on the binder type, the binder content and the loading direction. For a pinned laminate with a [0/90/90/0] stacking sequence and a 2% binder content, the stiffness can be decreased by 2% (for a vertical pin) or can be decreased by 16% (for an inclined pin, transversal on the pin inclination direction and pin inclination due to pin chamfering). For a stitched laminate with a [0/90/90/0] stacking sequence and a 2% stitch content, the stiffness is increased along the (longitudinal) stitch direction (1%) and decreased transversal on the (longitudinal) stitch direction (15%). For a 3D woven composite with a 2% binder content, the stiffness is increased along the in-plane weaving direction (2%) and decreased transversal to the binder direction (14%). The extent of increase and decrease enlarged for increasing binder content for each binder type.

3. Early damage initiation has been observed to take place for each binder type around the binder location. Transverse and shear cracking can take place in the in-plane fiber-reinfored distorted regions and the binder yarn depending on the stacking sequence and the loading direction. Matrix cracking took also place near the binder location.

4. The local fiber volume fraction has a large effect on transverse and shear cracking in the in-plane fiber-reinforced regions and the binder yarn, where local fiber

misalignment affected the stiffness, and damage initiation mechanisms and stress levels.

5. Geometrical features (as pin inclination due to pin chamfering, out-of-plane undulations, cross-section variations in fiber-bundles and the presence of the stitching yarn) were shown to affect stiffness and damage initiation and need to be properly accounted for in models.

The generated models can further be exploited to study the effect of the binder and their corresponding reinforcement distortions on the enhancement of the toughness properties for the 3D reinforced composites, as will be part of future work.

8.1.3 In summary

This research contributed in the development of a novel approach to introduce in a simple and fast way the complex shapes of the geometrical features of reinforcement distortions caused by binder insertion, as well as in a thorough understanding on the global and local effect of geometrical features on the mechanical in-plane behaviour for in-plane loading conditions. The framework can now be used in detailed parametrical studies on the effect of geometrical features and binder parameters on the stiffness and damage imitation levels to explain experimentally observed scatter in mechanical characteristics and to provide design guidelines in the binder parameter optimisation both of interest for industry.

8.2 Future work

8.2.1 Quantitative validation of the approach

The approach should ideally be validated through comparisons with experimental data. An explanation of why the methodology is not quantitatively compared with experimental data may rely on the following reasoning's:

1. A quantitative investigation would compare the dimensions of generated geometrical features with experimental observations. However, the dimensions of the geometrical features should be set itself by the experimental observations using the parametric design spaces in each corresponding section. The shape of the geometrical features, as the outcome of the geometrical operations, should however be compared with experimental observations, which was done qualitatively by referring to the images from experimentally observed features in corresponding chapters.

2. The literature did not provide quantitative geometrical data on all geometrical features of interest.

3. We have attempted to request Z-pinned laminates specimens from the Bristol University in order to analyse the fiber-reinforcement distorted zone near the Z-pin location by cross-sections cuts and SEM, but with no success.

A future work may consist in a quantitative (rather than a qualitative) investigation of the geometrical features in each 3D reinforced composites. Herefore, specimens can be requested at other research departments and companies, or produced on lab-scale at the MeMC department. The specimens can then be cut at desired locations and the cross-sections can further be analysed with the Scanning Electron Microscope present at the MACH department on the VUB.

8.2.2 Exploiting the framework

The inner-line configurations for lamina and fiber-bundles can be used to generate more realistic geometrical models of stitched and 3D woven composites which includes centerline deflections of lamina and fiber-bundles (that can arise for larger stitch or binder yarn tensioning or larger compaction levels in which the stitch or binder yarn is latterly compressed into the underlying fiber-reinforced regions). It suffices to replace in the modelling approach the border-line configuration with the inner-line configuration and to apply a similar generation strategy as presented in corresponding chapters. An investigation is then needed to validate whether the inner-line configuration and the geometrical-based framework are able to provide desired geometrical features and a comparison can be made with the digital element approach, which uses the (more expensive) finite-element based framework, in terms of generated geometrical features and computational time.

The multi-line configuration for fiber-bundles and the multi-line inflation operation can be investigated in their potential to suppress interpenetrations in simplified analytical woven composite models. Each fiber-bundle can hereby be transformed into a multi-line configuration which is then gradually inflated by the multi-line inflation in the model, while the contact treatment, accounting for line interactions, results in local distortions of the lines at interpenetration locations. The local distortions are afterwards smoothed using the straightening operation. Such an approach would give an alternative to existing interpenetration suppression methodologies [102, 179] in which the smooth shape of the cross-sections of the fiber-bundles remains preserved.

8.2.3 Embedding sensors and micro-vascular networks

Sensors and micro-vascular networks can be introduced in fiber-reinforced composites to detect and heal damage respectively [387–391]. Tubes are hereby inserted horizontally in the fiber-reinforcement architecture, which further causes distortions of the reinforcement architecture (as typical tube diameters range from 100 to 500μm). The in-plane and out-of-plane mechanical properties of these multi-functional composites materials are largely reduced by the presence of the tubes [246, 392–399]. Unit-cell models should therefore include the main geometrical features of the tubes and their distortions to be predictive in mechanical simulations.

Out-of-plane undulations of the lamina, eyelet-shaped regions around the tubes and deformable tubes are typically the main geometrical features present of these composites (see Fig. 8.1a). The out-of-plane undulations decrease gradually through-the-thickness

of the laminate. The eyelet-shaped regions transform into channel-shaped structure for decreasing tube spacing. Circular and elliptical shaped cross-section of the tubes can be present, depending on the tube material.

Analytical modelling approaches have been adopted to introduce these features in unit-cell models. [392, 399–401]. Cosine-shapes and cylindrical shapes are hereby used to model the undulations of the lamina and the cross-section of the tubes respectively. A similar computational approach (as in the void modelling) can then be used, in which (this time) tubes will be introduced inbetween discretised lines using a single or multi-point inflation procedure to model undeformable and deformable tubes respectively (see Fig. 8.1b).

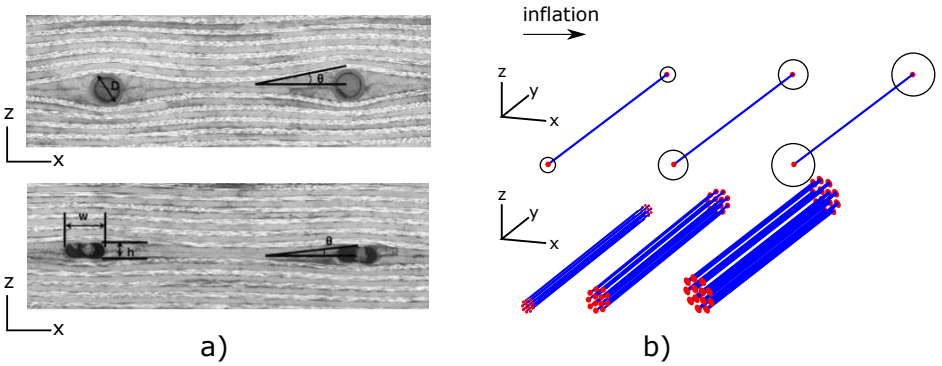

Fig. 8.1: Embedding sensors and micro-vascular networks: (a) experimental observations (images taken from [397]), (b) undeformable and deformable tube model.

8.2.4 Lamina waviness modelling

Lamina waviness can arise in multi-directional laminate due to thermal stresses and in non-crimp fabric composites due to nesting of lamina in neighbouring resin-rich regions during transverse compaction. This was shown to affect the in-plane mechanical properties [246, 402–404] and should therefore be included in the unit-cell models.

In one approach, an inner-line configuration for each lamina can be adopted in the pinned and stitched models, whereafter the flattening operation can be applied on the unit-cell models to mimic transverse compaction. A more simple approach consists in introducing lamina waviness analytically in unit-cell models, but followed by the use of the geometrical-based framework to include for example binder distortions on top of the lamina waviness introduced in the unit-cell models.

8.2.5 Extending the finite element models

First, more advanced damage initiation models can be adopted (compared to the more-simple used maximum stress criteria) to account for the interaction between the normal and shear stress components in local strength models and to obtain data on the local

failure plane inclination orientation [331, 332, 405]. Second, continuum damage mechanics can be introduced to account for damage evolution in the fiber-reinforced region [406–410], in the matrix and at the interface [359], which will allow going from damage initiation only (as done in this work) towards real damage propagation. Third, crack mechanics can be introduced to initiate crack development in the fiber-reinforced region and at the interfaces [63, 359, 411–415]. Non-linear simulations can then be performed using specialised software as Abaqus with build-in damage and failure models. Examples of contributions including damage initiation, damage propagation and failure mechanisms in their mechanical simulations for different types of fiber-reinforced composites can be found in [96, 161, 309, 326, 416–422].

8.2.6 Out-of-plane finite element simulations

The out-of-plane mechanical behaviour of 3D-reinforced composites can be characterised by performing mechanical simulations in the out-of-plane direction on the unit-cell models generated in this work. Analytical mechanical model and simplified unit-cell models were already been proposed in the literature (pinned [86, 93, 423–427], stitched, 3D woven). The intended out-of-plane simulations will then contribute by introducing more realistic geometrical features. The response of the unit-cell models can then exploited in double cantilever beam (for mode-1) and end notched flexure (for mode-2) simulations as constitutive law for cohesive zone elements or connector elements [189, 263, 335, 428, 429], where full-scale models (as adopted in [355]) might be computationally too expensive.

List of publications

Journal papers accepted

1. **G. Pierreux**, L. Wu, D. Van Hemelrijck, & T. J. Massart (2018). Evaluation of microdamage initiation in Z-pinned laminates by means of automated RVE computations. *Composite Structures*, 206, 104-115. `https://doi.org/10.1016/j.compstruct.2018.07.122`

Journal papers under review

1. **G. Pierreux**, D. Van Hemelrijck, & T. J. Massart. Automated RVE computations for evaluation of microdamage initiation in stitched non-crimp fabric composites *Under review*.

2. **G. Pierreux**, D. Van Hemelrijck, & T. J. Massart. Automated generation of 3D woven composites RVEs including yarn cross-section variations *Under review*.

Bibliography

[1] P Brøndsted, H Lilholt, and A Lystrup. Composite materials for wind power turbine blades. *Annu. Rev. Mater. Res.*, 35:505–538, 2005.

[2] G Marsh. Airbus a350 xwb update. *Reinforced plastics*, 54(6):20–24, 2010.

[3] C Soutis. Fibre reinforced composites in aircraft construction. *Progress in Aerospace Sciences*, 41(2):143–151, 2005.

[4] ER Fuchs, FR Field, R Roth, and RE Kirchain. Strategic materials selection in the automobile body: Economic opportunities for polymer composite design. *Composites science and technology*, 68(9):1989–2002, 2008.

[5] Tubular solution to light weighting/how hyperform benefits body engineering/mclaren cuts price of its carbon-fiber menu. `https://www.tatasteeleurope.com,https://www.nytimes.com`.

[6] Z Hashin and BW Rosen. The elastic moduli of fiber-reinforced materials. *Journal of applied mechanics*, 31(2):223–232, 1964.

[7] Z Hashin. Analysis of composite materials—a survey. *Journal of Applied Mechanics*, 50(3):481–505, 1983.

[8] PK Mallick. *Fiber-reinforced composites: materials, manufacturing, and design*. CRC press, 2007.

[9] J Chen, N Ding, Z Li, and W Wang. Organic polymer materials in the space environment. *Progress in Aerospace Sciences*, 83:37–56, 2016.

[10] J Karger-Kocsis, H Mahmood, and A Pegoretti. Recent advances in fiber/matrix interphase engineering for polymer composites. *Progress in Materials Science*, 73:1–43, 2015.

[11] M George, M Chae, and DC Bressler. Composite materials with bast fibres: Structural, technical, and environmental properties. *Progress in Materials Science*, 83:1–23, 2016.

[12] O Faruk, AK Bledzki, HP Fink, and M Sain. Biocomposites reinforced with natural fibers: 2000–2010. *Progress in polymer science*, 37(11):1552–1596, 2012.

[13] AB Strong. *Fundamentals of composites manufacturing: materials, methods and applications*. Society of Manufacturing Engineers, 2008.

[14] HJ Dirk, C Ward, and KD Potter. The engineering aspects of automated prepreg layup: History, present and future. *Composites Part B: Engineering*, 43(3):997–1009, 2012.

[15] C Cherif. *Textile Material for Lightweight Constructions*. Springer, 2015.

[16] V Romanov, SV Lomov, Y Swolfs, S Orlova, L Gorbatikh, and I Verpoest. Statistical analysis of real and simulated fibre arrangements in unidirectional composites. *Composites Science and Technology*, 87:126–134, 2013.

[17] Y Swolfs, RM McMeeking, I Verpoest, and L Gorbatikh. Matrix cracks around fibre breaks and their effect on stress redistribution and failure development in unidirectional composites. *Composites Science and Technology*, 108:16–22, 2015.

[18] L Yang, Y Yan, Y Liu, and Z Ran. Microscopic failure mechanisms of fiber-reinforced polymer composites under transverse tension and compression. *Composites Science and Technology*, 72(15):1818–1825, 2012.

[19] C González and J LLorca. Mechanical behavior of unidirectional fiber-reinforced polymers under transverse compression: microscopic mechanisms and modeling. *Composites Science and Technology*, 67(13):2795–2806, 2007.

[20] LE Asp, Lars A Berglund, and R Talreja. Prediction of matrix-initiated transverse failure in polymer composites. *Composites Science and Technology*, 56(9):1089–1097, 1996.

[21] B Fiedler, M Hojo, S Ochiai, K Schulte, and M Ando. Failure behavior of an epoxy matrix under different kinds of static loading. *Composites Science and Technology*, 61(11):1615–1624, 2001.

[22] E Totry, JM Molina-Aldareguía, C González, and J LLorca. Effect of fiber, matrix and interface properties on the in-plane shear deformation of carbon-fiber reinforced composites. *Composites Science and Technology*, 70(6):970–980, 2010.

[23] J Varna, R Joffe, NV Akshantala, and R Talreja. Damage in composite laminates with off-axis plies. *Composites Science and Technology*, 59(14):2139–2147, 1999.

[24] AE Bogdanovich, M Karahan, SV Lomov, and I Verpoest. Quasi-static tensile behavior and damage of carbon/epoxy composite reinforced with 3d non-crimp orthogonal woven fabric. *Mechanics of Materials*, 62:14–31, 2013.

[25] T Wehrkamp-Richter, R Hinterhölzl, and ST Pinho. Damage and failure of triaxial braided composites under multi-axial stress states. *Composites Science and Technology*, 150:32–44, 2017.

[26] R Gerlach, A Pabst, N Petrinic, A Hornig, J Wiegand, CR Siviour, and W Hufenbach. The interface between matrix pockets and fibre bundles under impact loading. *Composites Science and Technology*, 69(11-12):2024–2026, 2009.

[27] SV Lomov, Dmitry S Ivanov, I Verpoest, Masaru Zako, T Kurashiki, H Nakai, J Molimard, and A Vautrin. Full-field strain measurements for validation of meso-fe analysis of textile composites. *Composites Part A: Applied science and manufacturing*, 39(8):1218–1231, 2008.

[28] SV Lomov, DS Ivanov, TC Truong, I Verpoest, F Baudry, K Vanden Bosche, and H Xie. Experimental methodology of study of damage initiation and development in textile composites in uniaxial tensile test. *Composites Science and Technology*, 68(12):2340–2349, 2008.

[29] L Li, SV Lomov, X Yan, and V Carvelli. Cluster analysis of acoustic emission signals for 2d and 3d woven glass/epoxy composites. *Composite Structures*, 116:286–299, 2014.

[30] M Mehdikhani, M Aravand, B Sabuncuoglu, MG Callens, SV Lomov, and L Gorbatikh. Full-field strain measurements at the micro-scale in fiber-reinforced composites using digital image correlation. *Composite Structures*, 140:192–201, 2016.

[31] F Mathieu, P Aimedieu, JM Guimard, and F Hild. Identification of interlaminar fracture properties of a composite laminate using local full-field kinematic measurements and finite element simulations. *Composites Part A: Applied Science and Manufacturing*, 49:203–213, 2013.

[32] F Yu, Q Wu, Y Okabe, S Kobayashi, and K Saito. The identification of damage types in carbon fiber–reinforced plastic cross-ply laminates using a novel fiber-optic acoustic emission sensor. *Structural Health Monitoring*, 15(1):93–103, 2016.

[33] F Desplentere, SV Lomov, DL Woerdeman, I Verpoest, M Wevers, and A Bogdanovich. Micro-ct characterization of variability in 3d textile architecture. *Composites Science and Technology*, 65(13):1920–1930, 2005.

[34] A Yudhanto, G Lubineau, IA Ventura, N Watanabe, Y Iwahori, and H Hoshi. Damage characteristics in 3d stitched composites with various stitch parameters under in-plane tension. *Composites Part A: Applied Science and Manufacturing*, 71:17–31, 2015.

[35] M Karahan, SV Lomov, AE Bogdanovich, D Mungalov, and I Verpoest. Internal geometry evaluation of non-crimp 3d orthogonal woven carbon fabric composite. *Composites Part A: Applied Science and Manufacturing*, 41(9):1301–1311, 2010.

[36] PJ Schilling, BR Karedla, AK Tatiparthi, MA Verges, and PD Herrington. X-ray computed microtomography of internal damage in fiber reinforced polymer matrix composites. *Composites Science and Technology*, 65(14):2071–2078, 2005.

[37] SM Sisodia, SC Garcea, AR George, DT Fullwood, SM Spearing, and EK Gamstedt. High-resolution computed tomography in resin infused woven carbon fibre composites with voids. *Composites Science and Technology*, 131:12–21, 2016.

[38] AE Scott, M Mavrogordato, P Wright, I Sinclair, and SM Spearing. In situ fibre fracture measurement in carbon–epoxy laminates using high resolution computed tomography. *Composites Science and Technology*, 71(12):1471–1477, 2011.

[39] AE Scott, I Sinclair, SM Spearing, A Thionnet, and Anthony R Bunsell. Damage accumulation in a carbon/epoxy composite: comparison between a multiscale model and computed tomography experimental results. *Composites Part A: Applied Science and Manufacturing*, 43(9):1514–1522, 2012.

[40] LP Canal, C González, J Segurado, and J LLorca. Intraply fracture of fiber-reinforced composites: microscopic mechanisms and modeling. *Composites science and technology*, 72(11):1223–1232, 2012.

[41] M Bodaghi, C Cristóvão, R Gomes, and NC Correia. Experimental characterization of voids in high fibre volume fraction composites processed by high injection pressure rtm. *Composites Part A: Applied Science and Manufacturing*, 82:88–99, 2016.

[42] L Salvo, P Cloetens, E Maire, S Zabler, JJ Blandin, JY Buffière, W Ludwig, E Boller, D Bellet, and C Josserond. X-ray micro-tomography an attractive characterisation technique in materials science. *Nuclear instruments and methods in physics research section B: Beam interactions with materials and atoms*, 200:273–286, 2003.

[43] J Viguié, P Latil, L Orgéas, PJJ Dumont, SR du Roscoat, JF Bloch, C Marulier, and O Guiraud. Finding fibres and their contacts within 3d images of disordered fibrous media. *Composites Science and Technology*, 89:202–210, 2013.

[44] SV Lomov, DS Ivanov, I Verpoest, M Zako, T Kurashiki, H Nakai, and S Hirosawa. Meso-fe modelling of textile composites: Road map, data flow and algorithms. *Composites Science and Technology*, 67(9):1870–1891, 2007.

[45] V Carvelli and C Poggi. A homogenization procedure for the numerical analysis of woven fabric composites. *Composites Part A: Applied Science and Manufacturing*, 32(10):1425–1432, 2001.

[46] G Ernst, M Vogler, C Hühne, and R Rolfes. Multiscale progressive failure analysis of textile composites. *Composites Science and Technology*, 70(1):61–72, 2010.

[47] J LLorca, C González, JM Molina-Aldareguía, J Segurado, R Seltzer, F Sket, M Rodríguez, S Sádaba, R Muñoz, and LP Canal. Multiscale modeling of composite materials: a roadmap towards virtual testing. *Advanced Materials*, 23(44):5130–5147, 2011.

[48] F Feyel and JL Chaboche. Fe2 multiscale approach for modelling the elastoviscoplastic behaviour of long fibre sic/ti composite materials. *Computer methods in applied mechanics and engineering*, 183(3-4):309–330, 2000.

[49] M Groeber, S Ghosh, MD Uchic, and DM Dimiduk. A framework for automated analysis and simulation of 3d polycrystalline microstructures.: Part 1: Statistical characterization. *Acta Materialia*, 56(6):1257–1273, 2008.

[50] J Wimmer, B Stier, JW Simon, and S Reese. Computational homogenisation from a 3d finite element model of asphalt concrete—linear elastic computations. *Finite Elements in Analysis and Design*, 110:43–57, 2016.

[51] G Pierreux. Homogenisation and multi-scale methods for the failure of reinforced concrete slabs. *Master thesis*.

[52] TJ Massart, RH Peerlings, and MG Geers. An enhanced multi-scale approach for masonry wall computations with localization of damage. *International journal for numerical methods in engineering*, 69(5):1022–1059, 2007.

[53] BCN Mercatoris, Ph Bouillard, and TJ Massart. Multi-scale detection of failure in planar masonry thin shells using computational homogenisation. *Engineering fracture mechanics*, 76(4):479–499, 2009.

[54] B Sonon. *On advanced techniques for generation and discretization of the microstructure of complex heterogeneous materials*. PhD thesis, Universite Libre de Bruxelles, 2014.

[55] VG Kouznetsova. *Computational homogenization for the multi-scale analysis of multi-phase materials*. PhD thesis, Technische Universiteit Eindhoven, 2002.

[56] Y Fujita, T Kurashiki, H Yamatsuka, and M Zako. A proposal of fe modeling of unidirectional composite considering uncertain micro structure. In *18th Iternational Conference on Composite Materials (ICCM18)*, 2011.

[57] JJ Crookston, S Kari, NA Warrior, IA Jones, and AC Long. 3d textile composite mechanical properties prediction using automated fea of the unit cell. In *Proc. of the 16th Int. Conf. on Composite Materials*, pages 1–7, 2007.

[58] Y Swolfs, L Gorbatikh, V Romanov, S Orlova, SV Lomov, and I Verpoest. Stress concentrations in an impregnated fibre bundle with random fibre packing. *Composites Science and Technology*, 74:113–120, 2013.

[59] R Pyrz. Quantitative description of the microstructure of composites. part i: Morphology of unidirectional composite systems. *Composites Science and Technology*, 50(2):197–208, 1994.

[60] D Trias, J Costa, JA Mayugo, and JE Hurtado. Random models versus periodic models for fibre reinforced composites. *Computational materials science*, 38(2):316–324, 2006.

[61] AR Melro, PP Camanho, FM Pires, and ST Pinho. Micromechanical analysis of polymer composites reinforced by unidirectional fibres: Part ii–micromechanical analyses. *International Journal of Solids and Structures*, 50(11-12):1906–1915, 2013.

[62] TJ Vaughan and CT McCarthy. Micromechanical modelling of the transverse damage behaviour in fibre reinforced composites. *Composites Science and Technology*, 71(3):388–396, 2011.

[63] L Wu, D Tjahjanto, G Becker, A Makradi, A Jérusalem, and L Noels. A micro–meso-model of intra-laminar fracture in fiber-reinforced composites based on a discontinuous galerkin/cohesive zone method. *Engineering Fracture Mechanics*, 104:162–183, 2013.

[64] T Hobbiebrunken, M Hojo, KK Jin, and SK Ha. Influence of non-uniform fiber arrangement on microscopic stress and failure initiation in thermally and transversely loaded cf/epoxy laminated composites. *Composites Science and Technology*, 68(15-16):3107–3113, 2008.

[65] M Hojo, M Mizuno, T Hobbiebrunken, T Adachi, M Tanaka, and SK Ha. Effect of fiber array irregularities on microscopic interfacial normal stress states of transversely loaded ud-cfrp from viewpoint of failure initiation. *Composites Science and Technology*, 69(11-12):1726–1734, 2009.

[66] AR Melro, PP Camanho, and ST Pinho. Influence of geometrical parameters on the elastic response of unidirectional composite materials. *Composite Structures*, 94(11):3223–3231, 2012.

[67] T Kanit, S Forest, Ia Galliet, Va Mounoury, and D Jeulin. Determination of the size of the representative volume element for random composites: statistical and numerical approach. *International Journal of solids and structures*, 40(13-14):3647–3679, 2003.

[68] M Ostoja-Starzewski. Material spatial randomness: From statistical to representative volume element. *Probabilistic engineering mechanics*, 21(2):112–132, 2006.

[69] IM Gitman, H Askes, and LJ Sluys. Representative volume: existence and size determination. *Engineering fracture mechanics*, 74(16):2518–2534, 2007.

[70] D Trias, J Costa, A Turon, and JE Hurtado. Determination of the critical size of a statistical representative volume element (srve) for carbon reinforced polymers. *Acta materialia*, 54(13):3471–3484, 2006.

[71] K Terada, M Hori, T Kyoya, and N Kikuchi. Simulation of the multi-scale convergence in computational homogenization approaches. *International Journal of Solids and Structures*, 37(16):2285–2311, 2000.

[72] D Savvas, G Stefanou, and M Papadrakakis. Determination of rve size for random composites with local volume fraction variation. *Computer Methods in Applied Mechanics and Engineering*, 305:340–358, 2016.

[73] C Pelissou, J Baccou, Y Monerie, and F Perales. Determination of the size of the representative volume element for random quasi-brittle composites. *International Journal of Solids and Structures*, 46(14-15):2842–2855, 2009.

[74] A Vanaerschot, Brian N Cox, SV Lomov, and D Vandepitte. Stochastic multi-scale modelling of textile composites based on internal geometry variability. *Computers & Structures*, 122:55–64, 2013.

[75] A Vanaerschot, BN Cox, SV Lomov, and D Vandepitte. Experimentally validated stochastic geometry description for textile composite reinforcements. *Composites Science and Technology*, 122:122–129, 2016.

[76] NV De Carvalho, ST Pinho, and P Robinson. Reducing the domain in the mechanical analysis of periodic structures, with application to woven composites. *Composites Science and Technology*, 71(7):969–979, 2011.

[77] V Koissin, DS Ivanov, SV Lomov, and I Verpoest. Fibre distribution inside yarns of textile composite: geometrical and fe modelling. In *Proceedings of the 8th international conference on textile composites (TexComp-8), Nottingham*, 2006.

[78] M Mühlstädt, W Seifert, M Arras, S Maenz, KD Jandt, and J Bossert. 3d model of intra-yarn fiber volume fraction gradients of woven fabrics. *Composite Structures*, 180:944–954, 2017.

[79] S Sridharan. *Delamination behaviour of composites*. Elsevier, 2008.

[80] AP Mouritz and BN Cox. A mechanistic interpretation of the comparative in-plane mechanical properties of 3d woven, stitched and pinned composites. *Composites Part A: Applied Science and Manufacturing*, 41(6):709–728, 2010.

[81] JG Williams, TK Obrien, and AJ Chapman III. Comparison of toughened composite laminates using nasa standard damage tolerance tests. 1984.

[82] Y Tang, L Ye, Z Zhang, and K Friedrich. Interlaminar fracture toughness and cai strength of fibre-reinforced composites with nanoparticles–a review. *Composites Science and Technology*, 86:26–37, 2013.

[83] JR Reeder. Stitching vs. a toughened matrix: compression strength effects. *Journal of Composite Materials*, 29(18):2464–2487, 1995.

[84] DR Cartié, BN Cox, and NA Fleck. Mechanisms of crack bridging by composite and metallic rods. *Composites Part A: Applied Science and Manufacturing*, 35(11):1325–1336, 2004.

[85] BN Cox. Snubbing effects in the pullout of a fibrous rod from a laminate. *Mechanics of Advanced Materials and Structures*, 12(2):85–98, 2005.

[86] H Cui, Yulong Li, S Koussios, L Zu, and A Beukers. Bridging micromechanisms of z-pin in mixed mode delamination. *Composite Structures*, 93(11):2685–2695, 2011.

[87] K Dransfield, C Baillie, and YW Mai. Improving the delamination resistance of cfrp by stitching—a review. *Composites Science and Technology*, 50(3):305–317, 1994.

[88] D Shu and YW Mai. Delamination buckling with bridging. *Composites science and technology*, 47(1):25–33, 1993.

[89] H Heß and N Himmel. Structurally stitched ncf cfrp laminates. part 1: Experimental characterization of in-plane and out-of-plane properties. *Composites Science and Technology*, 71(5):549–568, 2011.

[90] SV Lomov, AE Bogdanovich, DS Ivanov, D Mungalov, M Karahan, and I Verpoest. A comparative study of tensile properties of non-crimp 3d orthogonal weave and multi-layer plain weave e-glass composites. part 1: Materials, methods and principal results. *Composites part a: applied science and manufacturing*, 40(8):1134–1143, 2009.

[91] LC Dickinson, GL Farley, and MK Hinders. Prediction of effective three-dimensional elastic constants of translaminar reinforced composites. *Journal of composite materials*, 33(11):1002–1029, 1999.

[92] M Grassi, X Zhang, and M Meo. Prediction of stiffness and stresses in z-fibre reinforced composite laminates. *Composites Part A: applied science and manufacturing*, 33(12):1653–1664, 2002.

[93] B Zhang, G Allegri, M Yasaee, and SR Hallett. Micro-mechanical finite element analysis of z-pins under mixed-mode loading. *Composites Part A: Applied Science and Manufacturing*, 78:424–435, 2015.

[94] SV Lomov, EB Belov, T Bischoff, SB Ghosh, TT Chi, and I Verpoest. Carbon composites based on multiaxial multiply stitched preforms. part 1. geometry of the preform. *Composites Part A: Applied science and manufacturing*, 33(9):1171–1183, 2002.

[95] H Heß, YC Roth, and N Himmel. Elastic constants estimation of stitched ncf cfrp laminates based on a finite element unit-cell model. *Composites Science and Technology*, 67(6):1081–1095, 2007.

[96] H Heß and N Himmel. Structurally stitched ncf cfrp laminates. part 2: Finite element unit cell based prediction of in-plane strength. *Composites Science and Technology*, 71(5):569–585, 2011.

[97] T Kurashiki, N Watanabe, M Matsushima, M Zako, SV Lomov, and I Verpoest. Effects of stitching parameters on damage development for non-crimp fabric composites under tensile loading. In *15th European Conference on Composite Materials (ECCM-15)*, 2012.

[98] T Kurashiki, K Hamada, S Honda, M Zako, SV Lomov, and I Verpoest. Mechanical behaviors of non-crimp fabric composites based on multi-scale analysis. In *17th Int. Conf. on Composite Materials, Edinburgh, UK*, 2009.

[99] V Koissin, J Kustermans, SV Lomov, I Verpoest, B Van Den Broucke, and V Witzel. Structurally stitched ncf preforms: quasi-static response. *Composites science and technology*, 69(15):2701–2710, 2009.

[100] N Isart, JA Mayugo, N Blanco, L Ripoll, A Solà, and M Soler. Geometric model for 3d through-thickness orthogonal interlock composites. *Composite Structures*, 119:787–798, 2015.

[101] X Zeng, LP Brown, A Endruweit, M Matveev, and AC Long. Geometrical modelling of 3d woven reinforcements for polymer composites: Prediction of fabric permeability and composite mechanical properties. *Composites Part A: Applied Science and Manufacturing*, 56:150–160, 2014.

[102] H Lin, X Zeng, M Sherburn, AC Long, and MJ Clifford. Automated geometric modelling of textile structures. *Textile Research Journal*, 82(16):1689–1702, 2012.

[103] SD Green, AC Long, BSF El Said, and SR Hallett. Numerical modelling of 3d woven preform deformations. *Composite Structures*, 108:747–756, 2014.

[104] D Durville. A finite element approach of the behaviour of woven materials at microscopic scale. In *Mechanics of microstructured solids*, pages 39–46. Springer, 2009.

[105] B Wintiba, B Sonon, KEM Kamel, and TJ Massart. An automated procedure for the generation and conformal discretization of 3d woven composites rves. *Composite Structures*, 180:955–971, 2017.

[106] AP Mouritz. Compression properties of z-pinned composite laminates. *Composites Science and Technology*, 67(15-16):3110–3120, 2007.

[107] Y Liu. *Multi-scale damage modelling of 3D textile reinforced composites including microstructural variability generation and meso-scale reconstruction*. PhD thesis, Lille 1, 2017.

[108] CS Lopes, O Seresta, Y Coquet, Z Gürdal, PP Camanho, and B Thuis. Low-velocity impact damage on dispersed stacking sequence laminates. part i: Experiments. *Composites Science and Technology*, 69(7-8):926–936, 2009.

[109] CS Lopes, PP Camanho, Z Gürdal, P Maimí, and EV González. Low-velocity impact damage on dispersed stacking sequence laminates. part ii: Numerical simulations. *Composites Science and Technology*, 69(7-8):937–947, 2009.

[110] H Ghiasi, K Fayazbakhsh, D Pasini, and L Lessard. Optimum stacking sequence design of composite materials part ii: Variable stiffness design. *Composite Structures*, 93(1):1–13, 2010.

[111] SV Lomov, I Verpoest, T Peeters, D Roose, and M Zako. Nesting in textile laminates: geometrical modelling of the laminate. *Composites Science and Technology*, 63(7):993–1007, 2003.

[112] C Ayranci and J Carey. 2d braided composites: a review for stiffness critical applications. *Composite Structures*, 85(1):43–58, 2008.

[113] K Bilisik. Three-dimensional braiding for composites: a review. *Textile Research Journal*, 83(13):1414–1436, 2013.

[114] A Arteiro, G Catalanotti, J Xavier, and PP Camanho. Large damage capability of non-crimp fabric thin-ply laminates. *Composites Part A: Applied Science and Manufacturing*, 63:110–122, 2014.

[115] A Ramasamy, Y Wang, and J Muzzy. Characterization of flexible towpregs for textile processing. *ICCM/9. Composites Design:*, 4:518–525, 1993.

[116] RJ Palmer. Manufacture of dry fibre preforms and multiaxial stitch bonded fabrics. In *Proceedings of the 22nd International SAMPE Europe Conference, GR Griffith and RFJ McCarthy, Editors*, pages 281–292, 2001.

[117] KA Dransfield, LK Jain, and YW Mai. On the effects of stitching in cfrps—i. mode i delamination toughness. *Composites Science and Technology*, 58(6):815–827, 1998.

[118] LK Jain, KA Dransfield, and YW Mai. On the effects of stitching in cfrps—ii. mode ii delamination toughness. *Composites Science and Technology*, 58(6):829–837, 1998.

[119] F Edgren and LE Asp. Approximate analytical constitutive model for non-crimp fabric composites. *Composites Part A: Applied Science and Manufacturing*, 36(2):173–181, 2005.

[120] R Kamiya, BA Cheeseman, P Popper, and TW Chou. Some recent advances in the fabrication and design of three-dimensional textile preforms: a review. *Composites science and technology*, 60(1):33–47, 2000.

[121] IK Partridge and DR Cartié. Delamination resistant laminates by z-fiber® pinning: Part i manufacture and fracture performance. *Composites Part A: applied science and manufacturing*, 36(1):55–64, 2005.

[122] M Bannister, I Herszberg, A Nicolaidis, F Coman, and KH Leong. The manufacture of glass/epoxy composites with multilayer woven architectures. *Composites Part A: Applied Science and Manufacturing*, 29(3):293–300, 1998.

[123] KL Rugg, BN Cox, and R Massabo. Mixed mode delamination of polymer composite laminates reinforced through the thickness by z-fibers. *Composites Part A: applied science and manufacturing*, 33(2):177–190, 2002.

[124] B M'membe, S Gannon, M Yasaee, SR Hallett, and IK Partridge. Mode ii delamination resistance of composites reinforced with inclined z-pins. *Materials & Design*, 94:565–572, 2016.

[125] H Dexter and J Funk. Impact resistance and interlaminar fracture toughness of through-the-thickness reinforced graphite/epoxy. In *27th Structures, Structural Dynamics and Materials Conference*, page 1020, 1986.

[126] DT Fishpool, A Rezai, D Baker, SL Ogin, and PA Smith. Interlaminar toughness characterisation of 3d woven carbon fibre composites. *Plastics, Rubber and Composites*, 42(3):108–114, 2013.

[127] R Gerlach, CR Siviour, J Wiegand, and N Petrinic. In-plane and through-thickness properties, failure modes, damage and delamination in 3d woven carbon fibre composites subjected to impact loading. *Composites Science and Technology*, 72(3):397–411, 2012.

[128] FT Peirce. 5—the geometry of cloth structure. *Journal of the Textile Institute Transactions*, 28(3):T45–T96, 1937.

[129] S Drapier and MR Wisnom. A finite-element investigation of the interlaminar shear behaviour of non-crimp-fabric-based composites. *Composites Science and Technology*, 59(16):2351–2362, 1999.

[130] M Sherburn. *Geometric and mechanical modelling of textiles*. PhD thesis, University of Nottingham, 2007.

[131] G Karami and M Garnich. Effective moduli and failure considerations for composites with periodic fiber waviness. *Composite Structures*, 67(4):461–475, 2005.

[132] Hivet and P Boisse. Consistent 3d geometrical model of fabric elementary cell. application to a meshing preprocessor for 3d finite element analysis. *Finite Elements in Analysis and Design*, 42(1):25–49, 2005.

[133] RD Sevenois, D Garoz, FA Gilabert, SWF Spronk, S Fonteyn, M Heyndrickx, L Pyl, D Van Hemelrijck, J Degrieck, and W Van Paepegem. Avoiding interpenetrations and the importance of nesting in analytic geometry construction for representative unit cells of woven composite laminates. *Composites Science and Technology*, 136:119–132, 2016.

[134] FJ Guild and J Summerscales. Microstructural image analysis applied to fibre composite materials: a review. *Composites*, 24(5):383–393, 1993.

[135] NR Pal and SK Pal. A review on image segmentation techniques. *Pattern recognition*, 26(9):1277–1294, 1993.

[136] H Zhang, JE Fritts, and SA Goldman. Image segmentation evaluation: A survey of unsupervised methods. *computer vision and image understanding*, 110(2):260–280, 2008.

[137] N Otsu. A threshold selection method from gray-level histograms. *IEEE transactions on systems, man, and cybernetics*, 9(1):62–66, 1979.

[138] M Sezgin and B Sankur. Survey over image thresholding techniques and quantitative performance evaluation. *Journal of Electronic imaging*, 13(1):146–166, 2004.

[139] J Kittler and J Illingworth. Minimum error thresholding. *Pattern recognition*, 19(1):41–47, 1986.

[140] RE Guldberg, SJ Hollister, and GT Charras. The accuracy of digital image-based finite element models. *Journal of biomechanical engineering*, 120(2):289–295, 1998.

[141] A Doitrand, C Fagiano, F-X Irisarri, and M Hirsekorn. Comparison between voxel and consistent meso-scale models of woven composites. *Composites Part A: Applied Science and Manufacturing*, 73:143–154, 2015.

[142] C Osmiani, G Mohamed, JWG Treiber, G Allegri, and IK Partridge. Exploring the influence of micro-structure on the mechanical properties and crack bridging mechanisms of fibrous tufts. *Composites Part A: Applied Science and Manufacturing*, 91:409–419, 2016.

[143] I Straumit, C Hahn, E Winterstein, B Plank, SV Lomov, and M Wevers. Computation of permeability of a non-crimp carbon textile reinforcement based on x-ray computed tomography images. *Composites Part A: Applied Science and Manufacturing*, 81:289–295, 2016.

[144] J Martin-Herrero and C Germain. Microstructure reconstruction of fibrous c/c composites from x-ray microtomography. *Carbon*, 45(6):1242–1253, 2007.

[145] RM Sencu, Z Yang, YC Wang, PJ Withers, C Rau, A Parson, and C Soutis. Generation of micro-scale finite element models from synchrotron x-ray ct images for multidirectional carbon fibre reinforced composites. *Composites Part A: Applied Science and Manufacturing*, 91:85–95, 2016.

[146] G Fang, C Chen, S Yuan, S Meng, and J Liang. Micro-tomography based geometry modeling of three-dimensional braided composites. *Applied Composite Materials*, pages 1–15, 2017.

[147] P Badel, E Vidal-Sallé, E Maire, and P Boisse. Simulation and tomography analysis of textile composite reinforcement deformation at the mesoscopic scale. *Composites Science and Technology*, 68(12):2433–2440, 2008.

[148] F Gommer, KCA Wedgwood, and LP Brown. Stochastic reconstruction of filament paths in fibre bundles based on two-dimensional input data. *Composites Part A: Applied Science and Manufacturing*, 76:262–271, 2015.

[149] SR Roscoat, M Decain, X Thibault, C Geindreau, and JF Bloch. Estimation of microstructural properties from synchrotron x-ray microtomography and determination of the rev in paper materials. *Acta Materialia*, 55(8):2841–2850, 2007.

[150] H Bale, M Blacklock, MR Begley, DB Marshall, BN Cox, and RO Ritchie. Characterizing three-dimensional textile ceramic composites using synchrotron x-ray micro-computed-tomography. *Journal of the American Ceramic Society*, 95(1):392–402, 2012.

[151] Y Zhang, M Brady, and S Smith. Segmentation of brain mr images through a hidden markov random field model and the expectation-maximization algorithm. *IEEE transactions on medical imaging*, 20(1):45–57, 2001.

[152] D Wildenschild and AP Sheppard. X-ray imaging and analysis techniques for quantifying pore-scale structure and processes in subsurface porous medium systems. *Advances in Water Resources*, 51:217–246, 2013.

[153] Y Huang, Z Yang, W Ren, G Liu, and C Zhang. 3d meso-scale fracture modelling and validation of concrete based on in-situ x-ray computed tomography images using damage plasticity model. *International Journal of Solids and Structures*, 67:340–352, 2015.

[154] EN Landis and DT Keane. X-ray microtomography. *Materials characterization*, 61(12):1305–1316, 2010.

[155] E Maire and PJ Withers. Quantitative x-ray tomography. *International materials reviews*, 59(1):1–43, 2014.

[156] MW Czabaj, ML Riccio, and WW Whitacre. Numerical reconstruction of graphite/epoxy composite microstructure based on sub-micron resolution x-ray computed tomography. *Composites Science and Technology*, 105:174–182, 2014.

[157] JW Hearle and WJ Shanahan. 11—an energy method for calculations in fabric mechanics part i: Principles of the method. *Journal of the Textile Institute*, 69(4):81–91, 1978.

[158] SV Lomov, G Huysmans, Yiwen Luo, RS Parnas, Andreas Prodromou, I Verpoest, and FR Phelan. Textile composites: modelling strategies. *Composites Part A: applied science and manufacturing*, 32(10):1379–1394, 2001.

[159] TV Sagar, P Potluri, JW Hearle, et al. Mesoscale modelling of interlaced fibre assemblies using energy method. *Computational Materials Science*, 28(1):49–62, 2003.

[160] P Potluri and TV Sagar. Compaction modelling of textile preforms for composite structures. *Composite structures*, 86(1-3):177–185, 2008.

[161] A Doitrand, C Fagiano, V Chiaruttini, FH Leroy, A Mavel, and M Hirsekorn. Experimental characterization and numerical modeling of damage at the mesoscopic scale of woven polymer matrix composites under quasi-static tensile loading. *Composites Science and Technology*, 119:1–11, 2015.

[162] A Doitrand, C Fagiano, FH Leroy, A Mavel, and M Hirsekorn. On the influence of fabric layer shifts on the strain distributions in a multi-layer woven composite. *Composite Structures*, 145:15–25, 2016.

[163] F Stig and S Hallström. A modelling framework for composites containing 3d reinforcement. *Composite Structures*, 94(9):2895–2901, 2012.

[164] F Stig and S Hallström. Spatial modelling of 3d-woven textiles. *Composite structures*, 94(5):1495–1502, 2012.

[165] B El Said, S Green, and SR Hallett. Kinematic modelling of 3d woven fabric deformation for structural scale features. *Composites Part A: Applied Science and Manufacturing*, 57:95–107, 2014.

[166] SD Green, MY Matveev, AC Long, D Ivanov, and SR Hallett. Mechanical modelling of 3d woven composites considering realistic unit cell geometry. *Composite Structures*, 118:284–293, 2014.

[167] L Huang, Y Wang, Y Miao, D Swenson, Y Ma, and CF Yen. Dynamic relaxation approach with periodic boundary conditions in determining the 3-d woven textile micro-geometry. *Composite Structures*, 106:417–425, 2013.

[168] Y Wang and X Sun. Digital-element simulation of textile processes. *Composites science and technology*, 61(2):311–319, 2001.

[169] G Zhou, X Sun, and Y Wang. Multi-chain digital element analysis in textile mechanics. *Composites science and Technology*, 64(2):239–244, 2004.

[170] Y Miao, E Zhou, Y Wang, and BA Cheeseman. Mechanics of textile composites: Micro-geometry. *Composites Science and Technology*, 68(7-8):1671–1678, 2008.

[171] D Durville. Simulation of the mechanical behaviour of woven fabrics at the scale of fibers. *International journal of material forming*, 3(2):1241–1251, 2010.

[172] Y Mahadik and SR Hallett. Finite element modelling of tow geometry in 3d woven fabrics. *Composites Part A: Applied Science and Manufacturing*, 41(9):1192–1200, 2010.

[173] L Daelemans, J Faes, S Allaoui, G Hivet, M Dierick, L Van Hoorebeke, and W Van Paepegem. Finite element simulation of the woven geometry and mechanical behaviour of a 3d woven dry fabric under tensile and shear loading using the digital element method. *Composites Science and Technology*, 137:177–187, 2016.

[174] Y Wang, Y Miao, L Huang, D Swenson, CF Yen, J Yu, and JQ Zheng. Effect of the inter-fiber friction on fiber damage propagation and ballistic limit of 2-d woven fabrics under a fully confined boundary condition. *International Journal of Impact Engineering*, 97:66–78, 2016.

[175] S Joglekar and M Pankow. Modeling of 3d woven composites using the digital element approach for accurate prediction of kinking under compressive loads. *Composite Structures*, 160:547–559, 2017.

[176] AJ Thompson, B El Said, D Ivanov, JPH Belnoue, and SR Hallett. High fidelity modelling of the compression behaviour of 2d woven fabrics. *International Journal of Solids and Structures*, 2017.

[177] Z Yousaf, P Potluri, PJ Withers, D Mollenhauer, E Zhou, and S Duning. Digital element simulation of aligned tows during compaction validated by computed tomography (ct). *International Journal of Solids and Structures*, 2017.

[178] TD Vu, D Durville, and P Davies. Finite element simulation of the mechanical behavior of synthetic braided ropes and validation on a tensile test. *International Journal of Solids and Structures*, 58:106–116, 2015.

[179] B Sonon and TJ Massart. A level-set based representative volume element generator and xfem simulations for textile and 3d-reinforced composites. *Materials*, 6(12):5568–5592, 2013.

[180] ER Schwarz. Certain aspects of yarn structure. *Textile Research Journal*, 21(3):125–136, 1951.

[181] D Mattsson, R Joffe, and J Varna. Methodology for characterization of internal structure parameters governing performance in ncf composites. *Composites Part B: Engineering*, 38(1):44–57, 2007.

[182] Y Mahadik, KA Robson Brown, and SR Hallett. Characterisation of 3d woven composite internal architecture and effect of compaction. *Composites Part A: Applied Science and Manufacturing*, 41(7):872–880, 2010.

[183] L Li, Y Zhao, J Yang, J Zhang, and Y Duan. An experimental investigation of compaction behavior of carbon non-crimp fabrics for liquid composite molding. *Journal of materials science*, 50(7):2960–2972, 2015.

[184] B Chen, EJ Lang, and TW Chou. Experimental and theoretical studies of fabric compaction behavior in resin transfer molding1. *Materials Science and Engineering: A*, 317(1-2):188–196, 2001.

[185] N Vernet and F Trochu. Analysis and modeling of 3d interlock fabric compaction behavior. *Composites Part A: Applied Science and Manufacturing*, 80:182–193, 2016.

[186] CC Chamis. Mechanics of composite materials: past, present, and future. *Journal of Composites, Technology and Research*, 11(1):3–14, 1989.

[187] BW Rosen. Tensile failure of fibrous composites. *AIAA journal*, 2(11):1985–1991, 1964.

[188] T Hirai and H Yoshida. The effect of moulding on the mechanical properties of frp. *J Soc Mater Sci Jpn*, 23:254, 1974.

[189] M Grassi and X Zhang. Finite element analyses of mode i interlaminar delamination in z-fibre reinforced composite laminates. *Composites science and technology*, 63(12):1815–1832, 2003.

[190] Y Liu, I Straumit, D Vasiukov, SV Lomov, and S Panier. Prediction of linear and non-linear behavior of 3d woven composite using mesoscopic voxel models reconstructed from x-ray micro-tomography. *Composite Structures*, 179:568–579, 2017.

[191] JC Faes, A Rezaei, W Van Paepegem, and J Degrieck. Accuracy of 2d fe models for prediction of crack initiation in nested textile composites with inhomogeneous intra-yarn fiber volume fractions. *Composite Structures*, 140:11–20, 2016.

[192] RS Fertig, EM Jensen, and KA Malusare. Effect of fiber volume fraction variation across multiple length scales on composite stress variation: the possibility of stochastic multiscale analysis. *American Institute of Aeronautics and Astronautics*, pages 2–8, 2014.

[193] VV Silberschmidt. Effect of micro-randomness on macroscopic properties and fracture of laminates. *Journal of materials science*, 41(20):6768–6776, 2006.

[194] Piggott MR. Load bearing fiber composites, oxford: Pergamon press, 1980. p. 74.

[195] F Stig and S Hallström. Influence of crimp on 3d-woven fibre reinforced composites. *Composite structures*, 95:114–122, 2013.

[196] S Dai, PR Cunningham, S Marshall, and C Silva. Influence of fibre architecture on the tensile, compressive and flexural behaviour of 3d woven composites. *Composites Part A: Applied Science and Manufacturing*, 69:195–207, 2015.

[197] B Budiansky and NA Fleck. Compressive failure of fibre composites. *Journal of the Mechanics and Physics of Solids*, 41(1):183–211, 1993.

[198] MR Wisnom. Analysis of shear instability in compression due to fibre waviness. *Journal of reinforced plastics and composites*, 12(11):1171–1189, 1993.

[199] NA Fleck and JY Shu. Microbuckle initiation in fibre composites: a finite element study. *Journal of the Mechanics and Physics of Solids*, 43(12):1887–1918, 1995.

[200] SL Lemanski and MP Sutcliffe. Compressive failure of finite size unidirectional composite laminates with a region of fibre waviness. *Composites Part A: Applied Science and Manufacturing*, 43(3):435–444, 2012.

[201] MP Sutcliffe. Modelling the effect of size on compressive strength of fibre composites with random waviness. *Composites Science and Technology*, 88:142–150, 2013.

[202] L Zhang, S Zhang, Y Jiang, J Tao, and X Chen. Compressive behaviour of fibre reinforced plastic with random fibre packing and a region of fibre waviness. *Journal of Reinforced Plastics and Composites*, 36(5):323–337, 2017.

[203] HJ Chun, JY Shin, and IM Daniel. Effects of material and geometric nonlinearities on the tensile and compressive behavior of composite materials with fiber waviness. *Composites Science and Technology*, 61(1):125–134, 2001.

[204] JD Whitcomb. Three-dimensional stress analysis of plain weave composites. In *Composite Materials: Fatigue and Fracture (Third Volume)*. ASTM International, 1991.

[205] F Gao, L Boniface, SL Ogin, PA Smith, and RP Greaves. Damage accumulation in woven-fabric cfrp laminates under tensile loading: Part 1. observations of damage accumulation. *Composites science and technology*, 59(1):123–136, 1999.

[206] NV De Carvalho, ST Pinho, and P Robinson. An experimental study of failure initiation and propagation in 2d woven composites under compression. *Composites Science and Technology*, 71(10):1316–1325, 2011.

[207] X Tang and JD Whitcomb. Progressive failure behaviors of 2d woven composites. *Journal of composite materials*, 37(14):1239–1259, 2003.

[208] S Daggumati, I De Baere, W Van Paepegem, J Degrieck, J Xu, SV Lomov, and I Verpoest. Local damage in a 5-harness satin weave composite under static tension: Part i–experimental analysis. *Composites Science and Technology*, 70(13):1926–1933, 2010.

[209] MS Dadkhah, BN Cox, and WL Morris. Compression-compression fatigue of 3d woven composites. *Acta Metallurgica et Materialia*, 43(12):4235–4245, 1995.

[210] EM Jensen, DA Leonhardt, and RS Fertig. Effects of thickness and fiber volume fraction variations on strain field inhomogeneity. *Composites Part A: Applied Science and Manufacturing*, 69:178–185, 2015.

[211] S Zhang, L Zhang, Y Wang, J Tao, and X Chen. Effect of ply level thickness uncertainty on reliability of laminated composite panels. *Journal of Reinforced Plastics and Composites*, 35(19):1387–1400, 2016.

[212] D Mattsson, R Joffe, and J Varna. Damage in ncf composites under tension: effect of layer stacking sequence. *Engineering Fracture Mechanics*, 75(9):2666–2682, 2008.

[213] BD Davidson, R Krüger, and M König. Effect of stacking sequence on energy release rate distributions in multidirectional dcb and enf specimens. *Engineering Fracture Mechanics*, 55(4):557–569, 1996.

[214] J Andersons and M König. Dependence of fracture toughness of composite laminates on interface ply orientations and delamination growth direction. *Composites Science and Technology*, 64(13-14):2139–2152, 2004.

[215] TA Sebaey, N Blanco, J Costa, and CS Lopes. Characterization of crack propagation in mode i delamination of multidirectional cfrp laminates. *Composites Science and Technology*, 72(11):1251–1256, 2012.

[216] J Lee and C Soutis. A study on the compressive strength of thick carbon fibre–epoxy laminates. *Composites science and technology*, 67(10):2015–2026, 2007.

[217] DS Ivanov, SV Lomov, SG Ivanov, and I Verpoest. Stress distribution in outer and inner plies of textile laminates and novel boundary conditions for unit cell analysis. *Composites Part A: Applied Science and Manufacturing*, 41(4):571–580, 2010.

[218] BC Owens, JD Whitcomb, and J Varghese. Effect of finite thickness and free edges on stresses in plain weave composites. *Journal of composite materials*, 44(6):675–692, 2010.

[219] BH Le Page, FJ Guild, SL Ogin, and PA Smith. Finite element simulation of woven fabric composites. *Composites Part A: Applied Science and Manufacturing*, 35(7-8):861–872, 2004.

[220] M Olave, A Vanaerschot, SV Lomov, and D Vandepitte. Internal geometry variability of two woven composites and related variability of the stiffness. *Polymer Composites*, 33(8):1335–1350, 2012.

[221] J Pazmino, V Carvelli, and SV Lomov. Micro-ct analysis of the internal deformed geometry of a non-crimp 3d orthogonal weave e-glass composite reinforcement. *Composites Part B: Engineering*, 65:147–157, 2014.

[222] RS Bay and CL Tucker. Stereological measurement and error estimates for three-dimensional fiber orientation. *Polymer Engineering & Science*, 32(4):240–253, 1992.

[223] MT Cann, DO Adams, and CL Schneider. Characterization of fiber volume fraction gradients in composite laminates. *Journal of composite materials*, 42(5):447–466, 2008.

[224] F Gommer, LP Brown, and R Brooks. Quantification of mesoscale variability and geometrical reconstruction of a textile. *Journal of Composite Materials*, 50(23):3255–3266, 2016.

[225] MC Waterbury and LT Drzal. Determination of fiber volume fractions by optical numeric volume fraction analysis. *Journal of reinforced plastics and composites*, 8(6):627–636, 1989.

[226] DA Coker and S Torquato. Extraction of morphological quantities from a digitized medium. *Journal of Applied Physics*, 77(12):6087–6099, 1995.

[227] MP Sutcliffe, SL Lemanski, and AE Scott. Measurement of fibre waviness in industrial composite components. *Composites Science and Technology*, 72(16):2016–2023, 2012.

[228] CA Steeves and NA Fleck. In-plane properties of composite laminates with through-thickness pin reinforcement. *International Journal of Solids and Structures*, 43(10):3197–3212, 2006.

[229] K Mizukami, Y Mizutani, K Kimura, A Sato, A Todoroki, Y Suzuki, and Y Nakamura. Visualization and size estimation of fiber waviness in multidirectional cfrp laminates using eddy current imaging. *Composites Part A: Applied Science and Manufacturing*, 90:261–270, 2016.

[230] DC Charmpis, GI Schuëller, and MF Pellissetti. The need for linking micromechanics of materials with stochastic finite elements: a challenge for materials science. *Computational Materials Science*, 41(1):27–37, 2007.

[231] DJ Lekou and TP Philippidis. Mechanical property variability in frp laminates and its effect on failure prediction. *Composites Part B: Engineering*, 39(7-8):1247–1256, 2008.

[232] G Stefanou. The stochastic finite element method: past, present and future. *Computer Methods in Applied Mechanics and Engineering*, 198(9-12):1031–1051, 2009.

[233] M Chiachio, J Chiachio, and G Rus. Reliability in composites–a selective review and survey of current development. *Composites Part B: Engineering*, 43(3):902–913, 2012.

[234] NZ Chen, HH Sun, and CG Soares. Reliability analysis of a ship hull in composite material. *Composite structures*, 62(1):59–66, 2003.

[235] K Ho-Le. Finite element mesh generation methods: a review and classification. *Computer-aided design*, 20(1):27–38, 1988.

[236] MS Shephard and Marcel K Georges. Automatic three-dimensional mesh generation by the finite octree technique. *International Journal for Numerical methods in engineering*, 32(4):709–749, 1991.

[237] SJ Owen. A survey of unstructured mesh generation technology. In *IMR*, pages 239–267, 1998.

[238] R Radovitzky and M Ortiz. Tetrahedral mesh generation based on node insertion in crystal lattice arrangements and advancing-front-delaunay triangulation. *Computer Methods in Applied Mechanics and Engineering*, 187(3-4):543–569, 2000.

[239] JC Caendish, DA Field, and WH Frey. An apporach to automatic three-dimensional finite element mesh generation. *International journal for numerical methods in engineering*, 21(2):329–347, 1985.

[240] PL Baehmann, SL Wittchen, MS Shephard, KR Grice, and MA Yerry. Robust, geometrically based, automatic two-dimensional mesh generation. *International Journal for Numerical Methods in Engineering*, 24(6):1043–1078, 1987.

[241] LP Chew. Constrained delaunay triangulations. *Algorithmica*, 4(1-4):97–108, 1989.

[242] P Möller and P Hansbo. On advancing front mesh generation in three dimensions. *International Journal for Numerical Methods in Engineering*, 38(21):3551–3569, 1995.

[243] F Fritzen, T Böhlke, and E Schnack. Periodic three-dimensional mesh generation for crystalline aggregates based on voronoi tessellations. *Computational Mechanics*, 43(5):701–713, 2009.

[244] F Fritzen and T Böhlke. Periodic three-dimensional mesh generation for particle reinforced composites with application to metal matrix composites. *International Journal of Solids and Structures*, 48(5):706–718, 2011.

[245] T Blacker. Automated conformal hexahedral meshing constraints, challenges and opportunities. *Engineering with Computers*, 17(3):201–210, 2001.

[246] S Hörrmann, A Adumitroaie, C Viechtbauer, and M Schagerl. The effect of fiber waviness on the fatigue life of cfrp materials. *International Journal of Fatigue*, 90:139–147, 2016.

[247] HJ Kim and CC Swan. Voxel-based meshing and unit-cell analysis of textile composites. *International Journal for Numerical Methods in Engineering*, 56(7):977–1006, 2003.

[248] E Potter, ST Pinho, P Robinson, L Iannucci, and AJ McMillan. Mesh generation and geometrical modelling of 3d woven composites with variable tow cross-sections. *Computational Materials Science*, 51(1):103–111, 2012.

[249] J Ruppert and R Seidel. On the difficulty of triangulating three-dimensional non-convex polyhedra. *Discrete & Computational Geometry*, 7(3):227–253, 1992.

[250] JR Shewchuk. Triangle: Engineering a 2d quality mesh generator and delaunay triangulator. In *Applied computational geometry towards geometric engineering*, pages 203–222. Springer, 1996.

[251] JR Shewchuk. Constrained delaunay tetrahedralizations and provably good boundary recovery. In *IMR*, pages 193–204. Citeseer, 2002.

[252] H Si. Constrained delaunay tetrahedral mesh generation and refinement. *Finite elements in Analysis and Design*, 46(1-2):33–46, 2010.

[253] H Si. Tetgen, a delaunay-based quality tetrahedral mesh generator. *ACM Transactions on Mathematical Software (TOMS)*, 41(2):11, 2015.

[254] C Jamin, P Alliez, M Yvinec, and JD Boissonnat. Cgalmesh: a generic framework for delaunay mesh generation. *ACM Transactions on Mathematical Software (TOMS)*, 41(4):23, 2015.

[255] H Ghadyani, J Sullivan, and Z Wu. Boundary recovery for delaunay tetrahedral meshes using local topological transformations. *Finite Elements in Analysis and Design*, 46(1-2):74–83, 2010.

[256] JH Bramble and M Zlámal. Triangular elements in the finite element method. *Mathematics of Computation*, 24(112):809–820, 1970.

[257] I Babuška and AK Aziz. On the angle condition in the finite element method. *SIAM Journal on Numerical Analysis*, 13(2):214–226, 1976.

[258] J Shewchuk. What is a good linear finite element? interpolation, conditioning, anisotropy, and quality measures (preprint). *University of California at Berkeley*, 73:137, 2002.

[259] S Jacques, I De Baere, and W Van Paepegem. Application of periodic boundary conditions on multiple part finite element meshes for the meso-scale homogenization of textile fabric composites. *Composites Science and Technology*, 92:41–54, 2014.

[260] G Grail, M Hirsekorn, A Wendling, G Hivet, and R Hambli. Consistent finite element mesh generation for meso-scale modeling of textile composites with preformed and compacted reinforcements. *Composites Part A: Applied Science and Manufacturing*, 55:143–151, 2013.

[261] BN Cox, WC Carter, and NA Fleck. A binary model of textile composites—i. formulation. *Acta metallurgica et materialia*, 42(10):3463–3479, 1994.

[262] M Blacklock, H Bale, M Begley, and B Cox. Generating virtual textile composite specimens using statistical data from micro-computed tomography: 1d tow representations for the binary model. *Journal of the Mechanics and Physics of Solids*, 60(3):451–470, 2012.

[263] M Blacklock, MW Joosten, K Pingkarawat, and AP Mouritz. Prediction of mode i delamination resistance of z-pinned laminates using the embedded finite element technique. *Composites Part A: Applied Science and Manufacturing*, 91:283–291, 2016.

[264] O Vorobiov, SA Tabatabaei, and SV Lomov. Mesh superposition applied to meso-fe modelling of fibre-reinforced composites: Cross-comparison of implementations. *International Journal for Numerical Methods in Engineering*, 111(11):1003–1024, 2017.

[265] N Moës, M Cloirec, P Cartraud, and JF Remacle. A computational approach to handle complex microstructure geometries. *Computer methods in applied mechanics and engineering*, 192(28-30):3163–3177, 2003.

[266] M Kästner, G Haasemann, and V Ulbricht. Multiscale xfem-modelling and simulation of the inelastic material behaviour of textile-reinforced polymers. *International Journal for Numerical Methods in Engineering*, 86(4-5):477–498, 2011.

[267] A Wongsto and S Li. Micromechanical fe analysis of ud fibre-reinforced composites with fibres distributed at random over the transverse cross-section. *Composites Part A: Applied Science and Manufacturing*, 36(9):1246–1266, 2005.

[268] F Larsson, K Runesson, S Saroukhani, and R Vafadari. Computational homogenization based on a weak format of micro-periodicity for rve-problems. *Computer Methods in Applied Mechanics and Engineering*, 200(1-4):11–26, 2011.

[269] JJ Espadas-Escalante, NP van Dijk, and P Isaksson. A study on the influence of boundary conditions in computational homogenization of periodic structures with application to woven composites. *Composite Structures*, 160:529–537, 2017.

[270] VD Nguyen, E Béchet, C Geuzaine, and L Noels. Imposing periodic boundary condition on arbitrary meshes by polynomial interpolation. *Computational Materials Science*, 55:390–406, 2012.

[271] AI Akpoyomare, MI Okereke, and MS Bingley. Virtual testing of composites: Imposing periodic boundary conditions on general finite element meshes. *Composite Structures*, 160:983–994, 2017.

[272] BCN Mercatoris and TJ Massart. A coupled two-scale computational scheme for the failure of periodic quasi-brittle thin planar shells and its application to masonry. *International journal for numerical methods in engineering*, 85(9):1177–1206, 2011.

[273] EW Coenen, VG Kouznetsova, and MG Geers. Multi-scale continuous–discontinuous framework for computational-homogenization–localization. *Journal of the Mechanics and Physics of Solids*, 60(8):1486–1507, 2012.

[274] MG Geers, EW Coenen, and VG Kouznetsova. Multi-scale computational homogenization of structured thin sheets. *Modelling and Simulation in Materials Science and Engineering*, 15(4):S393, 2007.

[275] MG Geers, VG Kouznetsova, and WA Brekelmans. Multi-scale computational homogenization: Trends and challenges. *Journal of computational and applied mathematics*, 234(7):2175–2182, 2010.

[276] M Mistler, A Anthoine, and C Butenweg. In-plane and out-of-plane homogenisation of masonry. *Computers & Structures*, 85(17-18):1321–1330, 2007.

[277] C Geuzaine and JF Remacle. Gmsh: A 3-d finite element mesh generator with built-in pre-and post-processing facilities. *International journal for numerical methods in engineering*, 79(11):1309–1331, 2009.

[278] JA Bærentzen and H Aanæs. Generating signed distance fields from triangle meshes. *Informatics and Mathematical Modeling, Technical University of Denmark, DTU*, 20:23, 2002.

[279] MW Jones, JA Baerentzen, and M Sramek. 3d distance fields: A survey of techniques and applications. *IEEE Transactions on visualization and Computer Graphics*, 12(4):581–599, 2006.

[280] JA Bærentzen and H Aanaes. Signed distance computation using the angle weighted pseudonormal. *IEEE Transactions on Visualization and Computer Graphics*, 11(3):243–253, 2005.

[281] PJ Besl and RC Jain. Three-dimensional object recognition. *ACM Computing Surveys (CSUR)*, 17(1):75–145, 1985.

[282] M Hilaga, Y Shinagawa, T Kohmura, and TL Kunii. Topology matching for fully automatic similarity estimation of 3d shapes. In *Proceedings of the 28th annual conference on Computer graphics and interactive techniques*, pages 203–212. ACM, 2001.

[283] N Iyer, S Jayanti, K Lou, Y Kalyanaraman, and K Ramani. Three-dimensional shape searching: state-of-the-art review and future trends. *Computer-Aided Design*, 37(5):509–530, 2005.

[284] JD Boissonnat. Geometric structures for three-dimensional shape representation. *ACM Transactions on Graphics (TOG)*, 3(4):266–286, 1984.

[285] M Kazhdan and H Hoppe. Screened poisson surface reconstruction. *ACM Transactions on Graphics (ToG)*, 32(3):29, 2013.

[286] M Berger, A Tagliasacchi, L Seversky, P Alliez, J Levine, A Sharf, and C Silva. State of the art in surface reconstruction from point clouds. In *EUROGRAPHICS star reports*, volume 1, pages 161–185, 2014.

[287] H Hoppe, T DeRose, T Duchamp, J McDonald, and W Stuetzle. *Surface reconstruction from unorganized points*, volume 26. ACM, 1992.

[288] H Hoppe, T DeRose, T Duchamp, M Halstead, H Jin, J McDonald, J Schweitzer, and W Stuetzle. Piecewise smooth surface reconstruction. In *Proceedings of the 21st annual conference on Computer graphics and interactive techniques*, pages 295–302. ACM, 1994.

[289] FB Mittleman, HRC Silva, and G Taubin. The ball-pivoting algorithm for surface reconstruction. *IEEE Transactions on Visualization and Computer Graphics*, 5(4), 1999.

[290] MW Bern and AB Amenta. Method, apparatus and computer medium for surface reconstruction by voronoi filtering, May 7 2002. US Patent 6,384,826.

[291] B Curless and M Levoy. A volumetric method for building complex models from range images. In *Proceedings of the 23rd annual conference on Computer graphics and interactive techniques*, pages 303–312. ACM, 1996.

[292] M Kass, A Witkin, and D Terzopoulos. Snakes: Active contour models. *International journal of computer vision*, 1(4):321–331, 1988.

[293] TF Chan and LA Vese. Active contours without edges. *IEEE Transactions on image processing*, 10(2):266–277, 2001.

[294] W Welch and A Witkin. Free-form shape design using triangulated surfaces. In *Proceedings of the 21st annual conference on Computer graphics and interactive techniques*, pages 247–256. ACM, 1994.

[295] SJ Ahn, W Rauh, and HJ Warnecke. Least-squares orthogonal distances fitting of circle, sphere, ellipse, hyperbola, and parabola. *Pattern Recognition*, 34(12):2283–2303, 2001.

[296] RM Bolle and BC Vemuri. On three-dimensional surface reconstruction methods. *IEEE Transactions on Pattern Analysis & Machine Intelligence*, (1):1–13, 1991.

[297] P Mullen, F De Goes, M Desbrun, D Cohen-Steiner, and P Alliez. Signing the unsigned: Robust surface reconstruction from raw pointsets. In *Computer Graphics Forum*, volume 29, pages 1733–1741. Wiley Online Library, 2010.

[298] KQ Brown. Voronoi diagrams from convex hulls. *Information Processing Letters*, 9(5):223–228, 1979.

[299] DT Lee and BJ Schachter. Two algorithms for constructing a delaunay triangulation. *International Journal of Computer & Information Sciences*, 9(3):219–242, 1980.

[300] CB Barber, DP Dobkin, and H Huhdanpaa. The quickhull algorithm for convex hulls. *ACM Transactions on Mathematical Software (TOMS)*, 22(4):469–483, 1996.

[301] F Bernardini, J Mittleman, H Rushmeier, C Silva, and G Taubin. The ball-pivoting algorithm for surface reconstruction. *IEEE transactions on visualization and computer graphics*, 5(4):349–359, 1999.

[302] TK Dey and S Goswami. Provable surface reconstruction from noisy samples. *Computational Geometry*, 35(1-2):124–141, 2006.

[303] H Edelsbrunner and EP Mücke. Three-dimensional alpha shapes. *ACM Transactions on Graphics (TOG)*, 13(1):43–72, 1994.

[304] N Amenta and M Bern. Surface reconstruction by voronoi filtering. *Discrete & Computational Geometry*, 22(4):481–504, 1999.

[305] N Amenta, M Bern, and M Kamvysselis. A new voronoi-based surface reconstruction algorithm. In *Proceedings of the 25th annual conference on Computer graphics and interactive techniques*, pages 415–421. ACM, 1998.

[306] P Alliez, D Cohen-Steiner, Y Tong, and M Desbrun. Voronoi-based variational reconstruction of unoriented point sets. In *Symposium on Geometry processing*, volume 7, pages 39–48, 2007.

[307] H Fuchs, ZM Kedem, and SP Uselton. Optimal surface reconstruction from planar contours. *Communications of the ACM*, 20(10):693–702, 1977.

[308] A Drach, B Drach, and I Tsukrov. Processing of fiber architecture data for finite element modeling of 3d woven composites. *Advances in Engineering Software*, 72:18–27, 2014.

[309] J Xu, SV Lomov, I Verpoest, S Daggumati, W Van Paepegem, J Degrieck, and M Olave. A progressive damage model of textile composites on meso-scale using finite element method: static damage analysis. *Journal of Composite Materials*, 48(25):3091–3109, 2014.

[310] EJ Barbero, J Trovillion, JA Mayugo, and KK Sikkil. Finite element modeling of plain weave fabrics from photomicrograph measurements. *Composite Structures*, 73(1):41–52, 2006.

[311] H Lin, LP Brown, and AC Long. Modelling and simulating textile structures using texgen. In *Advanced Materials Research*, volume 331, pages 44–47. Trans Tech Publ, 2011.

[312] WE Lorensen and HE Cline. Marching cubes: A high resolution 3d surface construction algorithm. In *ACM siggraph computer graphics*, volume 21, pages 163–169. ACM, 1987.

[313] R Shekhar, E Fayyad, R Yagel, and JF Cornhill. Octree-based decimation of marching cubes surfaces. In *Proceedings of the 7th conference on Visualization'96*, pages 335–ff. IEEE Computer Society Press, 1996.

[314] PO Persson and G Strang. A simple mesh generator in matlab. *SIAM review*, 46(2):329–345, 2004.

[315] K Ehab Moustafa Kamel, B Sonon, and TJ Massart. An integrated approach for the generation and conformal discretization of complex inclusion-based microstructures. *Submitted for publication*.

[316] J Remacle, C Geuzaine, G Compère, and E Marchandise. High-quality surface remeshing using harmonic maps. *International Journal for Numerical Methods in Engineering*, 83(4):403–425, 2010.

[317] E Marchandise, CC de Wiart, WG Vos, C Geuzaine, and JF Remacle. High-quality surface remeshing using harmonic maps—part ii: Surfaces with high genus and of large aspect ratio. *International Journal for Numerical Methods in Engineering*, 86(11):1303–1321, 2011.

[318] S Kravchenko, O Kravchenko, M Wortmann, M Pietrek, P Horst, and RB Pipes. Composite toughness enhancement with interlaminar reinforcement. *Composites Part A: Applied Science and Manufacturing*, 54:98–106, 2013.

[319] M Yasaee, JK Lander, G Allegri, and SR Hallett. Experimental characterisation of mixed mode traction–displacement relationships for a single carbon composite z-pin. *Composites Science and Technology*, 94:123–131, 2014.

[320] DW Johnson, SA Garrett, JM Hook, and SG Moyers. Method of inserting z-axis reinforcing fibers into a composite laminate, November 11 2003. US Patent 6,645,333.

[321] AP Mouritz. Review of z-pinned composite laminates. *Composites Part A: applied science and manufacturing*, 38(12):2383–2397, 2007.

[322] AP Mouritz and P Chang. Tension fatigue of fibre-dominated and matrix-dominated laminates reinforced with z-pins. *International Journal of Fatigue*, 32(4):650–658, 2010.

[323] P Chang, AP Mouritz, and BN Cox. Properties and failure mechanisms of z-pinned laminates in monotonic and cyclic tension. *Composites Part A: Applied Science and Manufacturing*, 37(10):1501–1513, 2006.

[324] P Chang. *Mechanical properties and failure mechanisms of Z-pinned composites*. PhD thesis, RMIT University, 2006.

[325] CA Steeves and NA Fleck. In-plane properties of cfrp laminates containing throughthickness reinforcing rods (z-pins). *ICCM-12, Paris*, 1999.

[326] DS Ivanov, F Baudry, B Van Den Broucke, SV Lomov, H Xie, and I Verpoest. Failure analysis of triaxial braided composite. *Composites Science and Technology*, 69(9):1372–1380, 2009.

[327] AR Melro, PP Camanho, FM Andrade Pires, and ST Pinho. Numerical simulation of the non-linear deformation of 5-harness satin weaves. *Computational Materials Science*, 61:116–126, 2012.

[328] B Piezel, BCN Mercatoris, W Trabelsi, L Laiarinandrasana, A Thionnet, and TJ Massart. Bending effect on the risk for delamination at the reinforcement/matrix interface of 3d woven fabric composite using a shell-like rve. *Composite structures*, 94(8):2343–2357, 2012.

[329] DS Mikhaluk, TC Truong, AI Borovkov, SV Lomov, and I Verpoest. Experimental observations and finite element modelling of damage initiation and evolution in carbon/epoxy non-crimp fabric composites. *Engineering Fracture Mechanics*, 75(9):2751–2766, 2008.

[330] AS Kaddour, MJ Hinton, PA Smith, and S Li. Mechanical properties and details of composite laminates for the test cases used in the third world-wide failure exercise. *Journal of Composite Materials*, 47(20-21):2427–2442, 2013.

[331] Zvi Hashin. Failure criteria for unidirectional fiber composites. *Journal of applied mechanics*, 47(2):329–334, 1980.

[332] A Puck and H Schürmann. Failure analysis of frp laminates by means of physically based phenomenological models. In *Failure Criteria in Fibre-Reinforced-Polymer Composites*, pages 832–876. Elsevier, 2004.

[333] R Velmurugan and S Solaimurugan. Improvements in mode i interlaminar fracture toughness and in-plane mechanical properties of stitched glass/polyester composites. *Composites Science and Technology*, 67(1):61–69, 2007.

[334] KT Tan, N Watanabe, Y Iwahori, and T Ishikawa. Effect of stitch density and stitch thread thickness on compression after impact strength and response of stitched composites. *Composites Science and Technology*, 72(5):587–598, 2012.

[335] MDK Wood, X Sun, L Tong, A Katzos, AR Rispler, and YW Mai. The effect of stitch distribution on mode i delamination toughness of stitched laminated composites–experimental results and fea simulation. *Composites Science and Technology*, 67(6):1058–1072, 2007.

[336] E Wu and J Wang. Behavior of stitched laminates under in-plane tensile and transverse impact loading. *Journal of Composite Materials*, 29(17):2254–2279, 1995.

[337] AP Mouritz, KH Leong, and I Herszberg. A review of the effect of stitching on the in-plane mechanical properties of fibre-reinforced polymer composites. *Composites Part A: applied science and manufacturing*, 28(12):979–991, 1997.

[338] LE Asp, F Edgren, and A Sjögren. Effects of stitch pattern on the mechanical properties of non-crimp fabric composites. *Proceeding of the 11 ECCM*, pages 31–05, 2004.

[339] K Vallons, G Adolphs, P Lucas, SV Lomov, and I Verpoest. The influence of the stitching pattern on the internal geometry, quasi-static and fatigue mechanical properties of glass fibre non-crimp fabric composites. *Composites Part A: Applied Science and Manufacturing*, 56:272–279, 2014.

[340] F Edgren, C Soutis, and LE Asp. Damage tolerance analysis of ncf composite sandwich panels. *Composites Science and Technology*, 68(13):2635–2645, 2008.

[341] TC Truong, M Vettori, S Lomov, and I Verpoest. Carbon composites based on multi-axial multi-ply stitched preforms. part 4. mechanical properties of composites and damage observation. *Composites Part A: applied science and manufacturing*, 36(9):1207–1221, 2005.

[342] A Yudhanto, N Watanabe, Y Iwahori, and H Hoshi. Effect of stitch density on tensile properties and damage mechanisms of stitched carbon/epoxy composites. *Composites Part B: Engineering*, 46:151–165, 2013.

[343] Y Aono, K Hirota, SH Lee, T Kuroiwa, and K Takita. Fatigue damage of gfrp laminates consisting of stitched unit layers. *International Journal of Fatigue*, 30(10-11):1720–1728, 2008.

[344] AP Mouritz and BN Cox. A mechanistic approach to the properties of stitched laminates. *Composites part A: applied science and manufacturing*, 31(1):1–27, 2000.

[345] GL Farley and LC Dickinson. Removal of surface loop from stitched composites can improve compression and compression-after-impact strengths. *Journal of reinforced plastics and composites*, 11(6):633–642, 1992.

[346] Y Wei and J Zhang. Characterization of microstructure in stitched unidirectional composite laminates. *Composites Part A: Applied Science and Manufacturing*, 39(5):815–824, 2008.

[347] R Joffe, D Mattsson, J Modniks, and J Varna. Compressive failure analysis of non-crimp fabric composites with large out-of-plane misalignment of fiber bundles. *Composites Part A: applied science and manufacturing*, 36(8):1030–1046, 2005.

[348] S Drapier and MR Wisnom. Finite-element investigation of the compressive strength of non-crimp-fabric-based composites. *Composites Science and Technology*, 59(8):1287–1297, 1999.

[349] R Loendersloot, SV Lomov, R Akkerman, and I Verpoest. Carbon composites based on multiaxial multiply stitched preforms. part v: geometry of sheared biaxial fabrics. *Composites Part A: Applied Science and Manufacturing*, 37(1):103–113, 2006.

[350] GL Farley. A mechanism responsible for reducing compression strength of through-the-thickness reinforced composite material. *Journal of composite materials*, 26(12):1784–1795, 1992.

[351] M Nordlund and TS Lundstrom. Numerical study of the local permeability of noncrimp fabrics. *Journal of composite materials*, 39(10):929–947, 2005.

[352] A González, E Graciani, and F París. Prediction of in-plane stiffness properties of non-crimp fabric laminates by means of 3d finite element analysis. *Composites Science and Technology*, 68(1):121–131, 2008.

[353] LM Ferreira, E Graciani, and F París. Modelling the waviness of the fibres in non-crimp fabric composites using 3d finite element models with straight tows. *Composite Structures*, 107:79–87, 2014.

[354] LM Ferreira, E Graciani, and F París. Three dimensional finite element study of the behaviour and failure mechanism of non-crimp fabric composites under in-plane compression. *Composite Structures*, 149:106–113, 2016.

[355] J Netz, B Hannemann, and S Schmeer. Micro-leveled modeling of structural stitched frp joints as energy absorbing rupture points. *Composite Structures*, 157:131–140, 2016.

[356] G Pierreux, L Wu, D Van Hemelrijck, and TJ Massart. Evaluation of microdamage initiation in z-pinned laminates by means of automated rve computations. *Composite Structures*, 2018.

[357] B Sonon, B Francois, and TJ Massart. A unified level set based methodology for fast generation of complex microstructural multi-phase rves. *Computer methods in applied mechanics and engineering*, 223:103–122, 2012.

[358] L Ye. Role of matrix resin in delamination onset and growth in composite laminates. *Composites science and technology*, 33(4):257–277, 1988.

[359] A Turon, PP Camanho, J Costa, and CG Dávila. A damage model for the simulation of delamination in advanced composites under variable-mode loading. *Mechanics of Materials*, 38(11):1072–1089, 2006.

[360] VA Guénon, TW Chou, and JW Gillespie. Toughness properties of a three-dimensional carbon-epoxy composite. *Journal of materials science*, 24(11):4168–4175, 1989.

[361] Y Tanzawa, N Watanabe, and T Ishikawa. Interlaminar fracture toughness of 3-d orthogonal interlocked fabric composites. *Composites Science and Technology*, 59(8):1261–1270, 1999.

[362] Y Tanzawa, N Watanabe, and T Ishikawa. Fem simulation of a modified dcb test for 3-d orthogonal interlocked fabric composites. *Composites Science and Technology*, 61(8):1097–1107, 2001.

[363] DmS Ivanov, SV Lomov, AE Bogdanovich, M Karahan, and I Verpoest. A comparative study of tensile properties of non-crimp 3d orthogonal weave and multilayer plain weave e-glass composites. part 2: Comprehensive experimental results. *Composites part a: applied science and manufacturing*, 40(8):1144–1157, 2009.

[364] AE Bogdanovich. Advancements in manufacturing and applications of 3d woven preforms and composites. In *16th international conference on composite materials*, pages 1–10. Citeseer, 2006.

[365] KH Leong, B Lee, I Herszberg, and MK Bannister. The effect of binder path on the tensile properties and failure of multilayer woven cfrp composites. *Composites Science and Technology*, 60(1):149–156, 2000.

[366] PJ Callus, AP Mouritz, M Kt Bannister, and KH Leong. Tensile properties and failure mechanisms of 3d woven grp composites. *Composites Part A: Applied Science and Manufacturing*, 30(11):1277–1287, 1999.

[367] G Stegschuster, K Pingkarawat, B Wendland, and AP Mouritz. Experimental determination of the mode i delamination fracture and fatigue properties of thin 3d woven composites. *Composites Part A: Applied Science and Manufacturing*, 84:308–315, 2016.

[368] BN Cox, MS Dadkhah, and WL Morris. On the tensile failure of 3d woven composites. *Composites Part A: Applied Science and Manufacturing*, 27(6):447–458, 1996.

[369] WS Kuo and TH Ko. Compressive damage in 3-axis orthogonal fabric composites. *Composites Part A: Applied Science and Manufacturing*, 31(10):1091–1105, 2000.

[370] M Ansar, W Xinwei, and Z Chouwei. Modeling strategies of 3d woven composites: a review. *Composite structures*, 93(8):1947–1963, 2011.

[371] AR Labanieh, Y Liu, D Vasiukov, D Soulat, and Stéphane Panier. Influence of off-axis in-plane yarns on the mechanical properties of 3d composites. *Composites Part A: Applied Science and Manufacturing*, 98:45–57, 2017.

[372] N Naouar, E Vidal-Salle, J Schneider, E Maire, and P Boisse. 3d composite reinforcement meso fe analyses based on x-ray computed tomography. *Composite Structures*, 132:1094–1104, 2015.

[373] L Tong, AP Mouritz, and MK Bannister. *3D fibre reinforced polymer composites*. Elsevier, 2002.

[374] F Coman, L Herszberg, M Bannister, and S John. Design and analysis of 3d woven preforms for composite structures. *Science and Engineering of Composite Materials*, 5(2):83–96, 1996.

[375] L Lee, S Rudov-Clark, AP Mouritz, MK Bannister, and I Herszberg. Effect of weaving damage on the tensile properties of three-dimensional woven composites. *Composite Structures*, 57(1-4):405–413, 2002.

[376] SV Lomov, G Perie, DS Ivanov, I Verpoest, and D Marsal. Modeling three-dimensional fabrics and three-dimensional reinforced composites: challenges and solutions. *Textile Research Journal*, 81(1):28–41, 2011.

[377] G Pierreux, D Van Hemelrijck, and TJ Massart. Automated rve computations for evaluation of microdamage initiation in stitched non-crimp fabric composites. *Under review*.

[378] BN Cox, MS Dadkhah, WL Morris, and JG Flintoff. Failure mechanisms of 3d woven composites in tension, compression, and bending. *Acta metallurgica et materialia*, 42(12):3967–3984, 1994.

[379] PG Biragoni and SR Hallett. Finite element modelling of 3d woven composites for stiffness prediction. In *17th International Conference on Composite Materials (ICCM-17)*, 2009.

[380] XF Wang, XW Wang, GM Zhou, and CW Zhou. Multi-scale analyses of 3d woven composite based on periodicity boundary conditions. *Journal of Composite Materials*, 41(14):1773–1788, 2007.

[381] CS Lee, SW Chung, H Shin, and SJ Kim. Virtual material characterization of 3d orthogonal woven composite materials by large-scale computing. *Journal of composite materials*, 39(10):851–863, 2005.

[382] I Verpoest and SV Lomov. Virtual textile composites software wisetex: Integration with micro-mechanical, permeability and structural analysis. *Composites Science and Technology*, 65(15):2563–2574, 2005.

[383] F Gommer, A Endruweit, and Andrew C Long. Analysis of filament arrangements and generation of statistically equivalent composite micro-structures. *Composites Science and Technology*, 99:45–51, 2014.

[384] CM Van Wyk. 20—note on the compressibility of wool. *Journal of the Textile Institute Transactions*, 37(12):T285–T292, 1946.

[385] TG Gutowski and G Dillon. The elastic deformation of lubricated carbon fiber bundles: comparison of theory and experiments. *Journal of Composite Materials*, 26(16):2330–2347, 1992.

[386] G Requena, G Fiedler, B Seiser, P Degischer, M Di Michiel, and T Buslaps. 3d-quantification of the distribution of continuous fibres in unidirectionally reinforced composites. *Composites Part A: Applied Science and Manufacturing*, 40(2):152–163, 2009.

[387] SM Bleay, CB Loader, VJ Hawyes, L Humberstone, and PT Curtis. A smart repair system for polymer matrix composites. *Composites Part A: Applied Science and Manufacturing*, 32(12):1767–1776, 2001.

[388] AP Esser-Kahn, PR Thakre, H Dong, JF Patrick, VK Vlasko-Vlasov, NR Sottos, JS Moore, and SR White. Three-dimensional microvascular fiber-reinforced composites. *Advanced Materials*, 23(32):3654–3658, 2011.

[389] EB Murphy and F Wudl. The world of smart healable materials. *Progress in Polymer Science*, 35(1-2):223–251, 2010.

[390] KS Toohey, NR Sottos, JA Lewis, JS Moore, and SR White. Self-healing materials with microvascular networks. *Nature materials*, 6(8):581, 2007.

[391] G Williams, R Trask, and I Bond. A self-healing carbon fibre reinforced polymer for aerospace applications. *Composites Part A: Applied Science and Manufacturing*, 38(6):1525–1532, 2007.

[392] SW Case and GP Carman. Compression strength of composites containing embedded sensors or actuators. *Journal of intelligent material systems and structures*, 5(1):4–11, 1994.

[393] MU Saeed, BB Li, and ZF Chen. Mechanical effects of microchannels on fiber-reinforced composite structure. *Composite Structures*, 154:129–141, 2016.

[394] AM Coppola, PR Thakre, NR Sottos, and SR White. Tensile properties and damage evolution in vascular 3d woven glass/epoxy composites. *Composites Part A: Applied Science and Manufacturing*, 59:9–17, 2014.

[395] CY Huang, RS Trask, and IP Bond. Characterization and analysis of carbon fibre-reinforced polymer composite laminates with embedded circular vasculature. *Journal of the royal society Interface*, 7(49):1229–1241, 2010.

[396] CJ Norris, IP Bond, and RS Trask. The role of embedded bioinspired vasculature on damage formation in self-healing carbon fibre reinforced composites. *Composites Part A: Applied Science and Manufacturing*, 42(6):639–648, 2011.

[397] A Kousourakis and AP Mouritz. The effect of self-healing hollow fibres on the mechanical properties of polymer composites. *Smart Materials and Structures*, 19(8):085021, 2010.

[398] A Kousourakis, MK Bannister, and AP Mouritz. Tensile and compressive properties of polymer laminates containing internal sensor cavities. *Composites Part A: Applied Science and Manufacturing*, 39(9):1394–1403, 2008.

[399] K Shivakumar and A Bhargava. Failure mechanics of a composite laminate embedded with a fiber optic sensor. *Journal of composite materials*, 39(9):777–798, 2005.

[400] DJ Hartl, GJ Frank, and JW Baur. Effects of microchannels on the mechanical performance of multifunctional composite laminates with unidirectional laminae. *Composite Structures*, 143:242–254, 2016.

[401] ATT Nguyen and AC Orifici. Structural assessment of microvascular self-healing laminates using progressive damage finite element analysis. *Composites Part A: Applied Science and Manufacturing*, 43(11):1886–1894, 2012.

[402] DO Adams and SJ Bell. Compression strength reductions in composite laminates due to multiple-layer waviness. *Composites science and Technology*, 53(2):207–212, 1995.

[403] S Mukhopadhyay, MI Jones, and SR Hallett. Compressive failure of laminates containing an embedded wrinkle; experimental and numerical study. *Composites Part A: Applied Science and Manufacturing*, 73:132–142, 2015.

[404] S Eskandari, FMA Pires, PP Camanho, and AT Marques. Damage analysis of out of plane undulated fiber composites. *Composite Structures*, 152:464–476, 2016.

[405] R Talreja. Assessment of the fundamentals of failure theories for composite materials. *Composites Science and Technology*, 105:190–201, 2014.

[406] JL Chaboche. Continuum damage mechanics: Part ii—damage growth, crack initiation, and crack growth. *Journal of applied mechanics*, 55(1):65–72, 1988.

[407] J Lemaitre. How to use damage mechanics. *Nuclear engineering and design*, 80(2):233–245, 1984.

[408] P Ladeveze and E LeDantec. Damage modelling of the elementary ply for laminated composites. *Composites science and technology*, 43(3):257–267, 1992.

[409] ALJTR Matzenmiller, J Lubliner, and RL Taylor. A constitutive model for anisotropic damage in fiber-composites. *Mechanics of materials*, 20(2):125–152, 1995.

[410] P Maimí, PP Camanho, JA Mayugo, and CG Dávila. A continuum damage model for composite laminates: Part i–constitutive model. *Mechanics of Materials*, 39(10):897–908, 2007.

[411] A Hillerborg, M Modéer, and PE Petersson. Analysis of crack formation and crack growth in concrete by means of fracture mechanics and finite elements. *Cement and concrete research*, 6(6):773–781, 1976.

[412] R Krueger. Virtual crack closure technique: history, approach, and applications. *Applied Mechanics Reviews*, 57(2):109–143, 2004.

[413] AC Orifici, I Herszberg, and RS Thomson. Review of methodologies for composite material modelling incorporating failure. *Composite structures*, 86(1-3):194–210, 2008.

[414] SR Hallett, WG Jiang, B Khan, and MR Wisnom. Modelling the interaction between matrix cracks and delamination damage in scaled quasi-isotropic specimens. *Composites Science and Technology*, 68(1):80–89, 2008.

[415] PF Liu and JY Zheng. Recent developments on damage modeling and finite element analysis for composite laminates: A review. *Materials & Design*, 31(8):3825–3834, 2010.

[416] S Daggumati, W Van Paepegem, J Degrieck, J Xu, SV Lomov, and I Verpoest. Local damage in a 5-harness satin weave composite under static tension: Part ii–meso-fe modelling. *Composites Science and Technology*, 70(13):1934–1941, 2010.

[417] H Ullah, AR Harland, and VV Silberschmidt. Damage modelling in woven-fabric cfrp laminates under large-deflection bending. *Computational Materials Science*, 64:130–135, 2012.

[418] M Zako, Y Uetsuji, and T Kurashiki. Finite element analysis of damaged woven fabric composite materials. *Composites Science and Technology*, 63(3-4):507–516, 2003.

[419] A Doitrand, C Fagiano, F Hild, V Chiaruttini, A Mavel, and M Hirsekorn. Mesoscale analysis of damage growth in woven composites. *Composites Part A: Applied Science and Manufacturing*, 96:77–88, 2017.

[420] C Zhang, WK Binienda, RK Goldberg, and LW Kohlman. Meso-scale failure modeling of single layer triaxial braided composite using finite element method. *Composites Part A: Applied Science and Manufacturing*, 58:36–46, 2014.

[421] QD Yang and B Cox. Predicting failure in textile composites using the binary model with gauge-averaging. *Engineering Fracture Mechanics*, 77(16):3174–3189, 2010.

[422] L Wang, J Wu, C Chen, C Zheng, B Li, SC Joshi, and K Zhou. Progressive failure analysis of 2d woven composites at the meso-micro scale. *Composite Structures*, 178:395–405, 2017.

[423] M Meo, F Achard, and M Grassi. Finite element modelling of bridging micromechanics in through-thickness reinforced composite laminates. *Composite Structures*, 71(3-4):383–387, 2005.

[424] JT Vazquez, B Castanié, JJ Barrau, and N Swiergiel. Multi-level analysis of low-cost z-pinned composite joints: Part 1: Single z-pin behaviour. *Composites Part A: Applied Science and Manufacturing*, 42(12):2070–2081, 2011.

[425] F Bianchi and X Zhang. A cohesive zone model for predicting delamination suppression in z-pinned laminates. *Composites Science and Technology*, 71(16):1898–1907, 2011.

[426] AP Mouritz and TM Koh. Re-evaluation of mode i bridging traction modelling for z-pinned laminates based on experimental analysis. *Composites Part B: Engineering*, 56:797–807, 2014.

[427] G Allegri, M Yasaee, IK Partridge, and SR Hallett. A novel model of delamination bridging via z-pins in composite laminates. *International Journal of Solids and Structures*, 51(19-20):3314–3332, 2014.

[428] V Dantuluri, S Maiti, PH Geubelle, R Patel, and H Kilic. Cohesive modeling of delamination in z-pin reinforced composite laminates. *Composites science and technology*, 67(3-4):616–631, 2007.

[429] G Pappas, S Joncas, V Michaud, and J Botsis. The influence of through-thickness reinforcement geometry and pattern on delamination of fiber-reinforced composites: Part ii–modeling. *Composite Structures*, 181:379–390, 2017.